5. Chapter 5 - Damage evaluation using damage functions

5.1. Surface Recession

In order to predict the possible surface recession that can interest the materials belonging to the sites under study, the Lipfert function modified, according to Bonazza et al. (2009b), has been applied as follows:

$$L=K_{1,2}\cdot R$$

Where:

L: surface recession per year (μm year^{-1})

K_1: 18.8 intercept term based on the solubility of $CaCO_3$ in equilibrium with 330 ppm CO_2 (μm m^{-1})

K_2: 21.8 intercept term based on the solubility of $CaCO_3$ in equilibrium with 750 ppm CO_2 (μm m^{-1})

R: precipitation (m year^{-1})

We have utilized the rainfall data extracted from the monitoring stations and from the historic simulation of the models (for the past period), applying the K_1 constant (18.8). While parameters collected from the scenarios have been used for the future predictions.

Concerning the future, the surface recession predicted until the end of the century (2009-2100), has been obtained by utilizing the yearly total amount of precipitation from the Arpege scenarios FN2 (RCP 8.5); FN3 (RCP 4.5) and FN4 (RCP 2.6), and the 2039-2068 period of EC-Earth simulation, corresponding to 8.5 scenario. For the future, it has to be underlined that the constants utilized are two: one is K_1, the same utilized for the past situation, so equal to 18.8; while the other one is K_2 = 21.8, which represents the intercept term based on the solubility of $CaCO_3$ in equilibrium with 750 ppm CO_2 (μm m^{-1}), in order to enlarge the range and considering the most pessimistic situation.

Moreover, since this function is valid only for carbonate rocks having a porosity lower than 25%, the following stones containing calcium carbonate and with accessible porosity percentage not exceeding 25, have been selected among the typologies present at the sites, as a representation of what kind of stones can be interested by this deterioration phenomenon (Fig. 5.1.1).

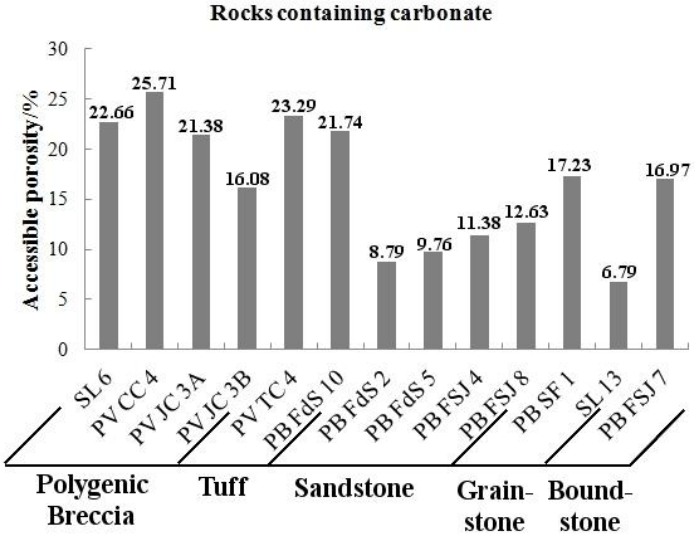

Figure 5.1. 1. Histogram showing rocks containing carbonate, with accessible porosity lower than 25 %.

5.1.1. Panamá Viejo area

Past

At Panamá Viejo area (Long.-79.45; Lat.9.1), the surface recession of the past situation (1979-2008) obtained by the data from monitoring stations shows a slight increase in the thirty years period, in both graphs (Fig. 5.1.2). The range is between 28-50 µm year^{-1}, considering the mean of values of Hato Pintado (HP) and Tocumen (T), while in Balboa FAA the minimum is 23 µm year^{-1}and maximum is 54 µm year^{-1}. The EC-Earth climate simulation shows a trend of a small increase, with a tendency similar to the measured data, while the Arpege-FN1 model presents a light decrease. In both cases, the minimum and maximum values are generally overestimated, respectively 33-52 µm year^{-1} (EC-Eart point Long. -79.45, Lat. 9.1), 36-53 µm year^{-1} (Arpege-FN1 point Long. -79.50; Lat 9.24), and 29-48 µm year^{-1} (EC-Earth: Long. -79.6, Lat. 8.9) and 25-56 µm year^{-1} (Arpege-FN1 point Long. -79.5; Lat. 8.74).

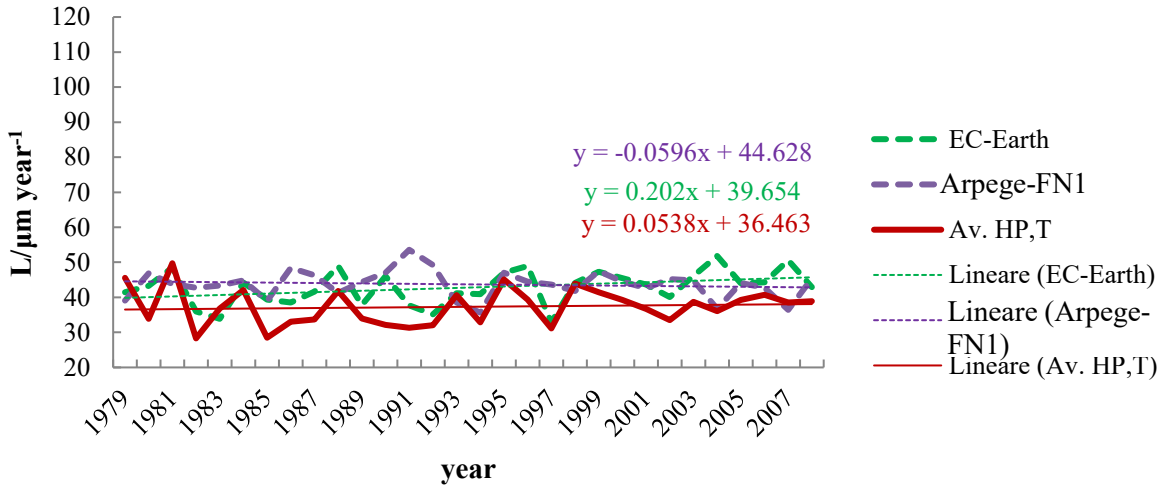

Figure 5.1. 2. Surface Recession on carbonate stones in Panamá Viejo area (1979-2008).

Applying the bias correction, the trend results similar to the previously illustrated ones, but the range describes better the surface recession obtained with the data collected from the monitoring stations, as shown in Table 5.1.1, where the average and the maximum and minimum values, of measured and simulated data, are listed and compared.

Table 5.1. 1 Comparison among the average, minimum and maximum values obtained from the 30 years (1979-2008), between monitoring stations and model data of the Panamá Viejo area.

L = R*18.8 / µm year^{-1}

	Av. HP + T	EC-Earth	EC-Earth + f_P	Arpege-FN1	Arpege-FN1 + f_P
Average	36	43	38	44	38
Minimum	28	33	29	36	31
Maximum	50	52	46	54	46

Future

In Panamá Viejo area (Arpege point Long.-79.50; Lat.9.24 and EC-Earth point Long. -79.45; Lat. 9.1), the surface recession range is among ≈ 30 μm year^{-1}, in the optimistic situation, and ≈ 70 μm year^{-1}, if we consider the worst situation. Every Arpege simulations shows an increase over the 90 years, while considering EC-Earth experiment, the tendency has a slight decrease (Figs. 5.1.3-4). This trend is present in each condition considered, so utilizing both constants and applying bias correction or not. Nevertheless, we have to take into account that it represents only the central 30 years (2039-2068), of the entire Arpege period.

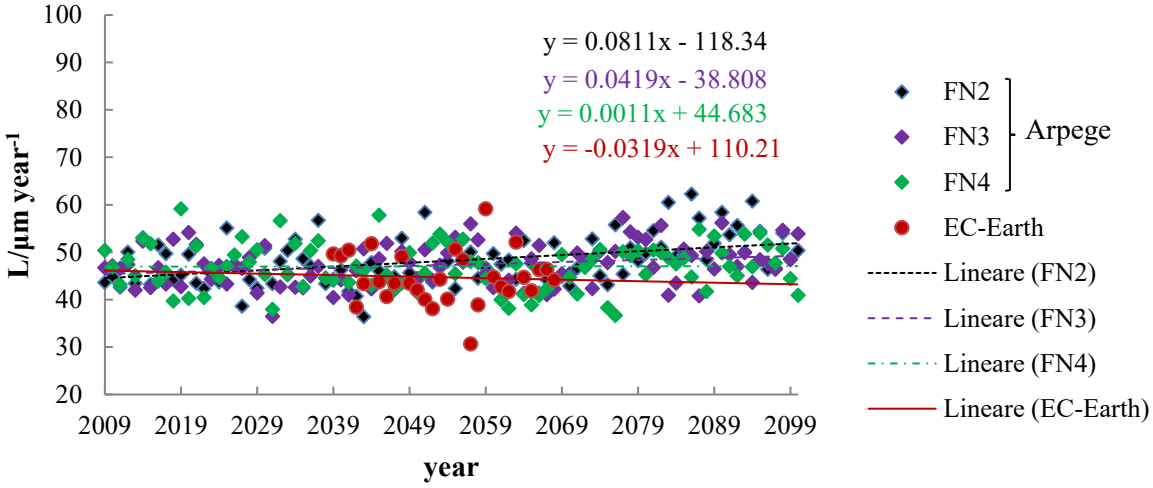

Figure 5.1. 3. Future (2009-2100) surface recession simulations for the Panamá Viejo area, utilizing L = R*18.8, data without bias correction.

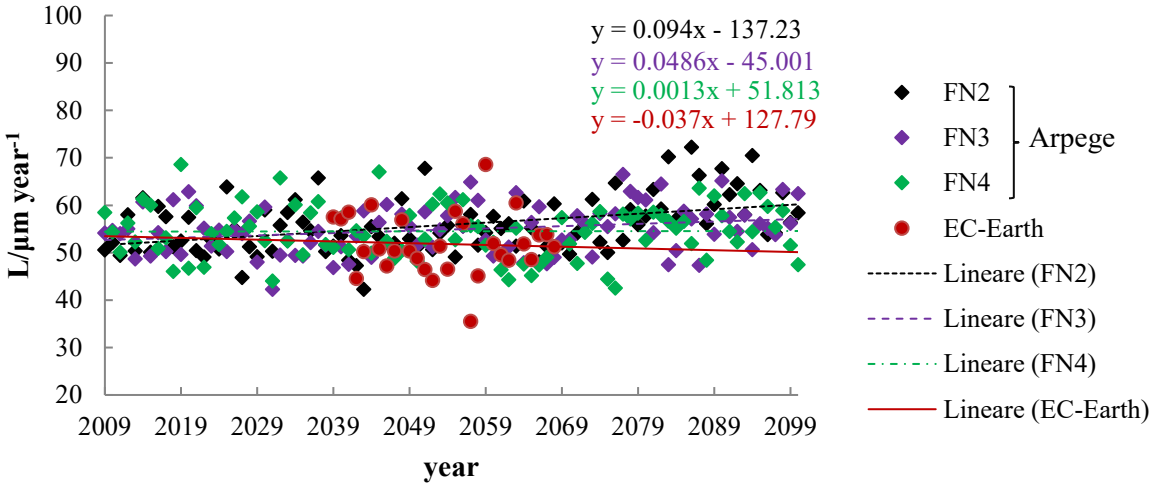

Figure 5.1. 4. Future (2009-2100) surface recession simulation for the Panamá Viejo area, utilizing L = R*21.8, data without bias correction.

In order to realize a more detailed comparison between the Arpege and EC-Earth simulation, it has been analysed the central period between 2039 and 2068 years (Tab. 5.1.2). It can be noticed that the values obtained by the application of L = R*21.8 are 6 to 8 μm year^{-1} higher than the one obtained by using L = R*18.8.

Table 5.1. 2. Comparison of the surface recession (L) values of average, minimum and maximum of the Arpege and EC-Earth simulations obtained for the future period, divided in 30 years, applying or not bias correction.

		L = R*18.8 / µm year^{-1}								L = R*21.8 / µm year^{-1}							
		Arpege								Arpege							
		FN2		FN3		FN4		EC-Earth		FN2		FN3		FN4		EC-Earth	
			+ f_P		+ f_P		+ f_P		+ f_P		+ f_P		+ f_P		+ f_P		+ f_P
2009-2038	**Av.**	47	40	46	40	48	41			54	47	53	46	55	47		
	Min.	39	33	36	31	38	33			45	39	42	36	44	38		
	Max.	57	49	54	47	59	51			66	57	63	54	69	59		
2039-2068	**Av.**	46	40	47	40	46	39	45	39	54	46	54	47	53	46	52	46
	Min.	36	31	40	35	38	33	31	27	42	36	47	40	44	38	36	31
	Max.	58	50	56	48	58	50	59	52	68	58	65	56	67	58	69	60
2069-2100	**Av.**	51	44	49	42	48	41			59	51	57	49	55	47		
	Min.	43	37	41	35	37	32			50	43	47	41	43	37		
	Max.	62	54	57	49	55	47			72	62	66	57	64	55		

5.1.2. Area near Panamá Viejo

Past

Considering the area next to Panamá Viejo (covered by the Arpege point Long.-79.50; Lat.8.74 and EC-Earth point Long. -79.6; Lat. 8.9), the recession obtained by Balboa FAA data has a range with a minimum of 23 µm year^{-1} and maximum of 54 µm year^{-1}, showing a slight increase in the thirty years period (1979-2008), as in the previous case. Both the simulations have the same trend observed at Panamá Viejo area, with the minimum and maximum values overestimated, respectively 29-48 µm year^{-1}, EC-Earth: Long. -79.6, Lat. 8.9, and 25-56 µm year^{-1}, Arpege-FN1 point Long. -79.5; Lat. 8.74 (Fig. 5.1.5).

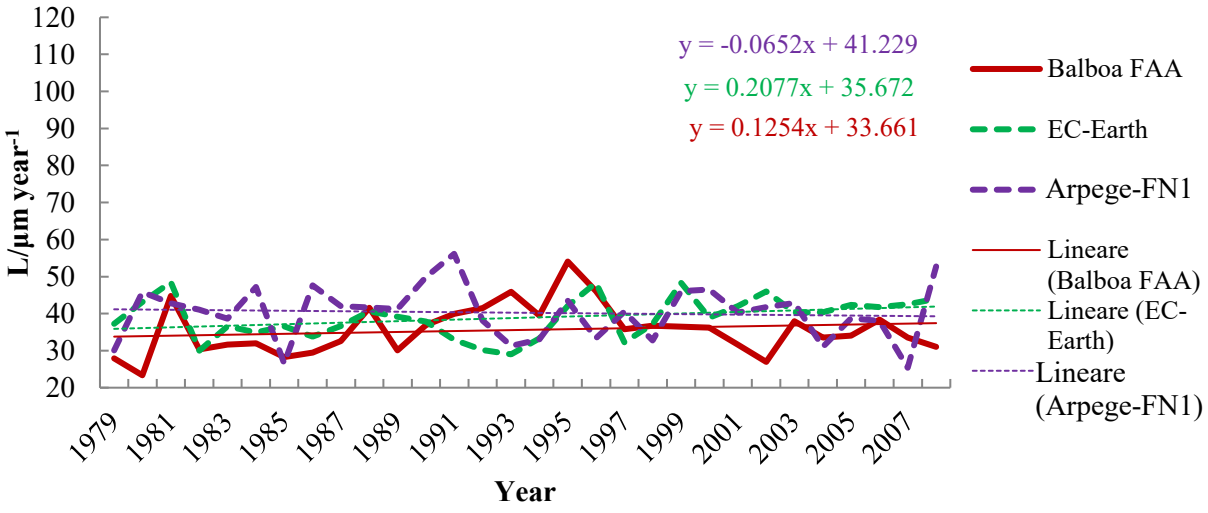

Figure 5.1. 5. Recession on carbonate stones near Panamá Viejo area (1979-2008).

Applying the bias correction, the range of surface recession obtained by the simulations describes better the surface recession with the data collected from the Balboa FAA monitoring stations (Tab.5.1.3), where the average and the maximum and minimum values, of measured and simulated data, are listed and compared.

Table 5.1. 3. Comparison among the average, minimum and maximum values obtained from the 30 years (1979-2008), between monitoring stations and model data of the area near Panamá Viejo.

L = R*18.8 / µm year^{-1}

	Balboa FAA	EC-Earth	EC-Earth + f_P	Arpege-FN1	Arpege-FN1 + f_P
Average	36	39	32	40	36
Minimum	23	29	23	25	23
Maximum	54	48	39	56	50

Future

In the future, the recession calculated with Arpege-FN2 and FN3 simulation shows a slight increase during the century, while with Arpege-FN4 and EC-Earth the situation is opposite, presenting a low decrease (Figs. 5.1.6-7). The range of surface recession average values obtained by applying K_2 constant shows a difference of 7-8 µm year^{-1} in comparison with the range calculated through the utilization of K_1 constant. While, considering the differences between the situation without bias to the condition corrected, the range shows a decrease of 4-5 µm year^{-1} for the predictions obtained with Arpege, and of 7-9 µm year^{-1} for the predictions obtained with EC-Earth (Table 5.1.4).

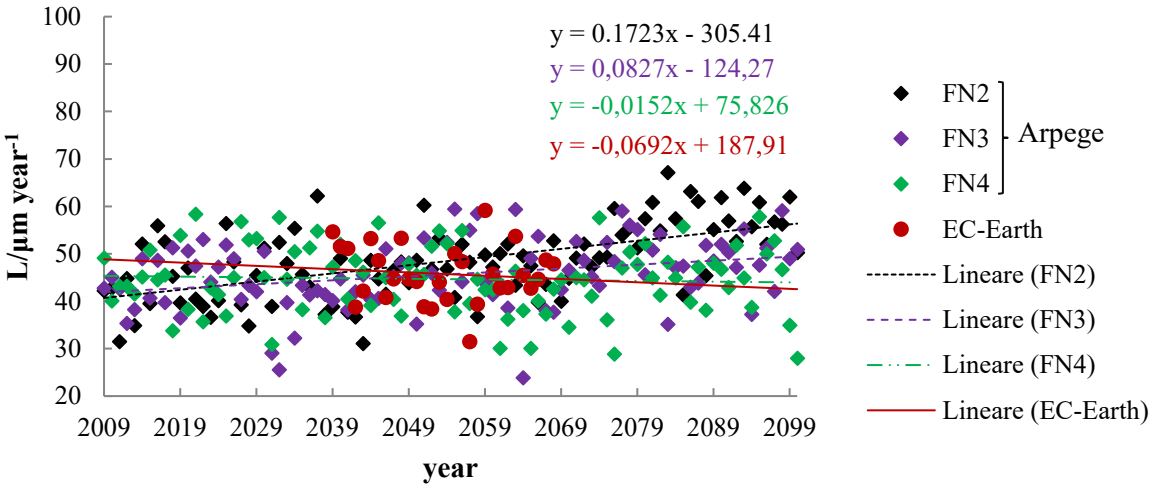

Figure 5.1. 6. Future (2009-2100) surface recession simulations for the simulation for the area near Panamá Viejo, utilizing L = R*18.8, data without bias correction.

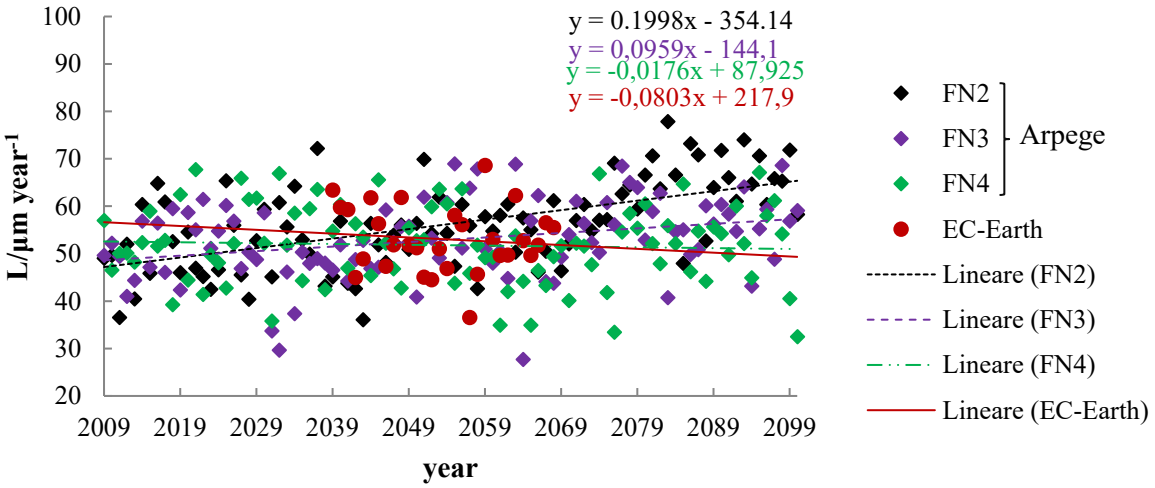

Figure 5.1. 7. Future (2009-2100) surface recession simulations for the simulation for the area near Panamá Viejo, utilizing L = R*21.8, data without bias correction.

Table 5.1. 4. Comparison of the surface recession (L) values of average, minimum and maximum of the Arpege and EC-Earth simulations obtained for the future period, divided in 30 years, applying or not bias correction.

		L = R*18.8 / µm year^{-1}								L = R*21.8 / µm year^{-1}							
		Arpege								Arpege							
		FN2		FN3		FN4		EC-Earth		FN2		FN3		FN4		EC-Earth	
			+ f_P		+ f_P		+ f_P		+ f_P		+ f_P		+ f_P		+ f_P		+ f_P
2009-2038	**Av.**	45	40	43	38	45	40			52	46	50	44	53	47		
	Min.	32	28	26	23	31	27			37	33	30	26	36	32		
	Max.	62	55	53	47	58	52			72	64	61	55	68	60		
2039-2068	**Av.**	46	41	45	40	44	39	46	37	53	47	53	47	51	45	53	43
	Min.	31	28	24	21	30	27	32	26	36	32	28	25	35	31	37	30
	Max.	60	54	59	53	57	50	59	48	70	62	69	61	66	58	69	56
2069-2100	**Av.**	55	49	49	43	45	40			63	56	56	50	52	46		
	Min.	40	36	35	31	28	25			46	41	41	36	32	29		
	Max.	67	60	59	53	58	51			78	69	69	61	67	60		

5.1.3. Area near San Lorenzo

Past

In the area in the proximity of San Lorenzo (Long.-79.85, Lat. 9.3), covered by the following points: EC-Earth Long.-79.85; Lat. 9.3; and Arpege-FN1 Long.-80.00; Lat. 9.24, the average of monitoring stations data has been compared to the simulated one. Although the measured data shown some peaks of minimum and maximum values quite different from the model experiments, the range of values and the tendency is quite well represented by EC-Earth model (Fig. 5.1.8 and Tab. 5.1.5).

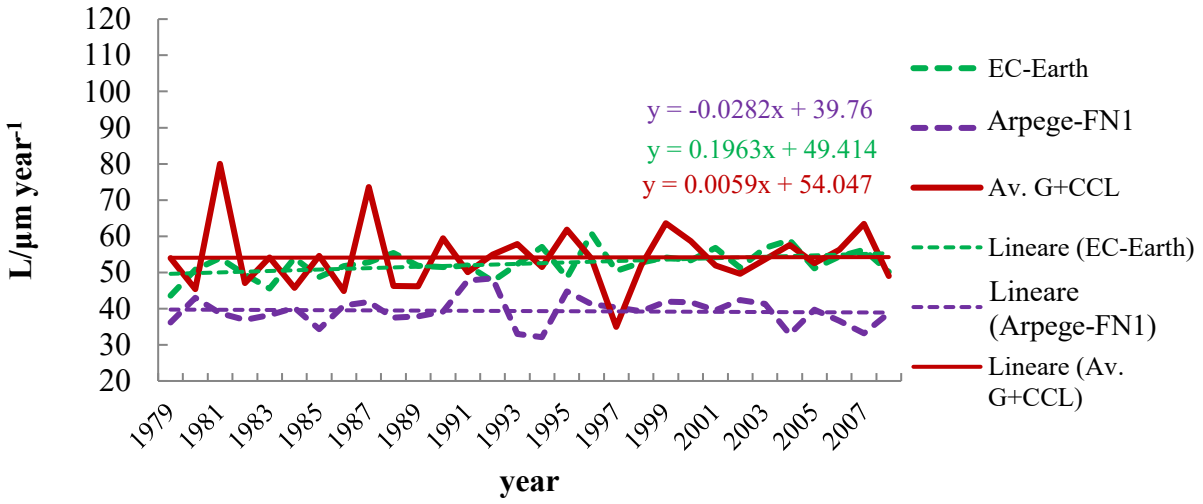

Figure 5.1. 8. Surface Recession on carbonate stones near San Lorenzo area (1979-2008).

Table 5.1. 5. Comparison among the average, minimum and maximum values obtained from the 30 years (1979-1998), between monitoring stations and model data of the area near San Lorenzo.

L = R*18.8 / µm year^{-1}

	Av. G+CCL	**EC-Earth**	**EC-Earth + f_P**	**Arpege-FN1**	**Arpege-FN1 + f_P**
Average	35	44	55	32	55
Minimum	80	61	45	48	45
Maximum	35	44	63	32	67

Future

Considering the future, the surface recession obtained by all Arpege simulations shows an increase during the entire century, while the one calculated with EC-Earth experiment has a slow decrease (Figs. 5.1.9-10). The range difference between the results obtained by applying the 21.8 constant shows higher values of 6-7 µm year^{-1} than the ones calculated with 18.8 constant. While between the Lipfert function calculated with and without bias the differences presented are of 16-19 µm year^{-1}, considering the recession obtained by Arpege, whereas considering EC-Earth the difference is lower of 2 µm year^{-1} (Tab.5.1.6). Finally, the range values of recession calculated by EC-Earth are higher than the ones obtained by Arpege.

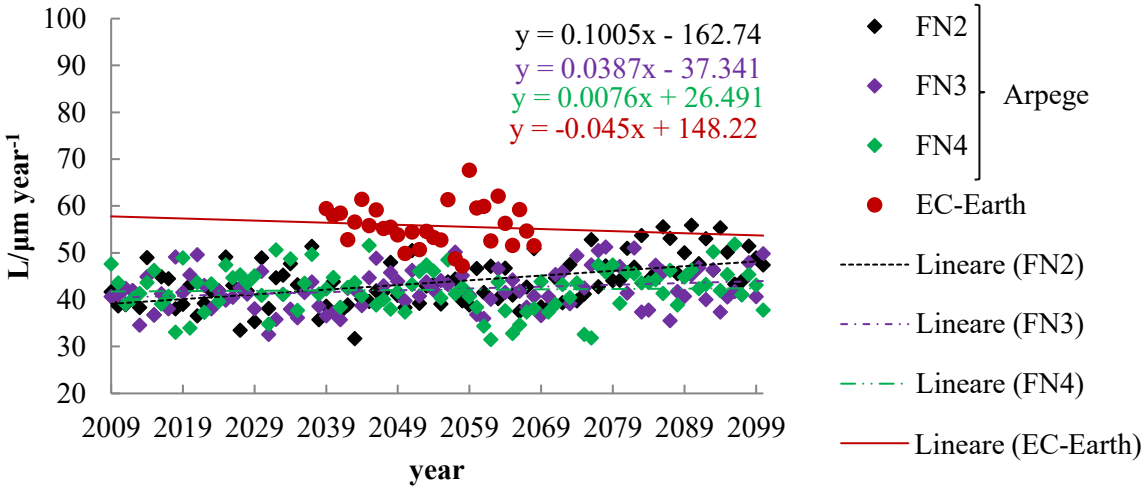

Figure 5.1. 9. Future (2009-2100) surface recession simulation for the area near San Lorenzo, utilizing L = R*18.8, data without bias correction.

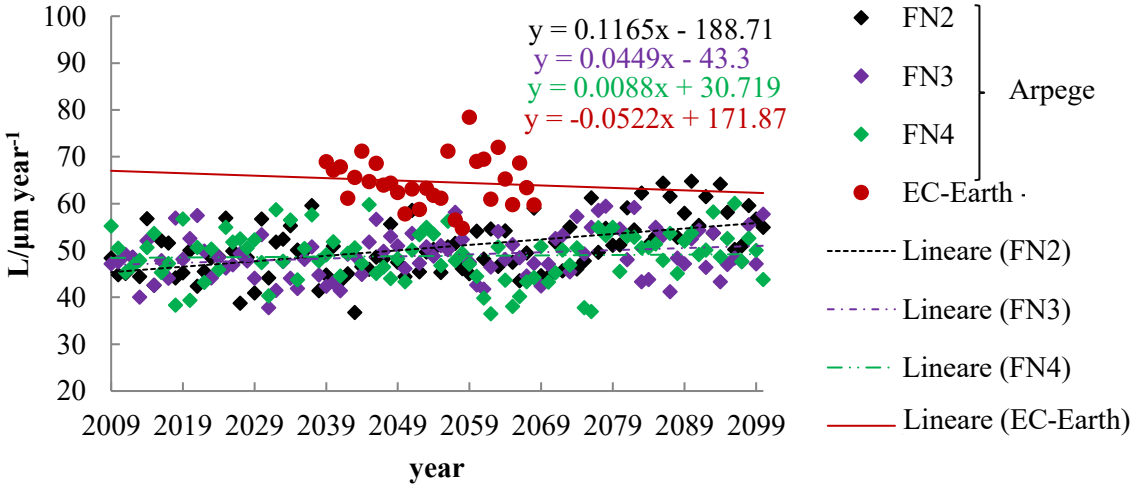

Figure 5.1. 10. Future (2009-2100) surface recession simulation for the area near San Lorenzo, utilizing L = R*21.8, data without bias correction.

Table 5.1. 6. Comparison of the surface recession (L) values of average, minimum and maximum of the Arpege and EC-Earth simulations obtained for the future period, divided in 30 years, applying or not bias correction.

		L = R*18.8 / µm year^{-1}								L = R*21.8 / µm year^{-1}							
		Arpege								Arpege							
		FN2		FN3		FN4		EC-Earth		FN2		FN3		FN4		EC-Earth	
			+ f_P		+ f_P		+ f_P		+ f_P		+ f_P		+ f_P		+ f_P		+ f_P
2009-2038	**Av.**	42	58	41	57	42	59			48	67	47	66	49	68		
	Min.	33	46	33	45	33	46			39	54	38	52	38	53		
	Max.	51	71	50	69	51	70			60	83	57	80	59	82		
2039-2068	**Av.**	42	58	42	58	41	57	56	58	49	67	49	68	47	66	65	67
	Min.	32	44	36	50	31	44	47	49	37	51	41	57	37	51	55	57
	Max.	51	71	50	70	52	72	68	70	59	82	58	81	60	83	78	82
2069-2100	**Av.**	47	65	44	61	43	60			55	76	51	70	50	69		
	Min.	38	53	36	49	32	44			44	62	41	57	37	51		
	Max.	56	78	51	71	52	72			65	90	59	83	60	83		

5.1.4. San Lorenzo area

Past

At San Lorenzo (Long.-80.05; Lat. 9.3), the compared period was of 19 years, 1979-1998 (1994 year is missing). As evident in Figure 5.1.11, the values of the Pina stations are higher than the simulated one. Therefore, the bias correction is necessary and observing the values present in Table 5.1.7, after applying it the average is similar to the Pina one. Nevertheless, the range is still smaller than the measured one and the trend is quite different.

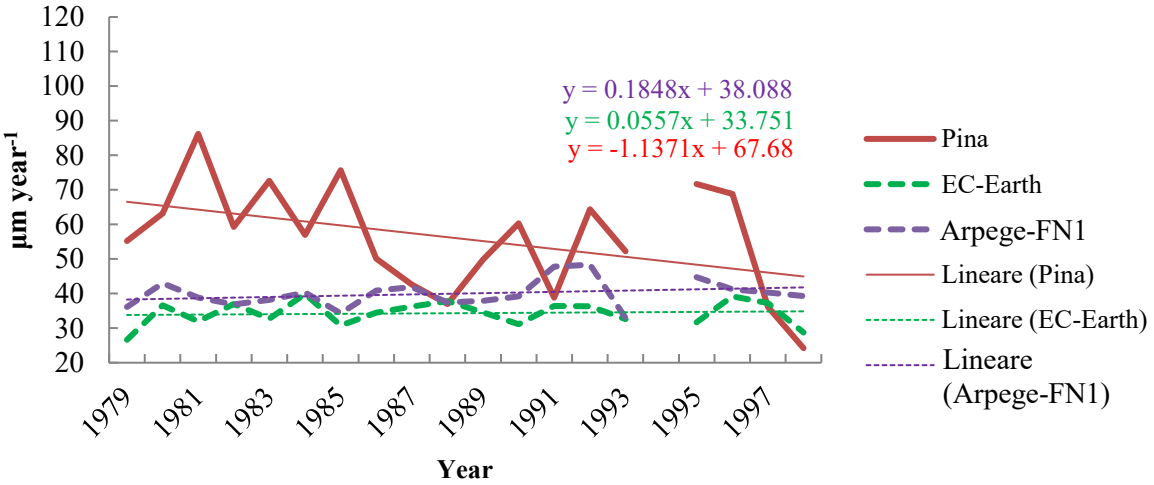

Figure 5.1. 11. Surface Recession on carbonate stones at San Lorenzo area (1979-2008).

Table 5.1. 7. Comparison among the average, minimum and maximum values obtained from the 19 years (1979-1998, 1994 missing), between monitoring stations and model data of the area of San Lorenzo.

L = R*18.8 / µm year^{-1}

	Pina	**EC-Earth**	**EC-Earth + f_P**	**Arpege-FN1**	**Arpege-FN1 + f_P**
Average	56	34	58	40	58
Minimum	24	27	45	33	48
Maximum	86	40	67	48	70

Future

The recession calculated by Arpege simulations is the same of the previous one, since the 50x50 km grid area covers also this part. As well as the previous area, in this case EC-Earth Lipfert function shows a slow decrease, but with an interval of values similar to the ones obtained by Arpege

simulation (Figs. 5.1.12-13). The differences between the function calculated with the corrected rainfall and the equivalent without bias are always higher, considering Arpege and smaller regarding EC-Earth, while the difference between the application of the two different constant are, for both models, around 6-7 µm year^{-1} (Table 5.1.8).

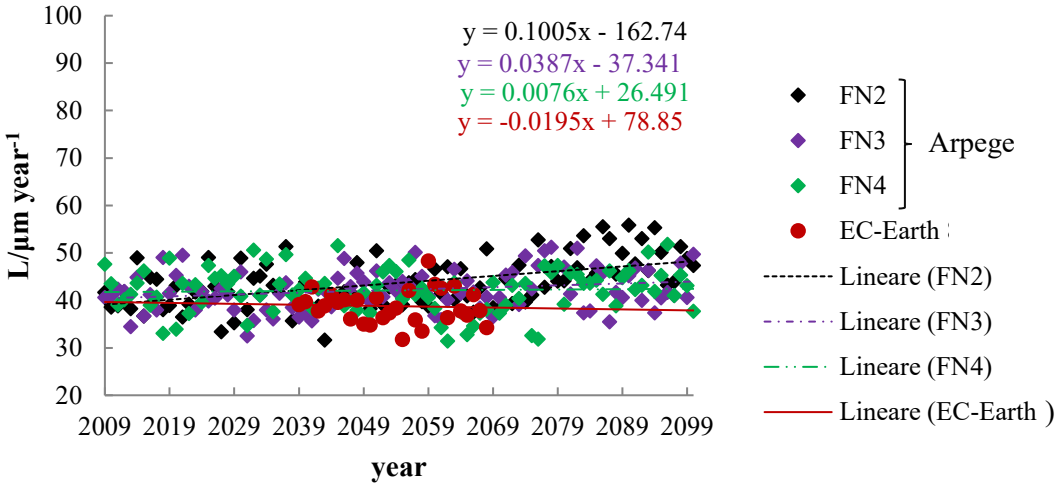

Figure 5.1. 12. Future (2009-2100) surface recession simulation for the area of San Lorenzo, utilizing L = R*18.8, data without bias correction.

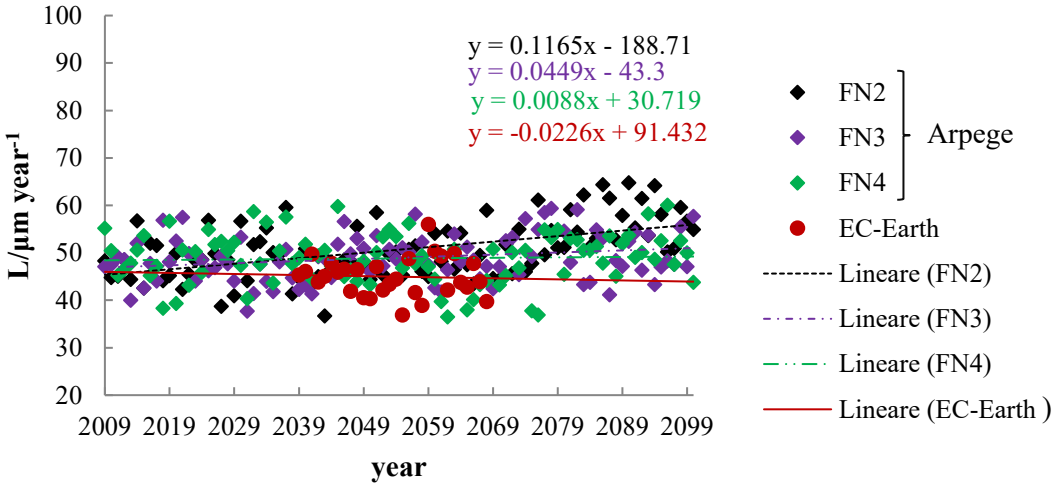

Figure 5.1. 13. Future (2009-2100) surface recession simulation for the area of San Lorenzo, utilizing L = R*21.8, data without bias correction.

Table 5.1. 8. Comparison of the surface recession (L) values of average, minimum and maximum of the Arpege and EC-Earth simulations obtained for the future period, divided in 30 years, applying or not bias correction.

		L = R*18.8 / µm year^{-1}								L = R*21.8 / µm year^{-1}							
		Arpege								Arpege							
		FN2		FN3		FN4		EC-Earth		FN2		FN3		FN4		EC-Earth	
			+ f_P		+ f_P		+ f_P		+ f_P		+ f_P		+ f_P		+ f_P		+ f_P
2009-2038	**Av.**	42	61	41	59	42	62			48	70	47	69	49	71		
	Min.	33	48	33	47	33	48			39	56	38	55	38	56		
	Max.	51	74	50	72	51	73			60	86	57	83	59	85		
2039-2068	**Av.**	42	61	42	61	41	59	39	65	49	70	49	71	47	69	45	76
	Min.	32	46	36	52	31	46	32	53	37	53	41	60	37	53	37	62
	Max.	51	74	50	73	52	75	48	81	59	86	58	84	60	87	56	94
2069-2100	**Av.**	47	68	44	63	43	62			55	79	51	73	50	72		
	Min.	38	55	36	51	32	46			44	64	41	60	37	54		
	Max.	56	81	51	74	52	75			65	94	59	86	60	87		

5.1.5. Portobelo area

Past

In Portobelo area the situation is the opposite, since the climate simulations underestimate the quantity of 20 years of surface recession, with maximum values of 118 µm year-1, obtained utilizing the monitoring stations data, almost 50 µm year^{-1} more than the modelled ones. While the minimum results more comparable, respectively 50 µm year^{-1} for the station, 51 for EC-Earth (Long. -79.65, Lat. 9.55) and 33 µm year^{-1} for Arpege-FN1 (Long. -79.50, Lat. 9.74). The trend of monitoring stations data is better represented by EC-Earth model, which show a slight increase (Fig. 5.1.14).

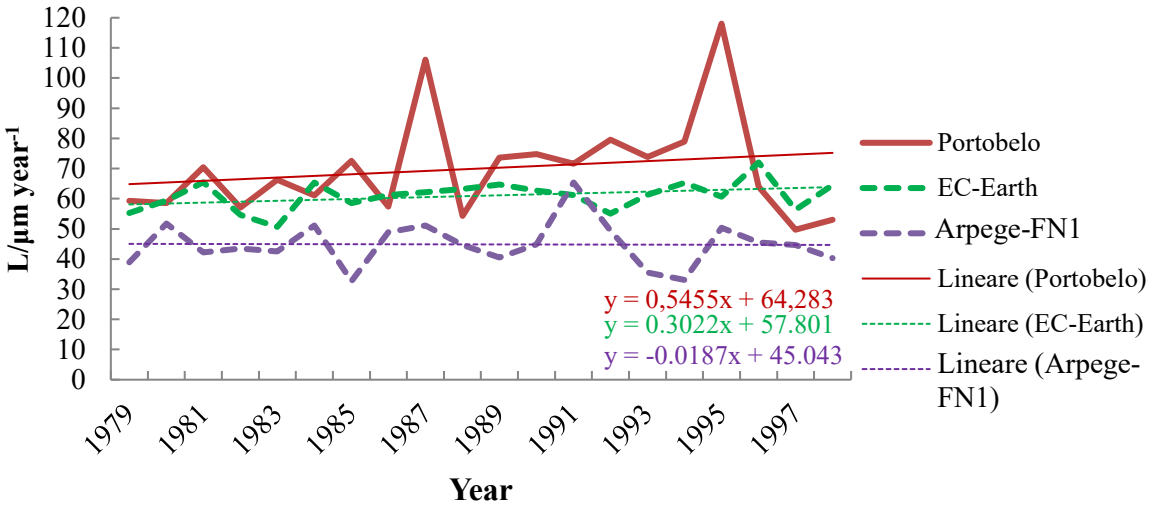

Figure 5.1. 14. Surface Recession on carbonate stones in Portobelo area (1979-1998).

Considering the bias correction, EC-Earth trend comes up to Portobelo station, even if the range is still underestimated by both simulations as noticeable in Table 5.1.9.

Table 5.1. 9. Comparison among the average, minimum and maximum values obtained from the 20 years (1979-1998), between monitoring stations and model data of the Portobelo area.

L = R*18.8 / µm year^{-1}

	Portobelo	**EC-Earth**	**EC-Earth + f_P**	**Arpege-FN1**	**Arpege-FN1 + f_P**
Average	70	61	69	45	69
Minimum	50	51	58	33	50
Maximum	118	72	82	65	101

Future

The future trend of surface recession is different considering the function applied with data form Arpege model respect to EC-Earth one. Indeed, the first one presents a slight increase in the future, while the second one shows a decrease, for the 2039-2068 period. Moreover, the EC-Earth-recession has a range of values higher compared with the same thirty years of Arpege projections (Figs. 5.1.15-16). The differences between the recession obtained by the corrected parameters with bias are similar to the previous ones described, while the difference between the application of the two different constants show an increment of ≈ 8 μm year^{-1}, in the case of Arpege, and ≈ 10 μm year^{-1} considering EC-Earth (Table 5.1.10).

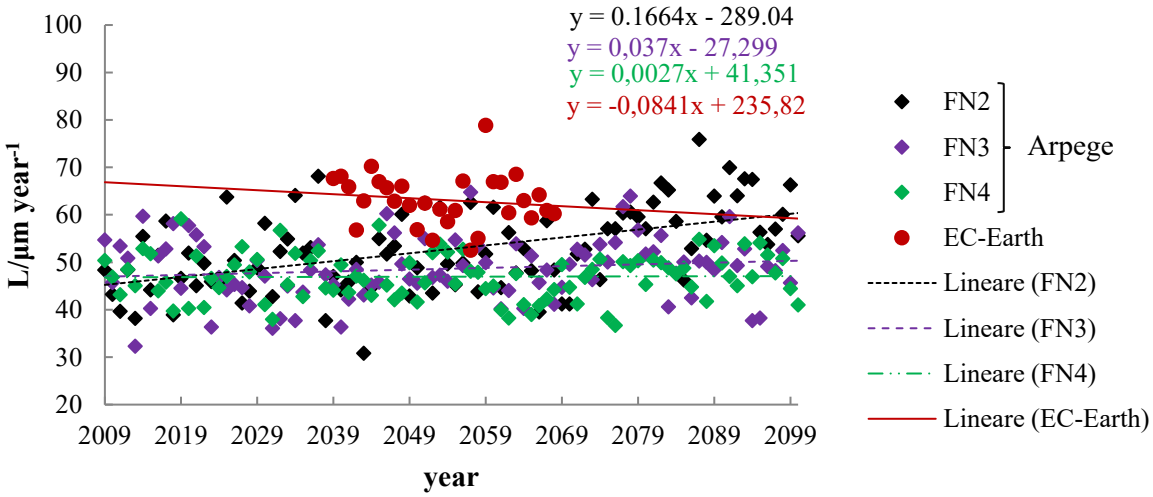

Figure 5.1. 15. Future (2009-2100) surface recession simulations for the simulation for the area of Portobelo, utilizing L = R*18.8, data without bias correction.

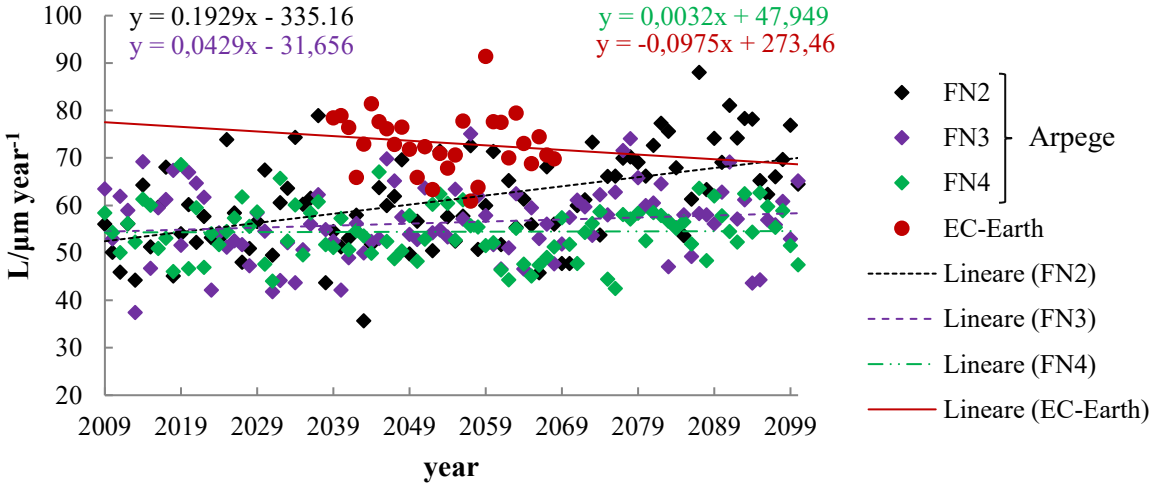

Figure 5.1. 16. Future (2009-2100) surface recession simulations for the simulation for the area of Portobelo, utilizing L = R*21.8, data without bias correction.

Table 5.1. 10. Comparison of the surface recession (L) values of average, minimum and maximum of the Arpege and EC-Earth simulations obtained for the future period, divided in 30 years, applying or not bias correction.

		L = R*18.8 / μm year^{-1}								L = R*21.8 / μm year^{-1}							
		Arpege								Arpege							
		FN2		FN3		FN4		EC-Earth		FN2		FN3		FN4		EC-Earth	
			+ f_P		+ f_P		+ f_P		+ f_P		+ f_P		+ f_P		+ f_P		+ f_P
2009-2038	**Av.**	49	76	47	73	47	77			57	88	55	84	55	89		
	Min.	38	58	32	50	38	60			44	67	37	58	44	70		
	Max.	68	105	60	92	59	100			79	122	69	107	69	116		
2039-2068	**Av.**	50	77	48	74	46	73	63	72	58	89	56	86	53	85	73	83
	Min.	31	47	36	56	38	47	53	60	36	55	42	65	44	55	61	69
	Max.	63	96	65	100	58	94	79	90	73	112	75	116	67	109	91	104
2069-2100	**Av.**	59	90	51	78	48	78			68	105	59	90	55	90		
	Min.	41	63	38	58	37	47			48	74	44	67	43	54		
	Max.	76	117	64	98	55	104			88	136	74	114	64	121		

5.1.6. Maps of Surface Recession

For comparing the results obtained for the past and the future situation, in order to understand better the differences between future-past and among the future predictions applying the two constants, K_1 = 18.8 and K_2 = 21.8, the Lipfert function under EC-Earth scenario has been plotted in an area of 100x100 km covering the partial Panama region, subject of this study. Since the resolution of EC-Earth is 25x25 km, we have obtained a grid of 4x4 areas, overlapping the Panamanian borders, as shown in the following maps. It has also to be underlined that the surface recession, hereafter graphed, is presented without bias correction for both the past and future simulations.

Considering the past simulated surface recession, the area of Portobelo is the most affected by this phenomenon, which shows values higher than 70 μm year^{-1}, as previously described. Instead, San Lorenzo area resulted as the less interested by it, with average values around 30 μm year^{-1}, followed by Panamá Viejo zone, with 40 μm year^{-1} (Fig. 5.1.6.1a).

The estimation of future surface recession calculated with L = 18.8*R (Fig. 5.1.6.1b), is similar to the past situation, but with a slight increase of 2 μm year^{-1} at Panamá Viejo and 4 μm year^{-1} at San Lorenzo, while Portobelo doesn't show any variations (as detectable in Figure 5.1.6.3a). While, if we consider the pessimistic future projection, applying L = 21.8*R (Fig. 5.1.6.2a), the increase respect to the optimistic future estimation of surface recession is of 10 μm year^{-1} at Portobelo, of 7 μm year^{-1} at Panamá Viejo and of 6 μm year^{-1} at San Lorenzo (Fig. 5.1.6.2b).

Therefore, the difference between the L = 21.8*R future and the L = 18.8*R past estimation of surface recession is around 12 μm year^{-1} near the area of San Lorenzo (Gatun, Cocosolo, Fort Sherman area), of 11 μm year^{-1} at Portobelo, of 10 μm year^{-1} at San Lorenzo and around 9 μm year^{-1} at Panamá Viejo (Fig. 5.1.6.3b).

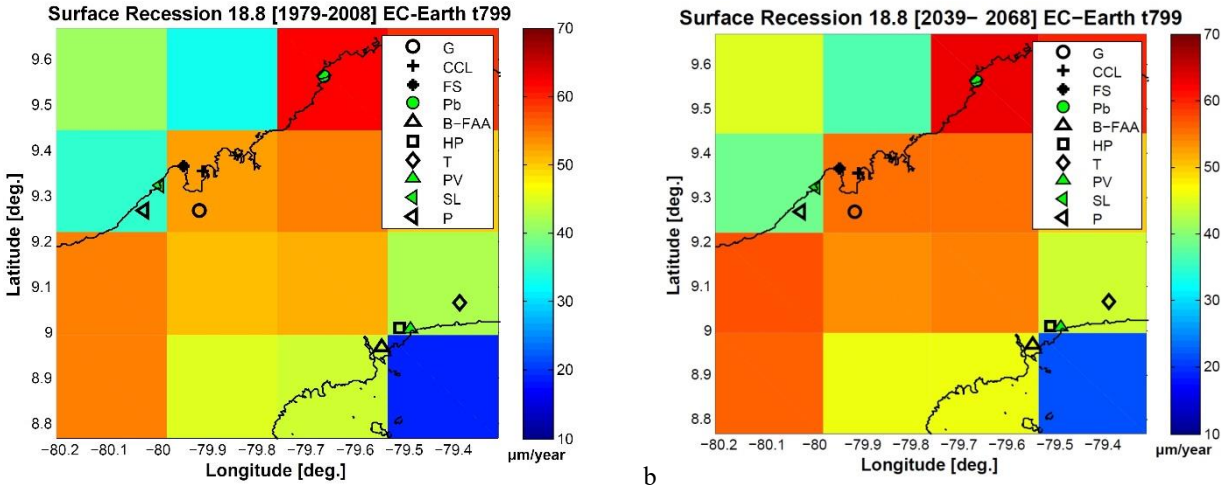

a b

Figure 5.1.6. 1. Estimated surface recession (L=18.8*R) under EC-Earth scenario.
a. For the past period 1979–2008 (baseline); b. For the middle future period (2039-2068).

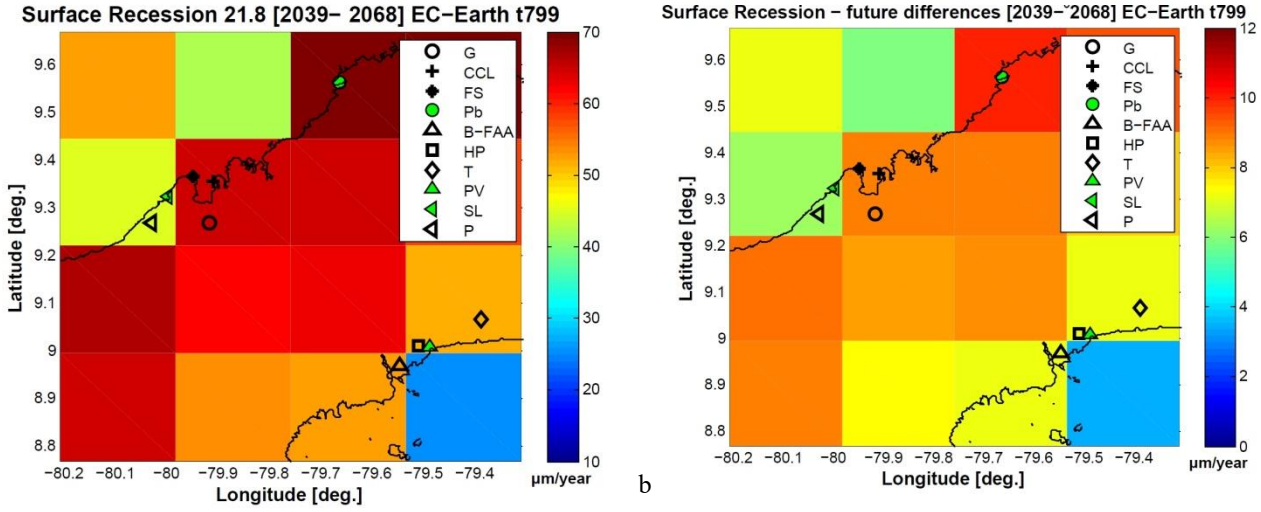

a b

Figure 5.1.6. 2. Middle future period (2039-2068): a. Estimated surface recession (L=21.8*R) under EC-Earth scenario;
b. Differences between the estimated future surface recessions under EC-Earth scenario applying the two constants: (L_1=21.8*R) - (L_2=18.8*R).

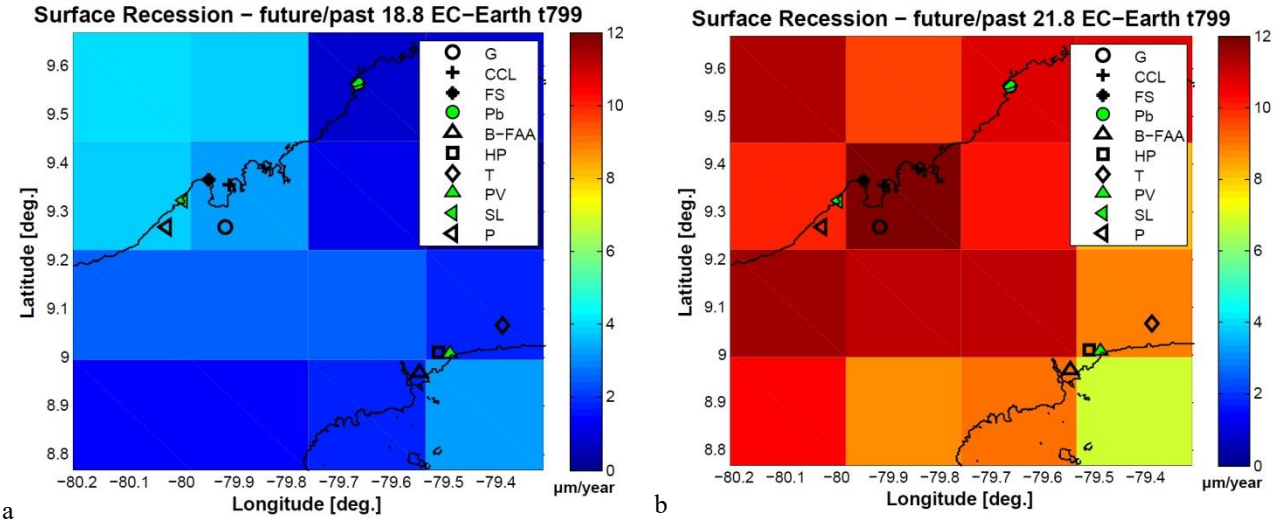

a b

Figure 5.1.6. 3. Differences between the estimated future surface recessions under EC-Earth scenario future - past: a. utilizing for the future projection (L=18.8*R); b. utilizing for the future projection (L=21.8*R).

Final remarks

While the situation in the area of Panamá Viejo and surroundings is quite similar between the two models, the prediction for the northern areas, Portobelo and San Lorenzo are significantly different, showing a major surface recession if we consider the EC-Earth experiment.
In order to understand the future trend, it can be considered the middle future estimation (2039-2068) of surface recession under Arpege scenarios, which shows an increase respect to the past estimation from 6 μm $year^{-1}$, measured at Panamá Viejo area, to 10 μm $year^{-1}$ at San Lorenzo area. Considering the EC-Earth projections, it also shows an increase higher at San Lorenzo area and surroundings than at Panamá Viejo.
Therefore, it can be assumed that in the future the site situated at the North Panamanian coast can be more affected by surface recession, related to the karst effect, than the site at South coast.

5.2. Salt Transitions

In considering the salts cycles of dissolution and crystallization, halite has been selected as priority phase of investigation, since sodium and chloride resulted ones of the most abundant ions in the stone samples, detected in all sites, also taking into account their proximity to the sea.
In the following paragraphs, the past and future monthly transitions of NaCl are represented, considering as an event the passage from RH values higher than 75.3% to values smaller than this threshold, counted only if happened in consecutive days. In addition, since the temperature of existence of this process should be 25°C, and, especially the future scenarios show highest temperatures, it has been considered also 75.1% as threshold, corresponding to the RH of NaCl transition at 30°C (Grossi et al., 2011; Sabbioni et al., 2012).
Finally, only data from EC-Earth simulations are presented, since this model has been demonstrated to be the most representative one in terms of relative humidity and temperature parameters reliability.

5.2.1. Panamá Viejo area

Past

In Panamá Viejo area, only Tocumen station presented relative humidity data, therefore the following comparison have been realized with only its records. As clearly observable, the highest frequency of these transitions are concentrated during the dry season, from the end of December until the beginning of April, both considering data with or without bias correction and utilizing the two thresholds, as observable in Figure 5.2.1. It has to be taken into account also the temperature, which shows an average of 26°C in this period, with the highest values present during the dry season, when the average is equal to 27°C. Nevertheless, if we make a comparison between the two threshold of RH applied, 75.3% (Fig. 5.2.1a) and 75.1% (Fig.5.2.1b), the number of cycles does not undergo significant variations.

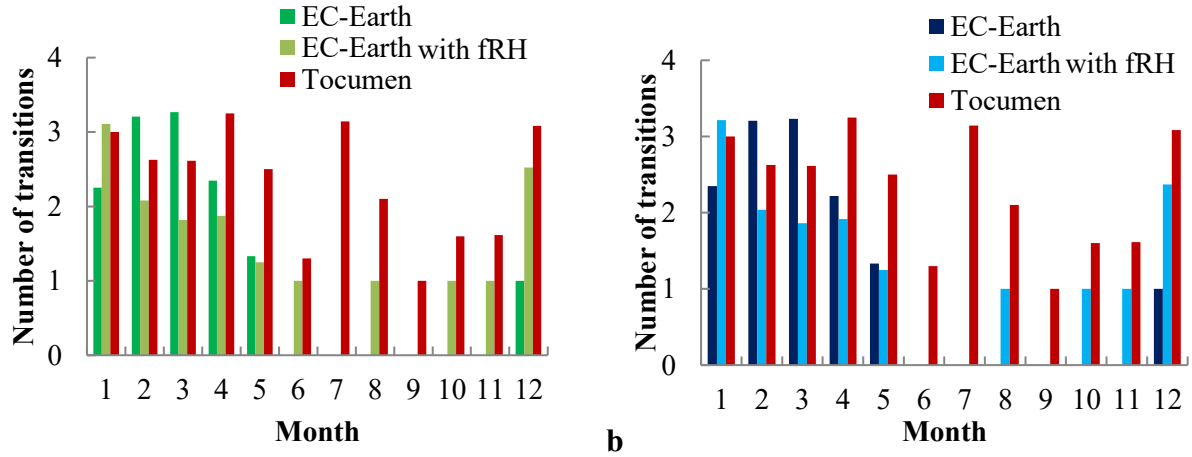

Figure 5.2. 1. Average of NaCl monthly transitions 1979-2008 in Panamá Viejo area.
a. considering 75.3% as threshold; b. considering 75.1% .

Future

Considering the future condition, the temperature situation is the same of the past one, presenting an average, over the thirty years, of 26°C, while it correspond to 27°C applying the bias. Therefore the utilization of the two thresholds (75.1% and 75.3%) shows a similar monthly trend of the halite transitions, especially regarding the model with the bias correction. In this latter case, the number of cycles will be more frequent during the dry season (end of November/December to April/beginning of May). Nevertheless, observing Figure 5.2.2, it has to be noticed that the month with the highest value resulted July, but this value is due to only one year (2057), thus overestimating the number of cycles for this period. In any case, the future situation results quite similar to the past, with only a slight decrease in the number of months interested by NaCl cycles over the thirty years: in consideration of EC-Earth simulation, 5 future months versus 6 past months, while the model projection with bias presents 9 future months versus 10 past months.

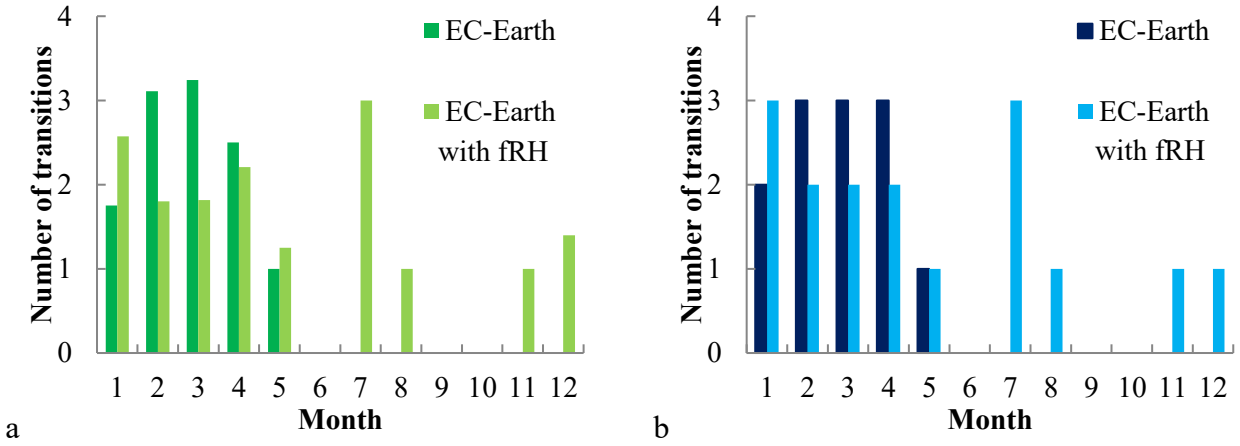

Figure 5.2. 2. Average of NaCl monthly transitions 2039-2068 in Panamá Viejo area.
a. considering 75.3% as threshold; b. considering 75.1% .

5.2.2. Area near Panamá Viejo

Past

In order to have another idea of the surroundings of Panamá Viejo, the area close to the site has been taken into account. The average of temperature of the past period, 1979-2008, is 27°C at Balboa FAA monitoring station, while EC-Earth simulation measures an average of T 25°C without f_T and 27°C with f_T. In this case, observing the halite cycles obtained by the monitoring station data the months with the highest number of transitions are from May to August, period underestimate by EC-Earth experiment. However, the rest of the year is well represented utilizing both the thresholds (Fig. 5.2.3).

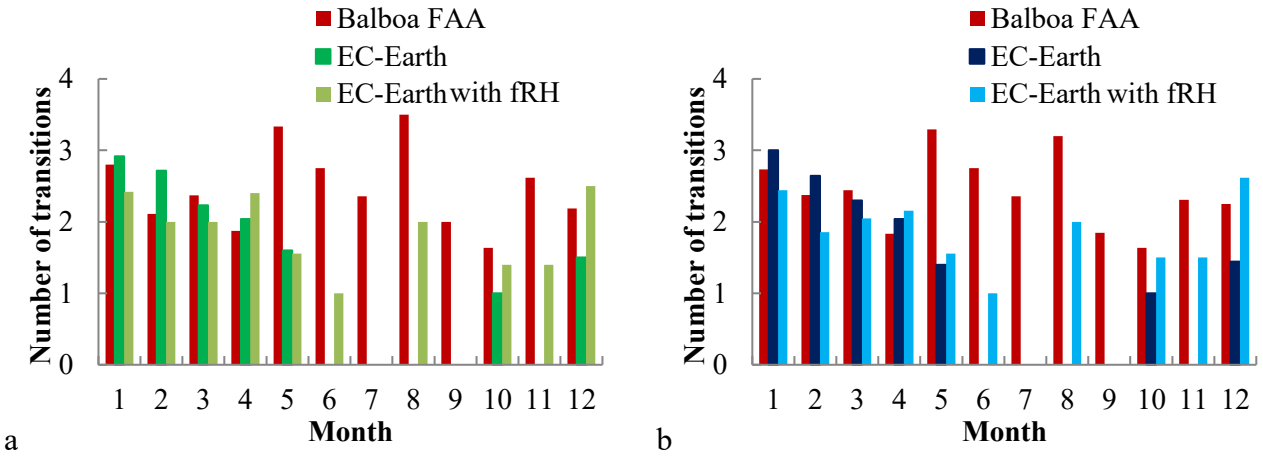

Figure 5.2. 3. Average of NaCl monthly transitions 1979-2008 near Panamá Viejo area.
a. considering 75.3% as threshold; b. considering 75.1% .

Future

In the future, the temperature undergoes an increase, indeed the average of T obtained by EC-Earth is 27°C, with the bias 29°C, thus in this case the most suitable situation should be represented by utilizing the 75.1% of threshold. The months showing the highest and most frequent values are from December to May, during the dry season. In addition, in this case, 2057 year presents cycles of halite also during the rainy season, in particular in July (Fig. 5.2.4).

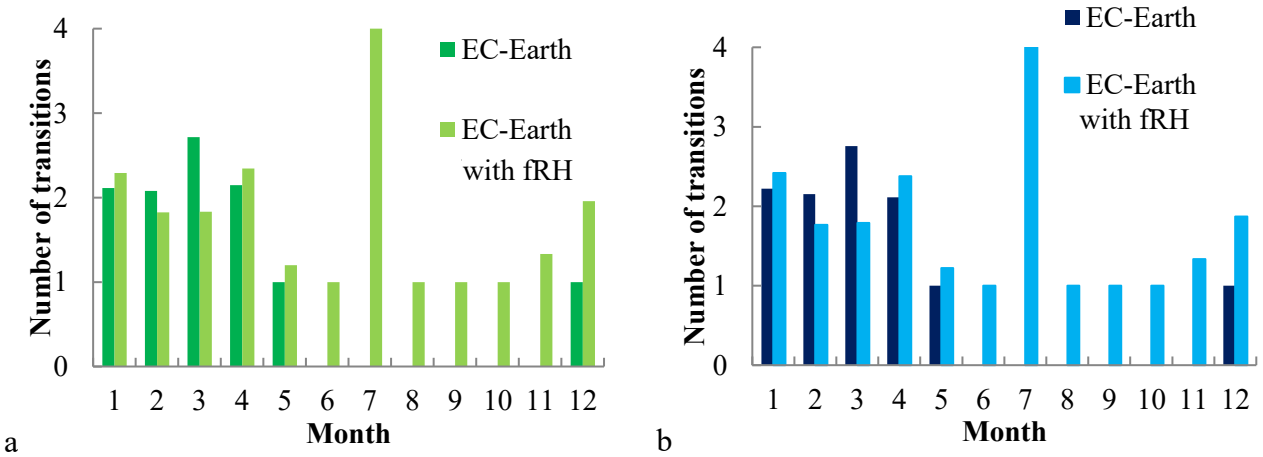

Figure 5.2. 4. Average of NaCl monthly transitions 2039-2068 near Panamá Viejo area.
a. considering 75.3% as threshold; b. considering 75.1% .

5.2.3. Area near San Lorenzo

Past

In the area near San Lorenzo, the period under study is from 1979 to 2004, since the other years are missing. During this period, at Gatun station the yearly average of T is of 27°C, without showing variations during the annual period. Considering EC-Earth experiment, the T average is of 25°C without applying f_T and 27°C applying f_T. As previously observed, also in this case the number of cycles of the dry season are well represented by the model simulation, while the rainy season is partially underestimated (Fig.5.2.5).

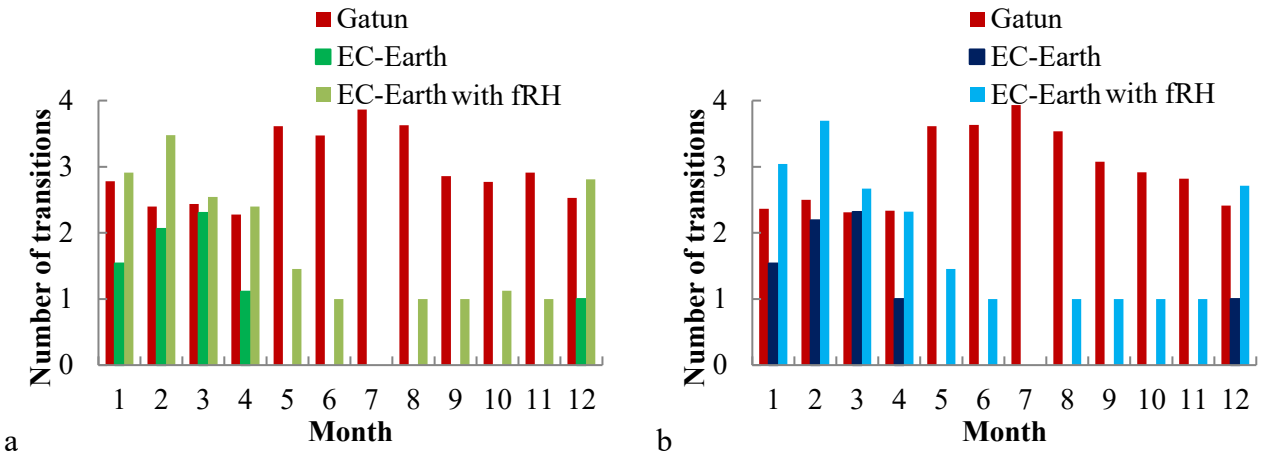

Figure 5.2. 5. Average of NaCl monthly transitions 1979-2004 near San Lorenzo area.
a. considering 75.3% as threshold; b. considering 75.1% .

Future

The future average of T simulated is of 26°C, adding the bias 29°C, therefore the most suitable situation should be represented by utilizing the 75.1% of threshold. Observing the distribution of the halite cycles, they result spread all over the year, with an increase during the driest season (Fig.5.2.6). Furthermore, making a comparison with the modelled past situation, it does not show significant variations, except a slight increase, since every month show at least one cycle.

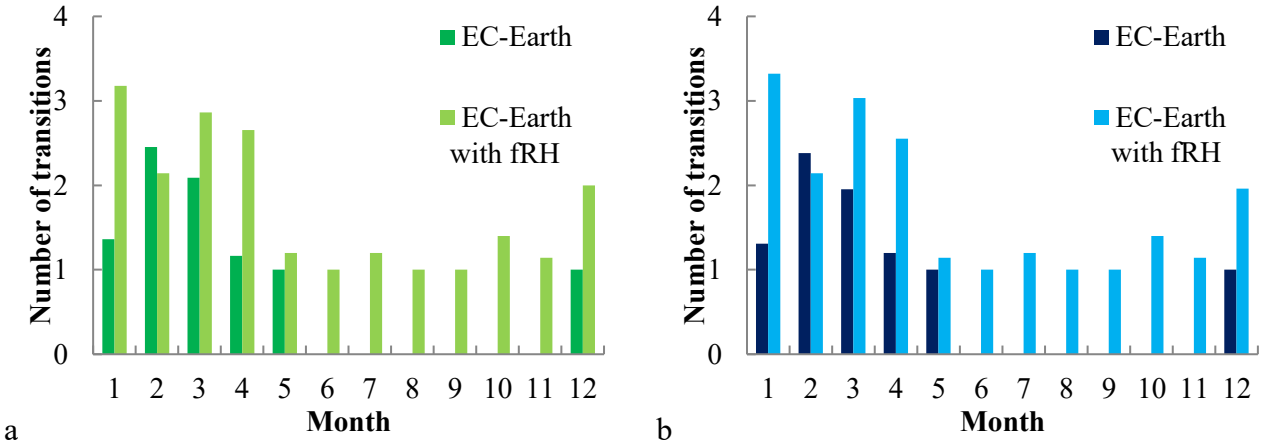

Figure 5.2. 6. Average of NaCl monthly transitions 2039-2068 near San Lorenzo area.
a. considering 75.3% as threshold; b. considering 75.1%.

5.2.4. San Lorenzo area

Past

Considering the area of San Lorenzo, there are no records of monitoring stations data. Thus, basing on the EC-Earth data, the T average is of 25°C (Fig.5.2.7a), thus the most suitable situation is represented by the use of 75.3% of threshold. Number of halite cycles are concentrated in proximity of the dry season, from October to April, included (Fig. 5.2.7b).

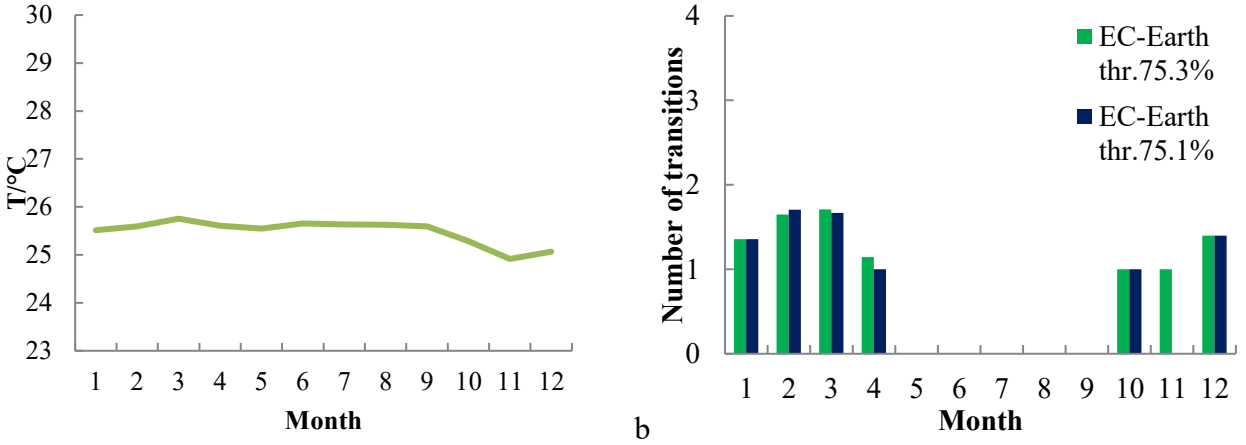

Figure 5.2. 7. 1979-2008 San Lorenzo area: a. average of monthly T over the thirty years; b. average of NaCl monthly transitions considering 75.3% and 75.1% thresholds.

Future

In the future situation, whit a T average of 27°C (Fig.5.2.8a), we can consider both the thresholds. In comparison with the past, it can be observed an increase of the period interested by the salts cycles, from September to May, included (Fig.5.2.8b).

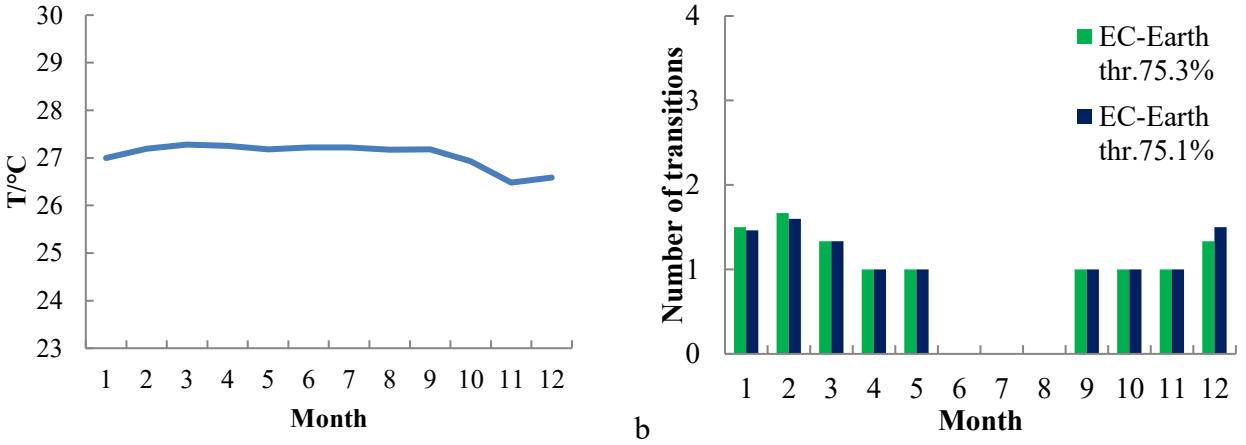

Figure 5.2. 8. 2039-2068 San Lorenzo area: a. average of monthly T over the thirty years; b. average of NaCl monthly transitions considering 75.3% and 75.1% thresholds.

5.2.5. Portobelo area

Past

As the previous case, also at Portobelo there are no records of monitoring stations data. Therefore, considering only the simulation, and with a T average of 24°C (Fig.5.2.9a), the most suitable situation is represented by the use of 75.3% of threshold. Cycles of halite are very scarce all over the year (one per month) and concentrated from December until April, included (Fig.5.2.9b).

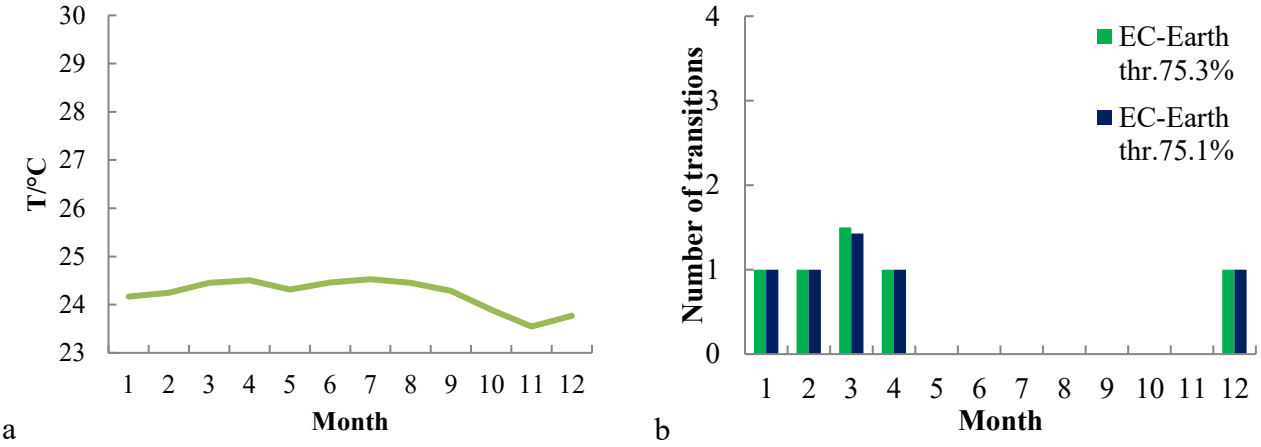

Figure 5.2. 9. 1979-2008 Portobelo area: a. average of monthly T over the thirty years; b. average of NaCl monthly transitions considering 75.3% and 75.1% thresholds.

Future

Considering the future situation, with a T average of 26°C (Fig.5.2.10a), the most suitable situation is always represented by the use of 75.3% of threshold. The NaCl cycles are always very low, and in this case there is an opposite situation respect the previous ones, indeed the period of cycles is reduced to four months, especially from January to April (Fig.5.2.10b).

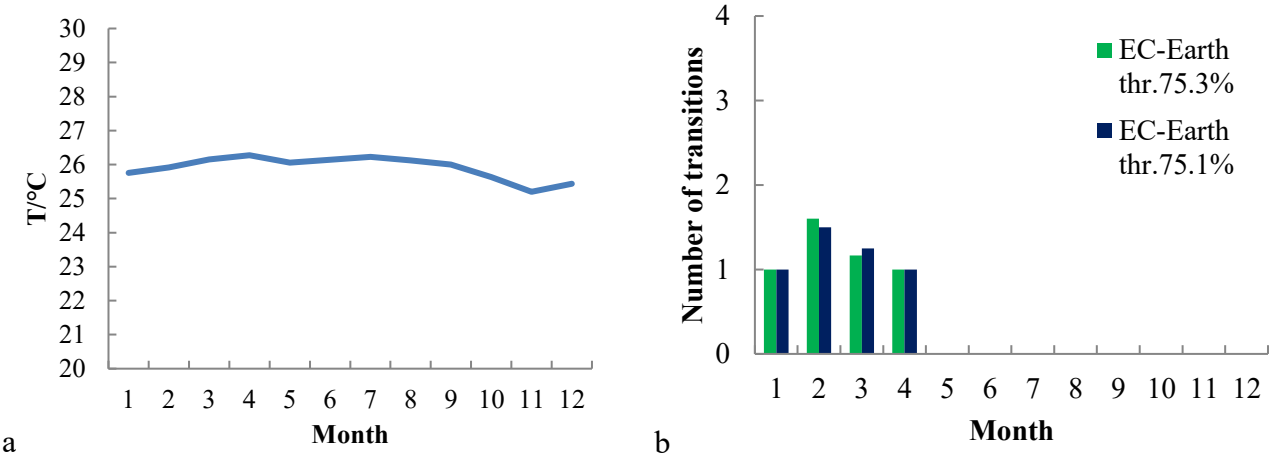

Figure 5.2. 10. 2039-2068 Portobelo area: a. average of monthly T over the thirty years; b. average of NaCl monthly transitions considering 75.3% and 75.1% thresholds.

Final remarks

Cycles of dissolution and crystallization of halite salt have been analyzed, highlighting the higher frequency of this phenomenon during the dry season (reaching 3-4 cycles per month). Nevertheless, it has to be taken into account the underestimation, done by the EC-Earth simulation, of the rainy season months in comparison with the monitoring station data. However, we have to bear in mind that the monitoring station represent a punctual situation and not an area, as the model simulation.

Making a comparison between the past and future conditions, generally the period of cycles tends to have a slight increase in the future, as observed in the area near Panamá Viejo, near San Lorenzo and San Lorenzo; while at Panamá Viejo and Portobelo area the trend is opposite.

Evaluating the difference between the sites, Portobelo results the less interested by this phenomenon, while the area near San Lorenzo should be the most affected.

5.3. Biomass Accumulation

As observed macroscopically and through analysis under microscope, one of the most diffused deterioration phenomenon is due to biological growth.
In order to estimate the biomass accumulation on hard acid stones, calculated considering the organic carbon accretion on the surfaces, we used the function developed by Gomez-Bolea et al. (2012). Where the quantity of biomass B (originally milligrams, but here expressed in grams), on surface unit (cm^{-2}) is obtained applying the annual amount of precipitation P (mm) and the annual mean of temperature T (°C) in the following expression:

$$B = \exp^{(-0.964 + 0.003P - 0.01T)}$$

Even if this function has been validated for horizontal surfaces of hard acid stones in nonurban European environments, it can allow us to understand the possible future trend of this phenomenon in comparison with the past situation.
In our case, the hard acid rocks are the rhyolites, the alterated rhyodacites and the polygenic breccias showing high amount of silica (see Chap. 3.4).

5.3.1. Panamá Viejo area

Past
Between the two models simulations, with and without bias, the most representative of the biomass accumulation obtained by the observed data is due to Arpege-FN1 without bias, showing a trend almost identical to the monitoring stations one (Figs. 5.3.1-2). Indeed, even if it overestimates of 0.2 g cm^{-2} the accumulation calculated with the measured data at Tocumen and Hato Pintado, the tendency over the past 30 years shows the same slight decrease of ≈ 0.02 g cm^{-2}. While considering the range, EC-Earth without bias show the most similar with the one represented by the observed data. It has to be mentioned that the bias for the precipitation was calculated from both the monitoring stations data, while the temperature additional factor has been obtained only form Tocumen series, since Hato Pintado missed T data.

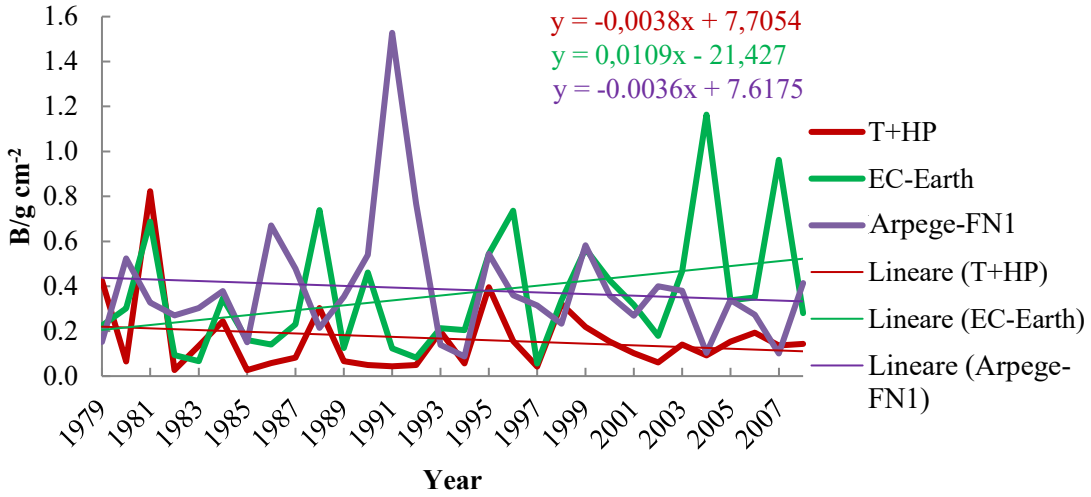

Figure 5.3. 1. Biomass accumulation (g cm^{-2}) at Panamá Viejo area (1979-2008): comparison between model simulations and the monitoring stations.

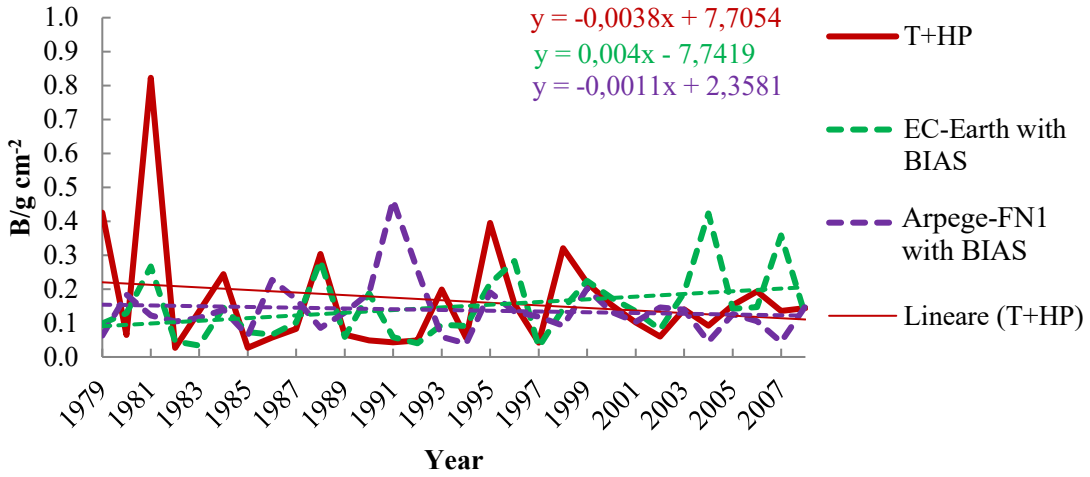

Figure 5.3. 2. Biomass accumulation (g cm^{-2}) at Panamá Viejo area (1979-2008): comparison between model simulations with bias and monitoring stations.

Future

Considering the future situation, Arpege-FN2 and FN3, both considering the function with or without the factor correction show an increase of the biomass range from the near future (2009-2038) to the far future (2069-2100), more consistent for Arpege-FN2. This latter one, during the middle future (2039-2068), presents average, minum and maximum similar to the accumulation obtained by EC-Earth data, without bias. Every simulation shows a strong decrease of the values applying the f_p and f_T (Tab. 5.3.1).

Moreover all the simulations show a slow increase during the future period, higher for Arpege-FN2 (of ≈1 g cm^{-2}) over the 90 years, except for Arpege-FN3 which has a very little decrease. Indeed, this one and EC-Earth are approximable to an invariant tendency (Fig. 5.3.3).

Table 5.3. 1. Future (2009-2100) biomass (g cm^{-2}) range of values (average, minimum and maximum) for the area of Panamá Viejo.

		Arpege							
		FN2		FN3		FN4		EC-Earth	
			+ f_p & f_T		+ f_p & f_T		+ f_p & f_T		+ f_p & f_T
2009-2038	av.	0.67	0.23	0.55	0.19	0.80	0.26		
	min.	0.14	0.06	0.10	0.04	0.13	0.05		
	max.	2.51	0.73	1.69	0.52	3.72	1.03		
2039-2068	av.	0.62	0.21	0.67	0.23	0.60	0.20	0.55	0.21
	min.	0.10	0.04	0.19	0.08	0.13	0.06	0.04	0.02
	max.	3.30	0.92	2.23	0.66	2.99	0.85	3.73	1.18
2069-2100	av.	1.44	0.43	0.91	0.29	0.73	0.24		
	min.	0.27	0.11	0.20	0.08	0.10	0.05		
	max.	5.96	1.54	2.75	0.79	1.87	0.57		

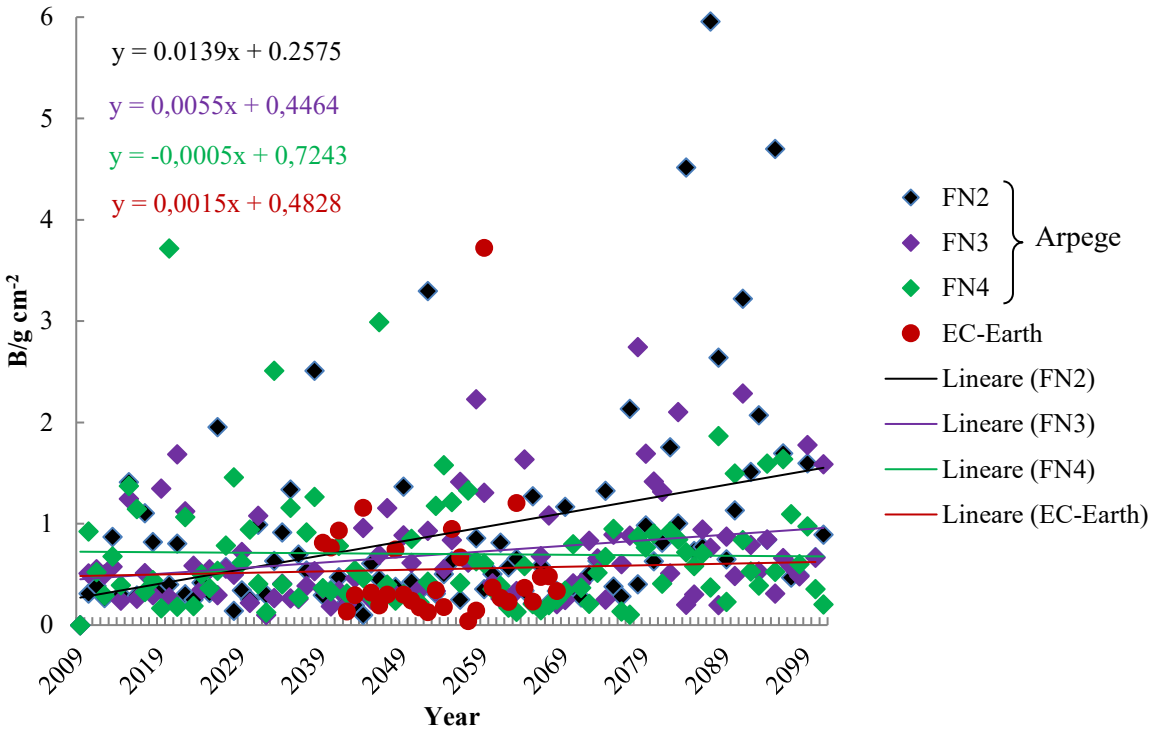

Figure 5.3. 3. Future (2009-2100) yearly biomass for the area of Panamá Viejo.

5.3.2. Area near Panamá Viejo

Past

In order to have the same period covered by measured and simulated data, 1983 and 2003 years are omitted since the Balboa FAA monitoring station showed lack of data in that years.

As previously observed, Arpege-FN1 is the simulation which better represents the biomass accumulation trend obtained by the observed data; indeed both show an approximable invariant tendency during the 30 years, both considering the climate parameters without or with bias (Figs. 5.3.4-5). Regarding the range is described quite well by both simulations without bias, even if Arpege simulation overestimates the maximum of Balboa FAA biomass, while EC-Earth overestimates the minimum.

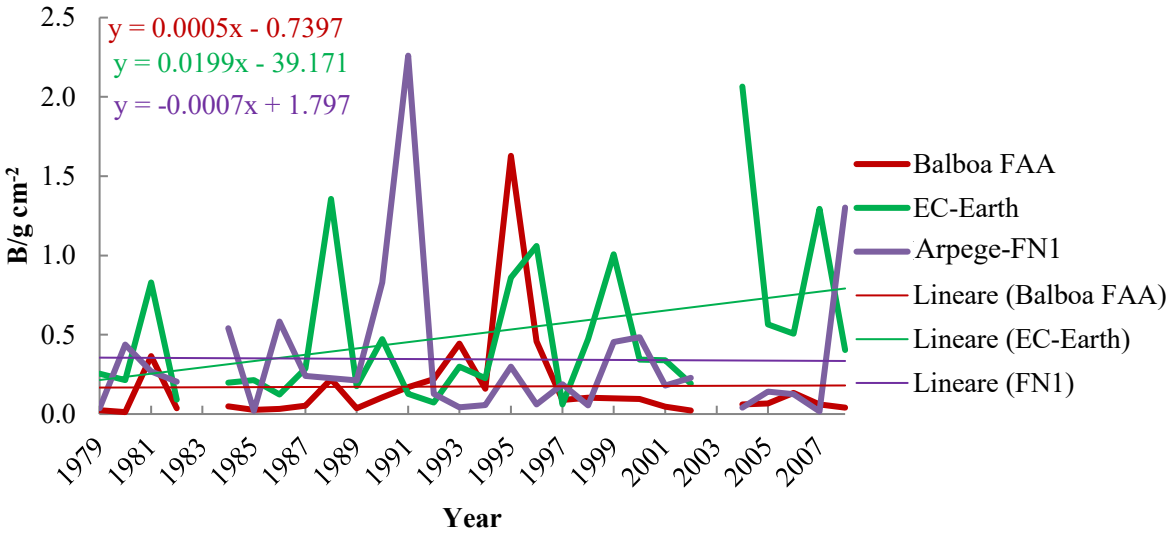

Figure 5.3. 4. Biomass accumulation (g cm^{-2}) near the Panamá Viejo area (1979-2008): comparison between model simulations and the monitoring stations.

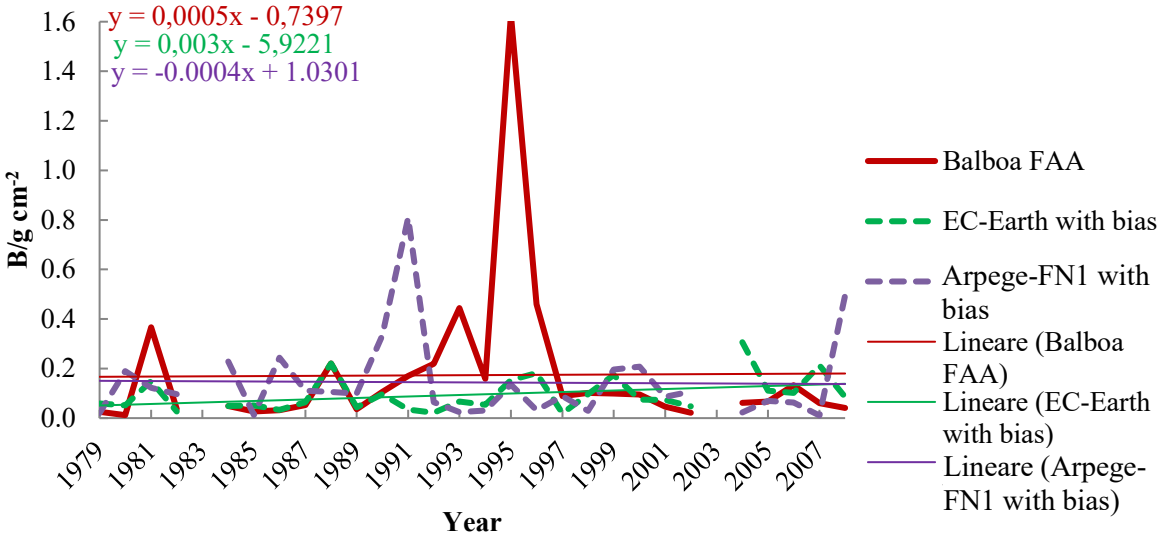

Figure 5.3. 5. Biomass accumulation (g cm^{-2}) near the Panamá Viejo area (1979-2008): comparison between model simulations with bias and monitoring stations.

Future

In the future, considering the situation without bias, the Arpege-FN 2 scenario shows a strong increase, over the 90 years, especially in the last part of the century (2069-2100) reaching maximum values of about 13 g cm^{-2}. While considering the others Arpege simulations FN3 and FN4, respectively, they present an invariant tendency and a slow decrease (Tab.5.3.2 and Fig.5.3.6). Concerning the range, during the middle future (2039-2068) EC-Earth and Arpege-FN3 show a similar trend, as expectable. Applying the bias, the trend results the same, but with a lower intensity (Tab. 5.3.2).

Table 5.3. 2. Future (2009-2100) biomass (g cm^{-2}) range of values (average, minimum and maximum) for the area near Panamá Viejo.

		Arpege							
		FN2		FN3		FN4		EC-Earth	
			+ f_P & f_T		+ f_P & f_T		+ f_P & f_T		+ f_P & f_T
2009-2038	av.	0.76	0.30	0.42	0.18	0.76	0.30		
	min.	0.04	0.03	0.02	0.01	0.04	0.02		
	max.	5.94	1.99	1.37	0.54	3.23	1.16		
2039-2068	av.	0.67	0.27	0.81	0.32	0.54	0.22	0.67	0.14
	min.	0.04	0.02	0.01	0.01	0.04	0.02	0.04	0.02
	max.	4.35	1.51	3.79	1.34	2.40	0.89	3.70	0.60
2069-2100	av.	2.73	0.96	0.97	0.39	0.65	0.27		
	min.	0.17	0.08	0.08	0.04	0.03	0.02		
	max.	12.79	3.94	3.59	1.27	2.95	1.07		

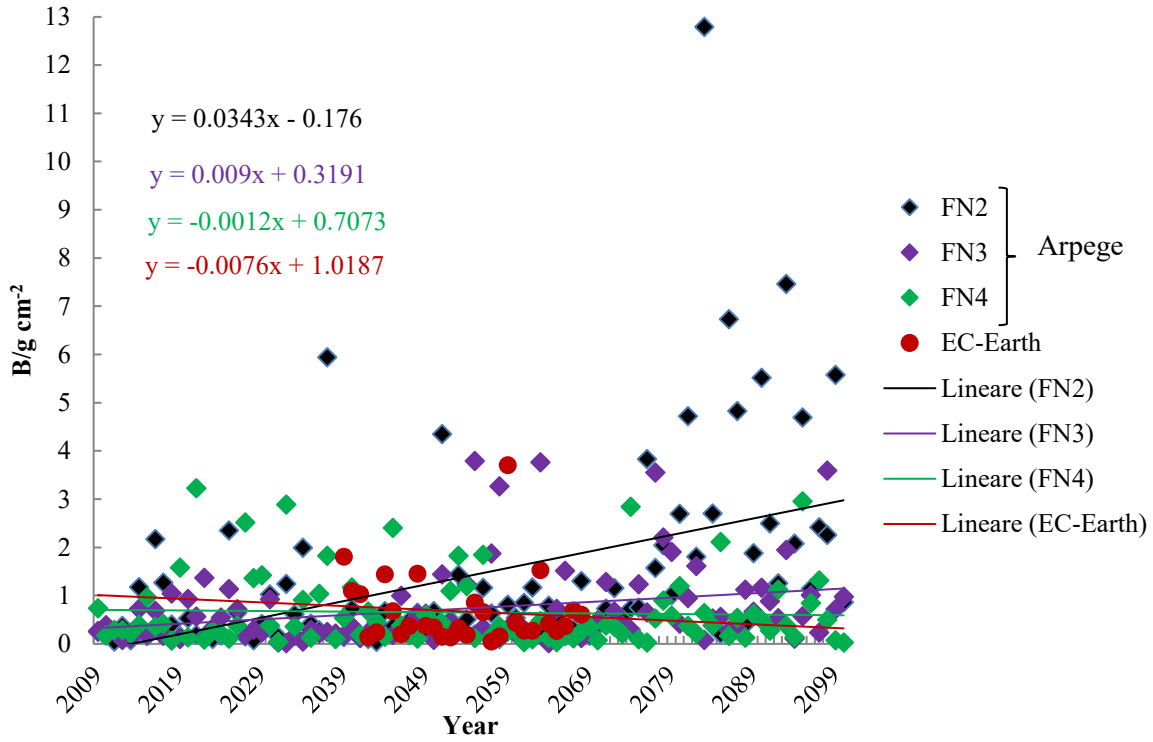

Figure 5.3. 6. Future (2009-2100) yearly biomass for the area near Panamá Viejo.

5.3.3. *Area near San Lorenzo*

Past

Considering the area near San Lorenzo, making a comparison with Gatun and Cocosolo+Cristobal+Limonbay monitoring stations, the most comparable biomass accumulation is represented by EC-Earth simulation, especially after applied the bias correction to the P and T parameters (Figs. 5.3.7-8). It has to be underlined that for the rainfall parameter, the bias correction it has been realized with the two stations data, while for the temperature correction, it was utilized only Gatun station data. Both the biomass accumulation obtained with the monitored P and T data and the simulated one by EC-Earth, show an increasing trend during the past thirty years of about 1-2 g cm^{-2}.

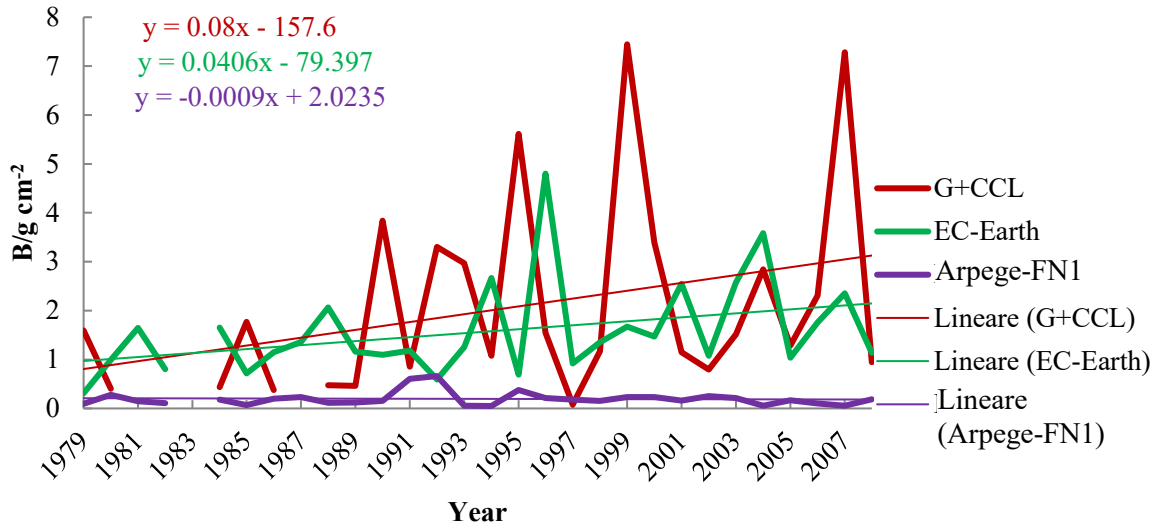

Figure 5.3. 7. Biomass accumulation (g cm^{-2}) near the San Lorenzo area (1979-2008): comparison between model simulations and the monitoring stations.

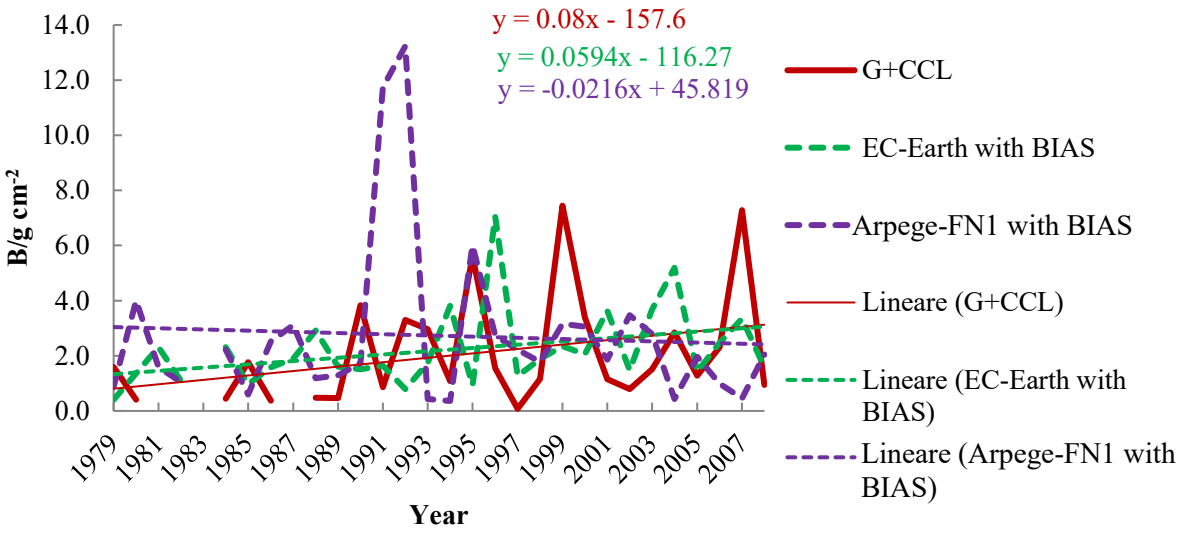

Figure 5.3. 8. Biomass accumulation (g cm^{-2}) near the San Lorenzo area (1979-2008): comparison between model simulations with bias and monitoring stations.

Future

The future situation presents a high increase considering the EC-Earth simulation, recording until 14 g cm^{-2} as maximum value. While Arpege scenarios show a smaller range, considering the projections without bias applied (Tab. 5.3.3 and Fig. 5.3.9). However, both EC-Earth and Arpege present a future increase of accumulation of biomass.

Table 5.3. 3. Future (2009-2100) biomass (g cm^{-2}) range of values (average, minimum and maximum) for the area near San Lorenzo.

		Arpege							
		FN2		FN3		FN4		EC-Earth	
			+ f_P & f_T		+ f_P & f_T		+ f_P & f_T		+ f_P & f_T
2009-2038	av.	0.30	5.1	0.24	3.6	0.33	5.6		
	min.	0.06	0.5	0.05	0.4	0.06	0.4		
	max.	1.06	25.7	0.80	17.3	0.95	21.9		
2039-2068	av.	0.29	4.8	0.28	4.5	0.26	4.1	2.82	4.0
	min.	0.05	0.3	0.09	0.8	0.04	0.3	0.54	0.7
	max.	0.97	22.8	0.87	19.6	1.10	26.9	14.26	21.5
2069-2100	av.	0.72	17.4	0.40	7.4	0.34	5.8		
	min.	0.13	1.4	0.08	0.8	0.05	0.3		
	max.	2.13	68.1	1.03	24.8	1.13	28.2		

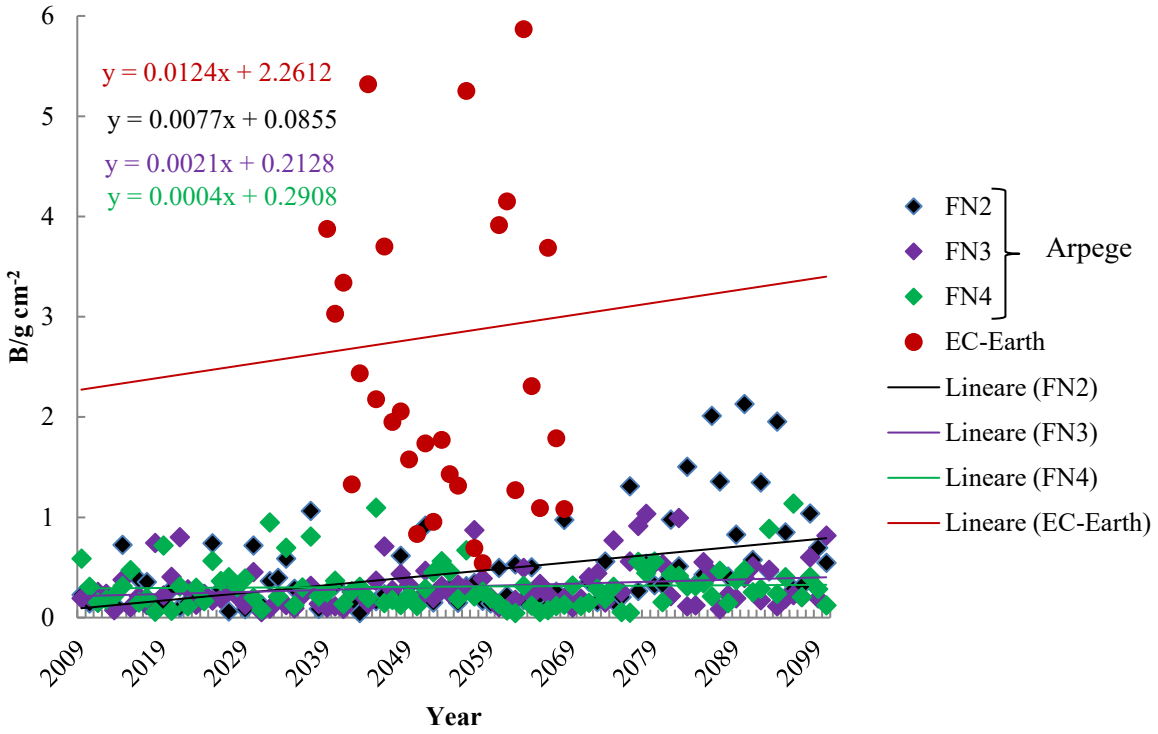

Figure 5.3. 9. Future (2009-2100) yearly biomass for the area near San Lorenzo.

5.3.4. San Lorenzo area

Past

In the area of San Lorenzo, monitoring station data were available only for rainfall parameter, since it wasn't possible to calculate the biomass accumulation function with measured data.

Comparing the damage function obtained by past simulated rainfall and temperature EC-Earth and Arpege demonstrate a similar trend, with no significant variation during the entire period. Nevertheless, Arpege-FN 1 shows a larger range, with a maximum value higher than 0.48 g cm^{-2} of the EC-Earth one (Fig. 5.3.10).

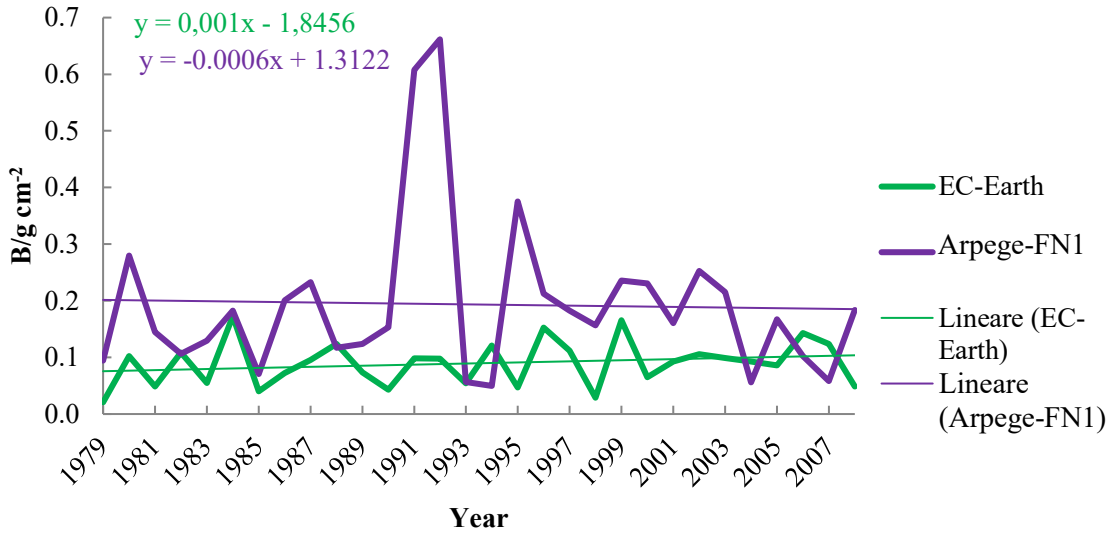

Figure 5.3. 10. Biomass accumulation (g cm^{-2}) at San Lorenzo area (1979-2008): comparison between model simulations.

Future

As observed in the past period, also in the future the trend of biomass accumulation will be without any consistent increase during the entire period, but with values higher than the detected during 1979-2008 of the order of 1 g cm^{-2}. Arpege-FN2 foresees the highest biomass accumulation, with a maximum value of 2.13 g cm^{-2} in the far future period (2069-2100) (Tab.5.3.4 and Fig.5.3.11).

Table 5.3. 4. Future (2009-2100) biomass (g cm^{-2}) range of values (average, minimum and maximum) for the area of San Lorenzo.

		Arpege			
		FN2	FN3	FN4	EC-Earth
2009-2038	av.	0.30	0.24	0.33	
	min.	0.06	0.05	0.06	
	max.	1.06	0.80	0.95	
2039-2068	av.	0.29	0.28	0.26	0.17
	min.	0.05	0.09	0.04	0.05
	max.	0.97	0.87	1.10	0.65
2069-2100	av.	0.72	0.40	0.34	
	min.	0.13	0.08	0.05	
	max.	2.13	1.03	1.13	

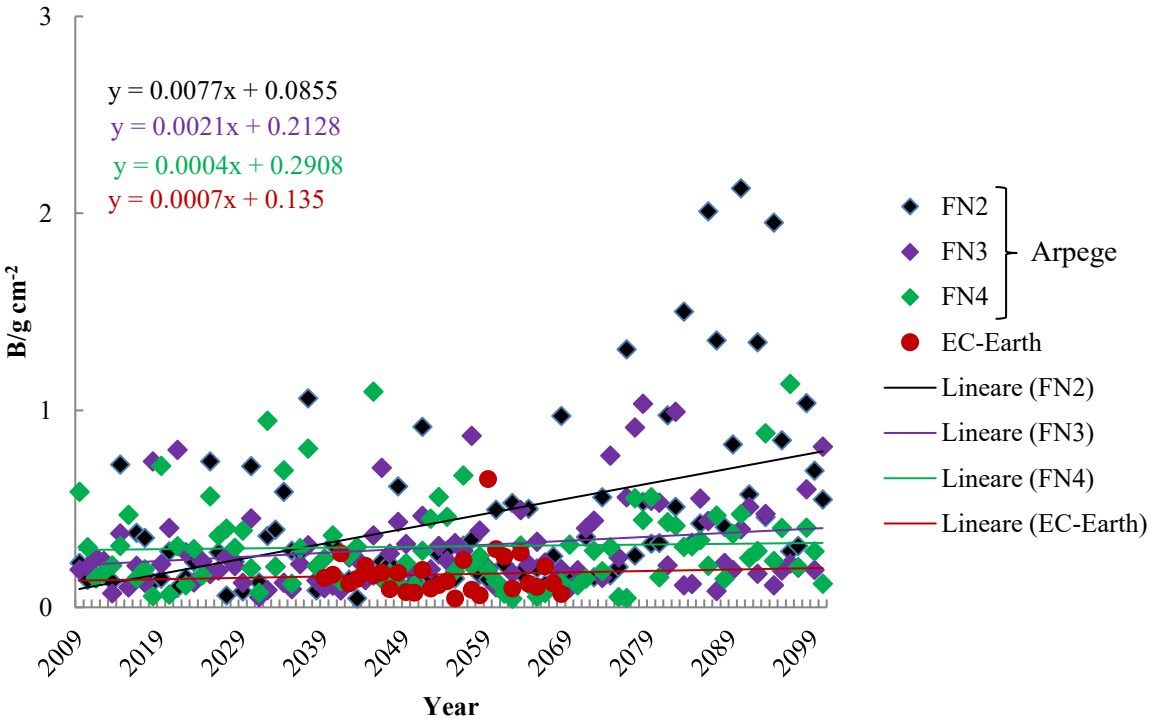

Figure 5.3. 11. Future (2009-2100) yearly biomass for the area of San Lorenzo.

5.3.5. Portobelo area

Past

Portobelo area shows an opposite situation in comparison with San Lorenzo. Indeed, in this case the biomass accumulation obtained by EC-Earth model presents values considerable higher than the one calculated with Arpege-FN1, reaching values of the order of tens of g cm^{-2}. Moreover, while the second one has a slight decrease during the thirty years, the first one shows a substantial increase (Fig. 5.3.12).

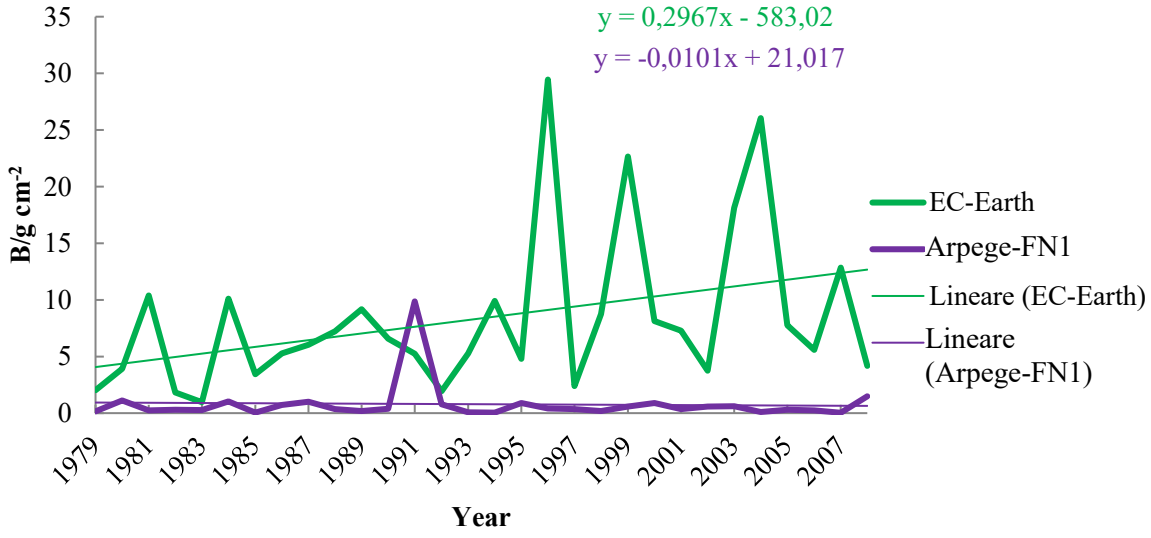

Figure 5.3. 12. Biomass accumulation (g cm^{-2}) at Portobelo area (1979-2008): comparison between model simulations.

Future

In the future, as predictable, generally biomass accumulation obtained by EC-Earth shows high values, comparable with Arpege pessimistic scenario, FN2 (Tab. 5.3.5 and Fig. 5.3.13). However, on the contrary of this latter one EC-Erath shows a decreasing trend, while FN2-biomass presents an increase during the all century. While considering the other two simulations, obtained by FN3 and FN4 scenarios, they have an invariant trend. Considering the range, EC-Earth and FN2 biomass accumulations present wider range, reaching respectively values of 21.87 and 19.95 g cm^{-2}; followed by FN4, 14.72 g cm^{-2} and FN3, 7.72 g cm^{-2} (Tab. 5.3.5).

Table 5.3. 5. Future (2009-2100) biomass (g cm^{-2}) range of values (average, minimum and maximum) for the area of Portobelo.

		Arpege			
		FN2	FN3	FN4	EC-Earth
2009-2038	av.	1.82	0.94	1.50	
	min.	0.12	0.05	0.15	
	max.	15.13	3.96	9.26	
2039-2068	av.	1.61	1.09	0.90	10.67
	min.	0.04	0.10	0.04	1.28
	max.	6.25	8.93	4.89	21.87
2069-2100	av.	6.44	1.42	1.85	
	min.	0.21	0.12	0.04	
	max.	19.95	7.72	14.72	

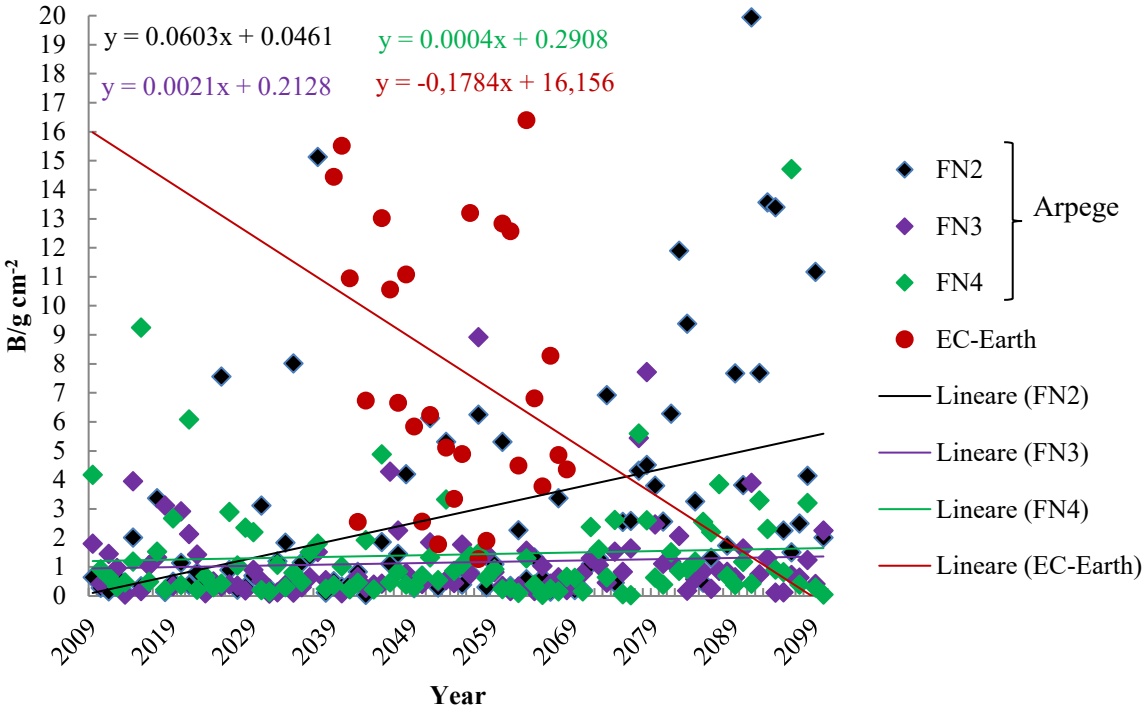

Figure 5.3. 13. Future (2009-2100) yearly biomass for the area of Portobelo.

5.3.6. Maps of Biomass Accumulation

In order to have a more complete overview of the past and the future situation of biomass accumulation , it has been decided to utilize EC-Earth data for calculating biological growth plotted as a grid map, of 4 x 4 areas (obtaining a whole area of 100x100 km^2), overlapped on Panama borders. The future (2039-2068) and the past (1979-2008) simulations don't differ significantly (respectively Figs. 5.3.6.1a and b), except for the Portobelo area and the zone near San Lorenzo (highlighted in Fig.5.3.6.2) which show an average increase of an 1 g cm^{-2} .

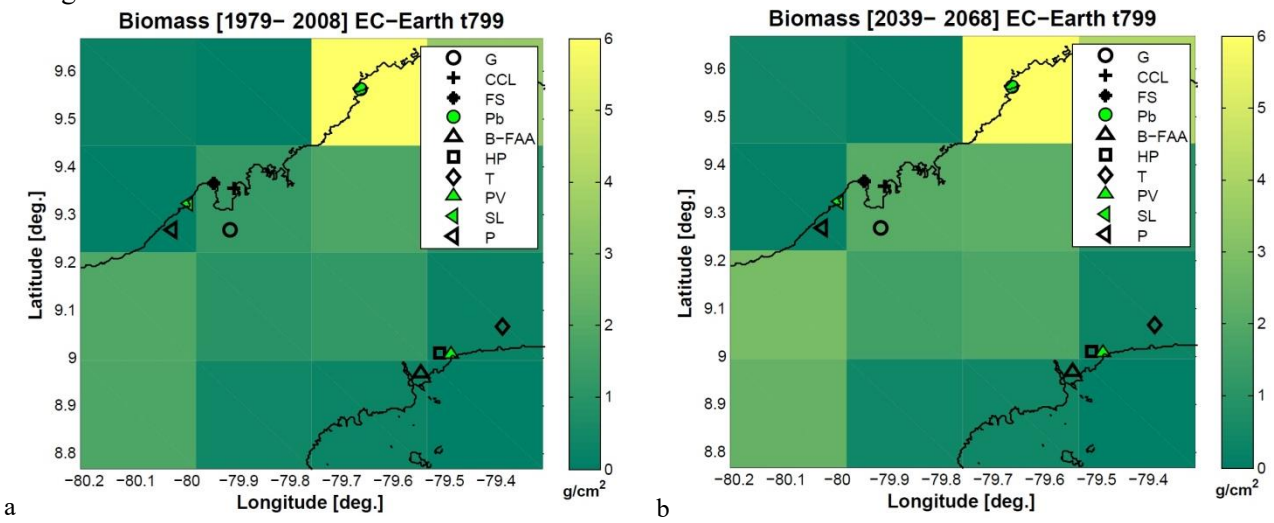

Figure 5.3.6. 1 Estimated biomass accumulation under EC-Earth scenario.
a. For the past period 1979–2008 (baseline); b. For the middle future period (2039-2068)

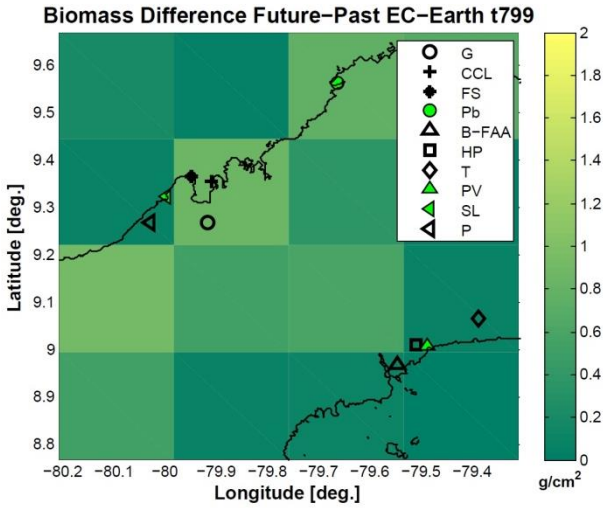

Figure 5.3.6. 2. Difference between the estimated biomass accumulation between the future and the past period.

Final remarks

Considering the past trend of biomass accumulation calculated with model data and compared with the biomass estimated with monitoring station data, Arpege-FN1 represents better the Panamá Viejo area and surroundings, while EC-Earth is more similar to the results obtained at the area near San Lorenzo. Moreover, EC-Earth represents better the range of values of Panamá Viejo and near San Lorenzo area.

Regarding the future situation, the estimation of biomass, under both Arpege and EC-Earth scenarios, at Portobelo area shows the highest values, followed by the area near San Lorenzo, the area near Panamá Viejo, then Panamá Viejo and San Lorenzo zones. Therefore, the highest differences between future and past are recorded at the areas on the North shore, especially Portobelo.

6. Chapter 6 – Final considerations

6.1 Conclusions

The aim of the PhD research work here presented is the evaluation of the environmental impact on materials belonging to two UNESCO sites located in Panama: the Monumental site of Panamá Viejo and the Caribbean Fortifications of Portobelo and San Lorenzo. For reaching this objective, the first step needed is the matter knowing, in order to identify the materials composition and their state of conservation. This allowed us to understand better the current problems and the potential damages connected to the exposition at the Panamanian environment. Moreover, through the utilization of climate parameters extracted from climate models and applied in damage functions, it has been possible to assess the deterioration phenomena occurring on these materials, producing also future projections of them, considering the climate change impacts on the Panamanian heritage.
Concluding remarks and future perspectives of this study are described in the following paragraphs.

6.1.1 Materials Characterization and Damage Evaluation

Through the analyses performed, for the mineralogical-petrographic characterization and the evaluation of the state of conservation (stereo, polarized light and electronic microscopy, XRPD and XRF), it has been possible to realize a classification of the lithotypes present in the several sites understudy.
In particular, considering Panamá Viejo, the masonries are mainly composed by sedimentary rocks of volcanic and marine sediments origin, as polygenic breccias, identified at almost all the complexes sampled, in particular at the *Convento de la Concepción*, *Casas Reales, Convento de San Francisco, Fortín de la Natividad* and *Convento de la Compañia de Jesus*. Moreover, basaltic andesites have been detected at the *Fortín de la Natividad*, while rhyodacites have been collected and analysed at the *Convento de San Francisco* and the *Hospital de San Juan de Dios*. Finally, the *Torre de la Catedral* results mainly composed by tuffite and a wall in the *Casa Terrín* complex is totally formed by rhyolite.
On the opposite littoral, in the bay of Portobelo, coral limestones and sandstones have been identified as principal building materials at the *Fuerte de San Jeronimo* and *Fuerte de Santiago*. Moreover, in this latter one there is also the presence of tuffite. On the North coast of the inlet, at the *Fuerte de San Fernando*, coral limestone resulted the most utilized material in the masonries, followed by basaltic andesite, especially in the masonries of the Upper Battery and in the pavements in the Lower Battery. Finally, it was observed also the use of grainstone especially in the corners of the embrasures. Also at the *Fuerte San Lorenzo* grainstones were mainly utilized for composing corners (as ornamental parts of the portals and the base blocks); moreover, tuffite has been detected in the masonry of this fort.
Considering the outcrops, identified in proximity of the archaeological area of Panamá Viejo, volcanic breccias and basaltic andesites have been detected. A basaltic andesite outcrop was identified also in Portobelo, specifically near the Fort of San Fernando; while, at San Lorenzo Fortress, a tuffite/sandstone outcrop was recognised. In addition, 5 km far from the defence construction, a potential grainstone supply area was found.

Concerning the state of conservation, the most diffused deterioration phenomena are due to biological growth, exfoliation and detachment, disintegration (sanding and pulverization), salt encrustations and chromatic alteration (in particular affecting rhyolites).
Through microscopic analyses, altered parts (as zeolitized areas) have been observed featured by cracks. This zeolitization process was detected mainly in volcanoclastic stones by XRPD investigations, indeed though it, the identification of the different types of zeolites present was possible, that are: clinotptilolite, detected in all the sites, while mordenite has been identified only at Panamá Viejo. In addition, the PV FC 6, PV FC 9 and PV SJdD samples, which have been classified as rhyodacite, according to Winchester & Floyd (1977) classification for altered volcanic rocks, are mainly formed respectively by mordenite (PV FC 6) and clinoptilolite.
The zeolitized parts, as the clay expanded minerals (detected montmorillonite and vermiculite), resulting hygroscopic, can be affected by humidity cycles, thus representing a co-responsible factor of the detachment and exfoliation processes observed macroscopically.
In general, MIP analysis revealed that the majority of samples analysed present an average pore diameter lower than the 0.2 μm, threshold of micro-pores. Furthermore, almost all samples show a range of pore distribution between 0.01 and 10 μm, except for rhyodacites and rhyolites, which tend to have the majority of pore diameters between 0.01 and 1 μm and coral limestones, showing a predominance towards to 10 μm. Indeed, by PLM analysis coral boundstones and grainstones/packstones show very high intergranular and intragranular porosity.
Moreover, salts encrustations have been identified at Portobelo Fortifications, presenting a process of calcite crystallization developed in several steps, with a different duration, understandable thanks to the alternation of sparitic and micritic minerals belonging to different layers. Through the IC investigations, it was possible to determine the soluble salts present in the samples, defining calcium as the most abundant cation in all specimens and in every site. Moreover, high presence of sulphates and nitrates has been detected, particularly at Panamá Viejo since it is within an urban area in proximity to a high traffic road, thus interested by heavy anthropogenic pollution. While, considering Portobelo and San Lorenzo, the most abundant anion is chloride, and, considering the cations detected, it can form sodium, potassium, ammonium and magnesium chloride. Nevertheless, the presence of halite is presumable in every site, since chloride is largely present also in Panamá Viejo specimens. Furthermore, in presence of water, Cl^- can create the hydrochloric acid, as sulphates and nitrates can form respectively the sulphuric and nitric acid, causing the dissolution of carbonates, which can re-crystallize inside the stone porosity, provoking internal tensions, or on the surface, forming superficial encrustations of calcite.

6.1.2. Determination of the environmental context and damage evaluation using damage functions

In order to determine the environmental context, monitoring stations of the Panamanian national net have been chosen near the sites of interest. In addition, two climate models have been selected, presenting two different resolutions, EC-Earth of 25 km and Arpege of 50 km. Then, climate parameters as near-surface air temperature, relative humidity and rainfall amount, were extracted both from monitoring stations and climate models, for the past reference period 1979-2008. Moreover, the same parameters have been collected also from future scenarios, in the period of middle future, 2039-2068, for EC-Earth (RCP 8.5) and from the near future to the far future, 2009-2100, for Arpege (RCP 8.5, RCP 4.5 and RCP 2.6).

Comparing the measured parameters with the simulated one, EC-Earth model resulted to reproduce better the seasonality of temperature and relative humidity. While considering the rainfall, generally Arpege-FN1 simulates better the measured data.
In addition, bias correction has been realized, obtained on the bases of the differences between the simulated data and the measured ones. Therefore, a multiply factor was applied for the rainfall and relative humidity model series, while an additive factor for the temperature model values.
Since the most diffused deterioration morphologies detected are loss of materials, salts crystallization and biological growth, damage functions have been selected and applied in order to evaluate and predict these phenomena.
Considering the surface recession, Lipfert function modified (related to the karst effect) have been utilized, valid for carbonate rocks having a porosity lower than 25%. The situation obtained in the area of Panama Viejo and surroundings is quite similar in both models, while the prediction for the northern areas, Portobelo and San Lorenzo are significantly different, showing a major surface recession if we consider the EC-Earth experiment.
In order to understand the future trend the function has been applied both in the most optimistic and in the most pessimistic form. If we consider the middle future estimation (2039-2068), equally Arpege and EC-Earth scenarios show an increase respect to the past evaluation from 6-7 μm $year^{-1}$, calculated at Panama Viejo area, to 10-12 μm $year^{-1}$ at San Lorenzo and Portobelo area. Therefore, it can be assumed that in the future, the sites situated at the North Panamanian coast can be more affected by surface recession, than the site at the Southern coast.
In consideration of the salts cycles of dissolution and crystallization, halite has been elected as a priority phase of investigation, since sodium and chloride resulted ones of the most abundant ions in the stone samples, detected in all sites, also taking into account their proximity to the sea. Therefore, the past and future monthly transitions of NaCl have been calculated, utilizing only data from EC-Earth, for the simulations, considering as an event the passage from RH values higher than 75.3% to values smaller than this threshold, counted only if happened in consecutive days. In addition, since the temperature of existence of this process should be 25°C, and, especially in the future highest temperatures are expected, it was considered also 75.1% as threshold, corresponding to the RH of NaCl transition at 30°C.
Past cycles of dissolution and crystallization of halite highlight that the higher frequency of this phenomenon is recorded during the dry season (end of November/December to April/beginning of May). However, since it has been noticed an underestimation of EC-Earth simulation during the rainy season, in comparison with the monitoring station data, sporadic events cannot be excluded also during this period. However, we have to bear in mind that the monitoring station represents a punctual situation and not an area, as the model simulation.
In general, making a comparison between the past and future conditions, the period of cycles tends to have a slight increase in the future, as observed in the area near Panama Viejo, near San Lorenzo and at San Lorenzo; while at Panama Viejo and Portobelo area the trend result opposite. Finally, evaluating the difference among the sites, Portobelo results the less interested by this phenomenon, while the area near San Lorenzo seems to be the most affected, reaching 3-4 cycles per month during the dry season.
In order to estimate the biomass accumulation on hard acid stones, calculated considering the organic carbon accretion on the surfaces, the function developed by Gomez-Bolea et al. (2012) has been applied. Regarding the past trend of biomass accumulation calculated with model data and compared

with the biomass estimated with monitoring station records, Arpege-FN1 represents better the Panama Viejo area and surroundings, while EC-Earth is more similar to the results obtained at the area near San Lorenzo. Moreover, EC-Earth represents better the range of values of Panama Viejo zone and the area near San Lorenzo.
In the future situation, the estimation of biomass, under both Arpege and EC-Earth scenarios, shows at Portobelo area the highest values (reaching 21 g cm^{-2}). Then followed by the area near San Lorenzo (up to 10-20 g cm^{-2} by EC-Earth simulation data), the area near Panama Viejo (up to ≈12 g cm^{-2}), then Panama Viejo and San Lorenzo zones (1-5 g cm^{-2}). Therefore, the highest differences between future and past are recorded at the areas on the North shore, especially Portobelo.

6.2 Future perspectives

6.2.1 Short-term in situ effects

This work determined a fundamental step for the current and future preservation of these sites. Indeed, it represents an instrument for organizing and enhancing the maintenance and restoration works, since it allows the operators of the sites to know the compositions of the building materials and to understand the problems related with their interaction with the environment.
Moreover, it will permits to:

- Decide how to intervene for limiting and preventing the causes of damages, having prioritised them.
- Select the most suitable restoration materials, as consolidants, protectives, mortars, etc.
- Choose the most compatible materials for possible replacements/integrations in the masonries, utilizing the outcrops identified. For that reason, it could be recommended to carry out perspective drawings, showing the material composition of the masonries.

With the purpose of supporting the realisation of the aforementioned points, it is intended the production of a "practical manual" with the main outcomes of this thesis, addressed to a larger public, from field workers to decision makers, thus, preferably in Spanish.
Furthermore, with the intention of enlarging and increasing the people consciousness on the thematic "environmental and climate change impact on cultural heritage", it has been considered the organization of courses, workshops, summer schools, etc. carrying on the collaboration with the Patronages and trying to attract the interest of people belonging to several sectors.

6.2.2 Long-term research activities

In relation to the construction materials, it can be useful to continue the investigation about the raw materials provenance, for identifying the possible supply of all the rock typologies distinguished.
Concerning the environmental impact, it should be necessary to complete the monitoring with also the pollution data, organizing in situ measurements of both climate and pollution parameters. This is fundamental also for planning field-exposure tests, for strengthening the validity of the damage functions in situ. Moreover, this kind of experiments are necessary as well for evaluating the efficiency of maintenance and restoration materials, applied on specimens of the different rocks present at the sites, exposed to the same conditions of the monuments.
Furthermore, since the biological growth resulted one of the most diffused damage phenomena, a study focused on the identification of the different kind of species colonizing the material surfaces

should be implemented, with the additional purpose of improving the effectiveness of the biomass accumulation equation.
Finally, to enhance the accuracy of all the damage functions, it will be significant to widen the comparison among climate simulations also with other models.

Acknowledgements

Three years of research allowed me to know and work with several people that helped and supported me in reaching the goals of this study.

First of all, I want to thank my Institute ISAC-CNR which let me start and complete this path, in particular Alessandra Bonazza, Paola De Nuntiis, Delia Fernández González, Nadia Ghedini, Paolo Mandrioli, Irene Natali, Izabela Ozga, Elisa Palazzi, Cristina Sabbioni, Alessandro Sardella, Giorgia Vidorni and Jost von Hardenberg. A special thanks to Franco Corticelli for the ESEM-EDX (and not only) support.

In addition, at the University of Ferrara I gratefully acknowledge Carmela Vaccaro, Annalisa Martucci, Michele Morsilli, Renzo Tassinari, Sabrina Russo, Salvatore Pepi, Lisa Volpe and all my PhD colleagues, for assisting me in several phases of my work, especially in performing analyses and in their interpretation. Moreover, I want to thank Orlando Favoni, Francesca Tittarelli and Chiara Giosuè of the Università Politecnica delle Marche for the support in XRPD, MIP and IC investigations.

This study was an opportunity that would never be possible without the endorsement of the Panamanian Patronages. In particular, at Panamá Viejo I am very grateful, for the on-site and "remote" cooperation, to Julieta de Arango, Silvia Arroyo, Félix Durán, Elizabeth García, Diana Engler, Marcelina Godoy, Jacinto Almendra, Mirta Linero Baroni, Aura Guerra and Daniel Cortéz. Furthermore, thank to Rodolfo Suñé and Wilhelm Franqueza for the collaboration at the sites belonging to the Patronato de Portobelo y San Lorenzo.

Last but not least, a personal thank to my family and my friends for supporting me with patience and tenacity.

References

Alba Carranza M. M. 1946. *Geografía descriptiva de la República de Panamá*. p. 27-29.

Amoroso G. G., 2002, *Trattato di scienza della conservazione dei monumenti. Etica della conservazione, degrado dei monumenti, interventi conservativi, consolidanti e protettivi*, Alinea Editrice.

Arnold A., Zehnder K. 1989. *Salt weathering on monuments*, proceedings, I Simposio Internazionale Bari 7-10 giugno La conservazione dei monumenti nel bacino del Mediterraneo, pp.31-58.

Arroyo S. I., 2010. *El plan maestro del conjunto monumental de Panamá Viejo. Diez años después,* Canto Rodado 5:191-218, ISSN 1818-2917.

Arroyo S. I., 2011. *Tareas Pendientes 2011/12 - Conservación preventiva y proyectos especiales*. Departamento de Arquitectura y Bienes Inmuebles - Patronato Panamá Viejo, Internal Report, August 2011.

Arroyo S. I., 2015. *El enigma de las Casas Reales del sitio arqueológico de Panamá Viejo.* P. 19 Defensive Architecture of the Mediterranean. XV to XVII centuries, Vol.II, Rodríguez-Navarro Ed. - Editorial Universitat Politècnica de València. http://dx.doi.org/10.4995/FORTMED2015.2015.1717

Autoridad Nacional del Ambiente, 2010. *Atlas Ambiental, de la República De Panamá (Primera Versión).*

Bertocci S. & Parrinello S. 2015. *Digital survey and documentation of the archaeological and architectural sities*. UNESCO world heritage list, EDIFIR.

Bonazza A., Sabbioni C., Messina P., Guaraldi C., De Nuntiis P., 2009a. *Climate change impact: Mapping thermal stress on Carrara marble in Europe.* Science of the Total Environment 407, pp.4506–4512.

Bonazza A., Messina P., Sabbioni C., Grossi C. M., Brimblecombe P. 2009b. *Mapping the impact of climate change on surface recession of carbonate buildings in Europe*. Science of the Total Environment 407, pp. 2039-2050.

Brandi C., 1977. *Teoria del restauro* di Cesare Brandi. Lezioni raccolte da L. Vlad Borrelli, J. Raspi Serra e G. Urbani, Roma 1963 - Edizioni di Storia e Letteratura; Collana Piccola Biblioteca, Torino, Einaudi.

Brimblecombe P., 2010. *Functional Descriptions of Damage to Heritage*. In L. R. C., CLIMATE CHANGE AND CULTURAL HERITAGE, CUEBC - Scienze e Materiali del Patrimonio Culturale (Vol. 10). EDIPUGLIA. pp. 57-63.

Brimblecombe P., 2016. *Urban Pollution and Changes to Materials and Building Surface*, Edition: Air Pollution Rewiews Vol.5, , Publisher: Imperial College Press, London.

Brimblecombe P., Grossi C.M., Harris I., 2006. *Climate change critical to cultural heritage*. In: Fort, R., Álvarez de Buergo, M., Gómez-Heras, C., Vázquez-Calvo, C. (Eds.), Heritage, Weathering and Conservation. Balkema, Rotterdam, pp. 387–393.

Brimblecombe P., Grossi C.M., 2009. *Millennium-long damage to building materials in London*. Science of the Total Environment 407, 1354-1361.

Camuffo D., 1995. *Physical weathering of stones*, The Science of the Total Environment 67, 1–14. http://dx.doi.org/10.1016/0048-9697(95)04565-I

Camuffo D., 2013. *Microclimate for Cultural Heritage*, [2nd Edition], Conservation, Restoration, and Maintenance of Indoor and Outdoor Monuments. Elsevier Science, pp. 182-191.

Camuffo D., 2016. *Weathering of Building Materials*, in Urban Pollution and Changes to Materials and Building Surface, Ed. Air Pollution Reviews Vol.5, Ch. 2., Publisher: Imperial College Press, London, Editors: Peter Brimblecombe, pp.19-64. DOI:10.1142/9781783268863_0002

Candanedo C., Fábrega O., 1999. *Mapa Hidrogeologico De Panama. Escala 1:1,000,000. Texto Explicativo.* Republica de Panama Empresa de Transmision Electrica. S.A. Departamento de Idrometeorologia.

Cassar M. and Pender R., 2005. *"The impact of climate change on cultural heritage: evidence and response", in Verger, I. (Ed.), ICOM 14th Triennial Meeting,* The Hague, 12-16 September, Maney Publishing, London, pp. 610-16 (preprints 2 Vol. Set).

Corbett J. J., Deans E., Silberman J., Morehouse E., Crafte E.and Norsworthy M., 2012. *Panama Canal expansion: emission changes from possible US west coast modal shift*. Carbon Management(3:6), pp. 569-588. doi:http://dx.doi.org/10.4155/cmt.12.65

Correa de Sanjur N., 1976. *Historia de Panamá Primer Año - Texto Oficial* .

Cunningham C. G., 1984. *Earth and Water Resources and Hazards in Central America.* GEOLOGICAL SURVEY CIRCULAR 925.

Davini P., von Hardenberg J., Corti S., Christensen H. M., Juricke S., Subramanian A., Watson P. A. G., Weisheimer A., and Palmer T. N., 2016. *Climate SPHINX: evaluating the impact of resolution and stochastic physics parameterisations in climate simulations*, Geosci. Model Dev. Discuss., doi:10.5194/gmd-2016-115, in review.

de Arango J. 2006. *El sitio de Panamá Viejo, Un ejemplo de gestión patrimonial.*

de Marucci S. 2012. *The expansion of the Panama Canal and its impact on CO_2 emissions*. Maritime Policy & Management, 39(6), p. 603-620. doi:http://dx.doi.org/10.1080/03088839.2012.733069

Déqué M., (2010). Regional climate simulation with a mosaic of RCMs. *Meteorologische Zeitschrift*, 19 (3), 259-266, doi:10.1127/0941-2948/2010/0455.

Dirección de Hidrometeorología, Empresa de Transmisión Eléctrica S.A.

Forte R. 2008. Panama, *Situación actual del monitoreo atmosférico*.

French C.D., Schenk, C.J., 2000. *Map Showing Geology, Oil and Gas Fields, and Geologic Provinces of the Caribbean Region.*

Gázquez F., Rull F., Medina J., Sanz-Arranz A., Sanz C., 2015. *Linking groundwater pollution to the decay of 15th-century sculptures in Burgos Cathedral (northern Spain)*. Environ. Sci. Pollut. Res. (22), pp. 15677–15689 http://dx.doi.org/10.1007/s11356-015-4754-6

Geology of Panama 1:250.000, 1990.

Gobierno Nacional República de Panamá, Instituto Nacional De Cultura Dirección Nacional Del Patrimonio Histórico, Oficina Del Casco Antiguo, Ciudad De Panamá (OCA), 2014. *Plan de emergencia de la propriedad C135, Fortificationes de la Costa Caribeña de Panamá: Portobelo - San Lorenzo*. pp.13-36.

Gomez-Bolea A., Llop E., Arino X., Saiz-Jimenez C., Bonazza A., Messina P., Sabbioni C., 2012. *Mapping the impact of climate change on biomass accumulation on stone*. J. Cult. Herit. 13 (3), 254–258.

Grajales Saavedra J. A., 2012. *Aplicación de los procesos de inversión 3D de pseudo-secciones de resistividad eléctrica aparente en los suelos del interior del Convento de Santo Domingo (Conjunto Monumental Histórico de Panamá Viejo), estratigrafía de los suelos peri metrales e identificación y patología de los materiales y los sistemas estructurales de sus ruinas*. Graduation Thesis in Civil Engineering, Universidad Tecnológica de Panamá.

Grossi C.M., Brimblecombe P., Menéndez B., Benavente D., Harris I., Déqué M. 2011. *Climatology of salt transitions and implications for stone weathering*. Science of the Total Environment 409, 2577–2585.

Harmon R., 2005. *Geological development of Panama, The Río Chagres*, Panama. p. 45-62. doi:10.1007/1-4020-3297-8_4

Honeyborne D., 1998. *Weathering and decay of masonry*. In A. J. F.G., Conservation of building and decorative stone (p. 153 - 84). Oxford: Butterworth - Heinemann.

http://faostat.fao.org/faostat/help-copyright/copyright-e.htm

http://plate-tectonic.narod.ru/central-america-plate-tectonics01.gif

http://whc.unesco.org/en/list/135

http://whc.unesco.org/en/list/790

http://whc.unesco.org/en/soc/3198

http://www.hidromet.com.pa/clima_historicos.php?sensor=2

http://www.nasa.gov/audience/forstudents/5-8/features/nasa-knows/what-is-climate-change-58.html

http://www.panamaviejo.org/

http://www.planur-e.es/

ICOMOS-ISCS, 2008. *Illustrated glossary on stone deterioration patterns - Glossaire illustré sur les formes d'altération de la pierre.* Champigny/Marne, France: MONUMENTS AND SITES.

Inkpen R, Viles H., Moses C., Baily B., 2012. *Modelling the impact of changing atmospheric pollution levels on limestone erosion rates in central London, 1980-2010*. Atmospheric Environment 61, 476-481 http://dx.doi.org/10.1016/j.atmosenv.2012.07.042

IPCC, 2014: Climate Change 2014: *Mitigation of Climate Change. Contribution of Working Group III to the Fifth Assessment. Report of the Intergovernmental Panel on Climate Change* [Edenhofer, O., R. Pichs-Madruga, Y. Sokona, E. Farahani, S. Kadner, K. Seyboth, A. Adler, I. Baum, S. Brunner, P. Eickemeier, B. Kriemann, J. Savolainen, S. Schlömer, C. von Stechow, T. Zwickel and J.C. Minx (eds.)]. Cambridge University Press, Cambridge, United Kingdom and New York, NY, USA.

Jay D. A., 2009. *Evolution of tidal amplitudes in the eastern Pacific Ocean*. GEOPHYSICAL RESEARCH LETTERS, VOL. 36, L04603, doi:10.1029/2008GL036185

Knutsen K., 2010. *La Yeguada Volcanic Complex, Western Panama: An Assessment of the Geologic Hazards Using New 40Ar/39Ar Ages,* Master Thesis. MICHIGAN TECHNOLOGICAL UNIVERSITY.

Kottek M., Grieser J., Beck C., Rudolf B., Rubel F., 2006. *World Map Of Köppen-Geiger Climate Classification Updated*. Meteorologische Zeitschrift, Vol. 15, No. 3, 259-263. doi:http://dx.doi.org/10.1127/0941-2948/2006/0130

Kovats R.S. and R. Akhtar, 2008. *Climate, climate change and human health in Asian cities*, Environment and Urbanization, Vol. 20, No. 1.

Kucera V., Tiblad J., Kreislova K., Knotkova D., Faller M., Reiss D., 2007. *UN/ECE ICP materials dose–response functions for the multi-pollutant situation*. In: Brimblecombe P., Hara H., Houle D., Novak M., editors. Acid Rain—Deposition to Recovery. Sprinter. p. 249–58.

Le Maitre R. W., 1984. *A proposal by the IUGS Subcommission on the Systematics of Igneous Rocks for a chemical classification of volcanic rocks based on the total alkali silica (TAS) diagram*, Australian Journal of Earth Sciences, Vol. 31, Iss. 2, 243-255, DOI: 10.1080/08120098408729295

Lipfert F.W., 1989. *Atmospheric damage to calcareous stones: comparison and reconciliation of recent experimental findings*. Atmos. Environ 1989;23:415–29.

Ma Yumo A.Y. 2013/2014. *Environmental impact on the Archaeological Site of Panamá Viejo: collection and elaboration of microclimate and air quality data*. Master Theisis in Environmental Impact on Materials, Deterioration and Ageing, University of Bologna, Supervisor: Prof. Alessandra Bonazza, Co-supervisor: Prof. Cristina Sabbioni and Dr Chiara Ciantelli.

Macedo M.F., Miller A.Z., Dionísio A. and Saiz-Jimenez C. (2009), *Biodiversity of cyanobacteria and green algae on monuments in the Mediterranean Basin: an overview*, Microbiology (2009), 155, 3476–3490

Markham A., Osipova, E., Lafrenz, Samuels, K. and Caldas, A. 2016. *World Heritage and Tourism in a Changing Climate*. United Nations Environment Programme, Nairobi, Kenya and United Nations Educational, Scientific and Cultural Organization, Paris, France.

Mena García M. del C., 1992. *La ciudad en un cruce de caminos: Panamá y sus orígenes urbanos*. España: Publicaciones de la Escuela de Estudios Hispanoamericanos de Sevilla.

Mena García M. Del C., 1997. *Panamá en el siglo XVIII: trazado urbano, materiales y técnica constructiva*, Revista de Indias. *LVII*(2).

Meteorological and Hydrological Branch of the Panama Canal Authority.

NorMaL - 1/88. *Alterazioni macroscopiche dei materiali lapidei: lessico*.

Ordóñez S., La Iglesia Á., Louis M., García-del-Cura M Á., 2016. *Mineralogical evolution of salt over nine years, after removal of efflorescence and saline crusts from Elche's Old Bridge (Spain)*, Construction and Building Materials, Volume 112, 1 June 2016, Pages 343-354, ISSN 0950-0618, http://dx.doi.org/10.1016/j.conbuildmat.2016.02.123.

Osorio Ugarte, K., 2015. *Report for the UNESCO World Heritage centre about the state of conservation. Fortifications On The Caribbean Side Of Panama: Portobelo -San Lorenzo*.

Paton S., 2015. *How do we know what could happen?* Science of El Niño, The driest year ever? Trópicos, Magazine of the Smithsonian Tropical Research Institute, Volume 1, Issue 9. Sept.2015. pp. 30-33.

Patronato Panamá Viejo y Embajada de España en Panama. (2006). *Panamá Viejo, de la aldea a la urbe, from village to city.*

Physical Monitoring Program of the Smithsonian Tropical Research Institute.

Pinzón R. and González G., 2004. *Parametrización de la conexión Casas Reales-Complejo arqueológico de Panamá Viejo mediante la inversión de pseudo-secciones de resistividad aparente*, Tesis de Licenciatura en Física de la Universidad de Panamá, 99 p.

República de Panamá - Ministerio de Economia y Finanzas, Decreto Ejecutivo No.35 (de 26 de febrero de 2007), "*Por el cual se aprueba la Política Nacional de Cambio Climático, sus principios, objetivos y líneas de Acción*", Gaceta Oficial Digital, miércoles 04 de abril de 2007- No 25764

Roden, G. I., 1963. Sea Level Variations at Panama. *Journal of Geophysical Research, 68*(20), p. 5701-5710. DOI: 10.1029/JZ068i020p05701

Sabbioni C., Brimblecombe P., Cassar M., 2012. *The Atlas of Climate Change Impact on European Cultural Heritage Scientific Analysis and Management Strategies*, Anthem Press.

Saccani E., 2014. *Petrografia delle Rocce Sedimentarie Terrigene*. Università di Ferrara.

Sanchez Nava M., 2000. *Diagnostico del Deterioro de los Materiales Petreos de Construccion de la Ciudad de Panama Viejo, midiante su caracterizacion fisicoquimica*. Thesis in quimica pharmaceutica biologa, Facultad de Quimica, Universidad Nacional Autonoma de Mexico.

Satterthwaite D., 2007. *Climate Change and Urbanization: effects and implications for urban governance*. UN/POP/EGM-URB/2008/16

Serrano L. F., 2011. *An integrative geologic, geochronologic and geochemical study of Gorgona Island, Colombia: Implications for the formation of the Caribbean Large Igneous Province*, Earth and Planetary Science Letters. *309* (3-4, 15), p. 324-336. doi:http://dx.doi.org/10.1016/j.epsl.2011.07.011

Smith B.J., 2003. *Background controls on urban stone decay: Lessons from natural rock weathering,* in The effects of air pollution on the Built Environment (Air pollution views vol. 2). ed. / P. Brimblecombe. Imperial College Press, London, 2003. p. 31-61.

Smithsonian Tropical Research Institute, 2011. *The Panamá Geology Project - Cenozoic Evolution of the Panamá Isthmus.*

Spiteri S.C., 1994. *Illustrated Glossary of Terms used in Military Architecture*.

Stewart R.H. and J.L, Woodring W.P., 1980. *Geological Map of the Panama Canal and Vicinity, Republic of Panama.* 1:25000. U.S. geological Survey.

Strlič M., Thickett D., Taylor J., and Cassar M., 2013. Damage functions in heritage science, Studies in Conservation, vol.58, n.2, pp.80-87.

Strong N. M., 2009. *Rates and patterns of coastal erosion for the Panamá Viejo historical and archaeological site*. Geological Society of America Annual Meeting.

Tejeira Davis, E., 2007. *Panamá Guía de arquitectura y paisaje.* Sevilla, España: Consejería de Obras Públicas y Transportes, Panamá, Panamá: Instituto Panameño de Turismo.

Torres Montes L., 1996. *Informe preliminar del examen mesoscópico de las ruinas de Panamá Viejo*

UNI 11182:2006 - Beni culturali - Materiali lapidei naturali ed artificiali - Descrizione della forma di alterazione - Termini e definizioni.

Urriola García W., Guerra Chang H. and Vásquez M. Almer E. 2014. *Determinación de material particulado PM2,5 en la Estación Digital de Calidad del Aire ubicada en el Campus Dr. Harmodio Arias Madrid de la Universidad de Panamá en la Ciudad de Panamá*. Revista Panameña de Salud Pública, Ocupacional y Ambiental Vol. 2 n. 3.

Whall C. S., 2010. *Defra UK Ship Emissions Inventory - Final report November 2010.* London: Entec UK Limited.

Winchester J. A., and Floyd P. A., 1977. *Geochemical discrimination of different magma series and their differentiation products using immobile elements*. Chemical geology 20: 325-343.

World Monuments Fund, Instituto Nacional de Cultura (Panama), American Express Company, World Monuments Watch. 2003. *Portobelo - San Lorenzo: An approach to integrated conservation for sites containing endangered cultural and natural resources*. pp.8-71.

Zúñiga J., Tarajia M., Herrera V., Urriola W., Gómez B. and Motta J., 2016. *Assessment of the Possible Association of Air Pollutants PM_{10}, O_3, NO_2 With an Increase in Cardiovascular, Respiratory, and Diabetes Mortality in Panama City. A 2003 to 2013 Data Analysis*. Medicine, Volume 95, Number 2. DOI: 10.1097/MD.0000000000002464.

Appendix

Figures and Tables

Figures

Figure 1.1. 1 Map showing the locations of Panamá Viejo monumental site and fortresses of Portobelo and San Lorenzo (modified from *http://www.freeworldmaps.net/centralamerica/panama/panama-map-physical.jpg*). 3

Figure 1.1.1. 1 Map of Panamá Viejo by Bautista Antonelli (XVI century) - Museo Naval de Madrid (Arroyo, 2015). 4

Figure 1.1.1. 2. Pictures of monuments at Panamá Viejo at the beginning of XX century - Biblioteca del Canal de Panamá. 4

Figure 1.1.2. 1 Pictures of San Fernando at the beginning of the XX century and during the 70s (from World Monument Fund et al, 2003). 7

Figure 1.2.1. 1. Particular of the World Map of Köppen-Geiger Climate Classification, showing the Panamanian Isthmus (Kottek et al, 2006). 8

Figure 1.2.1. 2. Panamanian Climate typologies according with A. McKay classification in 2000 (Autoridad Nacional del Ambiente, 2010). 9

Figure 1.2.1. 3. Comparison between the monthly maximum (red) and the average (violet) of precipitation in Portobelo (up, timespan 1908-2004) and near Panamá Viejo (Hato Pintado, down, timespan 1987-now), curtesy of Hidrometeorología de la Empresa de Transmisión Eléctrica, S.A. (http://www.hidromet.com.pa/clima_historicos.php?sensor=2). 10

Figure 1.2.1.4 Low tide view at Casco Antiguo bastion (Panama City). Picture took in the end of August 2014 at 11:00 a.m. 11

Figure 1.2.1.5 Walls of one of the structures belonging to the complex "Casas Reales" showing the erosion due to the sea waves action. 11

Figure 1.2.1. 6. Map of Portobelo Bay. With the red-dotted line is highlighted the 18th century seashore line (World Monument Fund et al., 2003). 12

Figure 1.2.1.7. External view of sea-front walls of Fort San Jeronimo. Picture took in the beginning of September 2014 at 4:00 p.m. 12

Figure 1.2.1.8. Inner view of sea-front walls of Fort San Jeronimo. Picture took in the beginning of September 2014 at 12:00 a.m. 13

Figure 1.2.1.9. Inner view of sea-front walls of Fort San Jeronimo. Picture took in the beginning of September at 2014 4:00-5:00 p.m. 13

Figure 1.2.1.10 Entrance of the "Batería Baja" of Fort San Fernando. The proximity of the sea is clearly visible. 13

Figure 1.2.1.11 Water emerging in the ground of Fort Santiago – Batería. 13

Figure 1.2.1. 12. Aerial view of Fort San Lorenzo (http://www.planur-e.es/). 14

Figure 1.2.2.1. http://plate-tectonic.narod.ru/central-america-plate-tectonics01.gif 15

Figure 1.2.2.2. Paleographic reconstruction of the development of the Central American isthmus since Middle Miocene time (from Harmon, 2005). 15

Figure 1.2.2.3. (Modified from French and Schenk, 2000). 16

Figure 1.2.2.4. Geological Map 1:25000 of a. San Lorenzo area and b. Portobelo area (modified from Stewart and Woodring, 1980). 16

Figure 1.2.2.5. Geological Map 1:25000 of Panama Viejo area (modified from Stewart and Woodring, 1980). 17

Figure 1.2.2. 6. Soil characterization of the monumental complex of Panamá Viejo (Pinzón y González, 2004). 19

Figure 1.2.3.1. Panama's population (1961-2003) Data FAOSTAT, year 2005 (http://faostat.fao.org/faostat/help-copyright/copyright-e.htm). 20

Figure 1.2.3.2. GDP (Gross Domestic Product) (Forte, 2008). 21

Figure 2.1.1. 1 Map of Panamá Viejo (http://www.patronatopanamaviejo.org/ppv2014/en/). On the left the monuments and outcrops sampled are listed. 36

Figure 2.1.1. 2. Fortín de la Natividad: a. western wall; b. Southern wall. It is clearly visible the different materials utilized for the lower and upper part. 38

Figure 2.1.1. 3. Plan of the Fortín de la Natividad and sampling points (Plans are Courtesy of the Patronato de Panamá Viejo). 38

Figure 2.1.1. 4. Fortín de la Natividad, outer part of the Southern wall, PV FN 1 sampling. 39

Figure 2.1.1. 5. Fortín de la Natividad, outer part of the Southern wall, PV FN 2 sampling. 39

Figure 2.1.1. 6. Fortín de la Natividad, inner part of the Western wall, PV FN 4 sampling. 39

Figure 2.1.1. 7. Macroscopic picture of sample PV FN 5. 39

Figure 2.1.1. 8. Overview of the San Francisco masonry mainly composed by yellowish-grey breccias. 40

Figure 2.1.1. 9. Plan of the Convento de San Francisco and sampling points (Plans are Courtesy of the Patronato de Panamá Viejo). 40

Figure 2.1.1. 10. Sampling of the yellowish breccia, PV FC 8 specimen. 41

Figure 2.1.1. 11. Sampling of the yellowish breccia, PV FC 4 specimen. 41

Figure 2.1.1. 12. Sampling of the breccia PV FC 5, showing a more reddish hue. 41

Figure 2.1.1. 13. Sampling of the breccia PV FC 7. 42

Figure 2.1.1. 14. Sampling of the breccia PV FC 11. 42

Figure 2.1.1. 15. Sampling of the creamy altered volcanic rock PV FC 6. 42

Figure 2.1.1. 16. Sampling of the creamy altered volcanic rock PV FC 9. 43

Figure 2.1.1. 17. Wall of the complex of the Hospital de San Juan de Dios, facing the old Via Cinquantenario. 43

Figure 2.1.1. 181. Macro photographs of sample PV SJdD. 43

Figure 2.1.1. 19. Pictures of the Convento de las Monjas de la Concepción. 44

Figure 2.1.1. 20. Plan of the Convento de las Monjas de la Concepción and sampling points (Plans are Courtesy of the Patronato de Panamá Viejo). 44

Figure 2.1.1. 212. Sampling of PV CC 4 specimen. 45

Figure 2.1.1.22. Sampling of PV CC 5 specimen. 45

Figure 2.1.1.23. Sampling of PV CC 6 specimen. 45

Figure 2.1.1. 24 Particular of a block of breccia, showing both greyish-greenish and yellowish colour. 46

Figure 2.1.1. 25. Plan of the Convento de la Compañia de Jesus and sampling points (Plans are Courtesy of the Patronato de Panamá Viejo). 46

Figure 2.1.1. 26. Sampling of PV JC 1 sample. 47

Figure 2.1.1. 27. Sampling of PV JC 2 sample. 47

Figure 2.1.1. 283. PV JC 3 sample. 47

Figure 2.1.1. 29. Sampling of PV JC 4 sample. 47

Figure 2.1.1. 304. Wall near the Casa Terrín, showing a reddish chromatic alteration. 48

Figure 2.1.1. 31. Plan of the Casa Terrin and sampling points (Plans are Courtesy of the Patronato de Panamá Viejo). 48

Figure 2.1.1. 32. Sampling of PV CT 1 specimen. 49

Figure 2.1.1. 335. PV CT 2 sample. 49

Figure 2.1.1. 34. Plan of the Cathedral Tower, sampling points and a picture of the West side of the Tower (Plans are Courtesy of the Patronato de Panamá Viejo). 50

Figure 2.1.1. 35. Sampling of PV TC 3 specimen. 51

Figure 2.1.1. 36. Sampling of PV TC 4 specimen. 51

Figure 2.1.1. 37. Effects due to the marine erosion. 52

Figure 2.1.1. 38. Plan of the Casas Reales, sampling points and an image of one monument (Plans are Courtesy of the Patronato de Panamá Viejo). 52

Figure 2.1.1. 39. Sampling of PV CR 4 specimen. 53

Figure 2.1.1. 40. Outcrops near the Casas Reales and sampling points (Plans are Courtesy of the Patronato de Panamá Viejo). 53

Figure 2.1.1. 416. a. PV vic CR sample; b. PV Q 1 sample. 53

Figure 2.1.1. 42. Sampling of PV Q 2 specimen. On the left image, with a red dotted line the tracks of quarrying are highlighted. 54

Figure 2.1.2. 1. Fuerte San Jeronimo a. View from the sea side; b. View of the Portobelo village. 56

Figure 2.1.2. 2. Plan of the Furte San Jeronimo and sampling points (Plans belongs to the Emergency Plan for Property C135 Fortifications on the Caribbean Side of Panama: Portobelo – San Lorenzo). Point 1: PB FSJ 1, 4; Point 3: PB FSJ 7,8. 56

Figure 2.1.2. 3. a. Sampling of PB FSJ 1 specimen; b. Sampling of PB FSJ 7. 57

Figure 2.1.2. 4. a. Sampling of PB FSJ 7 specimen; b. Sampling of PB SFJ 8 specimen. 57

Figure 2.1.2. 5. a. View of the Fuerte de Santiago de la Gloria from the Upper Battery; b; human settlements in a part of the Lower Battery. 58

Figure 2.1.2.6. Plan representing the Fuerte de Santiago de la Gloria and sampling points (Plans belongs to the Emergency Plan for Property C135 Fortifications on the Caribbean Side of Panama: Portobelo – San Lorenzo). 58

Figure 2.1.2. 7. Sampling of PB FdS 2 specimen. 59

Figure 2.1.2. 8. Sampling of PB FdS 5 specimen. 59

Figure 2.1.2. 9. Sampling of PB FdS 9 specimen. 59

Figure 2.1.2. 10. Sampling of PB FdS 5 specimen. 60

Figure 2.1.2. 11. Sampling of PB FdS 8 specimen. 60

Figure 2.1.2. 12. Sampling of PB FdS 10 specimen. 60

Figure 2.1.2. 13. a. Salts efflorescences and encrustations in the vault of the Camera de la inspecciòn; b. Sampling of PB FdS 5, specimen of salt encrustations. 61

Figure 2.1.2. 14. Fuerte San Fernando: a. Lower Battery; b. Upper Battery. 62

Figure 2.1.2. 15. Plan representing the Lower Battery of Fuerte San Fernando and sampling points (Plans belongs to the Emergency Plan for Property C135 Fortifications on the Caribbean Side of Panama: Portobelo – San Lorenzo). 62

Figure 2.1.2. 16. Sampling of PB SF 1 specimen. 63

Figure 2.1.2. 17. Coral limestone utilized in the masonry: a. in a wall; b. in the neck soles of the embrasures. 63

Figure 2.1.2. 18. Coral limestone utilized at the Fort entrance in the centreline of the pavement pavements. 63

Figure 2.1.2. 19. Sampling of PB SF 2 specimen. 64

Figure 2.1.2. 20. a. Basaltic andesite utilized in the pavement at the Fort Entrance; b. Sampling of PB SF ramp specimen. 64

Figure 2.1.2. 21. Sampling of PB SF 6 specimen. 64

Figure 2.1.2. 22. a. View of the inner part of the moat, particular of the salt encrustations; b. Sampling of PB SF 5 specimen. 65

Figure 2.1.2. 23. Plan of the Upper Battery of Fuerte San Fernando and sampling points (Plans belongs to the Emergency Plan for Property C135 Fortifications on the Caribbean Side of Panama: Portobelo – San Lorenzo). 65

Figure 2.1.2. 24. Examples of volcanic rock utilized in the sole of the embrasures neck. 65

Figure 2.1.2. 25. Sampling of PB SF 7 specimen. 66

Figure 2.1.2. 26. Sampling of PB SF 8 specimen. 66

Figure 2.1.2. 27. a. Outcrop of basaltic andesite; b. PB SF 11 sample. 66

Figure 2.1.3. 1. Two views of Fort San Lorenzo. 67

Figure 2.1.3. 2. Plan representing Fuerte San Lorenzo and sampling points (Plans belongs to the Emergency Plan for Property C135 Fortifications on the Caribbean Side of Panama: Portobelo – San Lorenzo). 67

Figure 2.1.3. 3. Sampling of SL 4 specimen. 68

Figure 2.1.3. 4. Sampling of SL 6 specimen. 68

Figure 2.1.3. 5. Sampling of SL 9 specimen. 69

Figure 2.1.3. 6. a. Grainstone forming the ornamental parts of the portal and the base blocks; b. Sampling of SL 8 specimen 69

Figure 2.1.3. 7. Outcrop of sandstone/tuffite forming the bastion foundation. 69

Figure 2.1.3. 8. a. Sampling of SL 1 specimen: b. Sampling of SL 2 specimen. 70

Figure 2.1.3. 9. a. Outcrop of grainstone; b. sampling of SL 13 specimen. 70

Figure 2.3. 1. Particular of the central area of the Panamanian isthmus. On the right the legend of the markers, in green the sites under study: PV=Panama Viejo; SL=San Lorenzo; P=Portobelo. This latter one coincides with a location of the Portobelo monitoring station. The white symbols indicate the monitoring stations, respectively: G=Gatun Rain Z.C., CCL=Cristobal-Cocosolo-Limonbay, FS=Fort Sherman, Pb=Portobelo, B-FAA=Balboa-FAA, HP=Hato Pintado, T=Tocumen, PV=Panamá Viejo, SL=San Lorenzo, P=Pina. 73

Figure 2.3. 2. Black squares represent the area extracted from the Arpege model overlapped the Panamanian region of interest. 75

Figure 2.3. 3. Grid areas of EC-Earth model. In yellow are highlighted the zones which overlap or are near of the sites of interest. On the right the legend of the markers, the white symbols indicate the monitoring stations, the green markers the sites, respectively: G=Gatun Rain Z.C., CCL=Cristobal- Cocosolo-Limonbay, FS=Fort Sherman, Pb=Portobelo(both monitoring station and site), B-FAA=Balboa-FAA, HP=Hato Pintado, T=Tocumen, PV=Panamá Viejo, SL=San Lorenzo, P=Pina. 76

Figure 3.1.1. 1. Photomicrograph of PV CC 5 breccia sample (xpl, 4x). Particular of a carbonate fragment. 78

Figure 3.1.1. 2. Photomicrograph of PV CC 4 breccia sample (xpl, 10x). a. Basalt/andesite fragments. 78

Figure 3.1.1. 3. Photomicrograph of PV CC 4 breccia sample (xpl, 10x). Particular of amygdales filled with zeolites. 78

Figure 3.1.1. 4. Photomicrograph of PV CC 6 breccia sample (xpl, 4x). a. Basalt/andesite fragments; b. fossil. 78

Figure 3.1.1. 5. Photomicrograph of PV CR 4 breccia sample (xpl, 4x). 78

Figure 3.1.1. 6. Photomicrograph of PV CR 4 breccia sample (xpl, 4x). 78

Figure 3.1.1. 7. Photomicrograph of PV JC 2 breccia sample (xpl, 4x), showing a. foraminifera; b. plagioclases and c. zeolitized parts. 79

Figure 3.1.1. 8. Photomicrograph of PV JC 3 breccia sample (xpl,4x). 79

Figure 3.1.1. 9. Photomicrograph of PV FC 4 breccia sample (xpl, 10x), showing subrounded basalt/andesite fragment. 79

Figure 3.1.1. 10. Photomicrograph of PV FC 5 breccia sample (xpl, 10x) showing alterated zoned plagioclase. 79

Figure 3.1.1. 11. Photomicrograph of PV FC 4 breccia sample (xpl, 10x) a. Basalt/andesite fragments; b. devitrified plagioclases. 80

Figure 3.1.1. 12. Photomicrograph of PV FC 4 breccia sample (xpl, 4x) showing diffused zeolitization. 80

Figure 3.1.1. 13. Photomicrograph of PV FC 11 breccia sample (xpl, 4x) showing a chert fragment. 80

Figure 3.1.1. 14. PV FC 11 breccia sample (xpl, 4x), particular of the ironstone. 80

Figure 3.1.1. 15. Photomicrograph of PV FC 11 breccia sample (xpl, 10x), particular showing the ironstone and an amygdale filled with zeolites. 80

Figure 3.1.1. 16. Photomicrograph of PV FC 11 breccia sample (xpl, 40x), particular of zeolites filling an amygdale. 80

Figure 3.1.1. 17. Photomicrograph of PV FC 7 breccia sample, present several foraminifera and a zeolitized part (on the right). 81

Figure 3.1.1. 18. Photomicrograph of PV FC 7 breccia sample (ppl, 10 x). Particular of the presence of metal oxides. 81

Figure 3.1.1. 19. Photomicrograph of PV FN 1 breccia sample (xpl, 10x): a. carbonate fragments; b. plagioclase; c. quartz, d. pyroxenes; e. volcanic fragment. 81

Figure 3.1.1. 20. Photomicrograph of PV FN 1 breccia sample (xpl, 10x), a. basalt/andesite fragments; b. altered plagioclase; presence of iron oxides. 81

Figure 3.1.1. 21. Photomicrograph of PV FN 1 breccia sample (ppl, 4x). Particular of a probable glass fragment (a.). 82

Figure 3.1.1. 22. Photomicrograph of PV FN 2 breccia sample (xpl, 10x) , a. zonate plagioclase; b. rounded - subrounded carbonate fragments; c. basalt fragment and d. iron oxides. 82

Figure 3.1.1. 23. Photomicrograph of PV FN 1 breccia sample (xpl, 10x) plagioclase surrounded by zeolites. 82

Figure 3.1.1. 24. Photomicrograph of FN 1 breccia sample (xpl, 40x), alterated sanidine in the zeolitized part. 82

Figure 3.1.1. 25. Photomicrograph of PV Q1 breccia sample (xpl, 4x), particular of melting inclusion and presence of pyroxenes clusters (a). 82

Figure 3.1.1. 26. Photomicrograph of PV Q1 breccia sample (xpl,4x), amygdales. 82

Figure 3.1.1. 27. Photomicrograph of PV FN 4 basaltic andesite sample (xpl, 4x). 83

Figure 3.1.1. 28. Photomicrograph of PV FN 4 basaltic andesite sample (xpl, 10x), amygdales filled with secondary minerals 83

Figure 3.1.1. 29. Photomicrograph of PV FN 4 basaltic andesite sample (xpl) pyroxenes glomerocrysts and amygdales. 83

Figure 3.1.1. 30. Photomicrograph of PV FN 5 basaltic andesite sample (xpl), large pyroxenes glomerocryst showing a beginning of melting process. 83

Figure 3.1.1. 31. Photomicrograph of PV vic. CR basaltic andesite sample (xpl, 4x). Presence of zoned plagioclase. 84

Figure 3.1.1. 32. Photomicrograph of PV Q 2 basaltic andesite sample (xpl, 10x). Particular of an amygdale. 84

Figure 3.1.1. 33. Photomicrograph of PV TC 4 tuffite sample (xpl, 4x), particular of foraminifera fossil. 84

Figure 3.1.1. 34. Photomicrograph of PV TC 3 tuffite sample (xpl,10x), zeolitized area. 84

Figure 3.1.1. 35 Photomicrograph of PV FC 9 altered volcanic rock sample (xlp, 10x). Clearly evident a chalcedony crystal surrounded by iron oxides. 85

Figure 3.1.1. 36. Photomicrograph of PV FC 6 altered volcanic rock sample (ppl, 10x); particular of superficial whitish "patina". 85

Figure 3.1.1. 37. Photomicrograph of PV FC 6 altered volcanic rock sample (xpl, 10x) Particular of the superficial reddish "patina". 85

Figure 3.1.1. 38. Photomicrograph of PV FC 6 altered volcanic rock sample (10x), reflected light. Particular of the superficial "patina". 85

Figure 3.1.1. 39. Photomicrograph of PV FC 9 altered volcanic rock sample (ppl, 4x); particular of the superficial mortar layer. 85

Figure 3.1.1. 40. Photomicrograph of PV SJdD altered volcanic rock sample (xpl, 4x); particular of the reddish external patina. 86

Figure 3.1.1. 41. Photomicrograph of PV SJdD altered volcanic rock sample (xpl, 4x); particular of the inner whitish patina. 86

Figure 3.1.1. 42. Photomicrograph of PV CT 2 rhyolite sample (xpl, 4x). Particular of a sanidine crystal. 86

Figure 3.1.1. 43. Photomicrograph of PV CT 1 rhyolite sample (xpl, 10x). Plagioclase and iron oxides. 86

Figure 3.1.1. 44. Stereomicroscope micrograph of PV CT 2 rhyolite sample, showing the iron (hydr)oxides concentrated on the external surface. 87

Figure 3.1.1. 45. Macrograph of PV CT 1 rhyolite sample. The increasing of iron (hydr)oxides near the external surfaces id clearly visible. 87

Figure 3.1.1. 46. Photomicrograph of PV JC 4 breccia sample (ppl, 10x). Particular of a zeolitized part showing several cracks. 87

Figure 3.1.1. 47. Photomicrograph of PV TC 4 tuffite sample (ppl, 4x).Cracks presence in proximity of a zeolitized area. 87

Figure 3.1.2. 1. Photomicrograph of PB SFJ 4 sandstone sample (ppl, 4x). 89

Figure 3.1.2. 2. Photomicrograph of PB SFJ 4 sandstone sample (ppl, 40x). Particular of globigerina filled by metal oxides 89

Figure 3.1.2. 3. Photomicrograph of PB SFJ 8 sandstone sample (xpl, 10x). 89

Figure 3.1.2. 4. Photomicrograph of PB SFJ 8 sandstone sample (xpl, 4x). Particular of a macrofossil presenting neomorphism. 89

Figure 3.1.2. 5. Photomicrograph of PB FdS 2 sandstone sample (xpl, 4x). 90

Figure 3.1.2. 6. Photomicrograph of PB FdS 2 sandstone sample (xpl, 10x). 90

Figure 3.1.2. 7. Photomicrograph of PB FdS 5 sandstone sample (xpl, 4x). 90

Figure 3.1.2. 8. Photomicrograph of PB FdS 5 sandstone sample (xpl, 10x). a. particular of a globigerina. 90

Figure 3.1.2. 9. Photomicrograph of PB FdS 9 sandstone sample (xpl, 4x). 90

Figure 3.1.2. 10. Photomicrograph of PB FdS 9 sandstone sample (xpl, 10x). a. particular of a coral fragment. 90

Figure 3.1.2. 11. Photomicrograph of PB FdS 10 tuffite sample (xpl, 4x), particular of the cineritic matrix and the bioclasts (a. coral fragment). 91

Figure 3.1.2. 12. Photomicrograph of PB FdS 10 tuffite sample (xpl, 10x), particular of the cineritic matrix and the bioclasts (a. globigerina; b. amphistegina). 91

Figure 3.1.2. 13. Photomicrograph of SL 1 sandstone/tuffite sample (external part) (xpl, 4x). 91

Figure 3.1.2. 14. Photomicrograph of SL 1 sandstone/tuffite sample (external part) (xpl, 10x). Presence of metal oxides within a bioclast. 91

Figure 3.1.2. 15. Photomicrograph of SL 1 sandstone/tuffite sample (internal part) (xpl, 4x). 92

Figure 3.1.2. 16. Photomicrograph of SL 1 sandstone/tuffite sample (internal part) (ppl, 4x). Volcanic ash showing cracks. 92

Figure 3.1.2. 17. Photomicrograph of SL 2 sandstone/tuffite sample (xpl, 4x) Volcanic ash showing cracks. 92

Figure 3.1.2. 18. Photomicrograph of SL 2 sandstone/tuffite sample (xpl, 10x). Particular of the bioclasts present in the sample (a. brachiopod spine; b. gastropod) filled with silicates. 92

Figure 3.1.2. 19. Photomicrograph of SL 4 tuffite sample (xpl, 4x). 93

Figure 3.1.2. 20. Photomicrograph of SL 4 tuffite sample (xpl, 10x). a. basalt/andesite fragments; b foraminifera fragments filled with silicates. 93

Figure 3.1.2. 21. Photomicrograph of SL 6 tuffite sample (xpl, 10x). a. volcanic rock fragment; b. foraminifera fragments. 93

Figure 3.1.2. 22. Photomicrograph of SL 6 tuffite sample (xpl, 10x). Particular of a coral showing a re-crystallization of calcite on the external part. 93

Figure 3.1.2. 23. Photomicrograph of SL 9 tuffite sample (ppl, 4x). Diffused cracks are clearly visible. 94

Figure 3.1.2. 24. Photomicrograph of SL 9 tuffite sample (xpl, 4x). Different granulometry between the bioclasts and the volcanic part. 94

Figure 3.1.2. 251. Photomicrograph of PB FSJ 1 coral boundstone sample (xpl, 4x). 94

Figure 3.1.2. 26. Photomicrograph of PB FSJ 1 coral boundstone sample (xpl, 4x). Particular of the biological patina. 95

Figure 3.1.2. 272. Photomicrograph of PB FSJ 1 coral boundstone sample (xpl, 4x). Particular of the porosity. 95

Figure 3.1.2. 28. Photomicrograph of PB FSJ 7 coral boundstone sample (xpl, 4x). Particular of the structure and the mortar layer. 95

Figure 3.1.2. 29. Photomicrograph of PB FdS 6 coral boundstone sample (xpl, 10x) calcite re-crystallization within the pores of the structure. 95

Figure 3.1.2. 30. Photomicrograph of PB FdS 6 coral boundstone sample (xpl, 4x), mortar remains. 95

Figure 3.1.2. 31. Photomicrograph of PB FdS 8 coral boundstone sample (xpl, 10x) calcite crystallization within the pores of the structure. 96

Figure 3.1.2. 32. Photomicrograph of PB FdS 8 coral boundstone sample (xpl, 4x), biological patina. 96

Figure 3.1.2. 33. Photomicrograph of PB SF 2 coral boundstone sample (xpl, 4x). Particular of calcite crystallization within the pores. 96

Figure 3.1.2. 34. Photomicrograph of PB SF 8 coral boundstone sample (xpl, 4x). Particular of calcite crystallization within the pores. 96

Figure 3.1.2. 35. Photomicrograph of PB SF 2 coral boundstone sample (xpl, 4x). Particular of the porosity. 96

Figure 3.1.2. 36. Photomicrograph of PB SF 8 coral boundstone sample (xpl, 4x). Particular of the porosity. 96

Figure 3.1.2. 37. Photomicrograph of SL 8 grainstone sample (ppl, 4x). a. Bryozoan fragment. 97

Figure 3.1.2. 38. Photomicrograph of SL 8 grainstone sample (xpl, 4x). a. Volcanic ejecta fragment. 97

Figure 3.1.2. 39. Photomicrograph of SL 13 grainstone sample (ppl, 4x). Bryozoan fragments. 97

Figure 3.1.2. 40. Photomicrograph of SL 13 grainstone sample (xpl, 4x). a. Echinoid fragment. 97

Figure 3.1.2. 41. Photomicrograph of PB SF 1 grainstone/packstone sample (xpl, 4x), particular of the packstone part. 98

Figure 3.1.2. 42. Photomicrograph of PB SF 1 grainstone/packstone sample (xpl, 4x), particular of the grainstone part.a. Bryozoans; b. Echinoids. 98

Figure 3.1.2. 43. Photomicrograph of PB SF 6 basaltic andesite sample (xpl, 4x). Particular of pyroxenes and plagioclases. 98

Figure 3.1.2. 44. Photomicrograph of PB SF 7 basaltic andesite sample (xpl, 4x). Augite crystal. 98

Figure 3.1.2. 45. Photomicrograph of PB SF 7 basaltic andesite sample (ppl, 4x). Particular of fluid circulation and iron oxides. 99

Figure 3.1.2. 46. Photomicrograph of PB SF 7 basaltic andesite sample (xpl, 4x). Particular of the sericitization of plagioclases and amygdales filled by zeolites. 99

Figure 3.1.2. 47. Photomicrograph of PB SF 11 basaltic andesite sample (xpl,4x). Particular of augite crystals. 99

Figure 3.1.2. 48. Photomicrograph of PB SF 11 basaltic andesite sample (xpl,4x). Particular of the sericitization of plagioclases. 99

Figure 3.1.2. 49. Photomicrograph of PB FdS 3 salt encrustation sample (xpl,4x). Particular of several calcite layers. 100

Figure 3.1.2. 50. Photomicrograph of PB FdS 3 salt encrustation sample (xpl, 10x). Particular of micritic and sparitic crystals of calcite. 100

Figure 3.1.2. 51. Photomicrograph of PB SF 5 salt encrustation sample (xpl,4x). Particular of several calcite layers. 100

Figure 3.1.2. 52. Photomicrograph of PB SF 5 salt encrustation sample (xpl, 10x). Particular of micritic and sparitic crystals of calcite. 100

Figure 3.2. 1. Randomly oriented diffractogram of PV FC 7 sample. On the right, diffractograms of PV FC 7 sample, in randomly oriented (black), oriented (blue) and saturated with glycol (red) state. 103

Figure 3.2. 2 Randomly oriented diffractogram of PV FN 5 sample. On the right, diffractograms of PV FN 5 sample, in randomly oriented (black), oriented (blue) and saturated with glycol (red) state. 106

Figure 3.3.1. 1. PLM photomicrograph of PV FN1 sample (xpl, 4x). Plagioclase crystal surrounded by zeolites; presence of brownish iron oxides. 108

Figure 3.3.1. 2. BSD-ESEM photomicrograph of PV FN1 sample. Plagioclase crystal surrounded by zeolites. The area under investigation is highlighted by a red rectangle. 108

Figure 3.3.1. 3. BSD-ESEM photomicrograph of PV FN1 sample. The blue rectangle indicates the area of EDS investigation 108

Figure 3.3.1. 4. ESEM-EDS spectrum of PV FN 1 sample, area shown in Fig. 3.3.1.3. 109

Figure 3.3.1. 5. BSD-ESEM photomicrograph of PV FN1 sample. The area under investigation is highlighted by a red rectangle. 109

Figure 3.3.1. 6. BSD-ESEM photomicrograph of PV FN1 sample. The blue rectangle indicates the area of EDS investigation. 109

Figure 3.3.1. 7. ESEM-EDS spectrum of PV FN 1 sample, area shown in Fig. 3.3.1.6. 110

Figure 3.3.1. 8. BSD-ESEM photomicrograph of PV FN1 sample. The blue rectangle indicates the area of EDS investigation. 110

Figure 3.3.1. 9. ESEM-EDS spectrum of PV FN 1 sample, area shown in Fig. 3.3.1.8. 111

Figure 3.3.1. 10. PLM photomicrograph of PV FC 4 sample (xpl, 10x). Particular of yellowish-brownish parts present in the zeolitized areas. 111

Figure 3.3.1. 11. BSD-ESEM photomicrograph of PV FC 4 sample. Particular of the yellowish-brownish parts present in the zeolitized areas. 111

Figure 3.3.1. 12. BSD-ESEM photomicrograph of PV FC 4 sample. a. zeolite; b. Particular of the yellowish-brownish parts. 112

Figure 3.3.1. 13. BSD-ESEM photomicrograph of PV FC 4 sample. The 3 points of EDS analysis are indicated with red dots. 112

Figure 3.3.1. 14. ESEM-EDS spectrum 1 of PV FC 4 sample, area shown in Fig. 3.3.1.13. 112

Figure 3.3.1. 15. ESEM-EDS spectrum 2 of PV FC 4 sample, area shown in Fig. 3.3.1.16. 113

Figure 3.3.1. 16. ESEM-EDS spectrum 3 of PV FC 4 sample, area shown in Fig. 3.3.1.16. 113

Figure 3.3.1. 17. BSD-ESEM photomicrograph of PV FC 4 sample. The area under investigation is highlighted by a red rectangle. 114

Figure 3.3.1. 18. BSD-ESEM photomicrograph of PV FC 4 sample. The EDS-Maps analysis has been performed on the area within the blue rectangle, so including also a plagioclase (on the left). 114

Figure 3.3.1. 19. ESEM-EDS spectrum of PV FC 4 sample, area shown in Fig. 3.3.1.18. 114

Figure 3.3.1. 20. Photomicrographs of PV FC 4 sample representing the EDS-maps analyses carried out on the area shown in a; b. EDS-map of Si; c. EDS-map of Al; d. EDS-map of Na; e. EDS-map of Ca; f. EDS-map of; g. EDS-map of Fe; h. EDS-map of Mg. 115

Figure 3.3.1. 21. BSD-ESEM photomicrograph of PV FC 7 sample. The area under investigation is highlighted by a red rectangle. 116

Figure 3.3.1. 22. BSD-ESEM photomicrograph of PV FC 7 sample. The blue rectangle indicates the area of EDS investigation. 116

Figure 3.3.1. 23. ESEM-EDS spectrum of PV FC 7 sample, area shown in Fig. 3.3.1.18. 116

Figure 3.3.1. 24. Stereomicroscope photomicrograph of PV FN 5 sample. 117

Figure 3.3.1. 25. Photomicrograph of PV FN 4 (xpl, 10x), amygdales filled with secondary minerals, 117

Figure 3.3.1. 26. Photomicrograph of PV FN 4 (ppl, 10x), amygdales filled with secondary minerals. 117

Figure 3.3.1. 27. BSD-ESEM photomicrograph of PV FN 4 sample showing amygdales filled with secondary minerals. 117

Figure 3.3.1. 28. BSD-ESEM photomicrograph of PV FN 4 sample. 117

Figure 3.3.1. 29. ESEM-EDS spectrum 1 of PV FN 4 sample, point shown in Fig. 3.3.1.28. 118

Figure 3.3.1. 30. ESEM-EDS spectrum 2 of PV FN 4 sample, point shown in Fig. 3.3.1.28. 118

Figure 3.3.1. 31. ESEM-EDS spectrum 3 of PV FN 4 sample, point shown in Fig. 3.3.1.28. 118

Figure 3.3.1. 32. BSD-ESEM photomicrograph of PV FN 4 sample showing an amygdale filled with secondary minerals. The red dots indicate the points of analysis 119

Figure 3.3.1. 33. BSD-ESEM photomicrograph of PV FN 4 sample. Particular of the fibrous structure of the minerals contained in the amygdale. 119

Figure 3.3.1. 34. ESEM-EDS spectrum 1 of PV FN 4 sample, point shown in Fig. 3.3.1.32. 119

Figure 3.3.1. 35. ESEM-EDS spectrum 2 of PV FN 4 sample, point shown in Fig. 3.3.1.32. 120

Figure 3.3.1. 36. ESEM-EDS spectrum 3 of PV FN 4 sample, point shown in Fig. 3.3.1.32. 120

Figure 3.3.1. 37. Stereomicroscope photomicrograph of PB SF 6 sample showing an amygdale. 121

Figure 3.3.1. 38. Stereomicroscope photomicrograph of PB SF 6 sample showing an amygdale. 121

Figure 3.3.1. 39. PLM photomicrograph of PB SF 6 sample showing an amygdale between plagioclases and a pyroxene (right, bottom). 121

Figure 3.3.1. 40. BSD-ESEM photomicrograph of PB SF 6 represented in Fig. 3.3.1.39. The red dot represents the point of EDS analysis. 121

Figure 3.3.1. 41. ESEM-EDS spectrum of PB SF 6 sample, point shown in Fig. 3.3.1.40. 122

Figure 3.3.1. 42. PLM photomicrograph of PB SF 6 sample showing an amygdale between plagioclases and a pyroxene cluster (right). 122

Figure 3.3.1. 43. BSD-ESEM photomicrograph of PB SF 6 represented in Fig. 3.3.1.42. The blue rectangle and the red dot represent respectively the area and the point of EDS analysis. 122

Figure 3.3.1. 44. ESEM-EDS spectrum 1 of PB SF 6 sample, area shown in Fig. 3.3.1.43. 123

Figure 3.3.1. 45. ESEM-EDS spectrum 1 of PB SF 6 sample, point shown in Fig. 3.3.1.43. 123

Figure 3.3.1. 46. PLM photomicrograph of PB SF 6 sample showing an amygdale. 124

Figure 3.3.1. 47. BSD-ESEM photomicrograph of PB SF 6 represented in Fig. 3.3.1.46. 124

Figure 3.3.1. 48. ESEM-EDS spectrum of PB SF 7 sample, area shown in Fig. 3.3.1.49a. 124

Figure 3.3.1. 49. Photomicrographs of PB SF 6 sample representing the EDS-maps analyses carried out on the area shown in a; b. EDS-map of Si; c. EDS-map of O; d. EDS-map of Al; e. EDS-map of Fe; f. EDS-map of Mg; g. EDS-map of Ca; h. EDS-map of K; i. EDS-map of Na. 125

Figure 3.3.1. 50. Stereo photomicrograph of PB SF 11 bulk sample showing an amygdale. 126

Figure 3.3.1. 51. BSD-ESEM photomicrograph of PB SF 11 bulk, represented in Fig. 3.3.1.50. The red dot represents the point of EDS analysis. 126

Figure 3.3.1. 52. ESEM-EDS spectrum of PB SF 11 bulk sample, area shown in Fig. 3.3.1.51. 126

Figure 3.3.1. 53. PLM photomicrograph of PV FN1 sample (xpl, 4x). Particular of the black fragment. 127

Figure 3.3.1. 54. BSD-ESEM photomicrograph of PV FN 1 sample. The blue rectangle indicates the area of EDS investigation. 127

Figure 3.3.1. 55. ESEM-EDS spectrum of PV FN 1 sample, area shown in Fig. 3.3.1.54. 127

Figure 3.3.2. 1 PLM photomicrograph of PV FC 6 (ppl, 10x), particular of superficial reddish "patina". 128

Figure 3.3.2. 2. BSD-ESEM photomicrograph of PV FC 6 sample. The blue rectangle indicates the area of EDS investigation. 128

Figure 3.3.2. 3. ESEM-EDS spectrum of PV FC 6 sample, area shown in Figure 3.3.2.2. 128

Figure 3.3.2. 4. Photomicrographs of PV FC 6 sample representing the EDS-maps analyses carried out on the area shown in Fig. 3.3.2.2 a. EDS-map of Si; b. EDS map of Al; c. EDS map of Mg; d. EDS map of Na; e. EDS map of O; f. EDS map of K; g. EDS map of Fe; h. EDS map of Ca. 129

Figure 3.3.2. 5. PLM photomicrograph of PV SJdD sample (xpl, 4x), particular of superficial whitish "patina". 130

Figure 3.3.2. 6. BSD-ESEM photomicrograph of PV SJdD sample. The blue rectangle indicates the area of EDS investigation. 130

Figure 3.3.2. 7. ESEM-EDS spectrum of PV SJdD sample, area shown in Fig. 3.3.2.7. 130

Figure 3.3.2. 8. Photomicrographs of PV SJdD sample representing the EDS-maps analyses carried out on the area shown in Fig. 3.3.2.6. a. EDS-map of Si; b. EDS map of Ca; c. EDS map of Al; d. EDS map of Mg; e. EDS map of Na; f. EDS map of O; g. EDS map of K. 131

Figure 3.3.2.9. Stereo photomicrograph of PV TC 4 sample, showing a superficial black algal patina. 132

Figure 3.3.2. 10. BSD-ESEM photomicrograph of PV TC 4 sample. Particular of the superficial black algal patina and of a cubic crystal, probably ascribable to NaCl. 132

Figure 3.3.2. 11. BSD-ESEM photomicrograph of PB SF 2 showing moss filaments on coral limestone. 132

Figure 3.3.2. 12. BSD-ESEM photomicrograph of PB SF 1 showing moss filaments on grainstone/packstone. 132

Figure 3.3.2. 13. BSD-ESEM photomicrograph of PB SF 1 showing moss filaments covering the surface except for the part in the middle. 133

Figure 3.3.2. 14. BSD-ESEM photomicrograph of PB SF 1 showing the presence of a cubic crystal. The red dots show the EDS analysis points. 133

Figure 3.3.2. 15. ESEM-EDS spectrum 1 of PB SF 1 sample, area shown in Fig. 3.3.2.14. 133

Figure 3.3.2. 16. ESEM-EDS spectrum 2 of PB SF 1 sample, area shown in Fig. 3.3.2.14. 133

Figure 3.3.2. 17. BSD-ESEM photomicrographs of PB SF 5 calcite encrustation. 134

Figure 3.3.2. 18. ESEM-EDS one spectrum obtained by EDS analyses on of PB SF 5 sample, area shown in Fig. 3.3.2.17. 134

Figure 3.3.2. 19. BSD-ESEM photomicrographs of PB SF 5 calcite encrustation, showing a biological patina (a, b different zoom). 135

Figure 3.3.2. 20. ESEM-EDS spectrum of PB SF 5 sample, area shown in Fig. 3.3.2.19b. 135

Figure 3.3.2. 21. Photomicrographs of PB SF 5 sample representing the EDS-maps analyses carried out on the area shown in Fig. 3.3.2.19b; a. EDS-map of O; b. EDS map of C; c. EDS map of Ca; d. EDS map of S; e. EDS map of Si; f. EDS map of Al; g. EDS map of Mg; h. EDS map of Na. 135

Figure 3.4. 1. TAS (Total Alkali/Silica) classification (Le Maitre, 1984). ○ = Masonry samples; ◊ = Outcrops samples. 140

Figure 3.4. 2. Winchester & Floyd (1977) classification for altered volcanic rocks. 141

Figure 3.4. 3. Binary diagram alumina versus silica. The different sets identify the diverse rock typologies: coral limestone (violet line); grainstone (yellow line); sandstone and grainstone (green line); breccia, basaltic andesite and tuffite (blue line); rhyolite (red line); rhyodacite (black line). 143

Figure 3.4. 4. Binary calcium oxide versus silica. The different sets identify the diverse rock typologies: coral limestone (violet line); grainstone (yellow line); sandstone and grainstone (green line); breccia, basaltic andesite and tuffite (blue line); rhyolite and rhyodacite (red line). 143

Figure 3.4. 5. Binary diagram iron oxide versus silica. The different sets identify the diverse rock typologies: coral limestone (violet line); grainstone (yellow line); sandstone and grainstone (green line); breccia, basaltic andesite and tuffite (blue lines); rhyolite (red line); rhyodacite (black line). 144

Figure 3.4. 6. Binary diagram alkali versus silica. The different sets identify the diverse rock typologies: coral limestone (violet line); grainstone (yellow line); sandstone and grainstone (green line); breccia, basaltic andesite and tuffite (blue lines); rhyolite (red line); rhyodacite (black line). 144

Figure 3.4. 7. Binary diagram sodium oxide versus potassium oxide. The different sets identify the diverse rock typologies: coral limestone (violet line); basaltic andesite (PV FN 4,5), rhyodacite (PV FC 9) and tuffite/sandstone (SL 1,4) (yellow line); grainstone, sandstone and tuffite (orange line); breccia and basaltic andesite (blue line); breccia (PV FN 1,2) (green line); rhyolite (red line). 145

Figure 3.5. 1. Pore size distribution of polygenic breccia sample, PV FC 4, showing bimodal distribution. 147

Figure 3.5. 2. Pore size distribution of polygenic breccia sample, PV CC 4, showing unimodal distribution. 147

Figure 3.5. 3. Pore size distribution of tuffite sample, PV TC 3, showing symmetrical multimodal distribution. 148

Figure 3.5. 4. Pore size distribution of tuffite sample, PB FdS 10, showing unimodal left skewed distribution. 148

Figure 3.5. 5. Pore size distribution of basaltic andesite sample, PV FN 4 showing multimodal distribution. 149

Figure 3.5. 6. Pore size distribution of basaltic andesite sample, PB SF 6 showing unimodal right skewed distribution. 149

Figure 3.5. 7. Pore size distribution of tuffite sandstone sample, PB FSJ 8 showing bimodal left skewed distribution. 150

Figure 3.5. 8. Pore size distribution of grainstone sample, PB SF1, showing symmetric multimodal distribution. 151

Figure 3.5. 9. Pore size distribution of grainstone sample, SL 13, showing multimodal distribution. 151

Figure 3.5. 10. Pore size distribution of boundstone sample, PB SF 2, showing unimodal, left skewed, distribution. 152

Figure 3.5. 11. Pore size distribution of a rhyodacite sample, PV FC 6, showing an approximately unimodal right skewed distribution. . 152

Figure 3.5. 12. Pore size distribution of a rhyolite sample, PV CT 1, showing a symmetric unimodal distribution. 153

Figure 3.6. 1. Ion concentration in Panama Viejo samples, calcium is excluded in order to have a clearer visualization of the other ions. 155

Figure 3.6. 2. Ion concentration in Portobelo and San Lorenzo samples, calcium is excluded in order to have a clearer visualization of the other ions. 156

Figure 4.1. 1. Black squares belong to Arpege model; red squares belong to EC-Earth model and the 5 areas here presented are highlighted on the left with yellow filling. 159

Figure 4.1.1. 1. EC-Earth selected area. In red is highlighted the zone under investigation in this paragraph. 160

Figure 4.1.1. 2. Arpege selected area. In red is highlighted the zone under investigation in this paragraph. 160

Figure 4.1.1. 3 Average of rainfall monthly amount over 20 years (1988-2008), at the area of Panama Viejo (Long.-79.49; Lat.9.01). Comparison among the historic series of the Hato Pintado and Tocumen monitoring stations and the historic simulation of the Arpege-FN1 and EC-Earth models. 161

Figure 4.1.1. 4. Rainfall data of EC-Earth vs Hato Pintado. 161

Figure 4.1.1. 5. Rainfall data of Arpege-FN1 vs Hato Pintado 161

Figure 4.1.1. 6. Comparison of monthly average of temperature of Tocumen monitoring station and Arpege-FN1 and EC-Earth experiments, over 30 years (1979-2008). 162

Figure 4.1.1. 7. Temperature data of EC-Earth vs Tocumen. 162

Figure 4.1.1. 8. Temperature data of Arpege-FN1 vs Tocumen. 162

Figure 4.1.1. 9. Comparison of monthly average of relative humidity of Tocumen monitoring station and Arpege-FN1 and EC-Earth experiments, over 30 years (1979-2008). 163

Figure 4.1.1. 10. Relative humidity data of EC-Earth vs Tocumen. 163

Figure 4.1.1. 11. Relative humidity data of Arpege-FN1 vs Tocumen. 163

Figure 4.1.2. 1 EC-Earth selected area. In red is highlighted the zone under investigation in this paragraph. 164

Figure 4.1.2. 2. Arpege selected area. In red is highlighted the zone under investigation in this paragraph. 164

Figure 4.1.2. 3. Average of rainfall monthly amount over 30 years (1979-2008), at the area near Panama Viejo (Long.-79.50; Lat.9.01). Comparison among the historic series of the Balboa FAA monitoring station and the historic simulation of the Arpege-FN1 and EC-Earth models. 165

Figure 4.1.2. 4. Rainfall data of EC-Earth vs Balboa FAA. 165

Figure 4.1.2. 5. Rainfall data of Arpege-FN1 vs Balboa FAA. 165

Figure 4.1.2. 6. Comparison of monthly average of temperature of Balboa FAA monitoring station and models data, over 30 years (1979-2008). 166

Figure 4.1.2. 7. Temperature data of EC-Earth vs Balboa FAA. 166

Figure 4.1.2. 8. Temperature data of Arpege-FN1 vs Balboa FAA. 166

Figure 4.1.2. 9. Comparison of monthly average of relative humidty of Balboa FAA monitoring station and models data, over 30 years (1979-2008). 167

Figure 4.1.2. 10. Relative humidity data of EC-Earth vs Balboa FAA. 167

Figure 4.1.2. 111. Relative humidity data of Arpege-FN1 vs Balboa FAA. 167

Figure 4.1.3. 1. EC-Earth selected area. In red is highlighted the zone under investigation in this paragraph 168

Figure 4.1.3. 2. Arpege selected area. In red is highlighted the zone under investigation in this paragraph. 168

Figure 4.1.3. 3. Average of rainfall monthly amount over 28 years (1981-2008), at the area Near San Lorenzo (Long.-80.00, Lat.9.32). Comparison among the historic series of the Gatún (G) and Cocosolo-Cristóbal-Limonbay (CCL)

monitoring stations and the historic simulation of the Arpege-FN1 and EC-Earth models. 169

Figure 4.1.3. 4. Rainfall data of EC-Earth vs average G-CCL. 169

Figure 4.1.3. 5. Rainfall data of Arpege-FN1 vs average G-CCL. 169

Figure 4.1.3. 6. Comparison of the average of rainfall monthly amount of Gatún (G), Cocosolo-Cristóbal-Limonbay (CCL) and Fort Sherman (FS) monitoring stations, and their average, and models data, over 12 years (1997-2008). 170

Figure 4.1.3. 7. Rainfall data of EC-Earth vs average G-CCL-FS. 171

Figure 4.1.3. 8. Rainfall data of Arpege-FN1 vs average G-CCL-FS. 171

Figure 4.1.3. 9. Comparison of the average of monthly temperature of Gatún (G) and Cocosolo-Cristóbal-Limonbay (CCL) monitoring stations, and their average, and models data, over 28 years (1979-2006). 172

Figure 4.1.3. 10. Temperature data of EC-Earth vs average G-CCL. 172

Figure 4.1.3. 11. Temperature data of Arpege-FN1 vs average G-CCL. 172

Figure 4.1.3. 12. Average of the air T (°C) monthly amount over 1997-2008 at the area near San Lorenzo. 173

Figure 4.1.3. 13. Temperature data of EC-Earth vs Average G-CCL. 174

Figure 4.1.3. 141. Temperature data of Arpege-FN1 vs Average G-CCL. 174
Figure 4.1.3. 15. Average of the RH monthly amount over 1979-2006 at the area near San Lorenzo. 175
Figure 4.1.3. 16. Relative humidity data of EC-Earth vs Average G-CCL. 175
Figure 4.1.3. 17. Relative humidity data of Arpege-FN1 vs Average G-CCL. 175
Figure 4.1.3. 18. Average of the RH monthly amount over 1997-2008 at the area near San Lorenzo. 176
Figure 4.1.3. 19. Relative humidity data of EC-Earth vs Mean G-CCL-FS. 176
Figure 4.1.3. 20. Relative humidity data of FN1 vs Mean G-CCL-FS. 176
Figure 4.1.4. 1. EC-Earth selected area. In red is highlighted the zone under investigation in this paragraph. 177
Figure 4.1.4. 2. Arpege selected area. In red is highlighted the zone under investigation in this paragraph. 177
Figure 4.1.4. 3. Average of the rainfall monthly amount over 1979-1998 at the area of San Lorenzo. 178
Figure 4.1.4. 4. Rainfall data of EC-Earth vs Pina. 178
Figure 4.1.4. 5. Rainfall data of FN1 vs Pina. 178
Figure 4.1.5. 1. EC-Earth selected area. In red is highlighted the zone under investigation in this paragraph. 179
Figure 4.1.5. 2. Arpege selected area. In red is highlighted the zone under investigation in this paragraph. 179
Figure 4.1.5. 3. Average of the rainfall monthly amount over 1979-2000 at the area of Portobelo. 180
Figure 4.1.5. 4. Rainfall data of EC-Earth vs Portobelo. 180
Figure 4.1.5. 5. Rainfall data of FN1 vs Portobelo. 180
Figure 4.2.1. 1. Comparison of the yearly rainfall amount HP-T / EC-Earth / FN1-Arpege (1979-2008). 183
Figure 4.2.1. 2. Comparison of the yearly R amount EC-Earth – Arpege-FN 2. 183
Figure 4.2.1. 3. RH monthly average over 30 years (1979-2008). 185
Figure 4.2.1. 4 RH monthly average over 30 years (2039-2068). 186
Figure 4.2.1. 5. T monthly average over 30 years (1979-2008). 187
Figure 4.2.1. 6. T monthly average over 30 years (2039-2068). 188
Figure 4.2.2. 1. Comparison of the yearly rainfall amount Balboa FAA/ EC-Earth / Arpege-FN1 (1979-2008). 190
Figure 4.2.2. 2. Comparison of the yearly R amount EC-Earth –Arpege-FN2. 190
Figure 4.2.2. 3. RH monthly average over past 30 years (1979-2008). 192
Figure 4.2.2. 4. RH monthly average over future 30 years (2039-2068). 193
Figure 4.2.2. 5. T monthly average over past 30 years (1979-2008). 194
Figure 4.2.2. 6. T monthly average over future 30 years (2039-2068). 195
Figure 4.2.3. 1. R yearly amount over past 28 years (1981-2008). 197
Figure 4.2.3. 2. R yearly amount over future 30 years (2039-2068). 197
Figure 4.2.3. 3. RH monthly average over past 27 years (1979-2005). 199
Figure 4.2.3. 4. RH monthly average over future 30 years (2039-2068). 200
Figure 4.2.3. 5. T monthly average over past 30 years (1979-2008). 201
Figure 4.2.3. 6. T monthly average over future 30 years (2039-2068). 202
Figure 4.2.4. 1. R yearly amount (mm), over the past period 1979-1998. 204
Figure 4.2.4. 2. Comparison of the yearly R amount EC-Earth - Arpege-FN2. 204
Figure 4.2.5. 1. R yearly amount (mm), over the past period 1979-2000. 207
Figure 4.2.5. 2. Comparison of the yearly R amount EC-Earth - Arpege-FN 2. 207
Figure 5.1. 1. Histogram showing rocks containing carbonate, with accessible porosity lower than 25 %. 209
Figure 5.1. 2. Surface Recession on carbonate stones in Panamá Viejo area (1979-2008). 210
Figure 5.1. 3. Future (2009-2100) surface recession simulations for the Panamá Viejo area, utilizing L = R*18.8, data without bias correction. 211

Figure 5.1. 4. Future (2009-2100) surface recession simulation for the Panamá Viejo area, utilizing L = R*21.8, data without bias correction. 211

Figure 5.1. 5. Recession on carbonate stones near Panamá Viejo area (1979-2008). 212

Figure 5.1. 6. Future (2009-2100) surface recession simulations for the simulation for the area near Panamá Viejo, utilizing L = R*18.8, data without bias correction. 213

Figure 5.1. 7. Future (2009-2100) surface recession simulations for the simulation for the area near Panamá Viejo, utilizing L = R*21.8, data without bias correction. 213

Figure 5.1. 8. Surface Recession on carbonate stones near San Lorenzo area (1979-2008). 214

Figure 5.1. 9. Future (2009-2100) surface recession simulation for the area near San Lorenzo, utilizing L = R*18.8, data without bias correction. 215

Figure 5.1. 10. Future (2009-2100) surface recession simulation for the area near San Lorenzo, utilizing L = R*21.8, data without bias correction. 215

Figure 5.1. 11. Surface Recession on carbonate stones at San Lorenzo area (1979-2008). 216

Figure 5.1. 12. Future (2009-2100) surface recession simulation for the area of San Lorenzo, utilizing L = R*18.8, data without bias correction. 217

Figure 5.1. 13. Future (2009-2100) surface recession simulation for the area of San Lorenzo, utilizing L = R*21.8, data without bias correction. 217

Figure 5.1. 14. Surface Recession on carbonate stones in Portobelo area (1979-1998). . Surface Recession on carbonate stones in Portobelo area (1979-1998). 218

Figure 5.1. 15. Future (2009-2100) surface recession simulations for the simulation for the area of Portobelo, utilizing L = R*18.8, data without bias correction. 219

Figure 5.1. 16. Future (2009-2100) surface recession simulations for the simulation for the area of Portobelo, utilizing L = R*21.8, data without bias correction. 219

Figure 5.1.6. 1. Estimated surface recession (L=18.8*R) under EC-Earth scenario. a. For the past period 1979–2008 (baseline); b. For the middle future period (2039-2068). 221

Figure 5.1.6. 2. Middle future period (2039-2068): a. Estimated surface recession (L=21.8*R) under EC-Earth scenario; b. Differences between the estimated future surface recessions under EC-Earth scenario applying the two constants: (L_1=21.8*R) - (L_2=18.8*R). 221

Figure 5.1.6. 3. Differences between the estimated future surface recessions under EC-Earth scenario future - past: a. utilizing for the future projection (L=18.8*R); b. utilizing for the future projection (L=21.8*R). 221

Figure 5.2. 1. Average of NaCl monthly transitions 1979-2008 in Panamá Viejo area.a. considering 75.3% as threshold; b. considering 75.1% . 223

Figure 5.2. 2. Average of NaCl monthly transitions 2039-2068 in Panamá Viejo area.a. considering 75.3% as threshold; b. considering 75.1% . 224

Figure 5.2. 3. Average of NaCl monthly transitions 1979-2008 near Panamá Viejo area. a. considering 75.3% as threshold; b. considering 75.1% . 225

Figure 5.2. 4. Average of NaCl monthly transitions 2039-2068 near Panamá Viejo area. a. considering 75.3% as threshold; b. considering 75.1% . 225

Figure 5.2. 5. Average of NaCl monthly transitions 1979-2004 near San Lorenzo area.a. considering 75.3% as threshold; b. considering 75.1% . 226

Figure 5.2. 6. Average of NaCl monthly transitions 2039-2068 near San Lorenzo area. a. considering 75.3% as threshold; b. considering 75.1%. 226

Figure 5.2. 7. 1979-2008 San Lorenzo area: a. average of monthly T over the thirty years; b. average of NaCl monthly transitions considering 75.3% and 75.1% thresholds. 227

Figure 5.2. 8. 2039-2068 San Lorenzo area: a. average of monthly T over the thirty years; b. average of NaCl monthly transitions considering 75.3% and 75.1% thresholds. 227

Figure 5.2. 9. 1979-2008 Portobelo area: a. average of monthly T over the thirty years; b. average of NaCl monthly transitions considering 75.3% and 75.1% thresholds. 228

Figure 5.2. 10. 2039-2068 Portobelo area: a. average of monthly T over the thirty years; b. average of NaCl monthly transitions considering 75.3% and 75.1% thresholds. 228

Figure 5.3. 1. Biomass accumulation (g cm-2) at Panamá Viejo area (1979-2008): comparison between model simulations and the monitoring stations. 230

Figure 5.3. 2. Biomass accumulation (g cm-2) at Panamá Viejo area (1979-2008): comparison between model simulations with bias and monitoring stations. 231

Figure 5.3. 3. Future (2009-2100) yearly biomass for the area of Panamá Viejo. 232

Figure 5.3. 4. Biomass accumulation (g cm-2) near the Panamá Viejo area (1979-2008): comparison between model simulations and the monitoring stations. 233

Figure 5.3. 5. Biomass accumulation (g cm-2) near the Panamá Viejo area (1979-2008): comparison between model simulations with bias and monitoring stations. 233

Figure 5.3. 6. Future (2009-2100) yearly biomass for the area near Panamá Viejo. 234

Figure 5.3. 7. Biomass accumulation (g cm-2) near the San Lorenzo area (1979-2008): comparison between model simulations and the monitoring stations. 235

Figure 5.3. 8. Biomass accumulation (g cm-2) near the San Lorenzo area (1979-2008): comparison between model simulations with bias and monitoring stations. 235

Figure 5.3. 9. Future (2009-2100) yearly biomass for the area near San Lorenzo 236

Figure 5.3. 10. Biomass accumulation (g cm-2) at San Lorenzo area (1979-2008): comparison between model simulations. 237

Figure 5.3. 11. Future (2009-2100) yearly biomass for the area of San Lorenzo. 238

Figure 5.3. 12. Biomass accumulation (g cm-2) at Portobelo area (1979-2008): comparison between model simulations. 238

Figure 5.3.6. 1. Estimated biomass accumulation under EC-Earth scenario. a. For the past period 1979–2008 (baseline); b. For the middle future period (2039-2068). 240

Figure 5.3.6. 2. Difference between the estimated biomass accumulation between the future and the past period. 240

Tables

Table 1.2.2.1. Legenda of Formations, Symbols and Descriptions of rocks showed in figures 1.2.2.4-5 (modified from Stewart and Woodring, 1980). 18

Table 1.3.1.1. 1. Equilibrium RH (%) and T (°C) of some soluble salts. Selected the T (°C) range and highlighted the RH values more suitable for the Panamanian area from Arnold and Zender (1989). 26

Table 1.3.1.2. 1. Legend of the Lipfert function terms. 28

Table 1.4.1. 1. Maintenance and restoration works, updated to 2011/2012, performed on monuments selected for the here presented PhD research. 33

Table 2.1. 1. Most diffused deterioration phenomena observed at Panamá Viejo, Portobelo and San Lorenzo sites. 35

Table 2.1.1. 1. Samples, lithotypes, state of conservation and location of sampling (for the description of the Fort elements see Spiteri, 1994; for the definition of breccia see Saccani, 2014). 36

Table 2.1.2. 1. Samples, lithotypes, state of conservation and location of sampling (for the description of the Fort elements Spiteri, 1994). 55

Table 2.1.3. 1. Samples, lithotypes, state of conservation and location of sampling (for the description of the Fort elements Spiteri, 1994). 68

Table 2.3. 1. Monitoring stations selected as the closest to the sites of interest, respectively: in grey to Panama Viejo; in blue to Portobelo and in green to San Lorenzo. 73

Table 3.1.1.1. List of samples belonging to Panama Viejo and their related lithotypes and provenance analysed through PLM observations of thin sections. 77

Table 3.1.2. 1. List of samples belonging to Portobelo and San Lorenzo and their related provenance and lithotypes analysed through PLM observations of thin sections 88

Table 3.2. 1. Legend: Cal: Calcite; Qtz: Quartz; Fsp: Feldspar; Px: Pyroxenes; Zeo: Zeolite (CPL = Clinoptilolite; MOR = Mordenite); Chl= Chlorite; Mnt: Montmorillonite; Vrm: Vermiculite. +++ = dominant; ++ = abundant; + = present, traces; - = absent. N.B. PV JC4a (interior part) e PV JC4b (external part) 103

Table 3.2. 2. Legend: Cal: Calcite; Qtz: Quartz; Fsp: Feldspar; Zeo: Zeolite (CPL = Clinoptilolite; MOR = Mordenite); Mnt: Montmorillonite. +++ = dominant; ++ = abundant; + = present, traces; - = absent 104

Table 3.2. 3. Legend: Cal: Calcite; Qtz: Quartz; Fsp: Feldspar; Zeo: Zeolite (CPL = Clinoptilolite); Chl= Chlorite. +++ = dominant; ++ = abundant; + = present, traces; - = absent 105

Table 3.2. 4. Legend: Cal: Calcite; Qtz: Quartz; Fsp: Feldspar; Px: Pyroxenes; Montmorillonite; Vrm: Vermiculite; Mag: Magnetite. +++ = dominant; ++ = abundant; + = present, traces; - = absent 105

Table 3.2. 5. Legend: Arg: Aragonite; Cal: Calcite. +++ = dominant; ++ = abundant; + = present, traces; - absent 106

Table 3.2. 6. Legend: Cal: Calcite; Qtz: Quartz; Fsp: Feldspar; Zeo: Zeolite (CPL = Clinoptilolite); Mnt: Montmorillonite. +++ = dominant; ++ = abundant; + = present, traces; - = absent 106

Table 3.2. 7. Legend: Qtz: Quartz; Fsp: Feldspar; Zeo: Zeolite (CPL = Clinoptilolite; MOR = Mordenite). +++ = dominant; ++ = abundant; + = present, traces; - = absent 107

Table 3.2. 8. Legend: Qtz: Quartz; Fsp: Feldspar; Kln: Kaolinite; Hem: Hematite. +++ = dominant; ++ = abundant; + = present, traces; - = absent 107

Table 3.2. 9. Legend: Cal: Calcite. +++ = dominant; ++ = abundant; + = present, traces; - = absent 107

Table 3.4. 1. Bulk rock major (wt %) and trace (ppm) element analyses for breccias. 137

Table 3.4. 2. Bulk Bulk rock major (wt %) and trace (ppm) element analyses for tuffites. Highlighted in blue the samples belonging to outcrops. 138

Table 3.4. 3. Bulk rock major (wt %) and trace (ppm) element analyses for igneous rocks. Highlighted in blue the samples belonging to outcrops. 139

Table 3.4. 4 Bulk rock major (wt %) element analyses for magmatic rocks. Highlighted in blue the samples belonging to outcrops. 140

Table 3.4. 5. Bulk rock major (wt %) and trace (ppm) element analyses for coral boundstones and grainstone. Highlighted in blue the sample belonging to outcrops. 142

Table 3.5. 1. Porosity and pore diameter results divided by rock typology. 146

Table 3.6. 1. Anions concentrations (ppm) in Panama Viejo samples. 154

Table 3.6. 2. Cations concentrations (ppm) in Panama Viejo samples. 154

Table 3.6. 3. Anions concentrations (ppm) in Portobelo and San Lorenzo samples. 155

Table 3.6. 4. Cations concentrations (ppm) in Panama Viejo samples. 156

Table 3.6. 5. Anions concentrations (ppm) in Portobelo samples of calcite encrustations. 157

Table 3.6. 6. Cations concentrations (ppm) in Portobelo samples of calcite encrustations. 157

Table 4.1.1. 1. Rainfall monthly amount (mm) of 20 years period (1988-2008), at the area of Panama Viejo (Long.-79.49; Lat.9.01). Comparison among the historic series of the Hato Pintado and Tocumen monitoring stations and the historic simulation of the Arpege-FN1 and EC-Earth models. 160

Table 4.1.1. 2. Comparison of monthly average of temperature of Tocumen monitoring station and models data, over 30 years (1979-2008). 162

Table 4.1.1. 3. Comparison of monthly average of relative humidity of Tocumen monitoring station and models data, over 30 years (1979-2008). 163

Table 4.1.2. 1. Comparison of average of rainfall monthly amount of Balboa FAA monitoring station and models data, over 30 years (1979-2008). 164

Table 4.1.2. 2. Comparison of monthly average of temperature of Balboa FAA monitoring station and models data, over 30 years (1979-2008). 166

Table 4.1.2. 3. Comparison of monthly average of relative humidity of Balboa FAA monitoring station and models data, over 30 years (1979-2008). 167

Table 4.1.3. 1. Comparison of the average of rainfall monthly amount of Gatún (G) and Cocosolo-Cristóbal-Limonbay (CCL) monitoring stations, and their average, and models data, over 28 years (1981-2008). 168

Table 4.1.3. 2. Comparison of the average of rainfall monthly amount of Gatún (G), Cocosolo-Cristóbal-Limonbay (CCL) and Sherman monitoring stations, and their average, and models data, over 12 years (1997-2008). 170

Table 4.1.3. 3. Comparison of the average of monthly temperature of Gatún (G) and Cocosolo-Cristóbal-Limonbay (CCL) monitoring stations, and their average, and models data, over 28 years (1979-2006). 171

Table 4.1.3. 4. Comparison of the average of monthly temperature of Gatún (G), Cocosolo-Cristóbal-Limonbay (CCL) and Fort Sherman (FS) monitoring stations, and their average, and models data, over 12 years (1997-2008). 173

Table 4.1.3. 5. Comparison of the average of monthly relative humidity of Gatún (G) and Cocosolo-Cristóbal-Limonbay (CCL) monitoring stations, and their average, and models data, over 28 years (1979-2008). 174

Table 4.1.3. 6. Comparison of the average of monthly relative humidity of Gatún (G) and Cocosolo-Cristóbal-Limonbay (CCL) and Fort Sherman (FS) monitoring stations, and their average, and models data, over 12 years (1997-2008). 176

Table 4.1.4. 1. Comparison of the average of monthly relative humidity of Pina (P) monitoring station and models data, over 20 years (1979-1998). 177

Table 4.1.5. 1. Comparison of the average of monthly relative humidity of Portobelo (Pb) monitoring station and models data, over 22 years (1979-2000). 179

Table 4.2.1. 1. Comparison of yearly amount of rainfall, over the past period 1979-2008, between the average of the monitoring stations records and the models data with or without bias (f_P). 182

Table 4.2.1. 2. Comparison of yearly amount of rainfall, over the future period 2039-2068, models data with or without bias (f_P). 184

Table 4.2.1. 3. Comparison of monthly average of Relative Humidity, over the past period 1979-2008, between the average of the monitoring station records and the models data with or without bias f_{RH}). 185

Table 4.2.1. 4. Comparison of monthly average of Relative Humidity, over the future period 2039-2068, between the average of the models data with or without bias (f_{RH}). 186

Table 4.2.1. 5. Comparison of monthly average of Temperature, over the past period 1979-2008, between the average of the monitoring station records and the models data with or without bias (f_{RH}). 187

Table 4.2.1. 6. Comparison of monthly average of Relative Humidity, over the future period 2039-2068, between the average of the models data with or without bias (f_{RH}). 188

Table 4.2.2. 1. Comparison of yearly amount of rainfall, over the past period 1979-2008, between the monitoring station records and the models data with or without bias (f_P). 189

Table 4.2.2. 2. Comparison of yearly amount of rainfall, over the future period 2039-2068, models data with or without bias (fP). 191

Table 4.2.2. 3. Comparison of monthly average of Relative Humidity, over the past period 1979-2008, between the average of the monitoring station records and the models data with or without bias (f_{RH}). 192

Table 4.2.2. 4 . Comparison of monthly average of Relative Humidity, over the future period 2039-2068, between the average of the monitoring station records and the models data with or without bias (f_{RH}). 193

Table 4.2.2. 5. Comparison of monthly average of Temperature, over the past period 1979-2008, between the average of the monitoring station records and the models data with or without bias (f_T). 194

Table 4.2.2. 6. Comparison of monthly average of Temperature, over the future period 2039-2068, between the average of the monitoring station records and the models data with or without bias (f_T). 195

Table 4.2.3. 1. Comparison of yearly amount of rainfall, over the past period 1981-2008, between the average of monitoring stations records and the models data with or without bias (f_P). 196

Table 4.2.3. 2. Comparison of yearly amount of rainfall, over the future period 2039-2068, between the models data with or without bias (f_P). 198

Table 4.2.3. 3. Comparison of monthly average of Relative Humidity, over the past period 1979-2005, between the average of the monitoring station records and the models data with or without bias (f_{RH}). 199

Table 4.2.3. 4. Comparison of monthly average of Relative Humidity, over the future period 2039-2068, between the average of the monitoring station records and the models data with or without bias (f_{RH}). 200

Table 4.2.3. 5. Comparison of monthly average of Temperature, over the past period 1979-2008, between the average of the monitoring station records and the models data with or without bias (f_T). 201

Table 4.2.3. 6. Comparison of monthly average of Temperature, over the future period 2039-2068, between the average of the monitoring station records and the models data with or without bias (f_T). 202

Table 4.2.4. 1. Comparison of yearly amount of rainfall, over the past period 1979-1998, between the monitoring station records and the models data with or without bias (f_P). In red are highlighted the maximum values. 203

Table 4.2.4. 2. Comparison of yearly amount of rainfall, over the future period 2039-2068, between the two models data with or without bias (fP). 205

Table 4.2.5. 1. Comparison of yearly amount of rainfall, over the past period 1979-2000, between the monitoring station records and the models data with or without bias (f_P). In red are highlighted the maximum values. 206

Table 4.2.5. 2. Comparison of yearly amount of rainfall, over the future period 2039-2068, between the two models data with or without bias (fP). 208

Table 5.1. 1. Comparison among the average, minimum and maximum values obtained from the 30 years (1979-2008), between monitoring stations and model data of the Panamá Viejo area. 210

Table 5.1. 2. Comparison of the surface recession (L) values of average, minimum and maximum of the Arpege and EC-Earth simulations obtained for the future period, divided in 30 years, applying or not bias correction. 212

Table 5.1. 3. Comparison among the average, minimum and maximum values obtained from the 30 years (1979-2008), between monitoring stations and model data of the area near Panamá Viejo. 213

Table 5.1. 4. Comparison of the surface recession (L) values of average, minimum and maximum of the Arpege and EC-Earth simulations obtained for the future period, divided in 30 years, applying or not bias correction. 214

Table 5.1. 5. Comparison among the average, minimum and maximum values obtained from the 30 years (1979-1998), between monitoring stations and model data of the area near San Lorenzo. 214

Table 5.1. 6. Comparison of the surface recession (L) values of average, minimum and maximum of the Arpege and EC-Earth simulations obtained for the future period, divided in 30 years, applying or not bias correction. 216

Table 5.1. 7. Comparison among the average, minimum and maximum values obtained from the 19 years (1979-1998, 1994 missing), between monitoring stations and model data of the area of San Lorenzo 216

Table 5.1. 8. Comparison of the surface recession (L) values of average, minimum and maximum of the Arpege and EC-Earth simulations obtained for the future period, divided in 30 years, applying or not bias correction. 218

Table 5.1. 9. Comparison among the average, minimum and maximum values obtained from the 20 years (1979-1998), between monitoring stations and model data of the Portobelo area. 218

Table 5.1. 10. Comparison of the surface recession (L) values of average, minimum and maximum of the Arpege and EC-Earth simulations obtained for the future period, divided in 30 years, applying or not bias correction. 220

Table 5.3. 1. Future (2009-2100) biomass (g cm-2) range of values (average, minimum and maximum) for the area of Panamá Viejo. 231

Table 5.3. 2. Future (2009-2100) biomass (g cm-2) range of values (average, minimum and maximum) for the area near Panamá Viejo. 234

Table 5.3. 3. Future (2009-2100) biomass (g cm-2) range of values (average, minimum and maximum) for the area near San Lorenzo. 236

Table 5.3. 4. Future (2009-2100) biomass (g cm-2) range of values (average, minimum and maximum) for the area of San Lorenzo. 237

Table 5.3. 5. Future (2009-2100) biomass (g cm-2) range of values (average, minimum and maximum) for the area of Portobelo. 239

ANNEX 1

Diffractograms

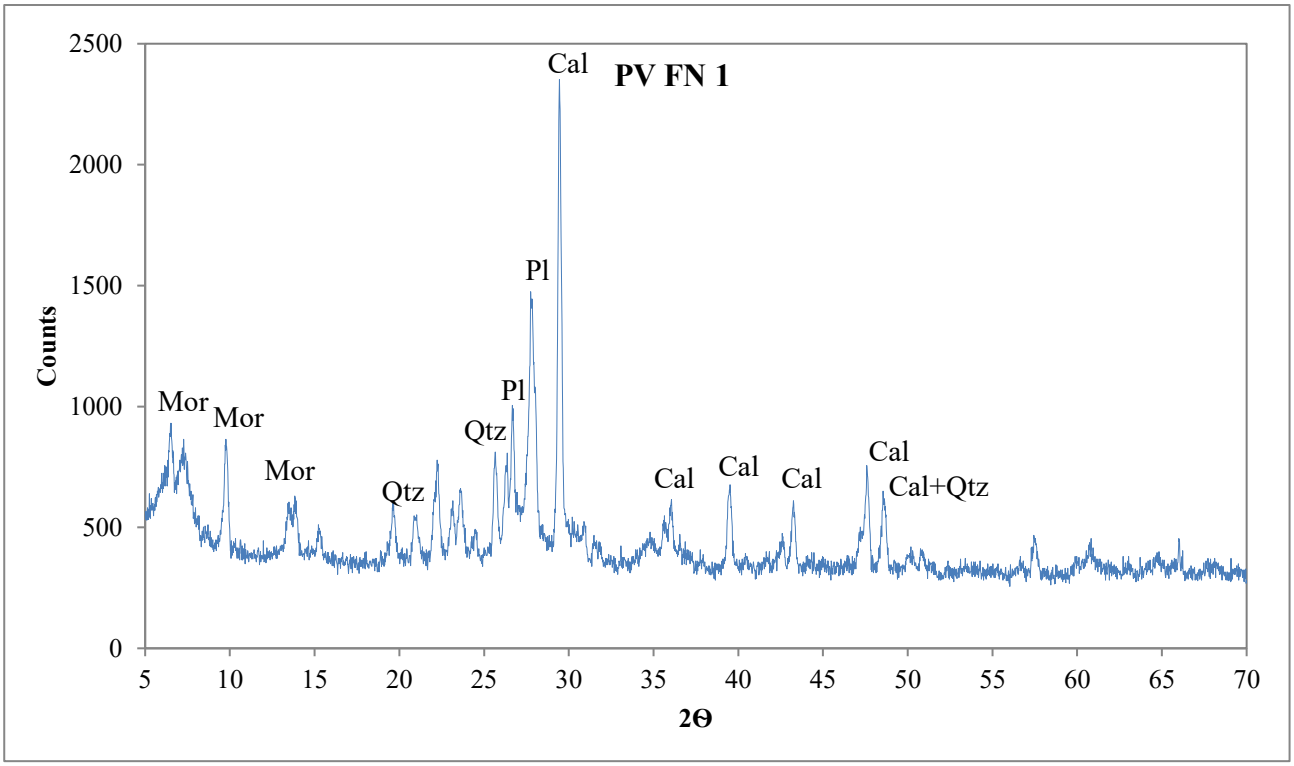
PV FN 1
Counts
2Θ
Cal
Pl
Pl
Mor
Mor
Mor
Qtz
Qtz
Cal
Cal
Cal
Cal
Cal+Qtz

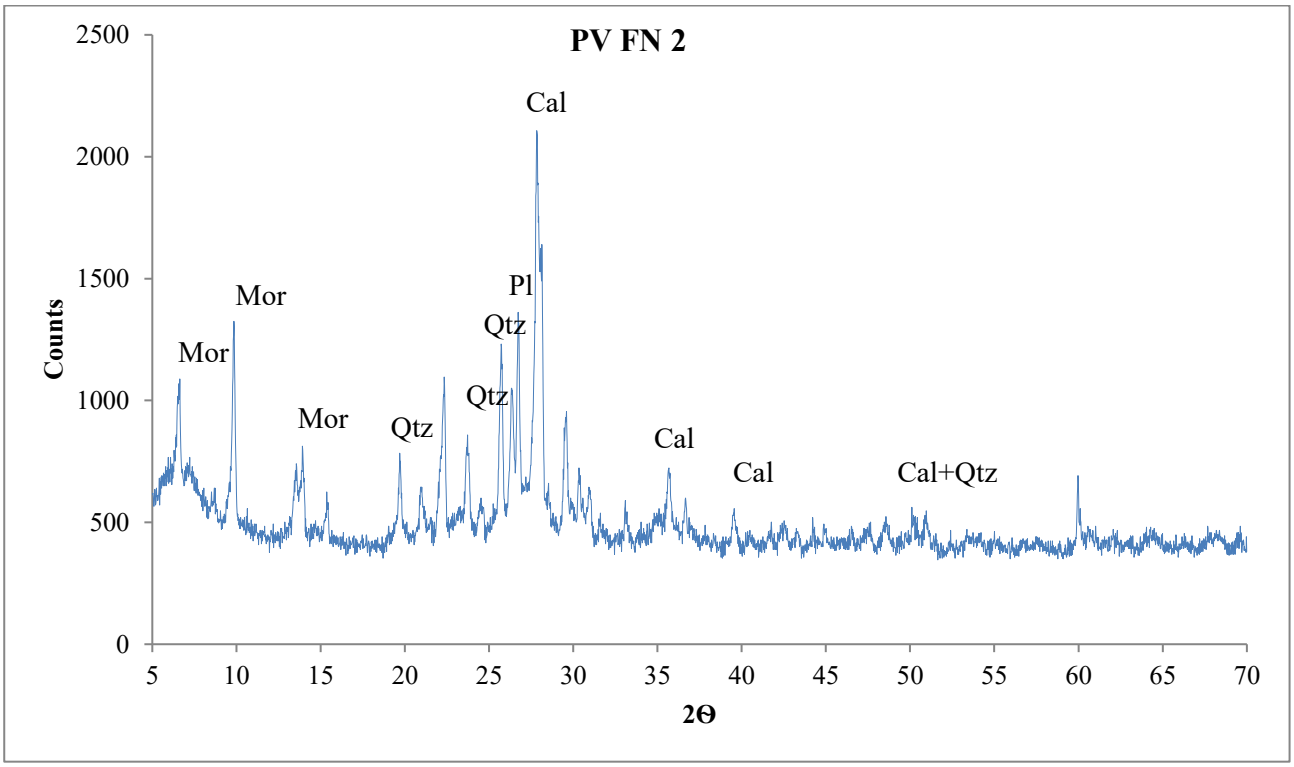
PV FN 2
Counts
2Θ
Cal
Pl
Mor
Mor
Qtz
Qtz
Mor
Qtz
Cal
Cal
Cal+Qtz

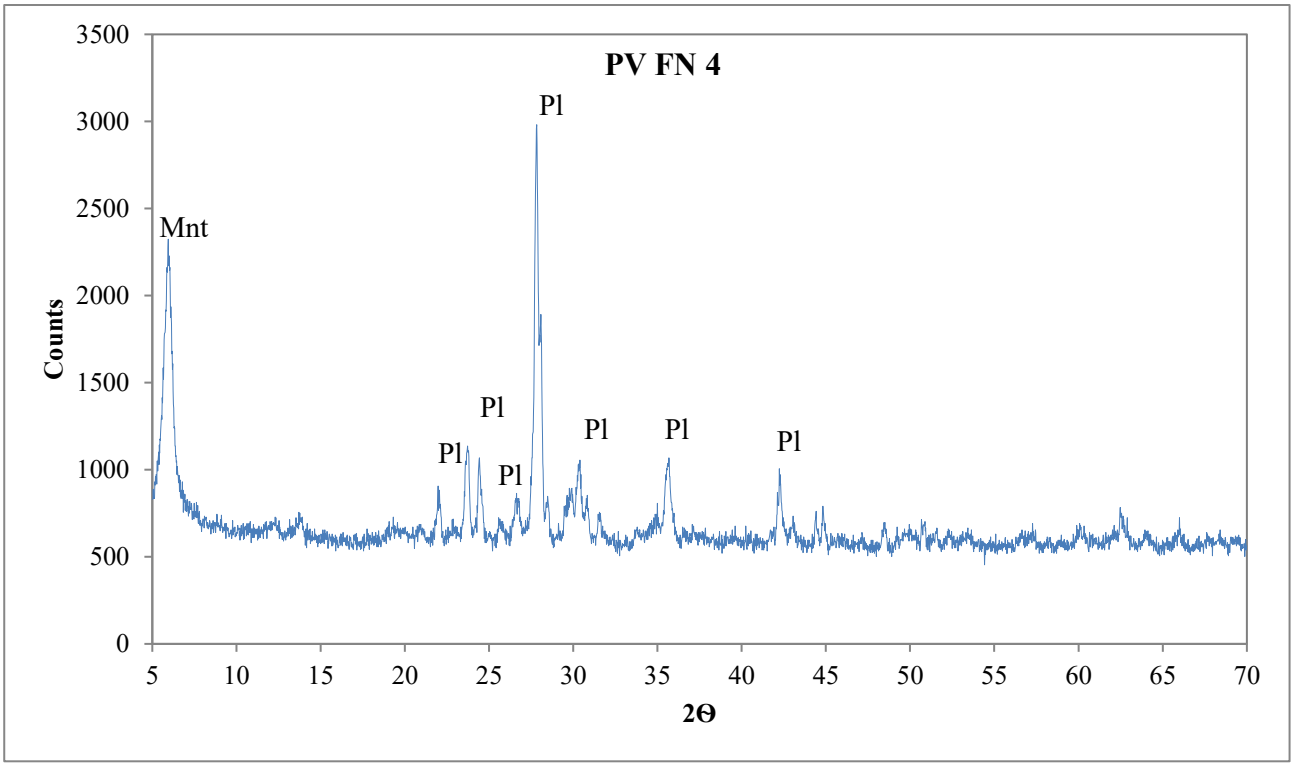
PV FN 4
Counts
2Θ
Mnt
Pl
Pl
Pl
Pl
Pl
Pl
Pl
0
500
1000
1500
2000
2500
3000
3500
5
10
15
20
25
30
35
40
45
50
55
60
65
70

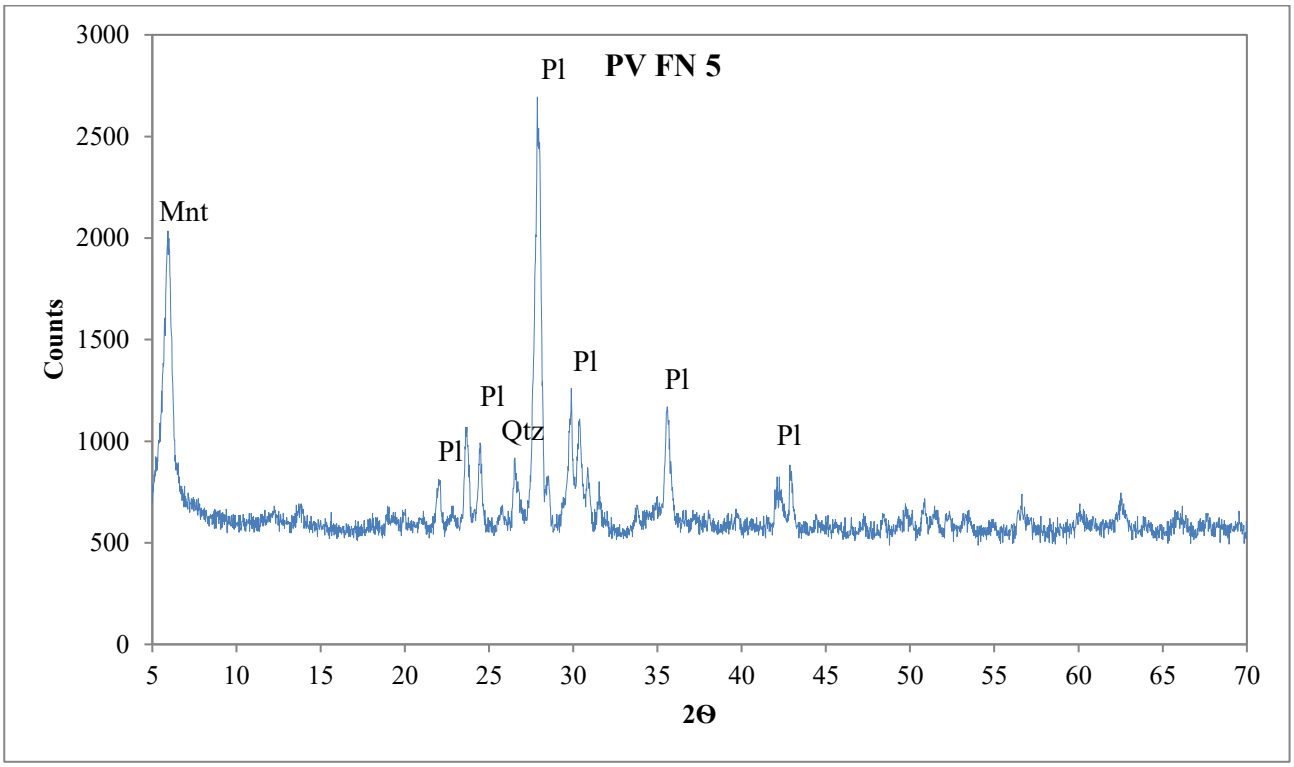
PV FN 5
Counts
2Θ
Mnt
Pl
Pl
Pl
Qtz
Pl
Pl
Pl
0
500
1000
1500
2000
2500
3000
5
10
15
20
25
30
35
40
45
50
55
60
65
70

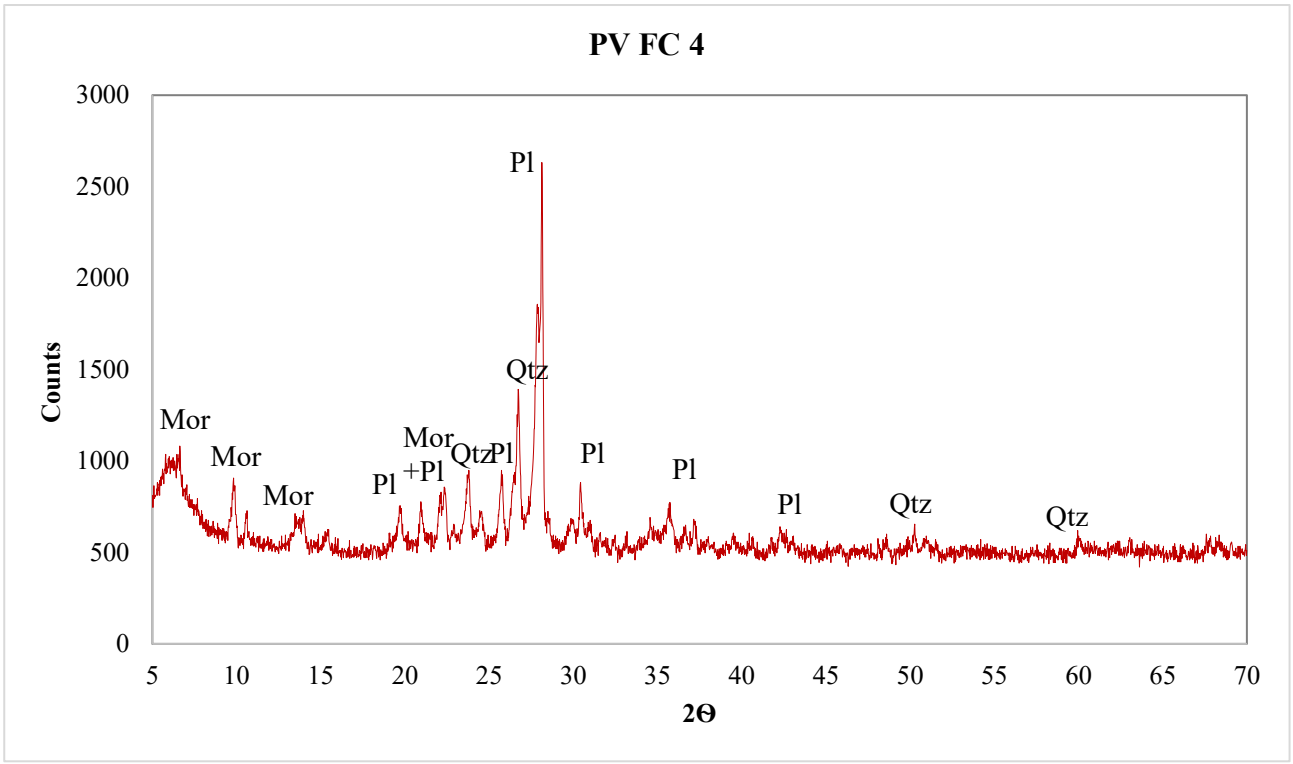
PV FC 4
Counts
2Θ
Mor
Mor
Mor
Pl
Mor +Pl
Qtz
Pl
Pl
Qtz
Pl
Pl
Pl
Qtz
Qtz

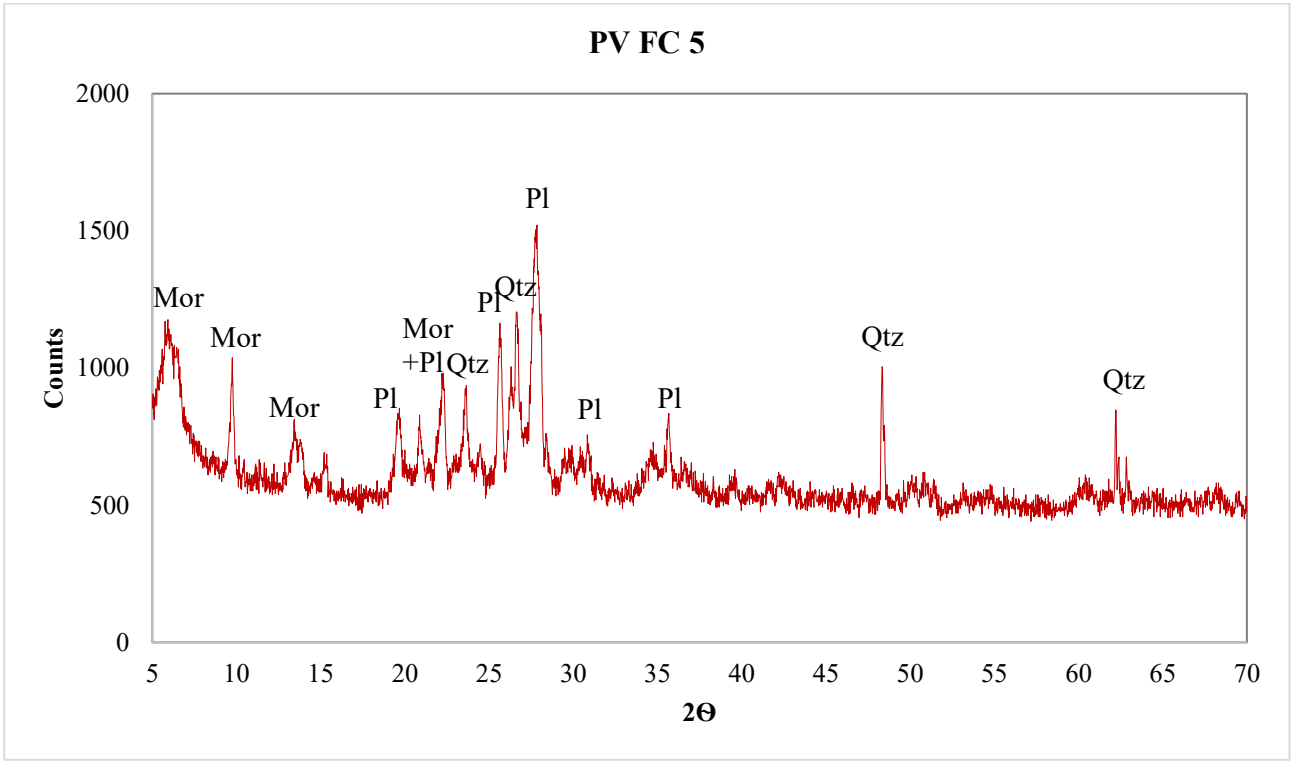
PV FC 5
Counts
2Θ
Mor
Mor
Mor
Pl
Mor +Pl
Qtz
Pl
Qtz
Pl
Pl
Pl
Qtz
Qtz

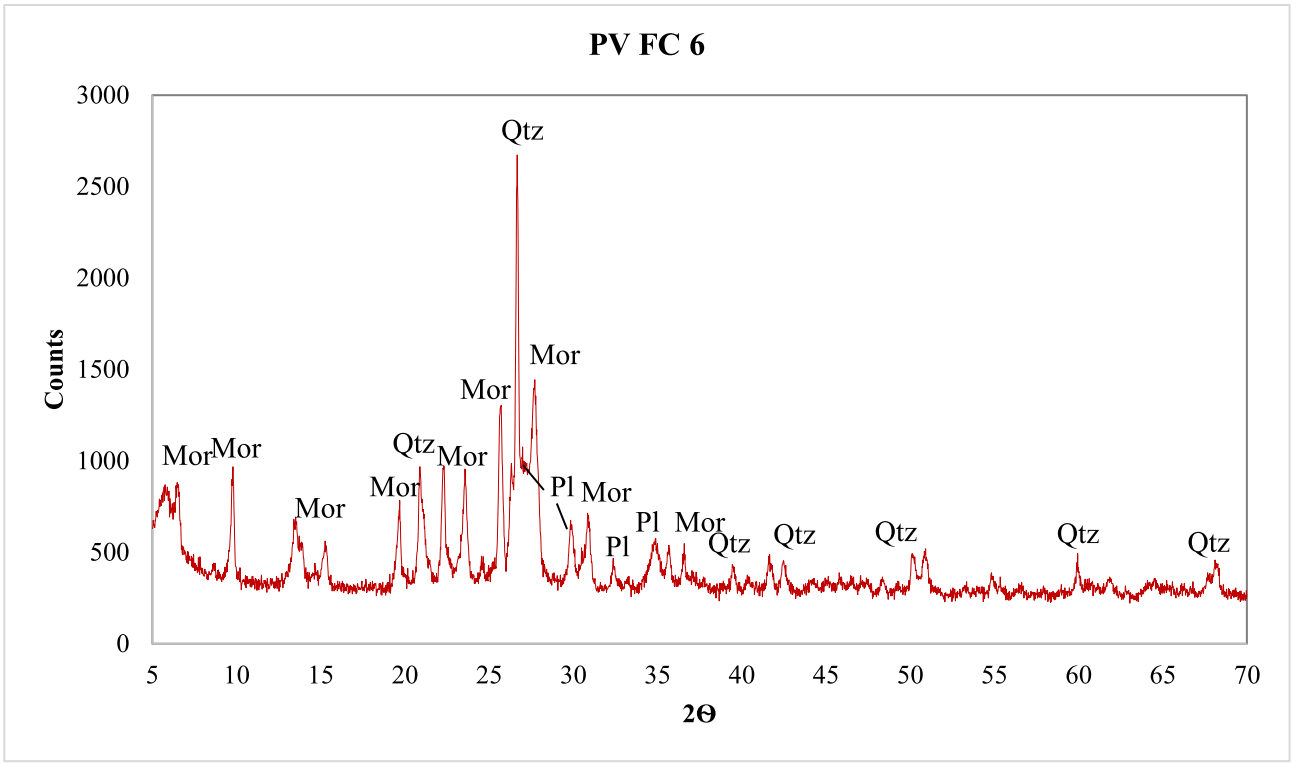
PV FC 6
Counts
2Θ
Qtz
Mor
Pl
Cal

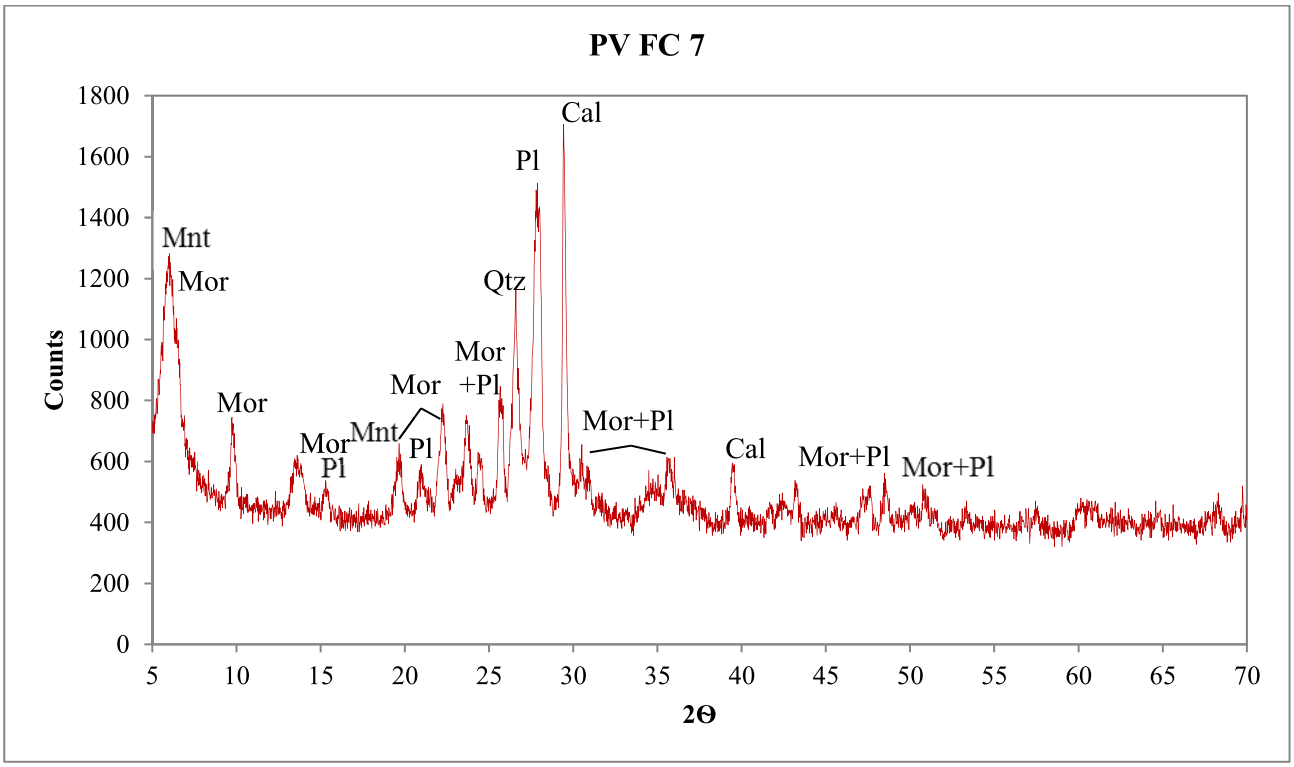
PV FC 7
Counts
2Θ
Mnt
Mor
Pl
Qtz
Cal
Mor+Pl

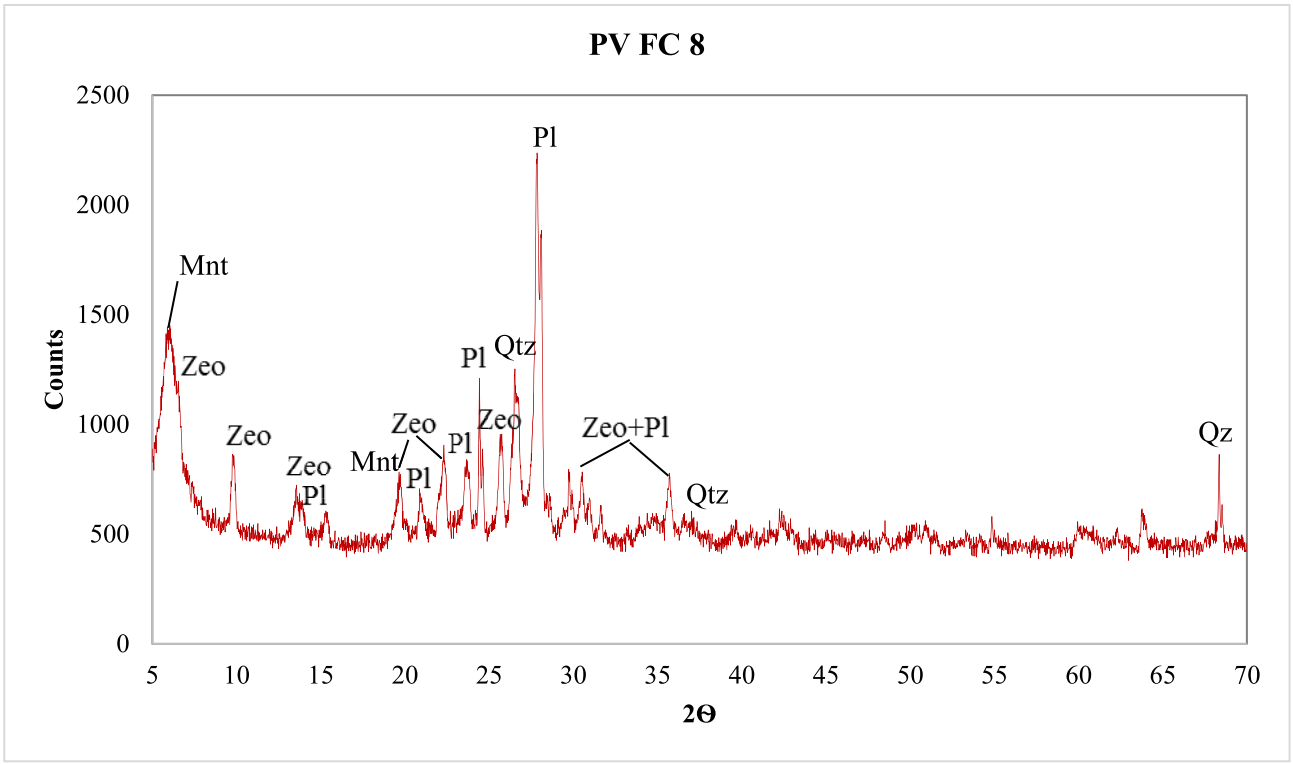
PV FC 8
Counts
2Θ
Mnt
Zeo
Zeo
Zeo
Pl
Mnt
Zeo
Pl
Pl
Pl
Qtz
Zeo
Zeo+Pl
Qtz
Qz

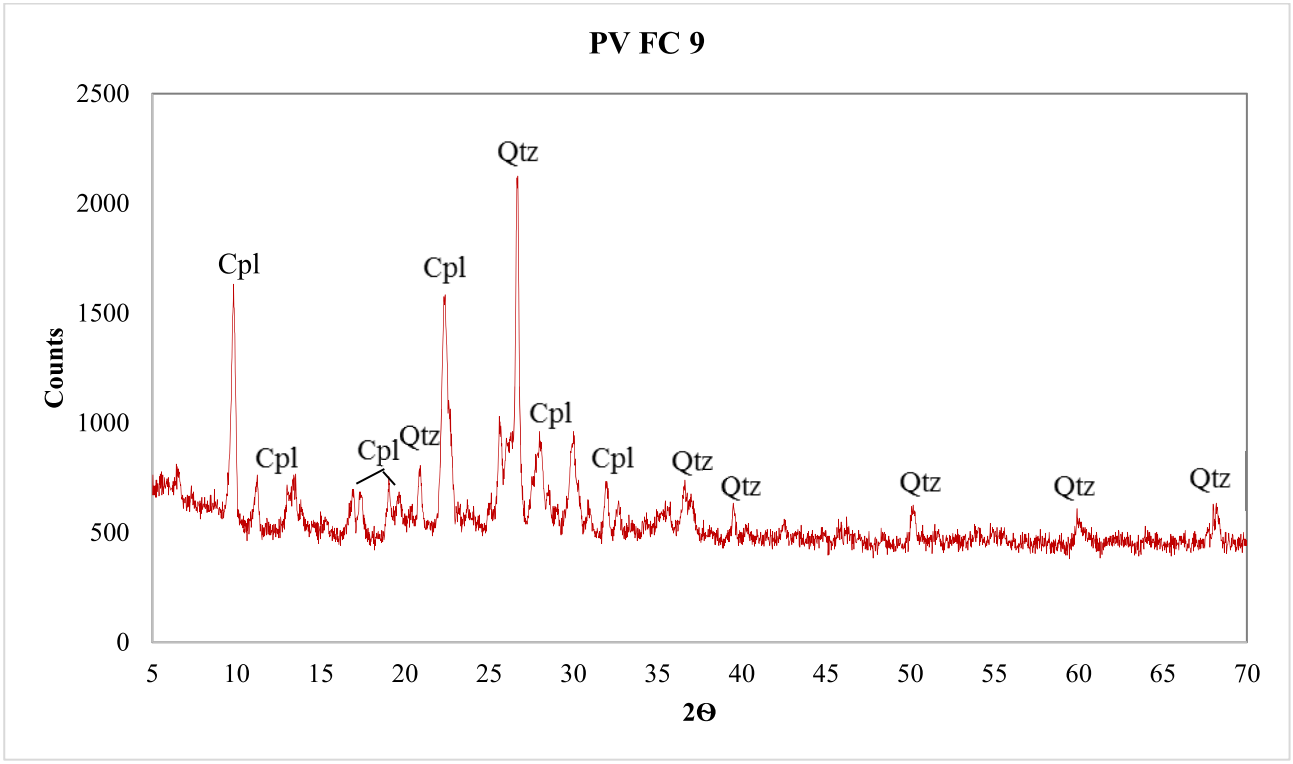
PV FC 9
Counts
2Θ
Cpl
Cpl
Cpl
Cpl
Cpl
Cpl
Qtz
Qtz
Qtz
Qtz
Qtz
Qtz
Qtz

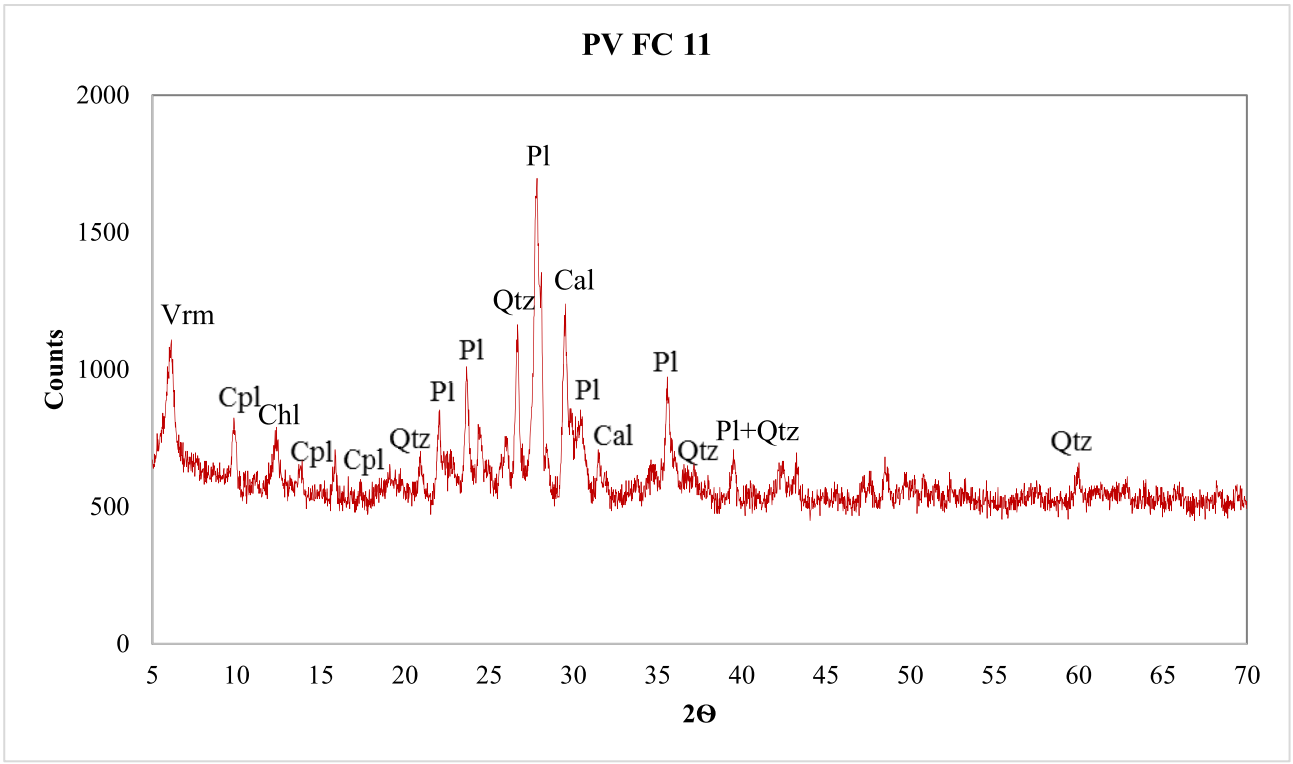
PV FC 11
Counts
2Θ
Vrm
Cpl
Chl
Cpl
Cpl
Qtz
Pl
Pl
Qtz
Pl
Cal
Pl
Cal
Qtz
Pl+Qtz
Qtz

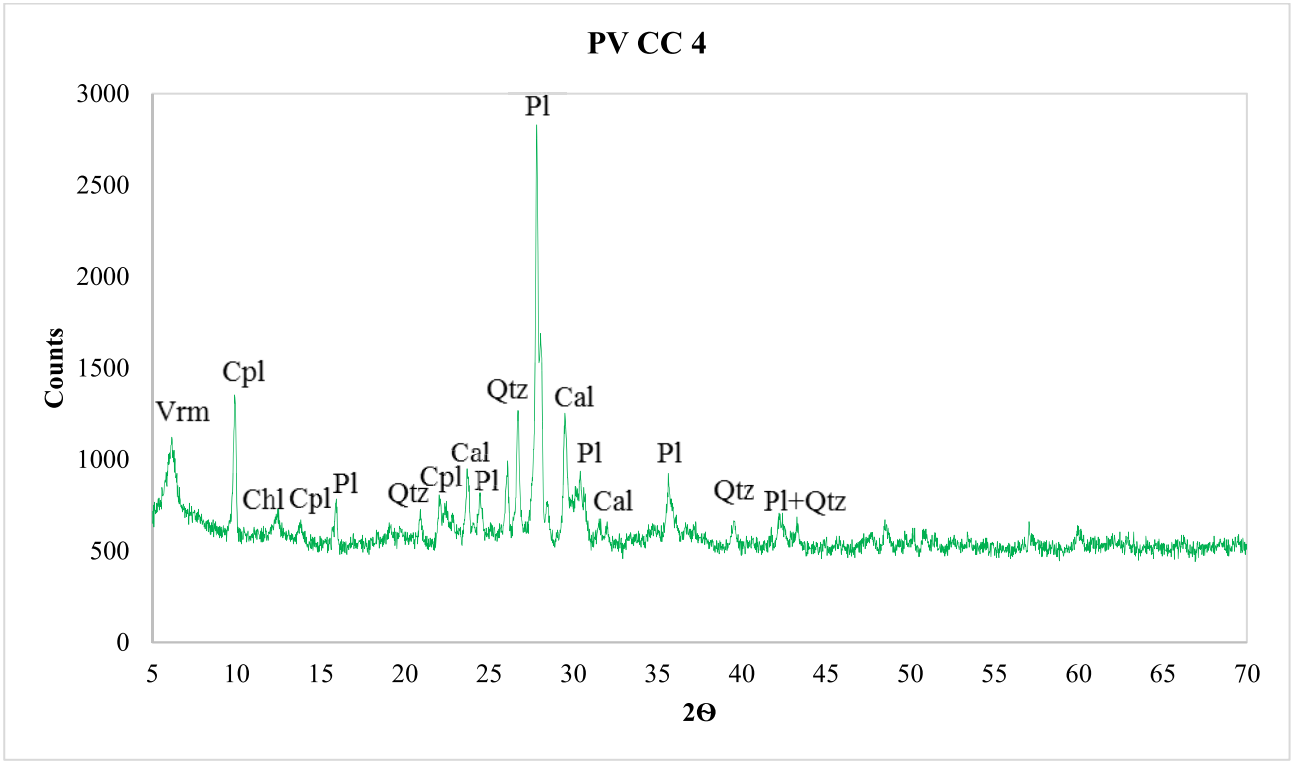
PV CC 4
Counts
2Θ
Vrm
Cpl
Chl
Cpl
Pl
Qtz
Cpl
Cal
Pl
Qtz
Cal
Pl
Cal
Pl
Qtz
Pl+Qtz

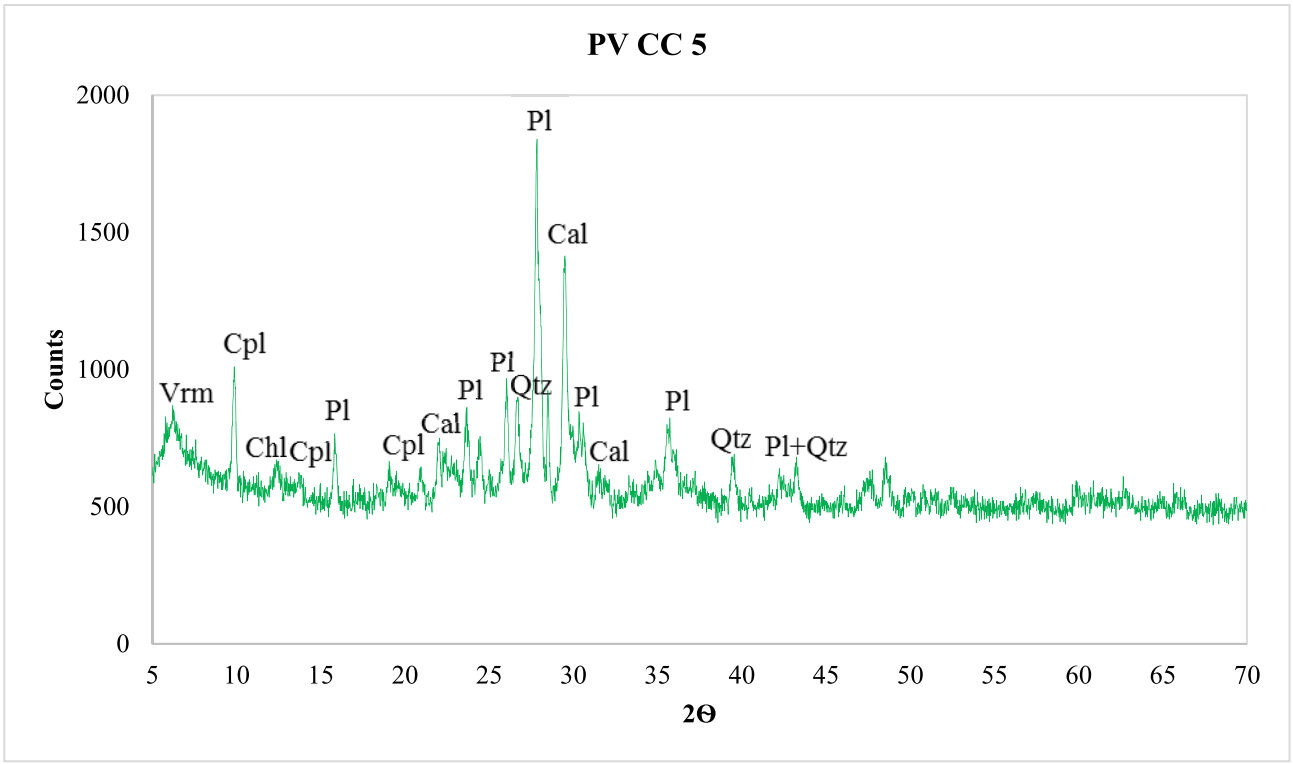
PV CC 5
Counts
2Θ
Pl
Cal
Cpl
Vrm
Chl
Cpl
Pl
Cpl
Cal
Pl
Pl
Qtz
Pl
Cal
Pl
Qtz
Pl+Qtz

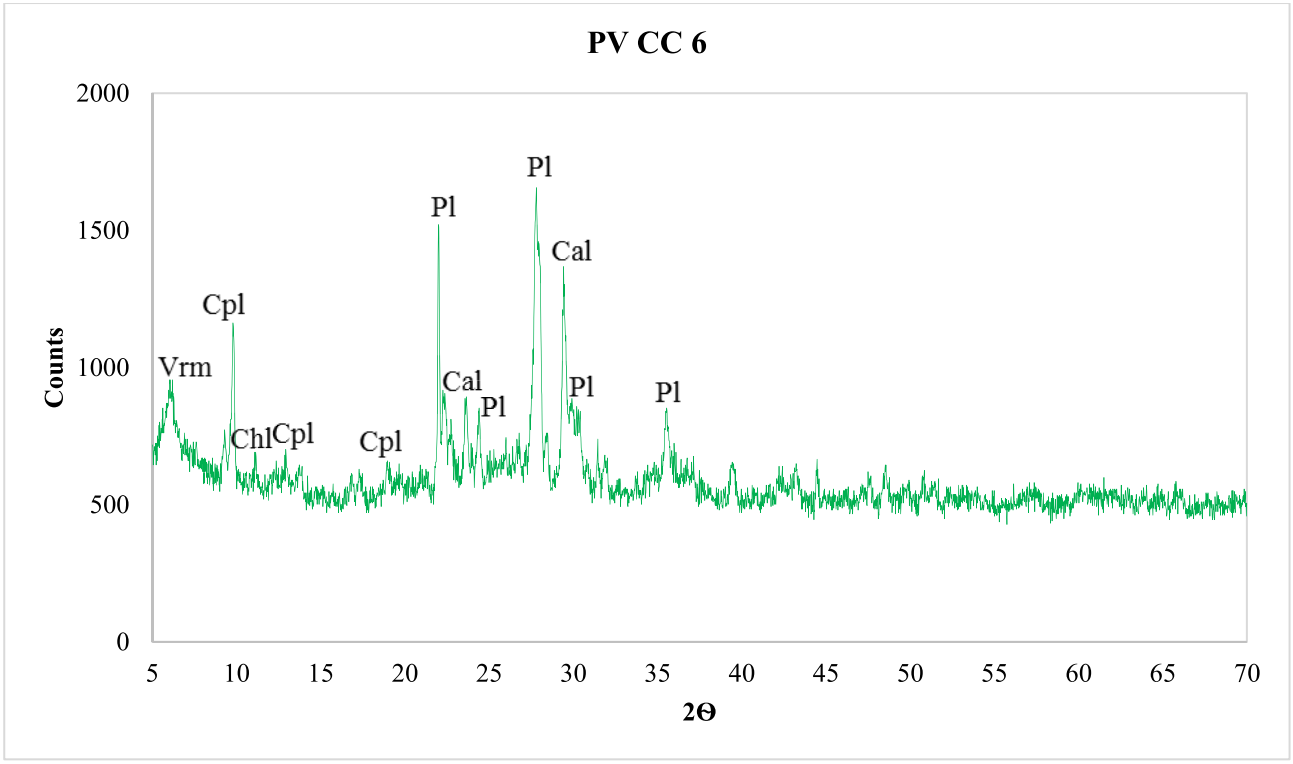
PV CC 6
Counts
2Θ
Pl
Pl
Cal
Cpl
Vrm
Cal
Pl
Pl
Chl
Cpl
Cpl
Pl
Pl

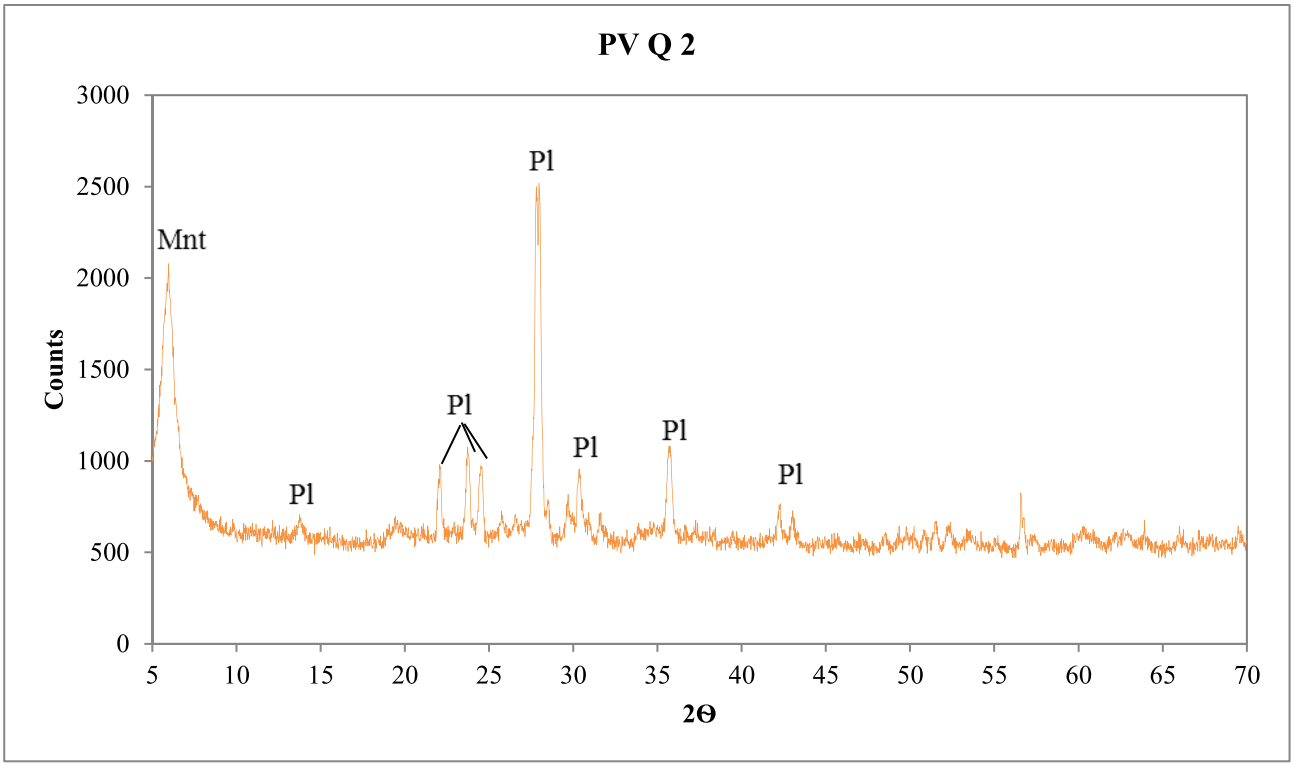
PV Q 2
Counts
2Θ
Mnt
Pl
Pl
Pl
Pl
Pl
Pl
3000
2500
2000
1500
1000
500
0
5
10
15
20
25
30
35
40
45
50
55
60
65
70

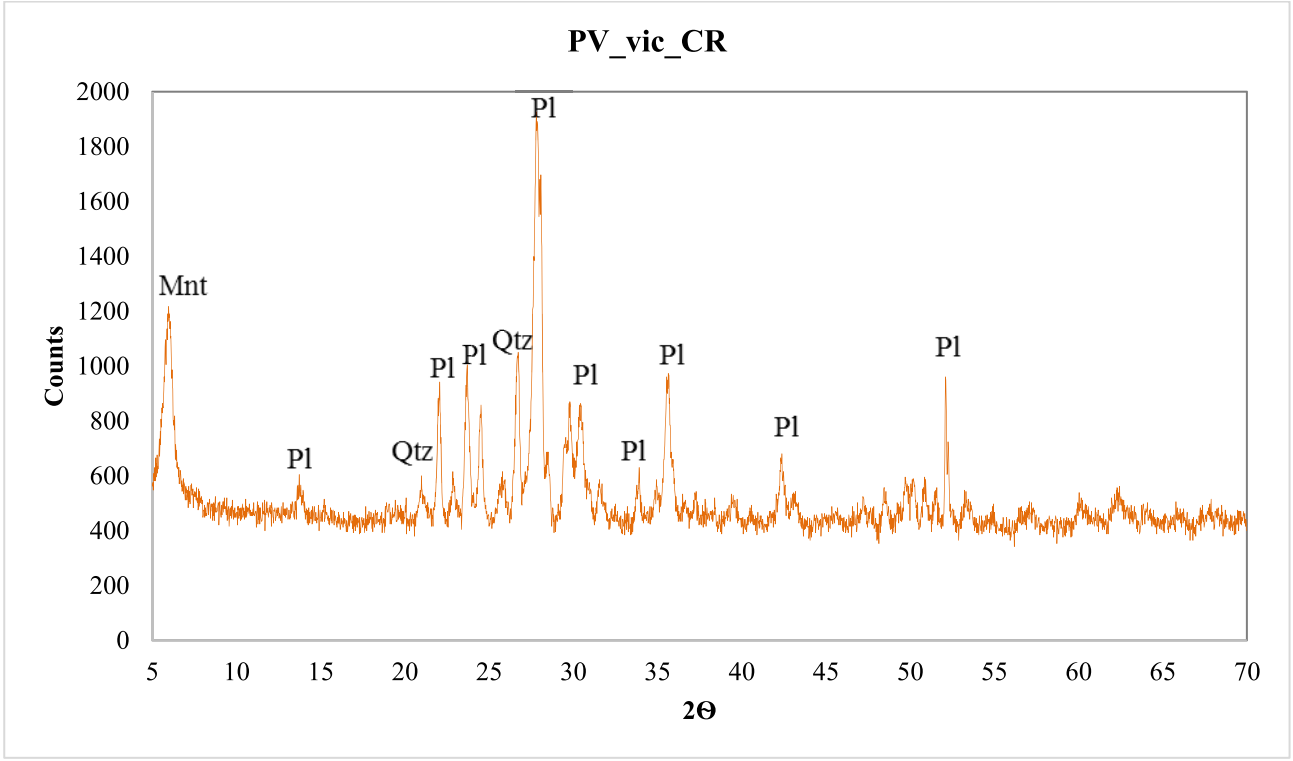
PV_vic_CR
Counts
2Θ
Mnt
Pl
Pl
Qtz
Pl
Pl
Qtz
Pl
Pl
Pl
Pl
Pl
2000
1800
1600
1400
1200
1000
800
600
400
200
0
5
10
15
20
25
30
35
40
45
50
55
60
65
70

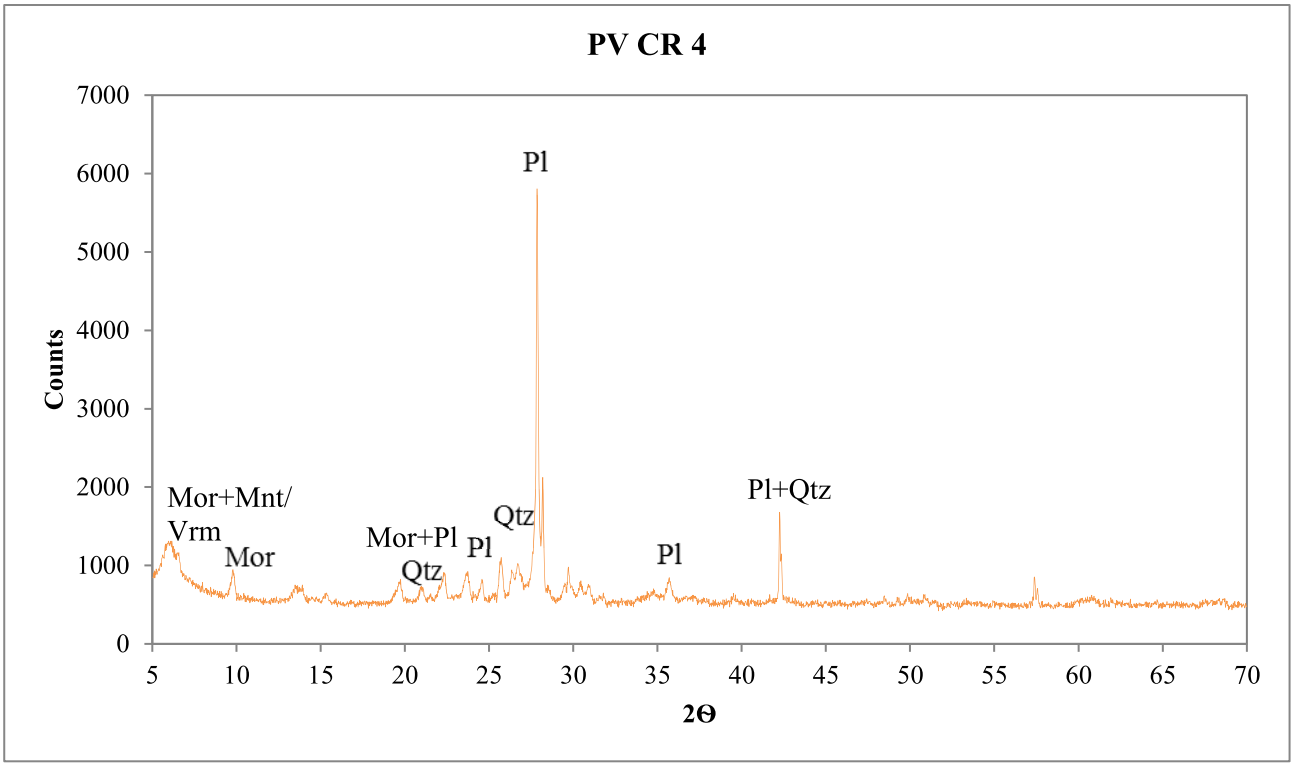
PV CR 4
Counts
2Θ
Pl
Mor+Mnt/
Vrm
Mor
Mor+Pl
Qtz
Pl
Qtz
Pl
Pl+Qtz

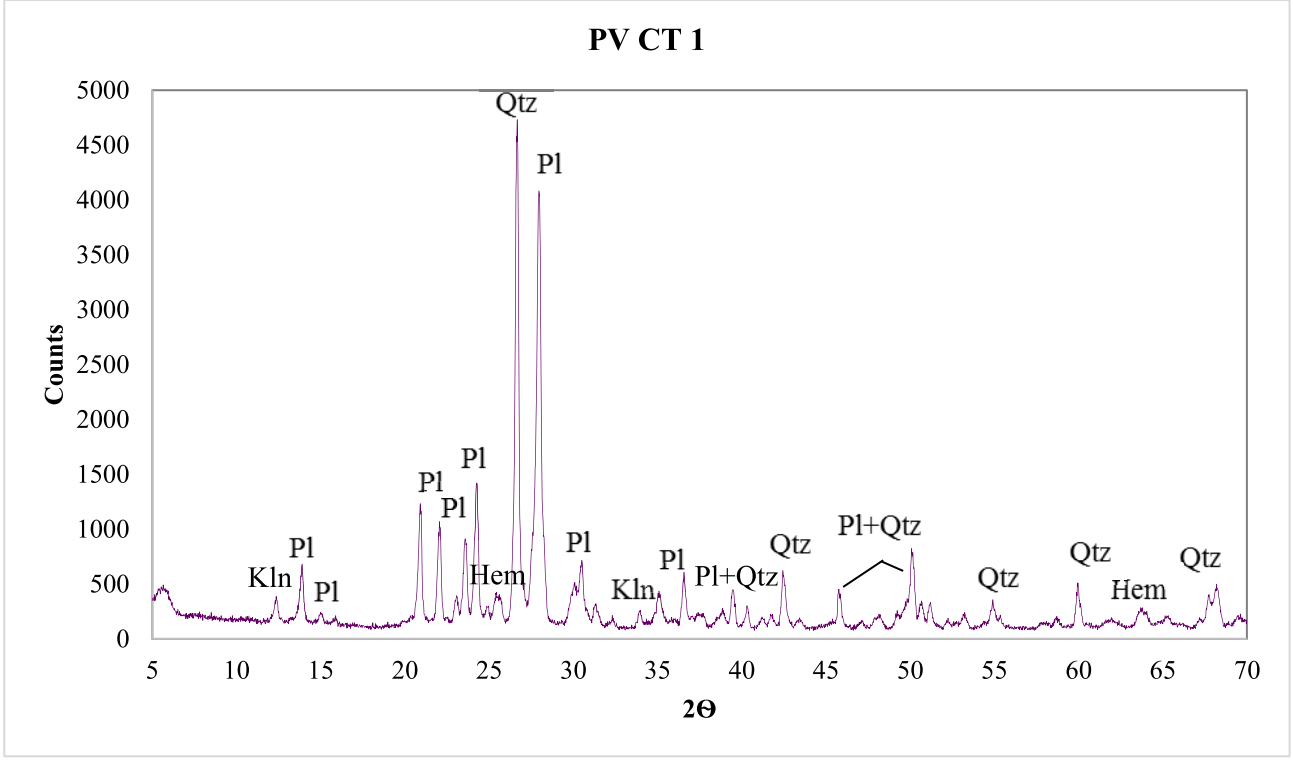
PV CT 1
Counts
2Θ
Qtz
Pl
Pl
Pl
Pl
Kln
Pl
Pl
Hem
Pl
Kln
Pl
Pl+Qtz
Qtz
Pl+Qtz
Qtz
Qtz
Hem
Qtz

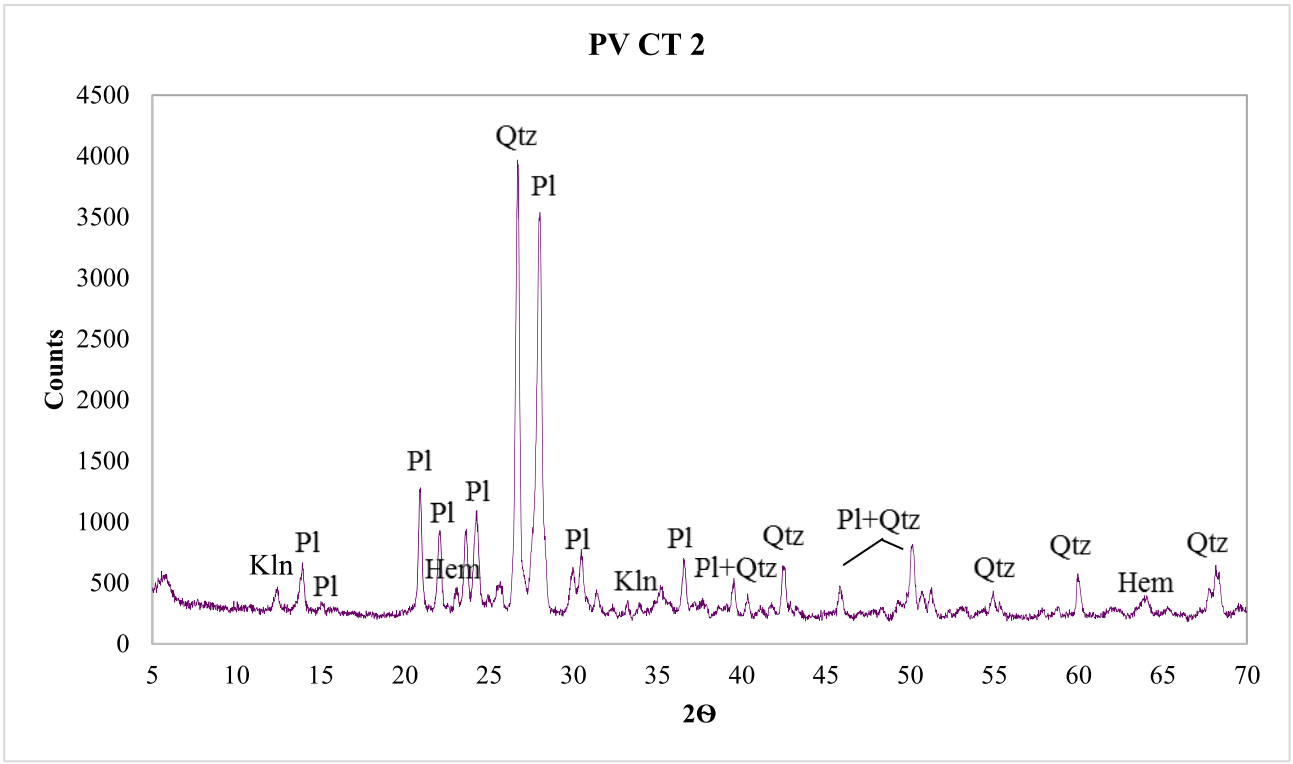
PV CT 2
Counts
2Θ
Qtz
Pl
Kln
Hem
Pl+Qtz

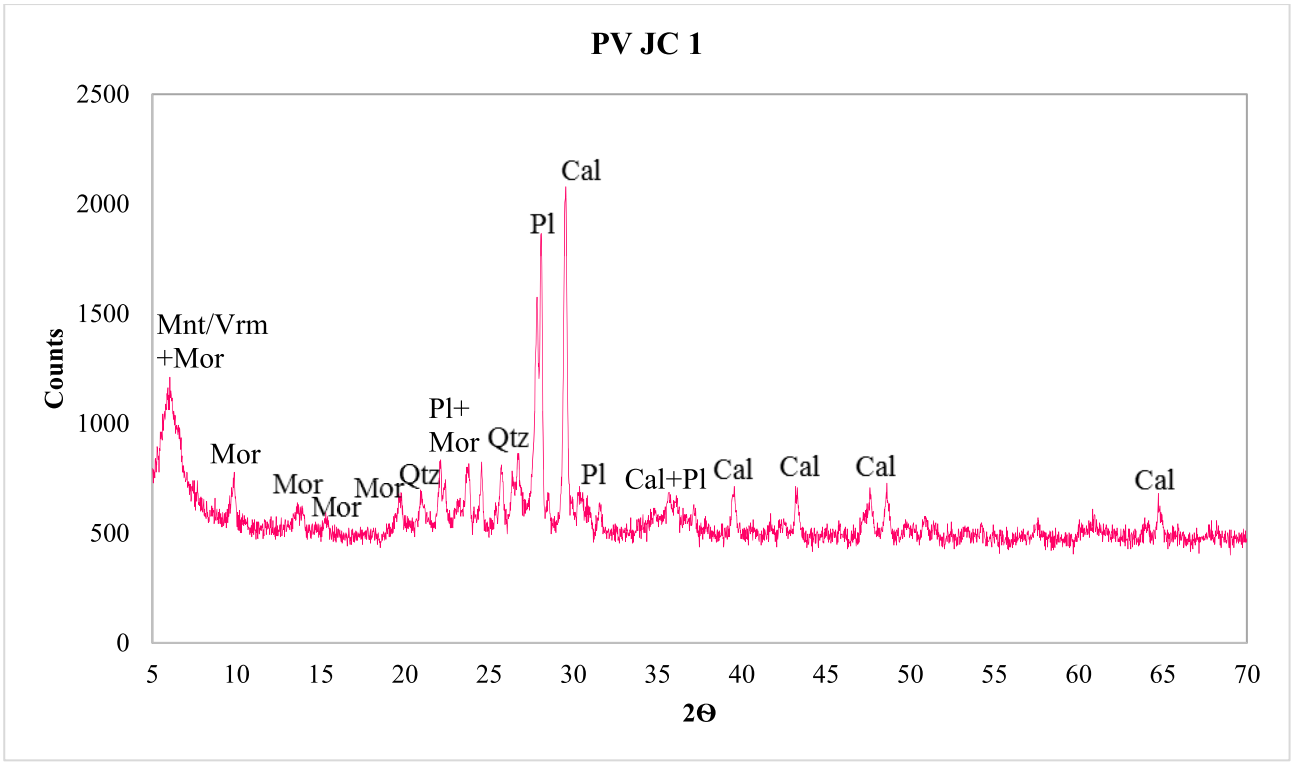
PV JC 1
Counts
2Θ
Cal
Pl
Mnt/Vrm
+Mor
Mor
Pl+
Mor
Qtz
Cal+Pl

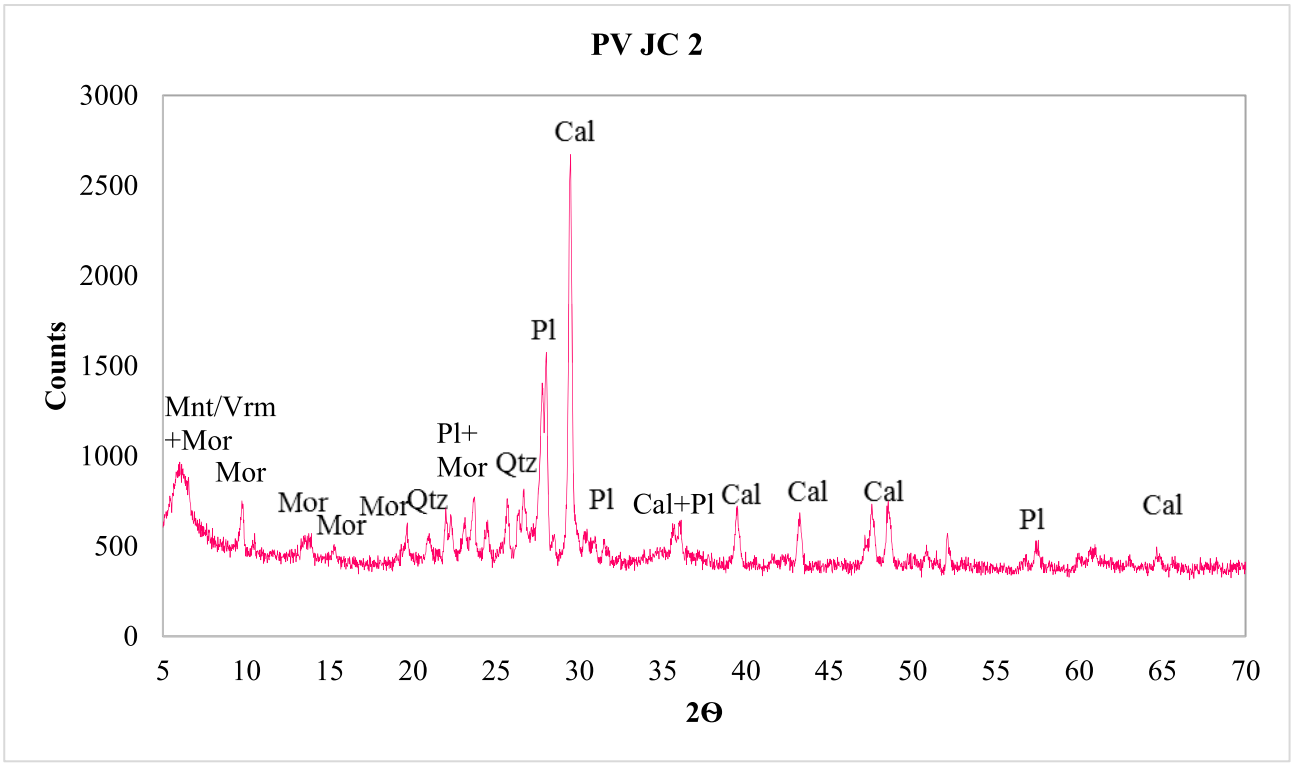
PV JC 2
Counts
2Θ
Cal
Pl
Mnt/Vrm
+Mor
Mor
Mor
Mor
Mor
Qtz
Pl+
Mor
Qtz
Pl
Cal+Pl
Cal
Cal
Cal
Pl
Cal

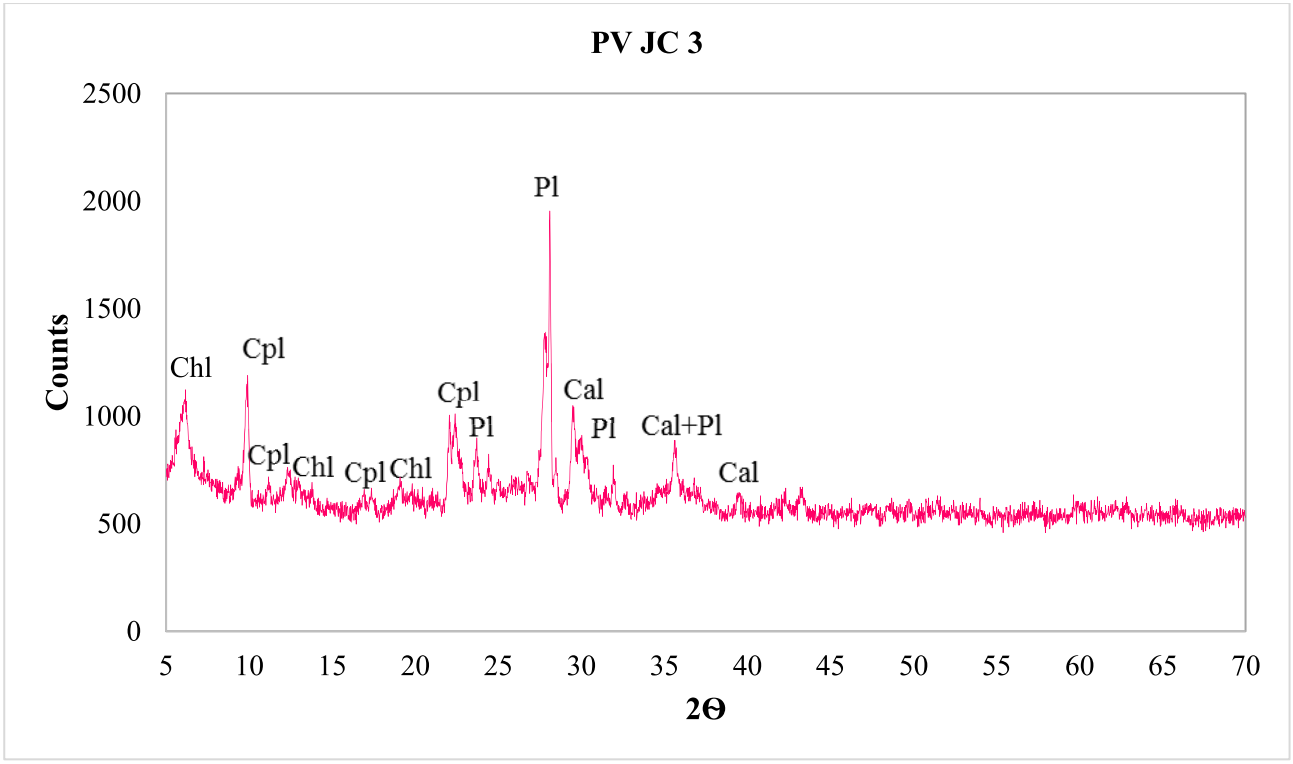
PV JC 3
Counts
2Θ
Pl
Chl
Cpl
Cpl
Chl
Cpl
Chl
Cpl
Pl
Cal
Pl
Cal+Pl
Cal

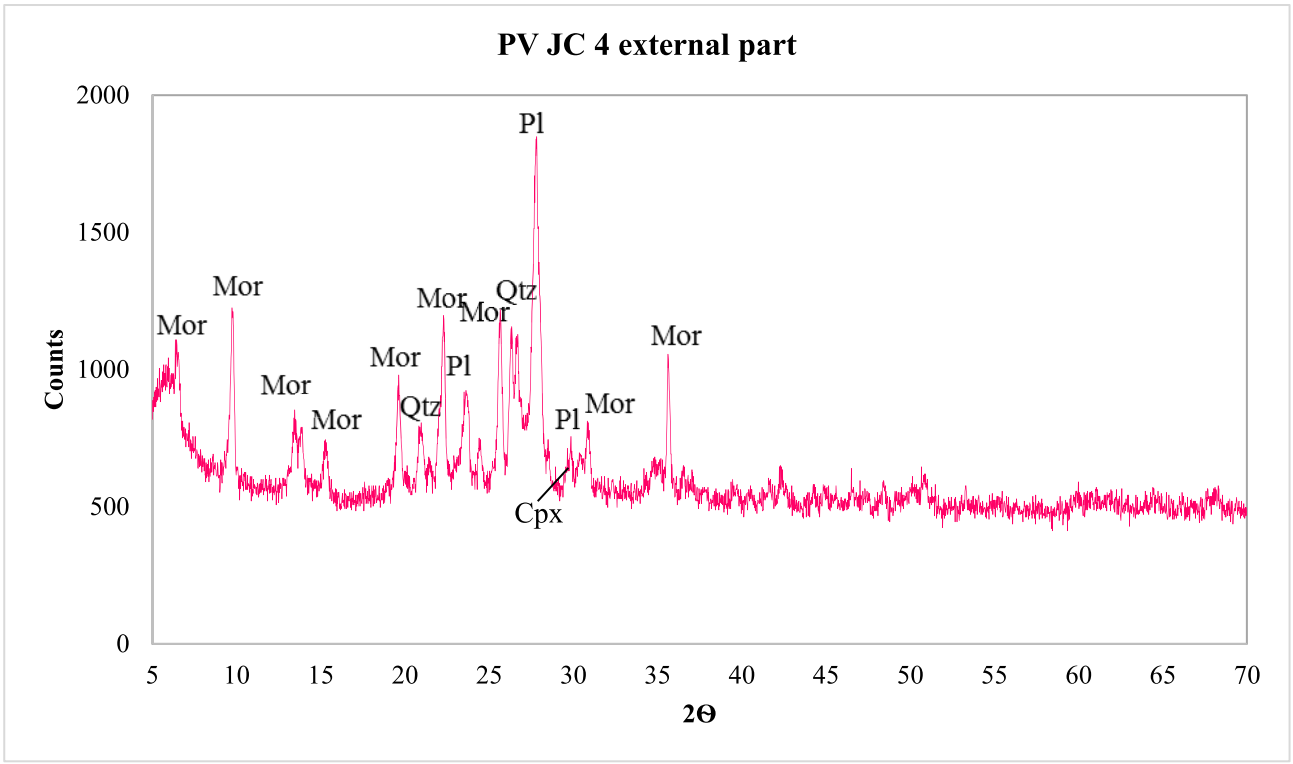
PV JC 4 external part
Counts
2Θ
Pl
Mor
Qtz
Cpx

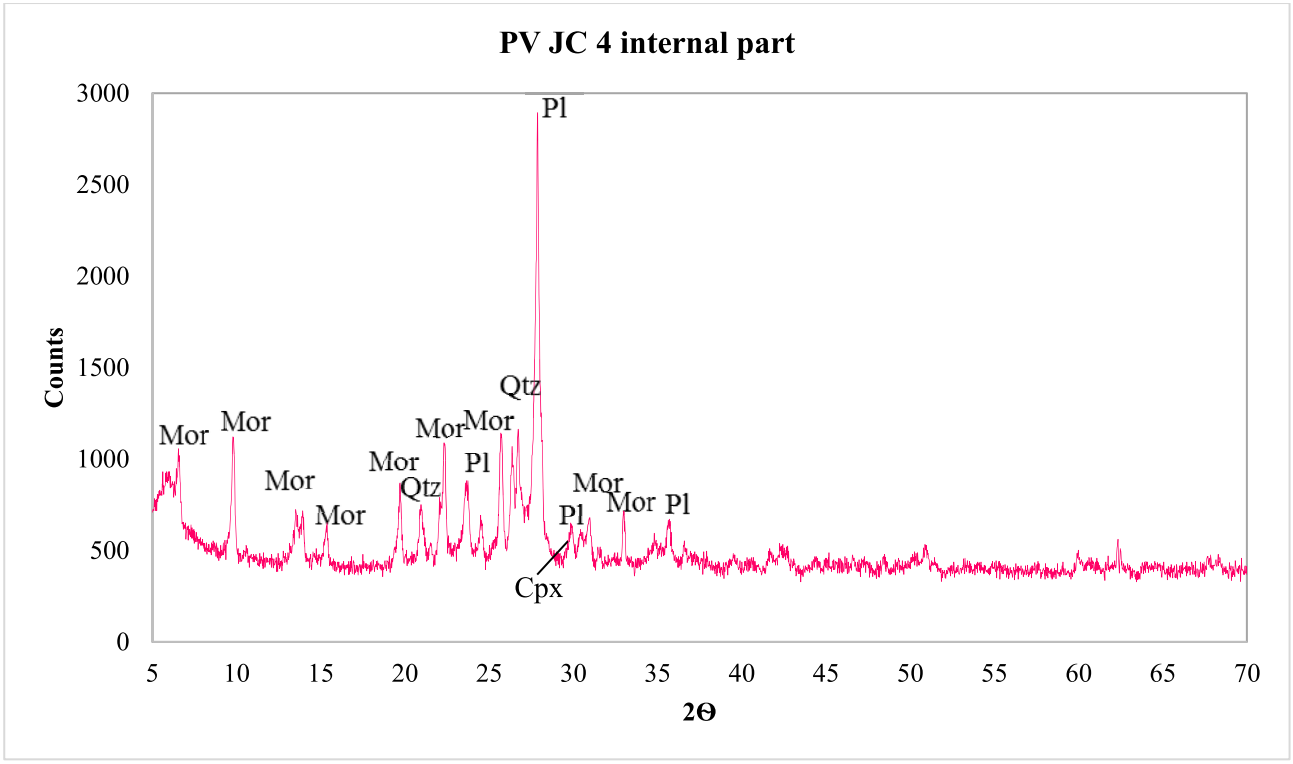
PV JC 4 internal part
Counts
2Θ
Pl
Mor
Qtz
Cpx

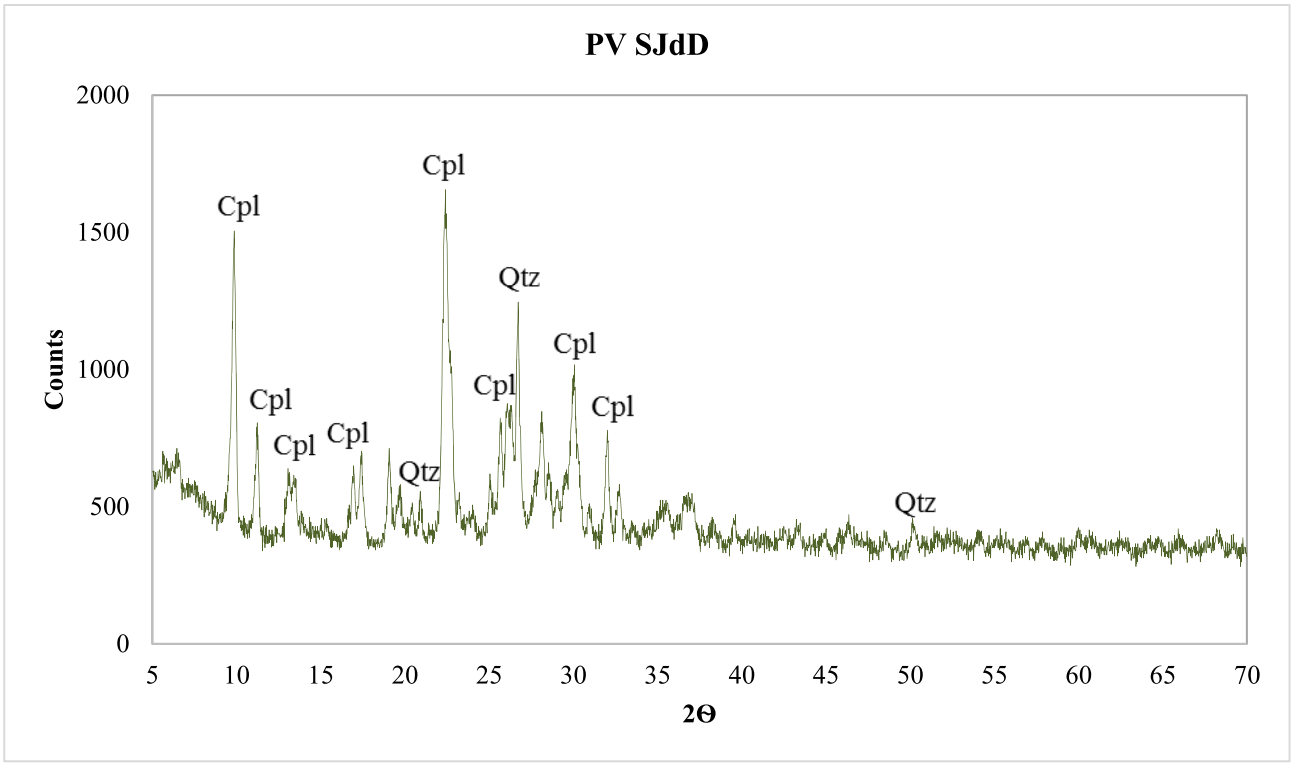
PV SJdD
Counts
2Θ
Cpl
Qtz

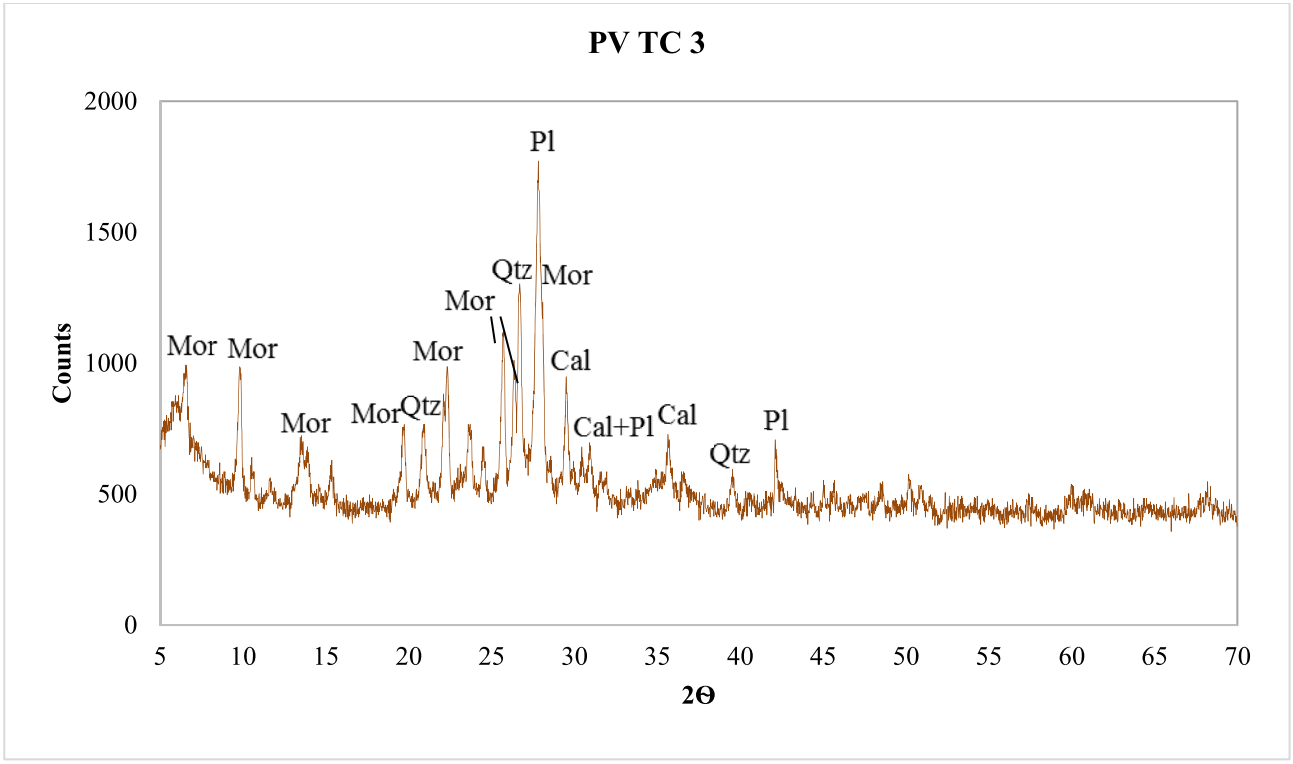
PV TC 3
Counts
2Θ
Pl
Mor
Qtz
Cal
Cal+Pl

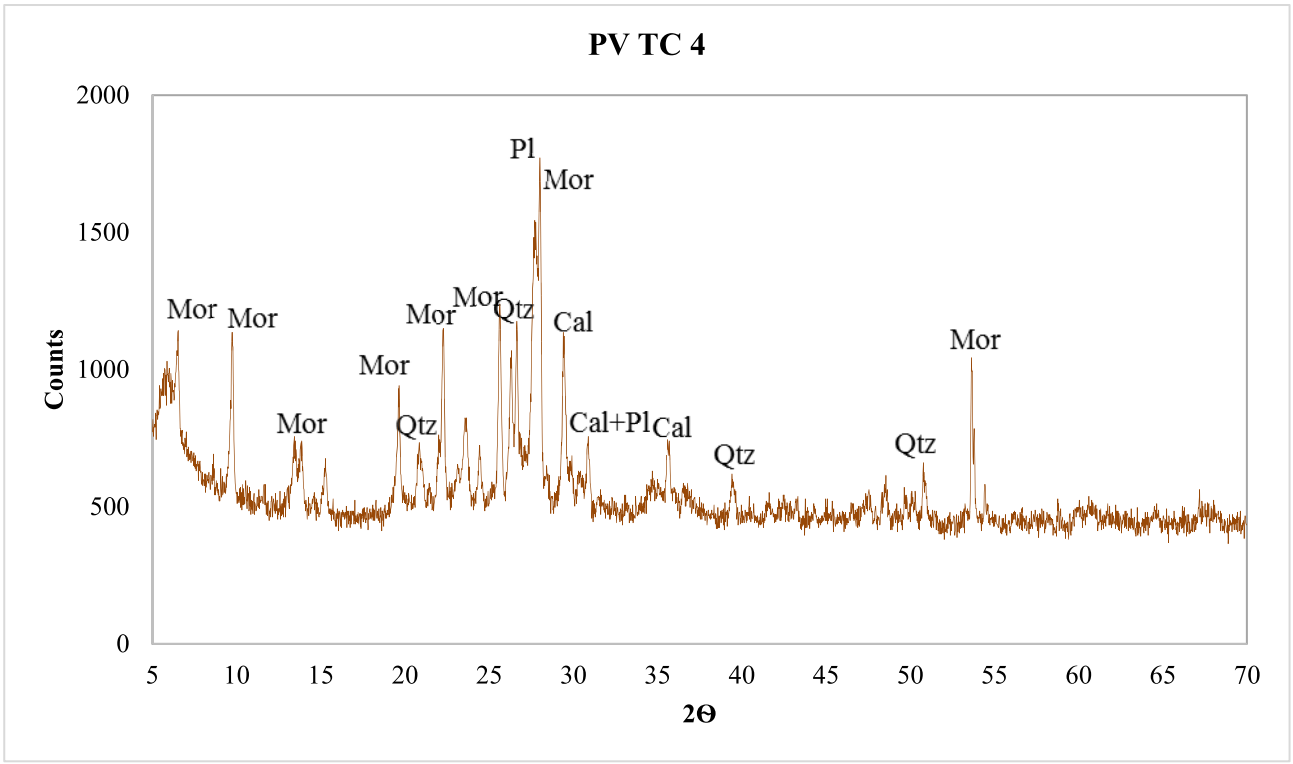
PV TC 4
Counts
2Θ
Mor
Pl
Qtz
Cal
Cal+Pl
Qtz

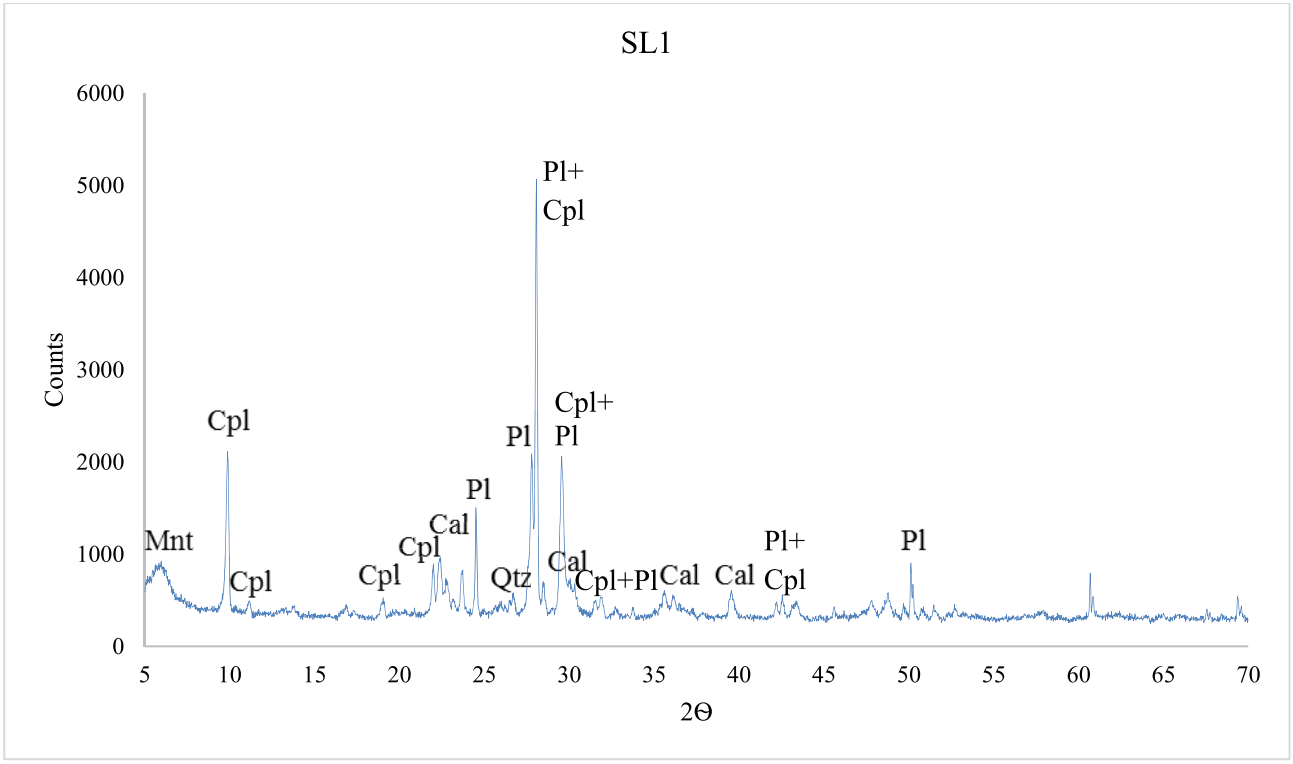
SL1
Counts
2Θ
Mnt
Cpl
Pl
Cal
Qtz
Cpl+Pl
Pl+
Cpl

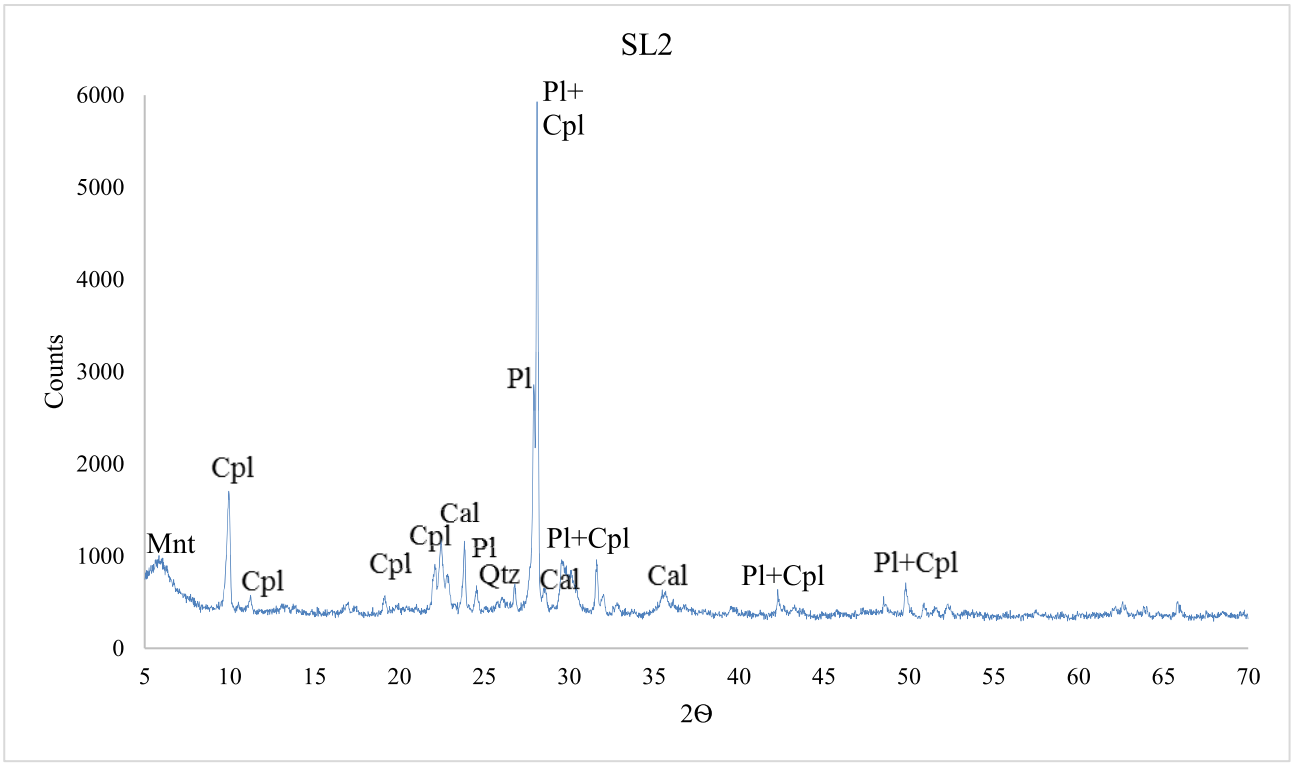
SL2
Counts
2Θ
Pl+
Cpl
Pl
Cpl
Mnt
Cpl
Cpl
Cal
Cpl
Pl
Qtz
Cal
Pl+Cpl
Cal
Pl+Cpl
Pl+Cpl

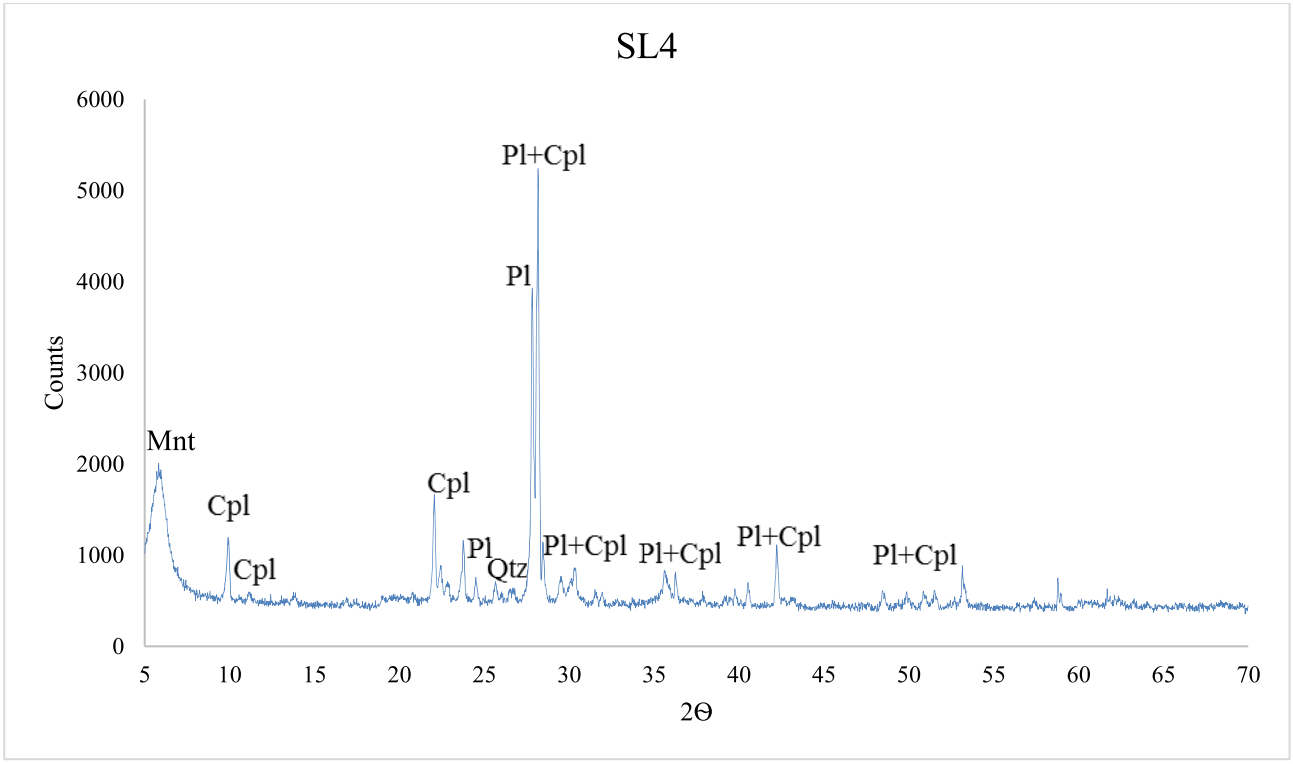
SL4
Counts
2Θ
Pl+Cpl
Pl
Mnt
Cpl
Cpl
Cpl
Pl
Qtz
Pl+Cpl
Pl+Cpl
Pl+Cpl
Pl+Cpl

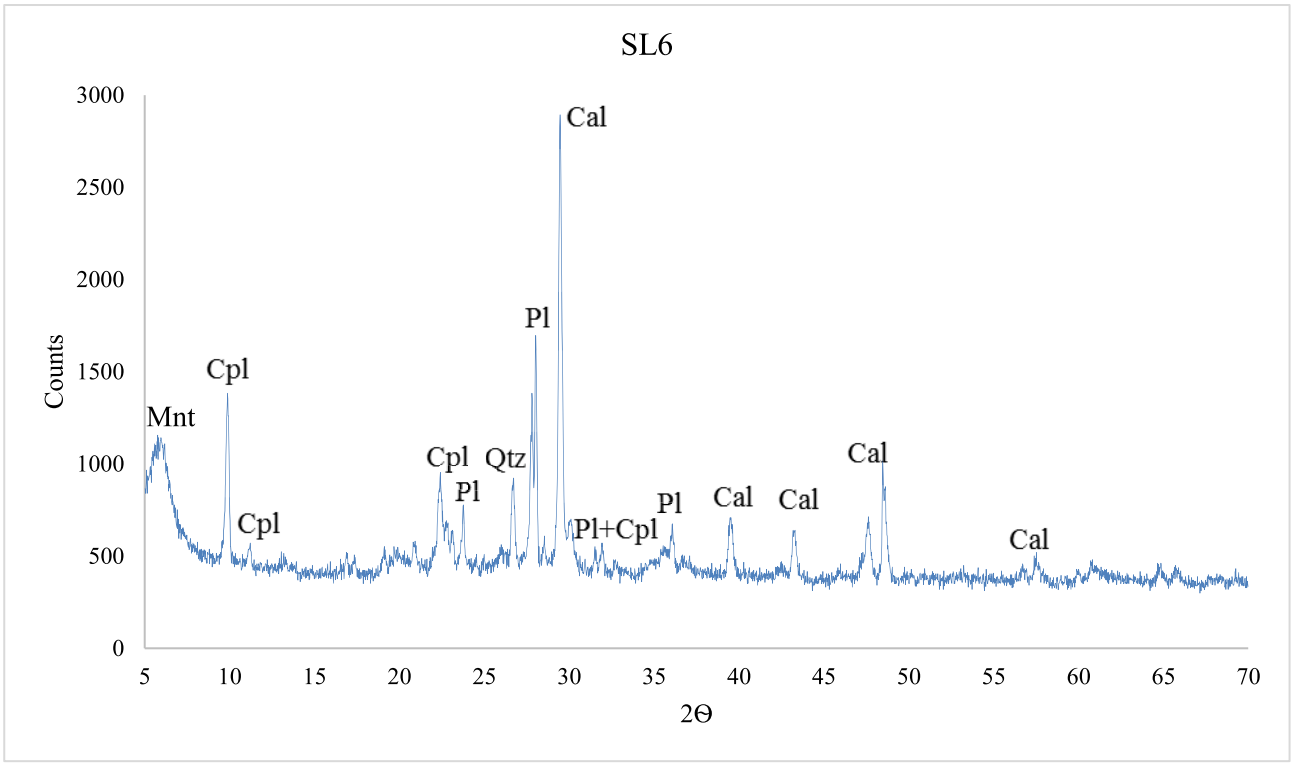
SL6
Counts
2Θ
Mnt
Cpl
Cpl
Cpl
Qtz
Pl
Pl
Cal
Pl+Cpl
Pl
Cal
Cal
Cal
Cal

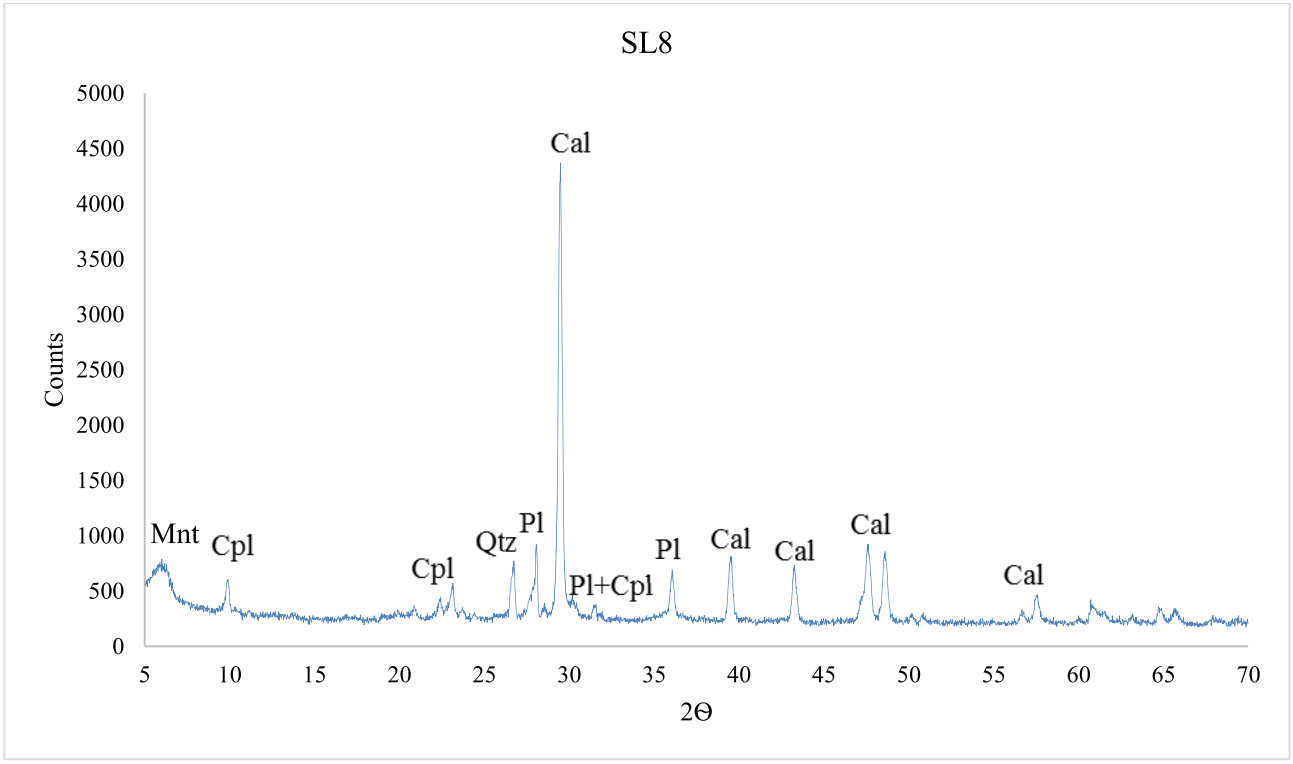
SL8
Counts
2Θ
Mnt
Cpl
Cpl
Qtz
Pl
Cal
Pl+Cpl
Pl
Cal
Cal
Cal
Cal

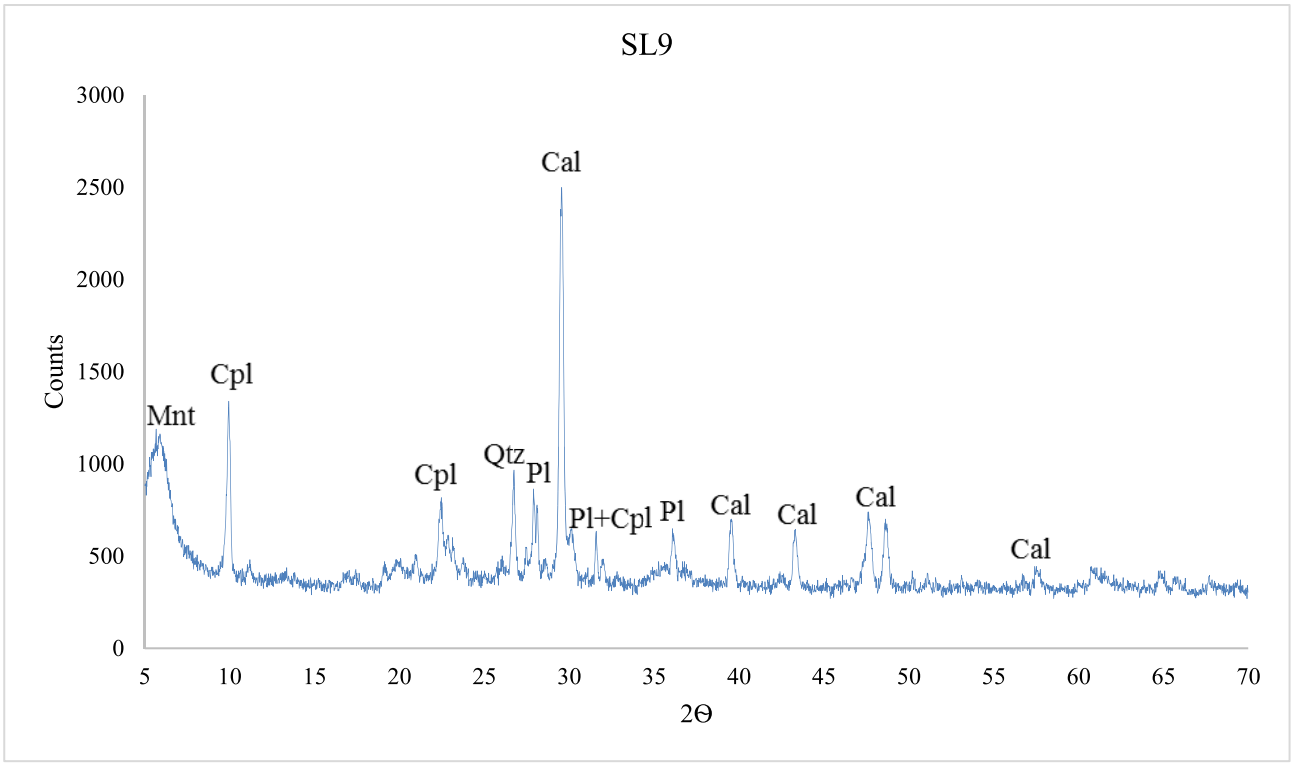
SL9
Counts
2Θ
Mnt
Cpl
Cpl
Qtz
Pl
Cal
Pl+Cpl
Pl
Cal
Cal
Cal
Cal

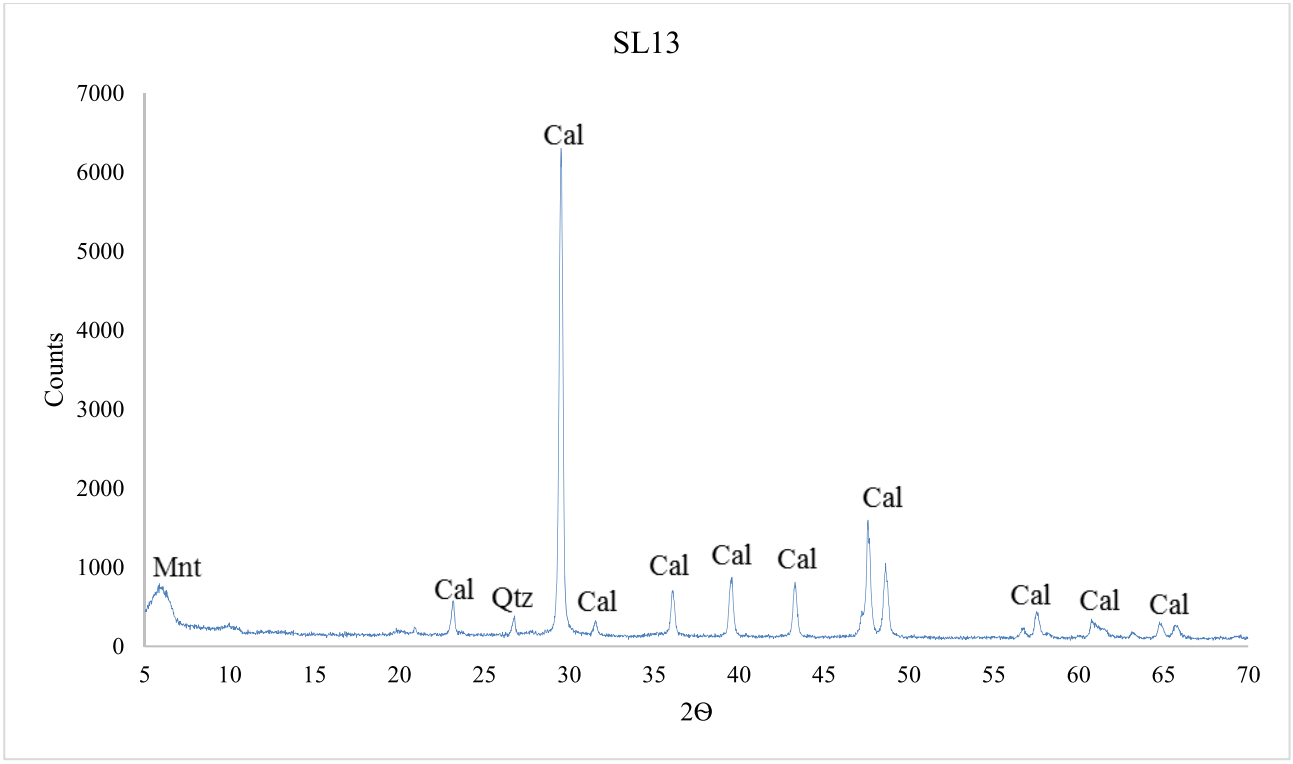
SL13
Counts
2Θ
Mnt
Cal
Qtz
Cal
Cal
Cal
Cal
Cal
Cal
Cal
Cal
Cal

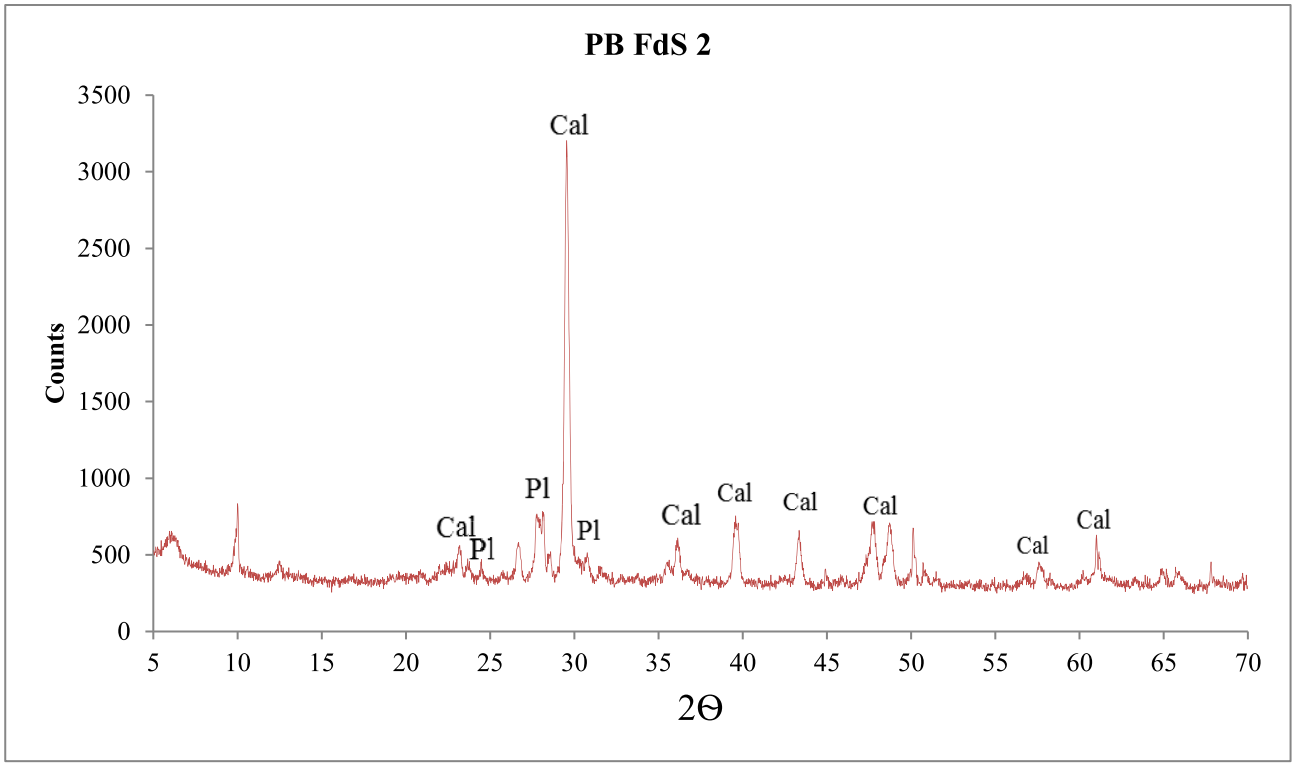
PB FdS 2
Counts
2Θ
Cal
Pl
Cal
Pl
Pl
Cal
Cal
Cal
Cal
Cal
Cal

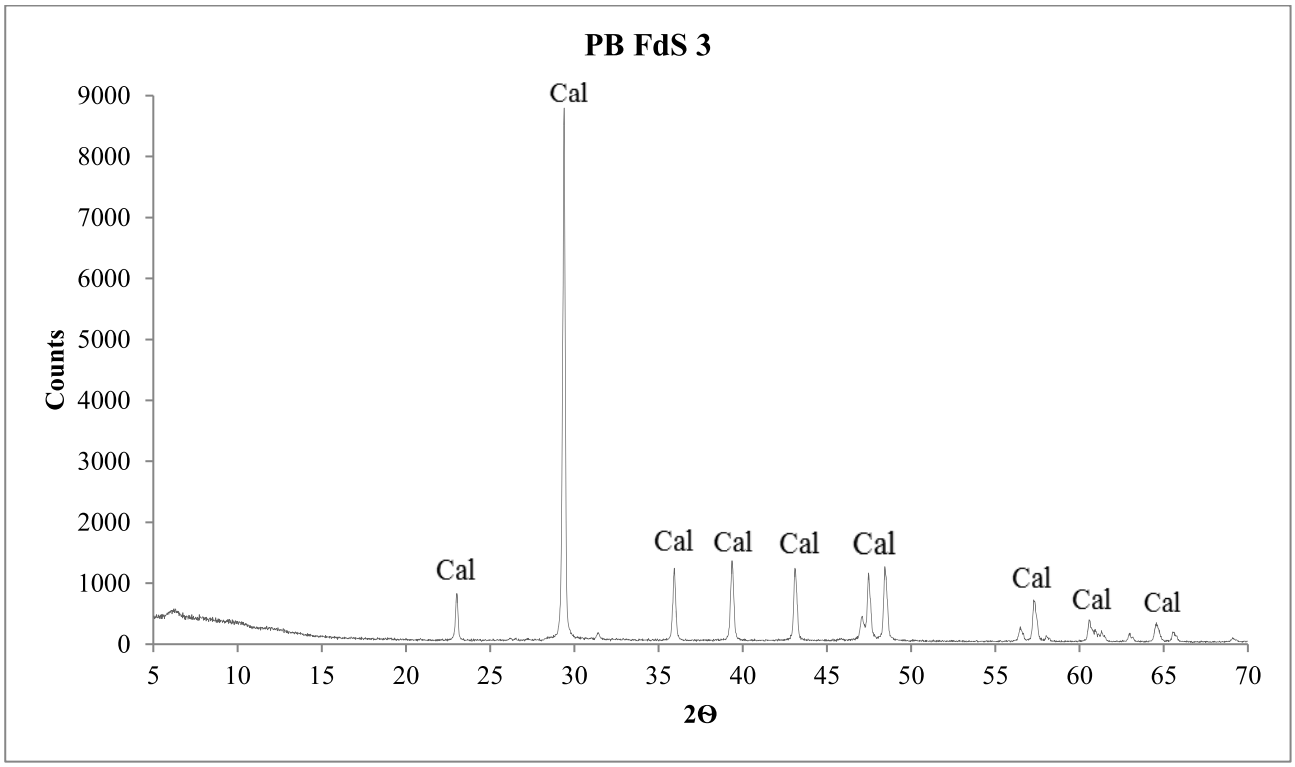
PB FdS 3
Counts
2Θ
Cal
Cal
Cal
Cal
Cal
Cal
Cal
Cal
Cal

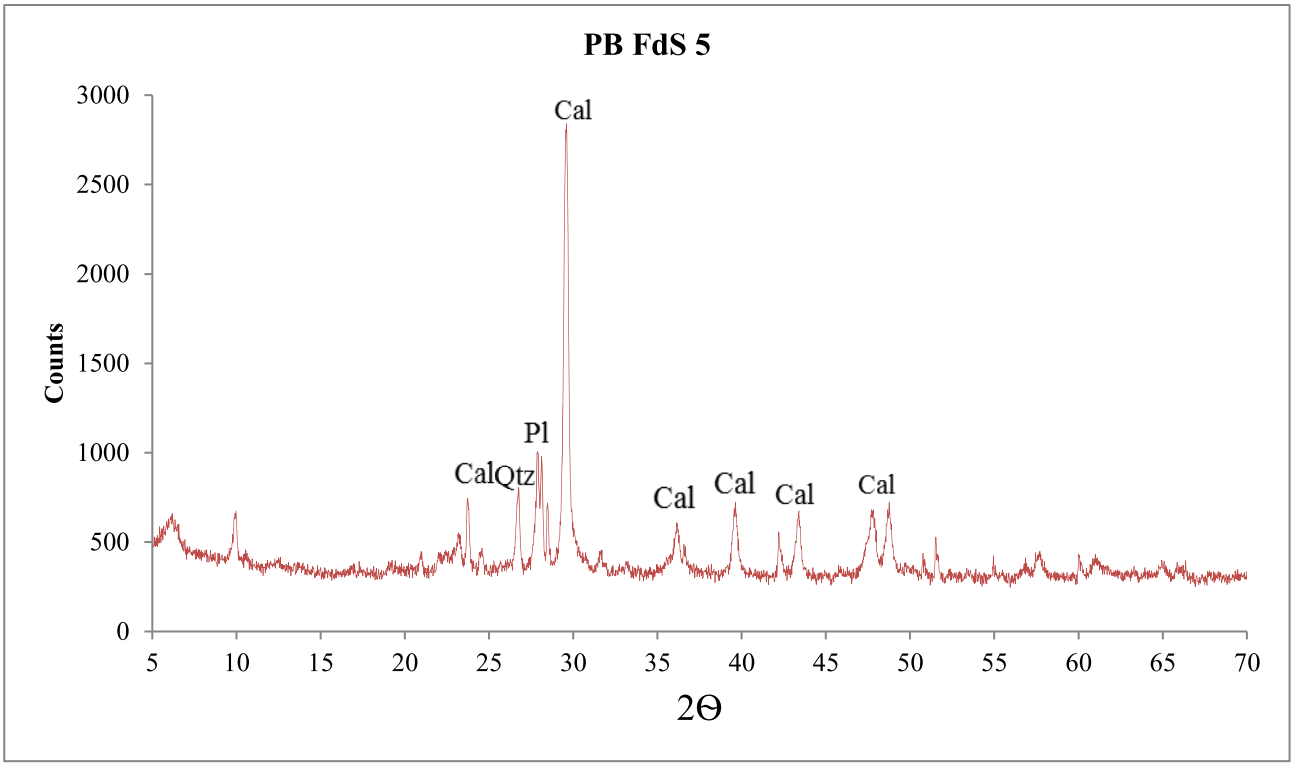
PB FdS 5
Counts
2Θ
Cal
Pl
CalQtz
Cal
Cal
Cal
Cal

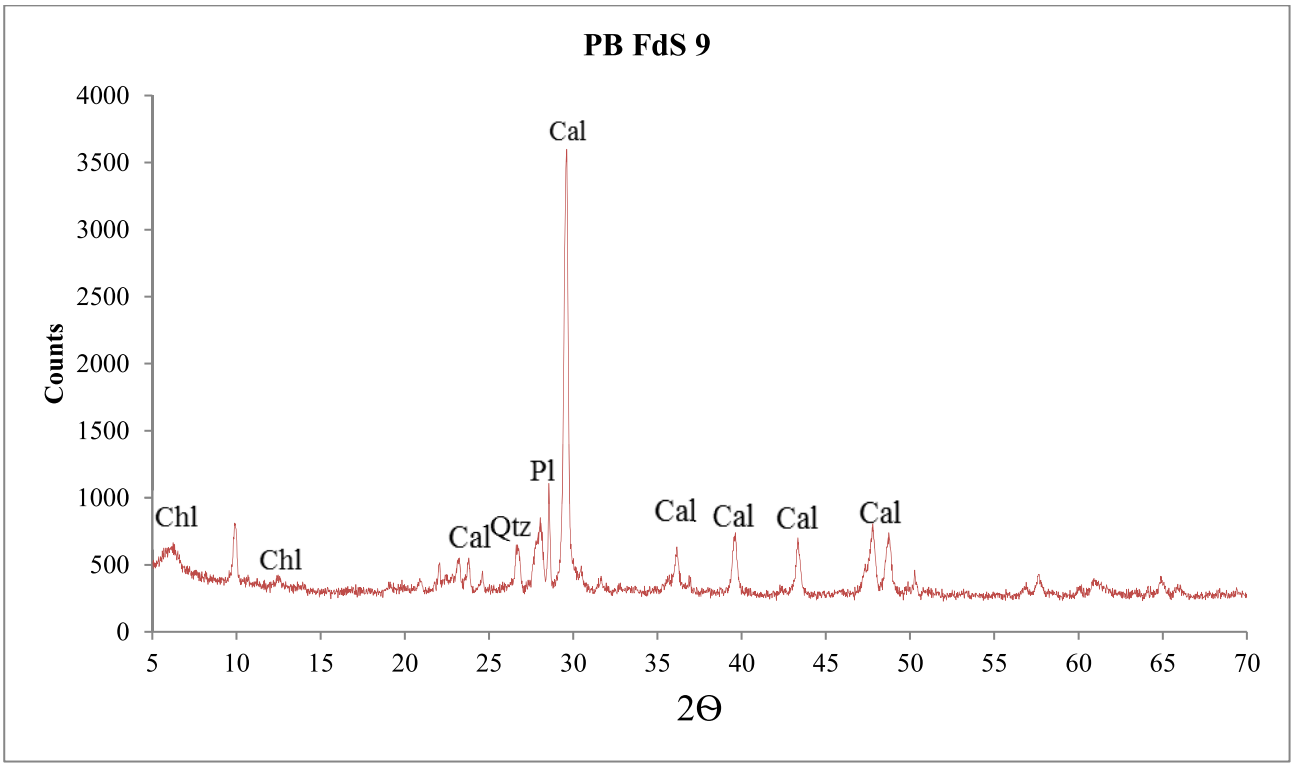
PB FdS 9
Counts
2Θ
Cal
Pl
Chl
Chl
CalQtz
Cal
Cal
Cal
Cal

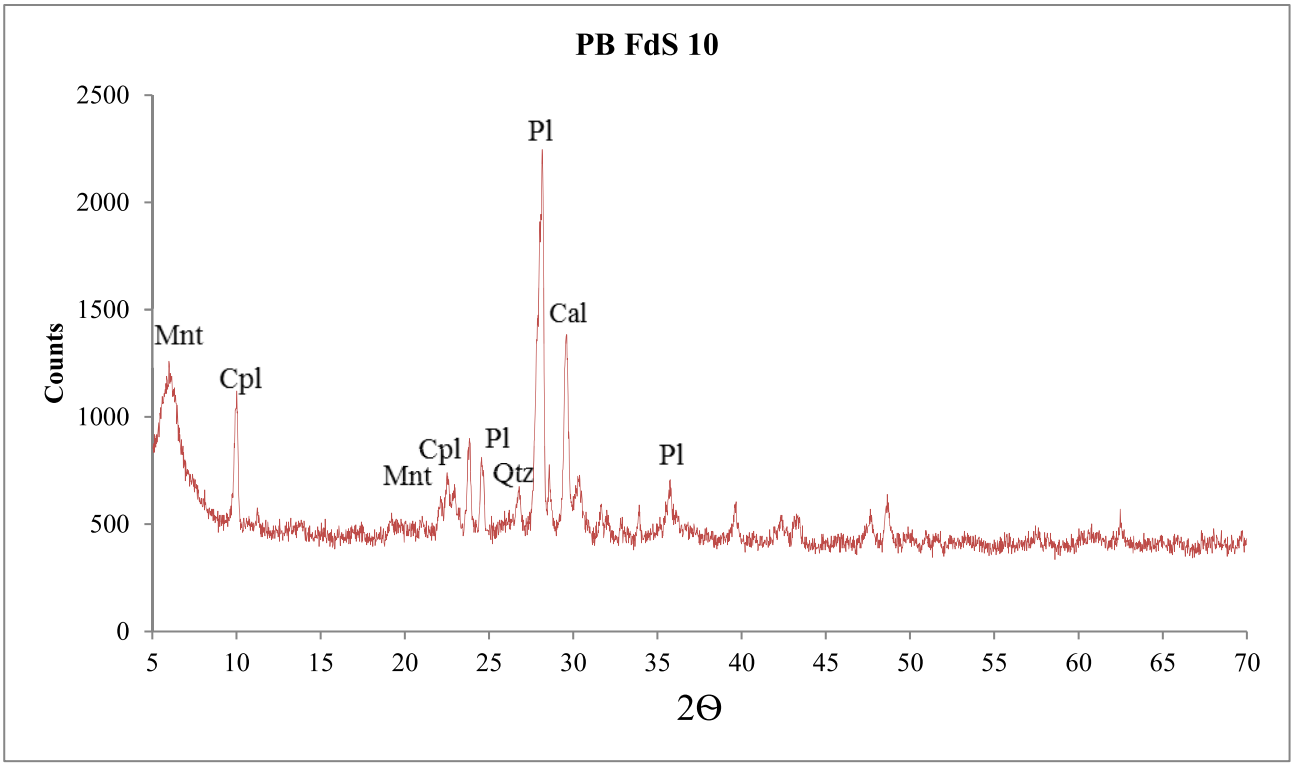
PB FdS 10
Counts
2Θ
Mnt
Cpl
Mnt
Cpl
Pl
Qtz
Pl
Cal
Pl

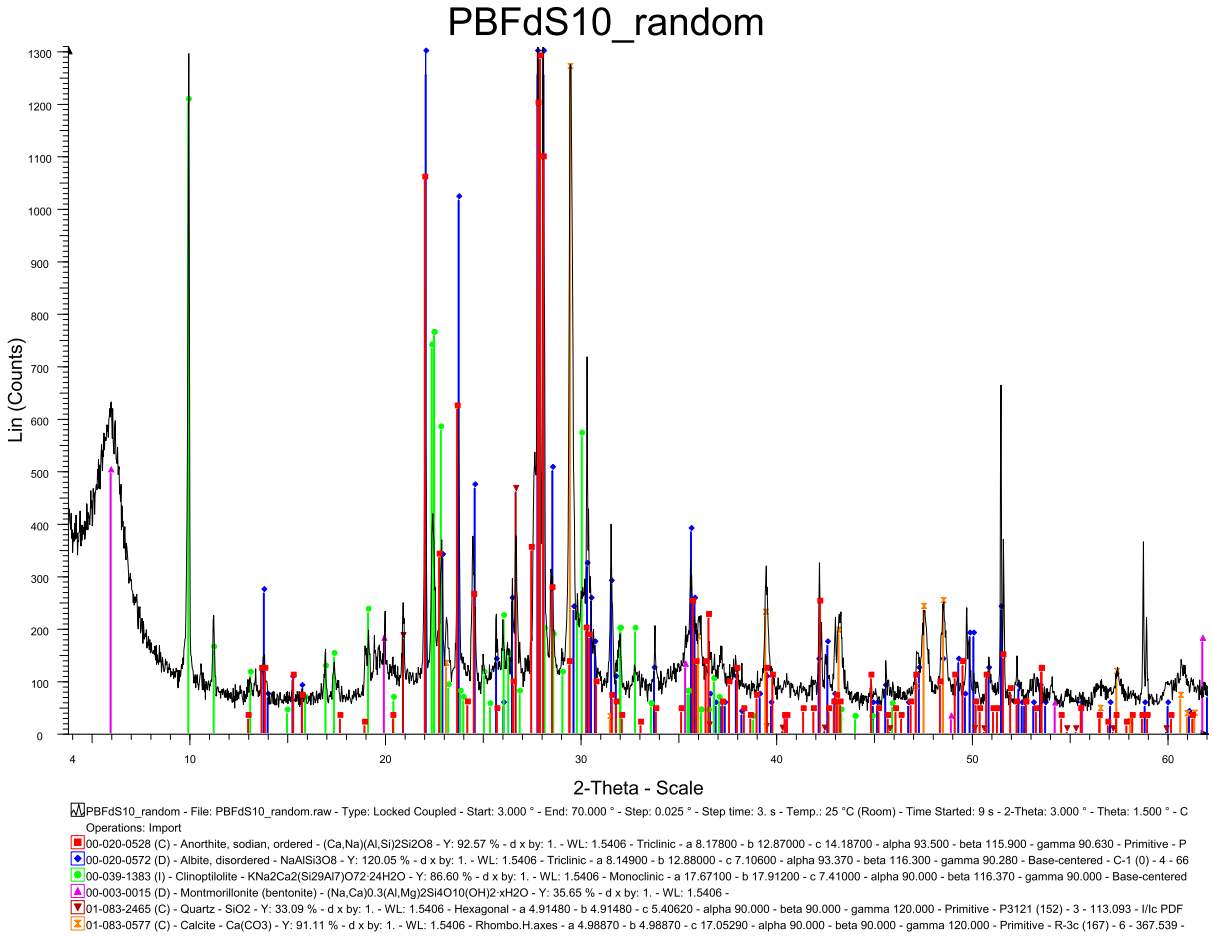
PBFdS10_random
Lin (Counts)
2-Theta - Scale
PBFdS10_random - File: PBFdS10_random.raw - Type: Locked Coupled - Start: 3.000 ° - End: 70.000 ° - Step: 0.025 ° - Step time: 3. s - Temp.: 25 °C (Room) - Time Started: 9 s - 2-Theta: 3.000 ° - Theta: 1.500 ° - C
Operations: Import
00-020-0528 (C) - Anorthite, sodian, ordered - (Ca,Na)(Al,Si)2Si2O8 - Y: 92.57 % - d x by: 1. - WL: 1.5406 - Triclinic - a 8.17800 - b 12.87000 - c 14.18700 - alpha 93.500 - beta 115.900 - gamma 90.630 - Primitive - P
00-020-0572 (D) - Albite, disordered - NaAlSi3O8 - Y: 120.05 % - d x by: 1. - WL: 1.5406 - Triclinic - a 8.14900 - b 12.88000 - c 7.10600 - alpha 93.370 - beta 116.300 - gamma 90.280 - Base-centered - C-1 (0) - 4 - 66
00-039-1383 (I) - Clinoptilolite - KNa2Ca2(Si29Al7)O72·24H2O - Y: 86.60 % - d x by: 1. - WL: 1.5406 - Monoclinic - a 17.67100 - b 17.91200 - c 7.41000 - alpha 90.000 - beta 116.370 - gamma 90.000 - Base-centered
00-003-0015 (D) - Montmorillonite (bentonite) - (Na,Ca)0.3(Al,Mg)2Si4O10(OH)2·xH2O - Y: 35.65 % - d x by: 1. - WL: 1.5406 -
01-083-2465 (C) - Quartz - SiO2 - Y: 33.09 % - d x by: 1. - WL: 1.5406 - Hexagonal - a 4.91480 - b 4.91480 - c 5.40620 - alpha 90.000 - beta 90.000 - gamma 120.000 - Primitive - P3121 (152) - 3 - 113.093 - I/Ic PDF
01-083-0577 (C) - Calcite - Ca(CO3) - Y: 91.11 % - d x by: 1. - WL: 1.5406 - Rhombo.H.axes - a 4.98870 - b 4.98870 - c 17.05290 - alpha 90.000 - beta 90.000 - gamma 120.000 - Primitive - R-3c (167) - 6 - 367.539 -

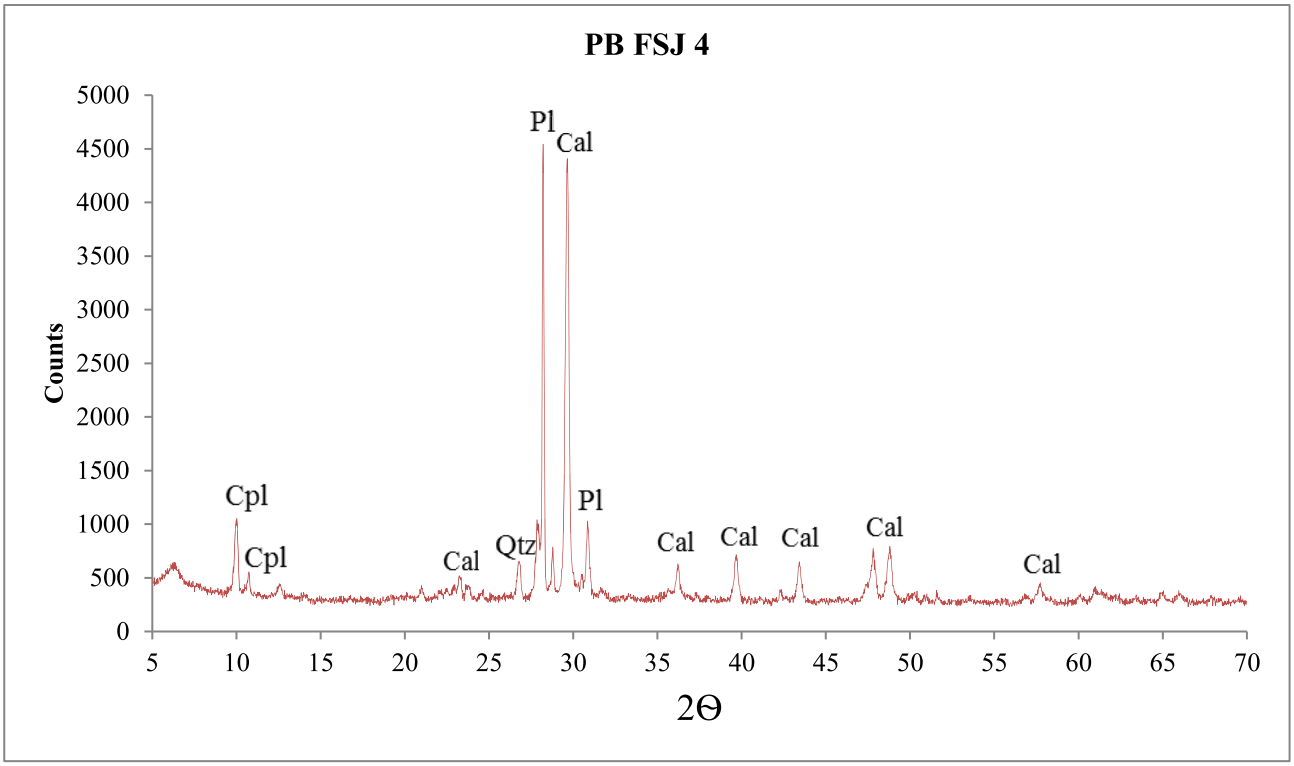
PB FSJ 4
Counts
2Θ
Pl
Cal
Cpl
Cpl
Cal
Qtz
Pl
Cal
Cal
Cal
Cal
Cal

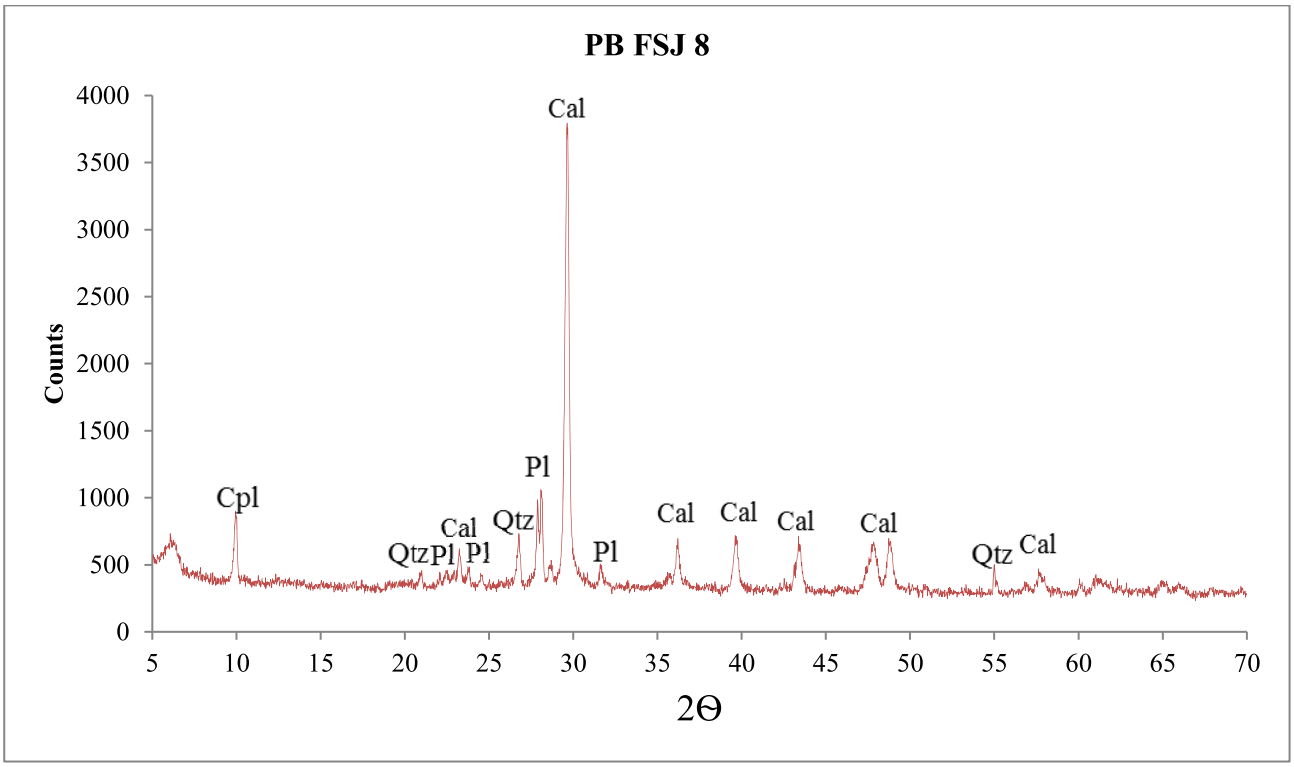
PB FSJ 8
Counts
2Θ
Cal
Cpl
Pl
Qtz
Cal
Qtz
Pl
Pl
Pl
Cal
Cal
Cal
Cal
Qtz
Cal

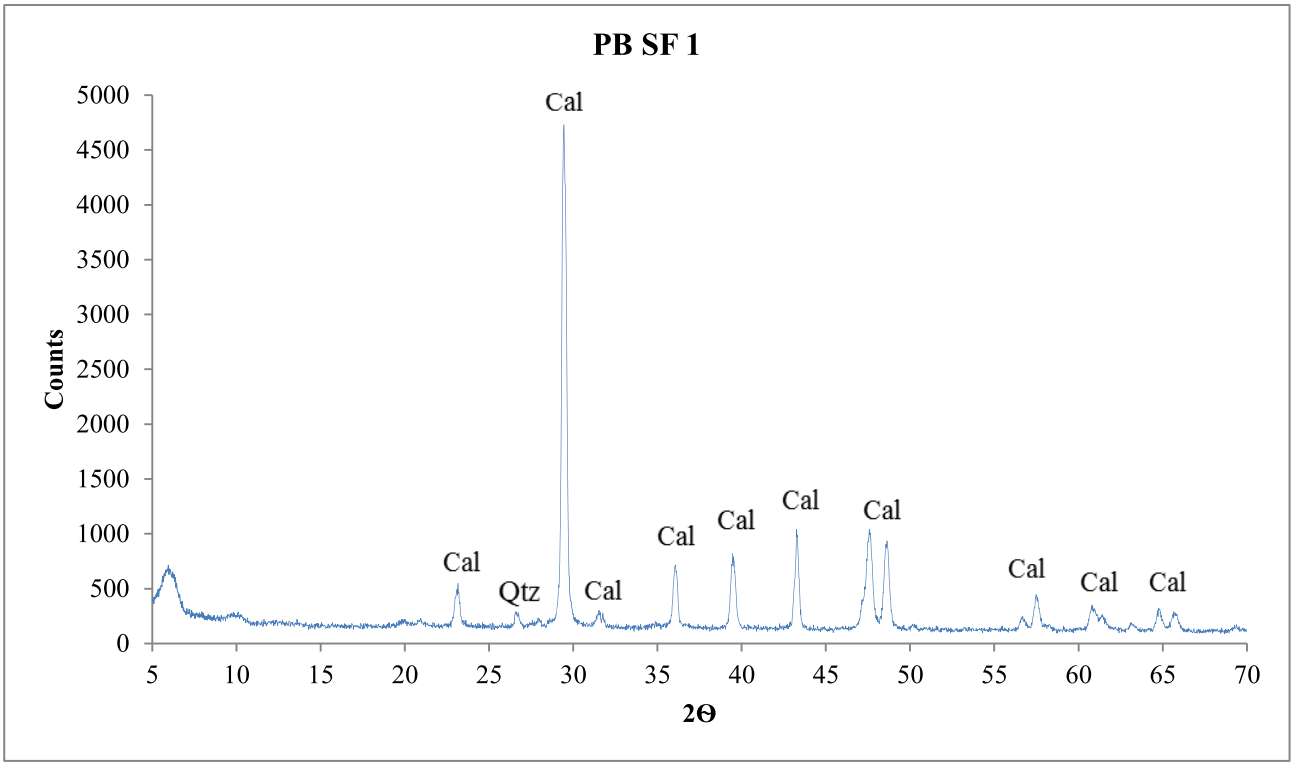
PB SF 1
Counts
2Θ
Cal
Cal
Qtz
Cal
Cal
Cal
Cal
Cal
Cal
Cal
Cal

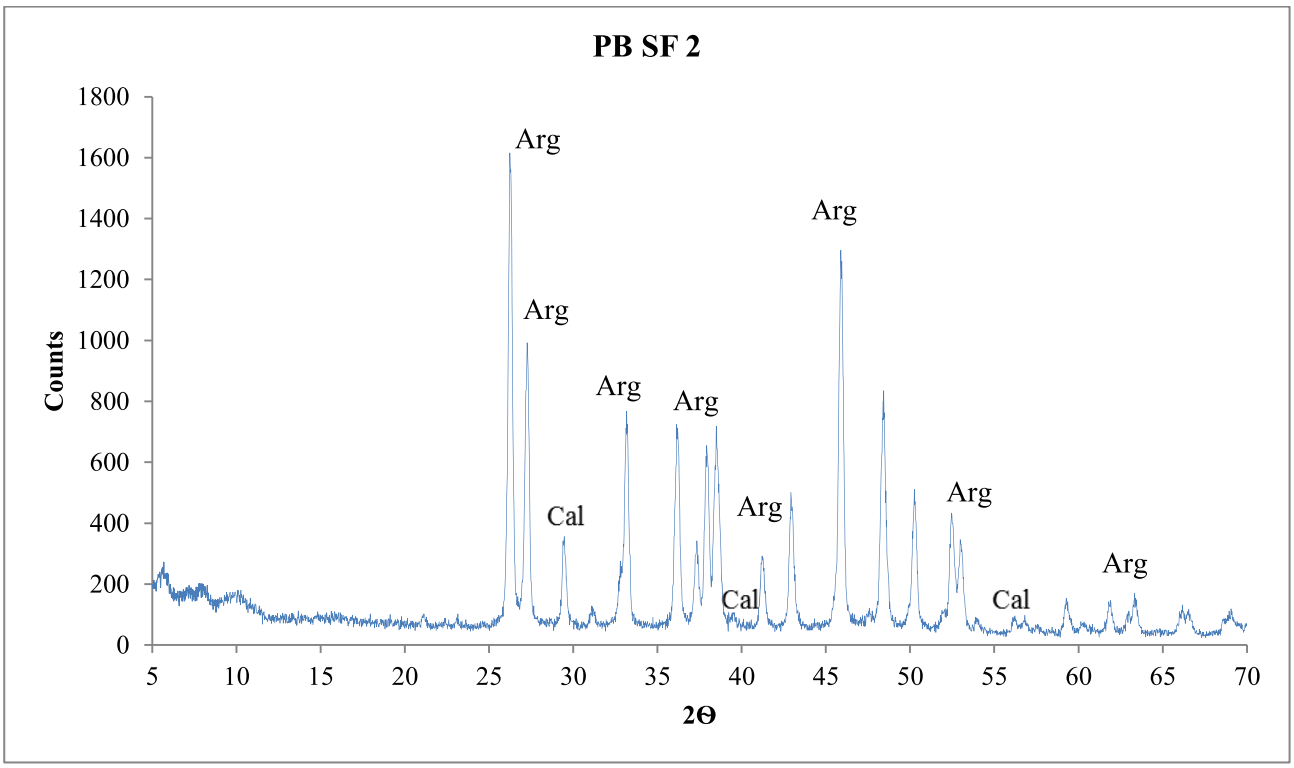
PB SF 2
Counts
2Θ
Arg
Arg
Arg
Arg
Cal
Arg
Cal
Arg
Arg
Cal
Arg

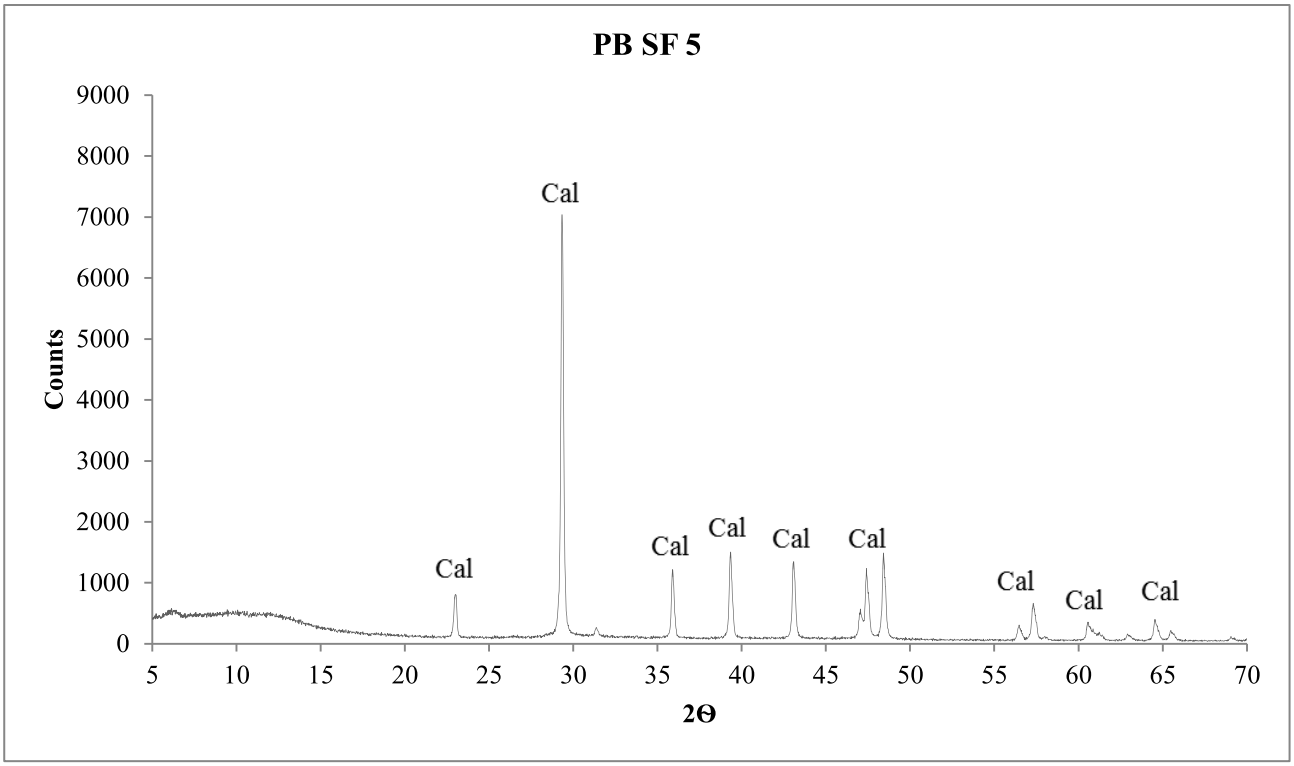
PB SF 5
Counts
2Θ
Cal
Cal
Cal
Cal
Cal
Cal
Cal
Cal

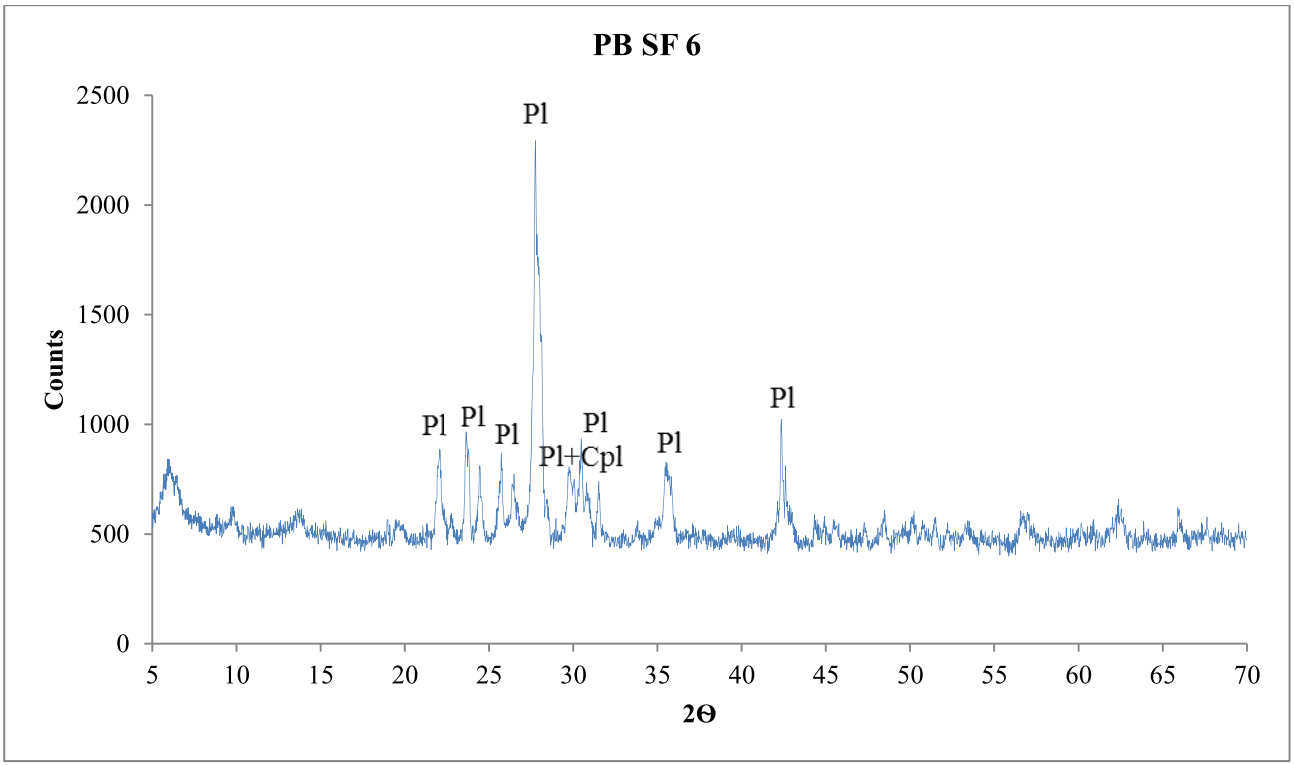
PB SF 6
Counts
2Θ
Pl
Pl
Pl
Pl
Pl+Cpl
Pl
Pl
Pl

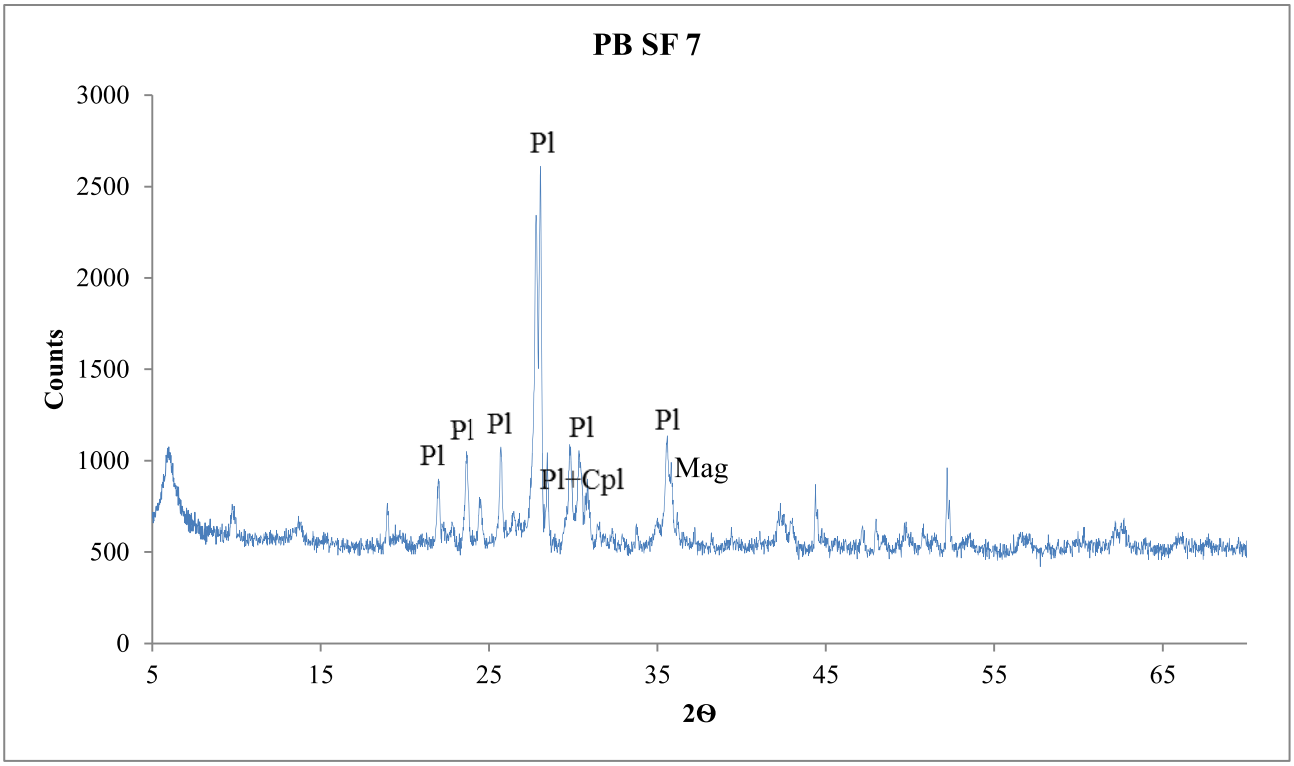
PB SF 7
Counts
2Θ
Pl
Pl
Pl
Pl
Pl
Pl
Pl–Cpl
Mag

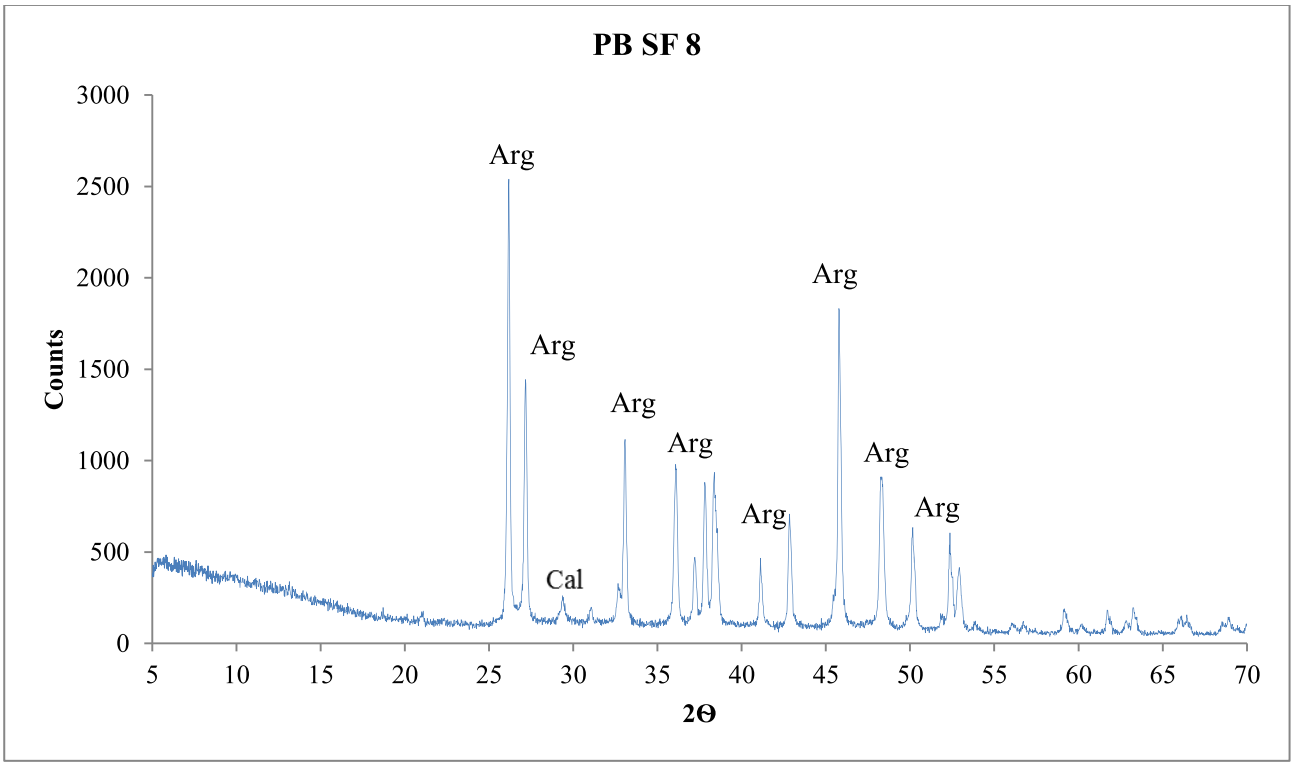
PB SF 8
Counts
2Θ
Arg
Arg
Arg
Arg
Arg
Arg
Arg
Arg
Cal

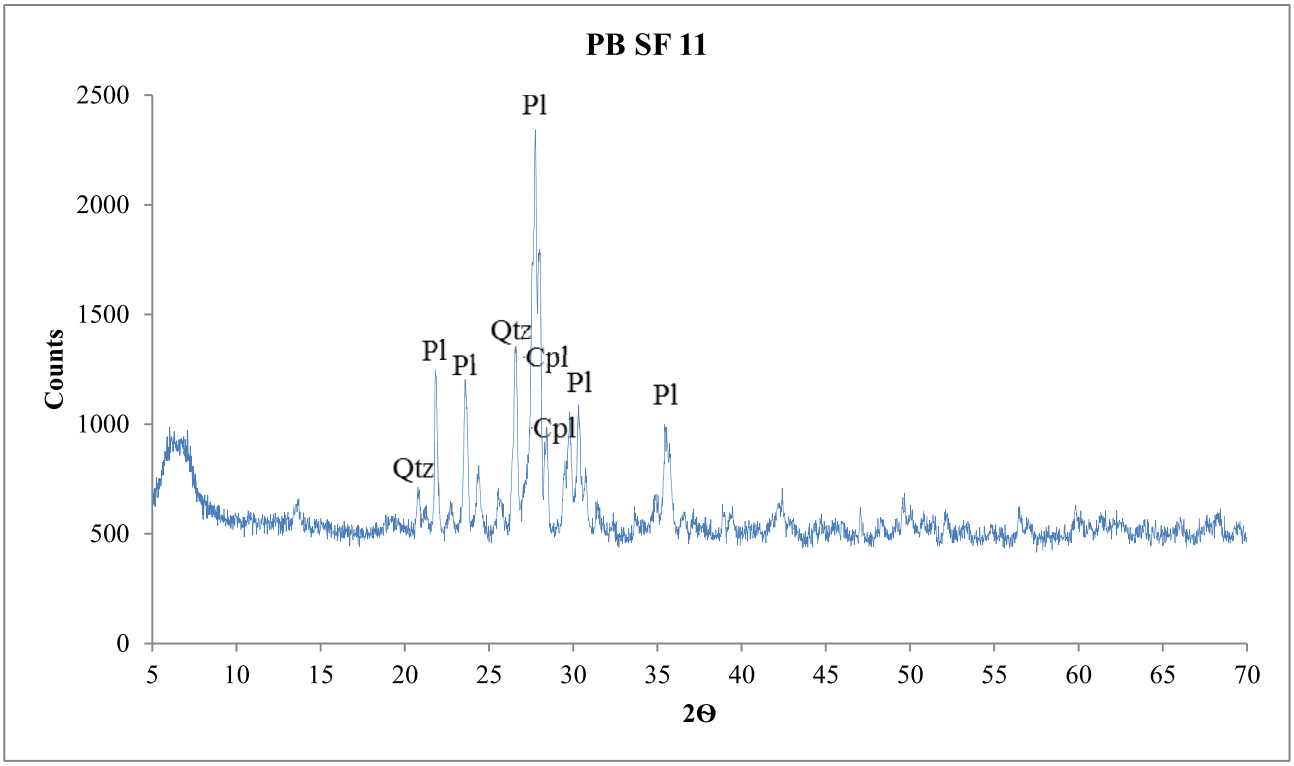
PB SF 11
Counts
2Θ
Pl
Pl
Pl
Qtz
Cpl
Pl
Pl
Cpl
Qtz
2500
2000
1500
1000
500
0
5
10
15
20
25
30
35
40
45
50
55
60
65
70

ANNEX 2

Publications, Proceedings, Presentations

Science of the Total Environment 575 (2017) 23–32

Contents lists available at ScienceDirect

Science of the Total Environment

journal homepage: www.elsevier.com/locate/scitotenv

Durability assessment to environmental impact of nano-structured consolidants on Carrara marble by field exposure tests

Alessandra Bonazza [a,*], Giorgia Vidorni [a], Irene Natali [a], Chiara Ciantelli [a], Chiara Giosuè [b], Francesca Tittarelli [a,b]

[a] Institute of Atmospheric Sciences and Climate, National Research Council (ISAC-CNR), Bologna, Italy
[b] Department of Materials and Environmental Engineering and Physics, Università Politecnica delle Marche, via Brecce Biance, 60131 Ancona, Italy

HIGHLIGHTS

- Cultural heritage increasingly at risk due to climate change impact
- Need of compatible and resilient consolidating products for marble
- Carrara marble models (treated and not) exposed at four European sites
- Rain principally affected the durability of $CaCO_3$-precursor consolidants.

GRAPHICAL ABSTRACT

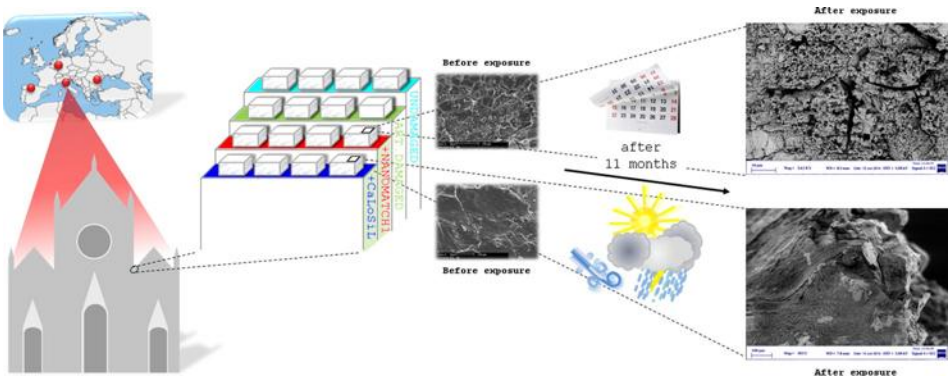

ARTICLE INFO

Article history:
Received 4 August 2016
Received in revised form 30 September 2016
Accepted 1 October 2016
Available online xxxx

Editor: D. Barcelo

Keywords:
Climate change
Durability
Metal alkoxide
Stone conservation
Cultural heritage

ABSTRACT

The EU policy of reducing the emissions of combustion generated pollutants entails climate induced deterioration to become more important. Moreover, products applied to preserve outdoor built heritage and their preliminary performance tests often turn out to be improper. In such context, the paper reports the outcomes of the methodology adopted to assess the durability and efficiency of nano-based consolidating products utilized for the conservation of carbonate artworks, performing field exposure tests on Carrara marble model samples in different sites in the framework of the EC Project NANOMATCH. Surface properties and cohesion, extent and penetration of the conservative products and their interactions with marble substrates and environmental conditions are here examined after outdoor exposure for eleven months in four different European cities and compared with the features of undamaged and of untreated damaged specimens undergoing the same exposure settings.

1. Introduction

The intensification of climate changes combined with the recent reduction in acidic air pollution in urban areas has made climate conditions to become more influential in the weathering of outdoor built heritage (Grossi et al., 2008). In this regard, research has been specifically devoted in the last decades by the European Union to assess the effects of environmental changes, including climatic ones, on cultural heritage and to develop mitigation strategies aiming at its protection and conservation (Kucera et al., 2005; Grossi et al., 2007; Sabbioni et al., 2007; Watt et al., 2009; Franzen et al., 2011; Bernardi et al., 2012; Sabbioni et al.,

* Corresponding author.
E-mail address: a.bonazza@isac.cnr.it (A. Bonazza).

http://dx.doi.org/10.1016/j.scitotenv.2016.10.004
0048-9697/

2012; Ashley-Smith et al., 2013; Ozga et al., 2014). In particular, available projections on climate change impact on cultural heritage have evidenced that decohesion and fracturing of carbonate stone, widely encountered in archaeological and historic built heritage, are likely to increase in Europe in the near (2010–2039) and the far future (2070–2099) induced mainly by (i) surface recession, (ii) thermal stress and (iii) salts crystallization (Bonazza et al., 2009a, 2009b; Grossi et al., 2011). Several efforts have been made since the 20th century in order to re-establish the original physical-mechanical properties of deteriorated stone and to increase their durability by the extensive use of both organic and inorganic consolidants. It is widely known that the performance and long-term efficiency of organic consolidants have been heavily reconsidered as they frequently undergo irreversibility of the treatments and chemical modifications caused by the interaction with both the environmental conditions and the substrate (Melo et al., 1999; Amoroso, 2002; Favaro et al., 2006, 2007). Although traditional inorganic consolidants as well as innovative nanomaterials (mainly dispersion of barium/calcium/magnesium hydroxide nanoparticles in alcohol) display better physical-chemical compatibility with carbonate stones and good chemical stability to environment, improvements should be introduced in order to ensure higher cohesive effect and better penetration into the porous matrix of damaged substrate (Camaiti, 2000; Giorgi et al., 2000; Amoroso, 2002; Doehne and Price, 2010; Chelazzi et al., 2013; Natali et al., 2014). In addition, possible interactions between the developed material and the outdoor environment should be evaluated, as pollution and weathering factors may act on the new product as well as on the historic substrates. In this regard, most of the studies have been carried out in laboratory, in accelerated and controlled environment. Unfortunately, climate simulation chamber is not designed to accurately replicate the real conditions of outdoor environment failing in the simulation of the synergetic action of environmental parameters as well as their variations at short and long time scale. Higher correspondence to the reality is although achieved by field exposure tests. Hence the need to define the most suitable ageing tests arises whenever resistant and compatible conservative materials are designed. In literature, most of field trials were performed to study damage mechanisms on building materials induced by weathering or pollutants (Zappia et al., 1998; Viles et al., 2002; Urosevic et al., 2012) or to evaluate new products' performance through their application directly on historic damaged substrate, with the risk to be sometimes unsuitable and irreversible applications (Favaro et al., 2005, 2006, 2007; Varas et al., 2007). On the contrary, field tests on model samples allow to evaluate the features of the examined product in response to different environmental conditions and to improve its performance without any damage to the works of art. Nevertheless, still scarce examples of published results on this issue are available (Simon and Snethlage, 1996).

In this paper we discuss the results obtained by performing field tests of model samples in Carrara marble exposed at four European monuments (Santa Croce Basilica in Florence, Cologne Cathedral, Oviedo Cathedral and Stravopoleos Monastery in Bucharest) in order to study the compatibility and environmental durability of the consolidating product developed within the EC Project NANOMATCH (Bernardi et al., 2012). The product's performance is also tested in comparison to CaLoSiL® and its consolidating use in the conservation of cultural heritage discussed. Because of the rising role of climate parameters in causing damage to heritage building materials and the expected increase of surface recession of carbonate stones due to rainfall, the samples under study were placed in unsheltered areas directly exposed to precipitation events. The integration of the results here presented with those carried out in laboratory as part of the EC NANOMATCH Project provided complete information on applicability, compatibility, efficiency and durability of the tested conservative products and allowed to identify and subsequently manage the possible drawbacks before their application on works of art.

2. Materials and methods

2.1. Investigated conservative products

Preliminary tests and application trials were performed to identify the proper alkaline earth alkoxide among those synthesized for consolidating carbonate stones to evaluate the most suitable methodology for its production at industrial scale and to optimize the application parameters (Favaro et al., 2008; Duchêne et al., 2012; Ossola et al., 2012; Favaro et al., 2014; Natali et al., 2015). The best results were obtained with nano-solution of calcium tetrahydrofurfuryloxide (Ca(OTHF)2) (NANOMATCH1) in 1:1 ethanol:ligroin at 20 g/L of calcium, applied by brush on quarried Carrara marble samples for two times on one surface (Natali et al., 2015). In order to compare the performance of the new consolidating agent, CaLoSiL® (IBZ-Salzchemie GmbH & Co.KG), product widely employed for stone consolidation, was selected and applied by brush on other samples. In CaLoSiL®, particles of calcium hydroxide were dispersed in ethanol at 20 g/L of calcium. The consolidating effect of these products is produced by calcium carbonate, obtained by the reaction of calcium hydroxide and calcium alkoxide with atmospheric moisture and carbon dioxide. Since both NANOMATCH1 and CaLoSiL® are precursors for the deposition of calcium carbonate, they could be effectively employed to treat carbonate substrates.

2.2. Field tests

We tested the compatibility and environmental durability of NANOMATCH1 and CaLoSiL® on Carrara marble, a metamorphic stone primarily composed of calcite crystals. Polished marble plaques with dimensions of 10 cm × 10 cm × 5 cm were placed outdoor in an unsheltered area, exposed to rain wash-out, in four European sites characterised by different meteorological and climatological conditions:

- Santa Croce Basilica in Florence (Italy);
- Cologne Cathedral (Germany);
- Oviedo Cathedral (Spain);
- Stavropoleos Monastery in Bucharest (Romania).

A stainless metallic rack, perforated and tilted with 30° slope, supported the samples and allowed the drainage of rainwater (Fig. 1). Field trials lasted for eleven months in each site, from April/May 2013 to March/April 2014.

In order to obtain a stone substrate characterised by a heavy intergranular decohesion, part of samples was previously artificially damaged by thermal stress (i.e. exposed at 600 °C for 1 h), which led to a total structural disintegration of Carrara marble (Bourguignon et al., 2014). Indeed, the anisotropy of calcite in thermal response leads Carrara marble to be affected by thermoclastism and therefore to granular

Fig. 1. Carrara marble model samples exposed on the rack at Santa Croce Basilica, Florence.

disaggregation and material exfoliation (Bonazza et al., 2009b). The experimental exposure included the evaluation and comparison of Carrara marble samples (i) sound (undamaged), (ii) artificially damaged by thermal stress, (iii) damaged and treated with NANOMATCH1 and (iv) damaged and treated with CaLoSiL®. An overall description of the methodological approach adopted is given by Natali et al. (2015), which reports also some of the preliminary results obtained.

2.3. Climatological characterisations of sites

The sites selected for exposure tests of stone models are characterised by different environmental conditions. All of them are urban areas and therefore their atmospheric composition is influenced by the gases and aerosol, including nanoparticles, emitted by stationary and mobile combustion sources (vehicular traffic, domestic heating/cooling systems and industries). Yearly air quality data for each site are reported in Natali et al. (2015). Following the Köppen-Geiger's climate classification (Kottek et al., 2006), Florence has a humid subtropical climate (Cfa), slightly influenced by the Mediterranean one (Csa). Precipitations are more pronounced in the intermediate seasons and in winter while the summer is dry (http://worldweather.wmo.int/); relative humidity values fluctuate between 65% and 76%. Cologne and Oviedo are characterised by warm damp temperate climate with warm summer (Cfb) (Kottek et al., 2006). Precipitations are abundant throughout the year and lead the average value of relative humidity to remain always above 75% (http://www.climatemps.com/). Bucharest belongs to the warm damp temperate climate with hot summers (Cfa) (Kottek et al., 2006) since the presence of the Carpathians Mountains (northward) and of the Black Sea (southward) mitigate the humid continental climate typical of south-eastern Europe. Precipitations are frequent in spring and modest during the other seasons; mean relative humidity therefore ranges from 65% to 85%.

During the eleven months of field tests, Florence and Bucharest showed the same temperature range in summer, with August as the hottest month (high average daily temperature of 31–33 °C), while in winter the Romanian city is cooler (reaching 12 consecutive days with temperatures strictly below freezing from the end of January and the beginning of February and simultaneously recording many snowfalls) (https://weatherspark.com/). Cologne and Oviedo show a general lower temperature in summer than the previous cities while considering the cool season Oviedo displays the mildest winter among all the exposure sites, hardly reaching the 0 °C. As reported by Natali et al. (2015), Florence and Oviedo experienced the highest monthly rain amounts (respectively 144 mm in October in Florence and 152 mm in November in Oviedo) as well as the highest cumulative amounts during the exposure period (both around 820 mm); the total mm of rainfall are lower in Cologne (460 mm) and Bucharest (275 mm). Moreover, the number of events of heavy rain (i.e. when precipitation rate is equal or >25 mm/day following Bradley and Jones, 1995) particularly hazardous for the preservation of carbonate stone were also taken into consideration. During the eleven months of exposure, Florence experienced 5 *heavy rain events* mainly during winter months, and 12 *medium rain events* (i.e. when rain rate is between 10 and 25 mm/day following Bradley and Jones, 1995) spread in summer (http://www.weatheronline.co.uk/). Also Oviedo was characterised by 8 *heavy rain events* during the exposure time, sometimes more than one per month. By contrast, these events turned out few (3) but intense in Bucharest, reaching even 70 mm/day, while almost absent in Cologne (http://www.weatheronline.co.uk/).

2.4. Analytical techniques

During the research work we investigated (i) the aesthetical properties (ii) surface cohesion of treated samples (iii) the distribution of the consolidants (iv) their surface penetration and interactions with both Carrara marble substrates and environmental agents by means of the following analyses:

- Quantitative colour evaluation of samples carried out by a portable spectrophotometer Konica Minolta CM-700d to measure CIE$L^*a^*b^*$ coordinates for the definition respectively of luminosity (L^*) and chromaticity coordinates (a^* and b^*) according to the UNI 8941: 1987 Standard Colored surfaces (1987). The data here presented are the average values of measurements repeated three times on the same selected area. The total colour difference (ΔE^*) between two measurements has been calculated from CIEL*a*b* coordinates $\Delta E^* = [(\Delta L^*)^2 + (\Delta a^*)^2 + (\Delta b^*)^2]^{½}$, and its perception by human sight and the threshold of acceptability was evaluated according to the classification supplied by Miliani et al. (2007).
- Optical Microscopy (OM) and Scanning Electron Microscopy coupled with Energy Dispersive X-ray spectroscopy (SEM-EDX) to investigate the morphology and microstructure of samples as well as the distribution of the applied conservative products. Observations of polished cross and thin sections of samples were performed by using a petrographic microscope Olympus BX 51 equipped with a scanner PRIMOPLUS 32. SEM-EDX investigation was carried out with a ZEISS 1530 instrument equipped with a dispersive X-ray analyser on bulk samples and polished cross sections coated with a thin gold layer.
- Scotch Tape Test (STT) or "peeling test" following the standard protocol procedure published by Drdácký et al. (2012) for the quantitative assessment of the cohesion of samples surface. Pressure-sensitive tape was applied at the investigated area and the amount of the material detached from the surface after the tape removal was quantified by weight. Each test was repeated 10 times in the same area of the selected stone sample. Moreover, two different areas in the same sample have been selected for the test to be conducted before and after exposure.
- Capillary water absorption measurement performed according to the standard UNI EN 15801:2010, 2010, in order to evaluate the amount of water absorbed by a specimen per surface unit (Q_i) over time. Q_i (kg/m^2) is defined as $Q_i = (m_i - m_0) / S$ where S is the surface of the specimen in contact with water, m_i and m_0 are the weights of the specimens measured during the test at time t_i and t_0 respectively. The capillary water absorption coefficient (WAC) is the slope of the linear section of the curve obtained plotting the mass change per area (Q_i) versus the root of time ($t_i^{1/2}$).
- Ultrasonic pulse velocity determination, carried out in accordance with the standard EN 14579, 2004, was measured using ultrasonic non-destructive digital indicator tester (PUNDIT) with an emitting frequency of the instrument transducer of 60 kMHz and a measurement resolution of 0.1 μs. The measurement was conducted in direct mode putting the two probes on two parallel surfaces of specimens (one treated and the opposite), where a thin layer of oil is previously applied to optimize the contact between the specimen and the probe. For each specimen the measurement has been carried out three times and the average results with the relative standard deviation have been reported.

Samples were analysed before treatment, after treatment/before exposure and after eleven months of exposure in order to investigate the surface properties and cohesion, as well as to estimate the extent of the penetration for both the conservative products, considering their interactions with marble substrate and environmental conditions. In addition, results obtained by analysing treated samples before exposure were compared with those obtained on sound and artificially damaged samples in order to verify the potential improvement of the physical-mechanical properties after treatment and the aesthetical compatibility of the treatment as well.

3. Results and discussion

3.1. Colorimetric characterisation of samples

The granular disintegration of marble samples due to thermal stress led to a general increase of all colorimetric parameters, causing a variation in total colour visible by human sight and above the threshold of

Table 1
Variation of colorimetric CIE$L^*a^*b^*$ parameters and of total colour (ΔE^*) between 1) artificially damaged samples and sound ones (before exposure); 2) treated samples and artificially damaged ones (before exposure); 3) treated samples after and before exposure.

			Florence	Cologne	Oviedo	Bucharest
Art. damaged samples - sound samples (before exposure)	AL*		6.44	4.16	4.65	6.38
	Aa*		0.94	0.86	0.97	0.60
	Ab*		2.31	3.13	3.74	1.98
	AE*		6.92	5.27	6.04	6.71
Treated samples - art. damaged (before exposure)	AL*	NANOMATCH1	−0.10	−0.49	−0.59	−0.29
		CaLoSiL®	0.20	0.31	0.73	2.44
	Aa*	NANOMATCH1	−0.20	0.01	−0.24	−0.01
		CaLoSiL®	0.06	0.40	0.03	0.01
	Ab*	NANOMATCH1	0.87	1.02	0.80	1.21
		CaLoSiL®	−2.22	0.53	−1.17	−1.60
	AE*	NANOMATCH1	0.92	1.14	1.02	1.25
		CaLoSiL®	2.40	2.12	1.38	2.92
Treated samples after exposure – treated samples before exposure	AL*	SOUND	1.64	0.52	1.16	−3.05
		ART. DAMAGED	−4.19	−5.19	−4.88	−9.26
		NANOMATCH1	−3.81	−3.23	−4.61	−6.45
		CaLoSiL®	−1.08	0.04	−2.76	−4.00
	Aa*	SOUND	0.38	0.25	1.33	0.52
		ART. DAMAGED	0.78	0.42	0.93	0.73
		NANOMATCH1	0.83	0.25	0.93	0.49
		CaLoSiL®	0.02	−0.38	0.27	0.09
	Ab*	SOUND	0.94	1.02	1.33	2.15
		ART. DAMAGED	4.26	1.54	1.62	3.22
		NANOMATCH1	2.46	−0.05	1.50	1.00
		CaLoSiL®	2.76	−0.98	2.42	1.59
	AE*	SOUND	1.93	1.17	1.85	3.77
		ART. DAMAGED	6.03	5.43	5.22	9.83
		NANOMATCH1	4.62	3.42	4.94	6.54
		CaLoSiL®	2.98	2.43	4.25	1.56

acceptability (i.e. $\Delta E > 5$) (Miliani et al., 2007), as shown in Table 1, where the results of all the variation of colorimetric CIE$L^*a^*b^*$ parameters and of total colour (ΔE^*) are summarized. In particular, artificially damaged samples showed a whitening effect ($\Delta L^* > 0$) induced by an increase in surface reflectivity and a shift toward the yellow component ($\Delta b^* > 0$). Analysing data acquired after the application of conservative products, NANOMATCH1 entails a small increase in the yellow component while CaLoSiL® induces a slight whitening of samples surface. In any case, the average values of the total colour differences calculated using colour parameters collected after and before consolidation treatments do not exceed the threshold value of acceptability, showing values below 3 units (Miliani et al., 2007).

The influence of environmental parameters on the chromatic appearance of marble samples was assessed inspecting colour measurement performed after in situ exposure.

Considering samples after and before exposure, Fig. 2 displays that marble artificially damaged exposed at each site shows a visible change in total colour ($5 < \Delta E^* < 10$) that is attenuated by the consolidation treatment. In particular samples treated with CaLoSiL® show $1 < \Delta E^* < 4$ while those treated with NANOMATCH1 present $3 < \Delta E^* < 5$, with the exception of the sample exposed in Bucarest ($\Delta E^* = 7$). Overall, the total colour variation of treated samples remains below the threshold of acceptability (i.e. $\Delta E < 5$) in Florence, Oviedo and Cologne. Analysing the single CIE$L^*a^*b^*$ parameters, the exposure of treated samples led to a slight increase in luminosity and to a small shift of b^* parameter toward the blue component in respect to samples artificially damaged, thus becoming more similar to sound samples.

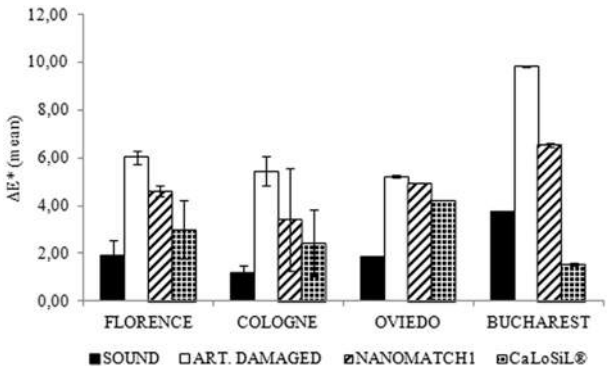

Fig. 2. Mean variation of total colour (ΔE^*) of stone samples exposed for eleven months compared with samples before exposure.

3.2. OM and SEM observations

OM and SEM investigation evidenced the intra and inter granular decohesion of marble samples as consequence of the thermal stress. The formation of cracks between grains and along their outlines is clearly visible in Fig. 3.

After the application, both NANOMATCH1 and CaLoSiL® were found to cover samples surface with a rather homogeneous layer but neither of them showed deep penetration inside fractures, remaining mainly

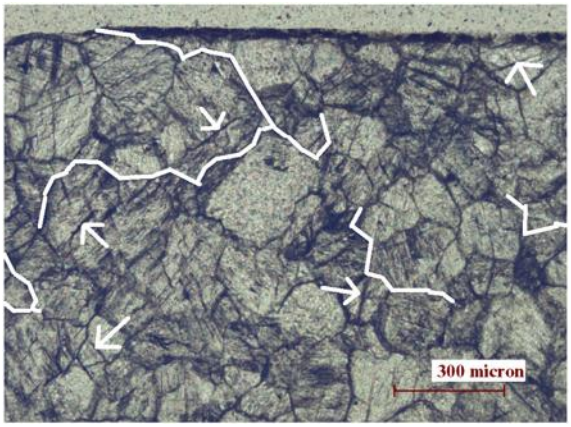

Fig. 3. Micrographs (OM) of thin section in plane polarised light of artificially damaged sample. White arrows indicate intragranular fractures and white lines highlight the presence of intergranular fractures of Carrara marble sample.

on surface or occasionally in the first micrometers of superficial chinks (Fig. 4).

By optical microscopy NANOMATCH1 appeared to be homogeneously distributed on samples surface, with a thickness of about 20–30 μm, which increases where marble surface presents cavities (Fig. 5a). In particular, SEM investigation highlighted that NANOMATCH1 displays a cracked surface (Fig. 4a) similar in the aspect to those formed by TEOS (tetraethoxysilane) based products when applied on stones. TEOS cracked layers on stone surfaces have been observed and extensively described in literature (Miliani et al., 2007; Mosquera et al., 2009). They are typically associated to the TEOS sol gel process in which two reactions (hydrolysis and consequent condensation) take place leading to the formation of a gel in which the solvent is trapped within the silica based network (Mosquera et al., 2009). The cracking occurs during the drying process as consequence of high capillary pressures supported by the gel network. Peruzzo et al. (2016) reviewed the sol gel process occurring in presence of mixture of alkoxides making a detailed description of results obtained by Mass Spectrometry for silicon alkoxides, titanium alkoxides, silicon/titanium alkoxides, germanium alkoxides, tin alkoxides. The formation of a xerogel for NANOMATCH1 after the complete evaporation of the solvent can be hypothesized although any evidences of copolymerization nor sol gel processes for calcium alkoxides are reported (Peruzzo et al., 2016; Turova et al., 2002).

The consolidation with CaLoSiL® caused instead the formation of a compact layer on all the surface of samples (Fig. 5b). This layer, generally thicker than that created by NANOMATCH1 application, was detected to reach a maximum thickness of about 40 μm in the hollowed areas of the surface.

Observations by OM and SEM conducted on not treated samples after the exposure in situ displayed calcite grains highly fragmented with rough surface particularly for samples artificially damaged exposed in Oviedo (Fig. 6). In addition sporadic areas covered by a thin layer of secondary calcite were detected both on sound and artificially damaged samples (Fig. 7).

After eleven months of exposure, treated samples underwent a general reduction in the presence and distribution on the surface of both consolidants. Where present, they displayed a decrease in thickness and lost their flat surface, becoming rough and pitted. The loss of consolidants, particularly NANOMATCH1, occurred mainly in samples exposed in Florence and Oviedo, while in Cologne and Bucharest CaLoSiL® was found to remain rather homogeneously distributed (Fig. 8).

3.3. Surface cohesion characteristics (STT)

As already discussed, the thermal stress carried out on samples led to the disaggregation of marble grains caused by the anisotropic behaviour of calcite. A reduction of the cohesive properties is therefore assumed and the amount of material peeled from the surface could be linked to surface cohesive properties of the stone. Taking into account that (i) even a non-consolidated stone may exhibit a decrease in the amount of removed material due to the higher cohesion of the material in the bulk (Drdácký et al., 2012) and (ii) the early peelings might remove dust and not penetrated consolidant, even so the peeling test can give information of cohesive surface properties if the entire trends referred to different sets of samples are compared.

The reduction of the cohesive properties of the samples artificially damaged linked to the disaggregation of marble grains caused by thermal stress was highlighted by the Scotch Tape Test trough an enhancement of the material peeled from the surface of all damaged samples in respect to that removed from sound samples. Following the results obtained by STT it can be also hypothesized that the treatment with both consolidants implied a general increase of cohesion of surface stone samples since the amount of material released from the surfaces of all consolidated samples is lower than that measured from samples subjected to artificial damage. In particular, Fig. 9 displays the weight difference between the quantity of material peeled from the surface of treated samples before exposure and that removed from the surface of artificially damaged samples before exposure (ΔW), showing a higher cohesive behaviour of NANOMATCH1 product (black dots) in respect to CaLoSiL® (white dots).

In Fig. 10 the difference of the amount of incoherent material peeled from the surface of exposed samples at the 4 sites with those removed from samples surface before exposure (ΔW) is presented. Following these results it may be argued that the exposure to the environment of the four European sites caused similar modification of the surface

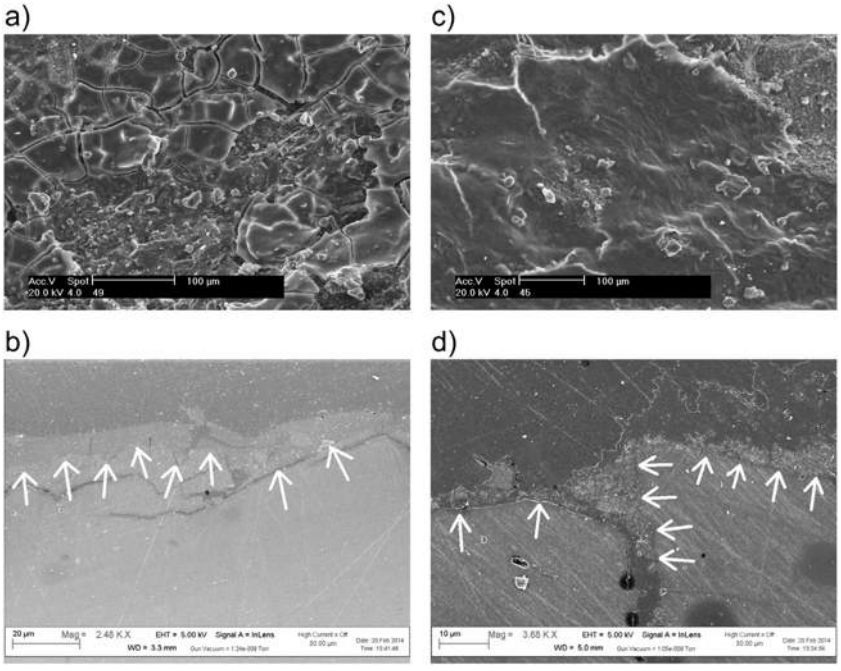

Fig. 4. SEM micrographs of marble samples treated with: NANOMATCH1 product before exposure, bulk sample (a) and polished cross section (b); CaLoSiL® before exposure, bulk sample (c) and polished cross section (d). White arrows highlight the distribution of the consolidants on samples.

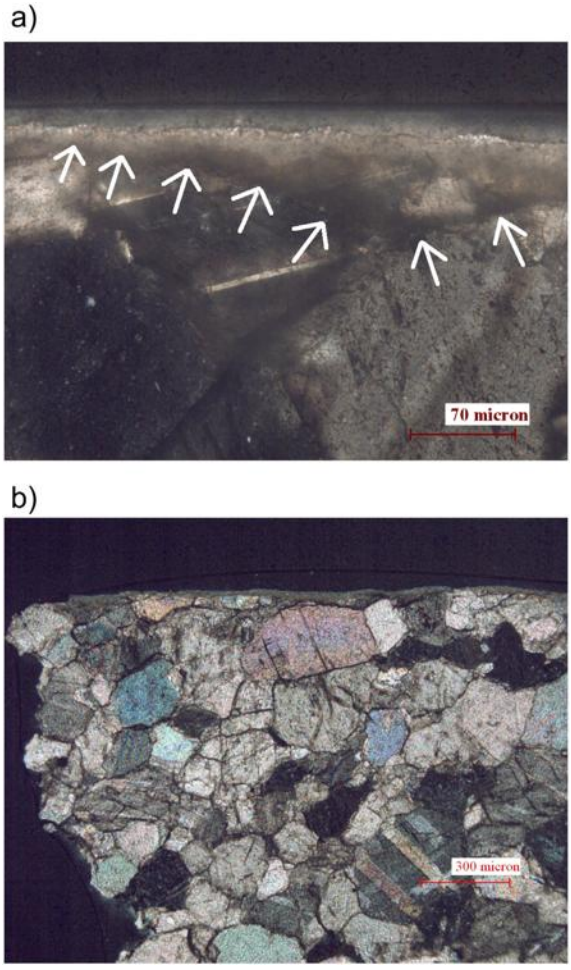

Fig. 5. a) Optical micrographs of thin sections in cross polarised light of sample treated with NANOMATCH1: white arrows indicate the distribution of the surface microcrystalline layer formed after the consolidating treatment. b) Optical micrographs of thin sections in cross polarised light of sample treated with CaLoSiL®.

cohesion in the same classes of samples and a general slight increase in the surface cohesive properties. Specifically, artificially damaged samples show the highest improvement of surface cohesion while the cohesive properties of sound samples and of those treated with CaLoSiL® slightly increase or remain equal to values measured before exposure. On the contrary, the exposure seems to have caused a slight reduction in cohesion of the most superficial part of samples treated with

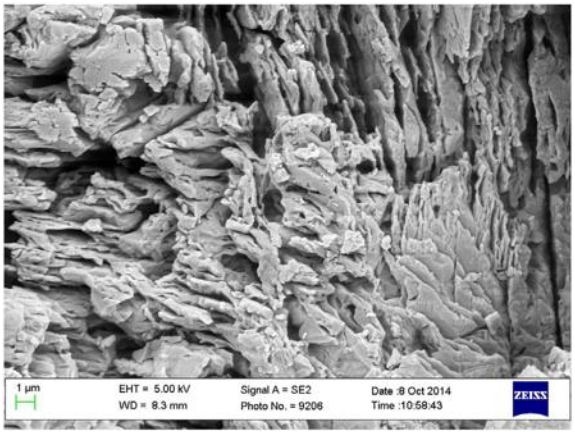

Fig. 6. SEM micrographs of artificially damaged marble sample after exposure in Oviedo.

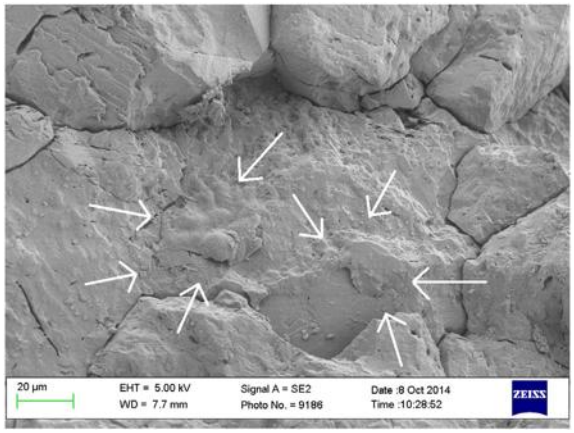

Fig. 7. SEM micrographs of undamaged marble sample after exposure in Oviedo. White arrows highlight the presence of secondary calcite.

NANOMATCH. It can be hypothesized that part of the consolidant surface layer was detached, not adhering to the substrate and therefore removed by the tape during the early peeling.

As evidenced by Drdácký et al. (2012) results of STT can yield to contradictions in the interpretation if not performed in a standardized way and are to be considered reliable only for surface and near-surface layers of the investigated material. Even though the results here presented cannot be ascribed to an effective cohesion or not of the samples in its entirety, the application of the standard protocol published by Drdácký et al. (2012) ensures a correct and reliable understanding of

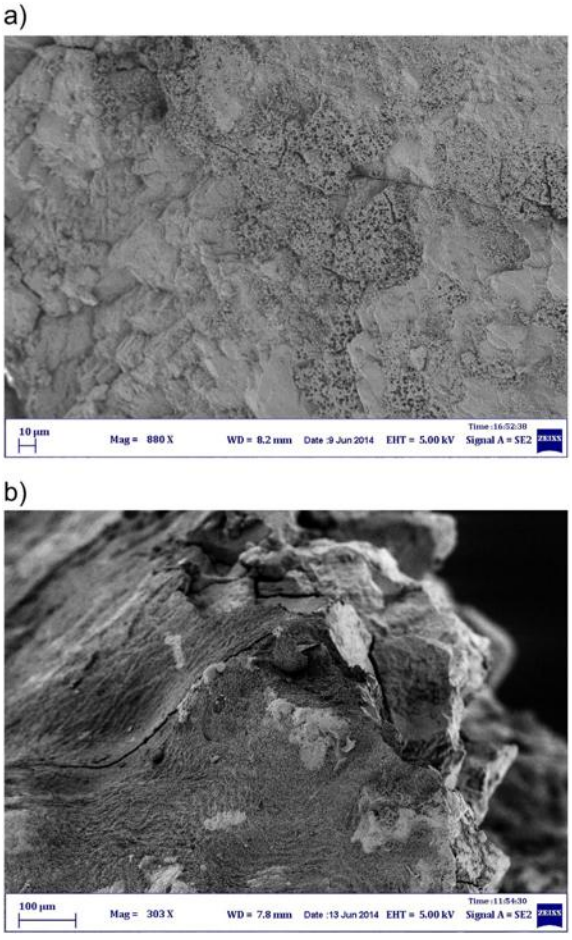

Fig. 8. SEM micrographs of marble samples treated with: a) NANOMATCH1 product after exposure in Florence (bulk sample); b) CaLoSiL® after exposure in Cologne (bulk sample).

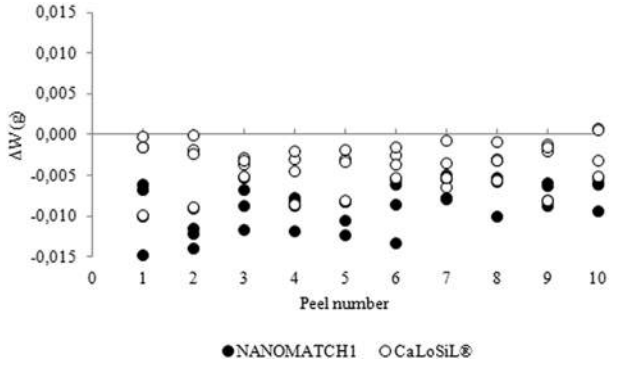

Fig. 9. Weight difference between material peeled from the surface of samples treated with NANOMATCH1 and that removed from the surface of artificially damaged samples (black dots). Weight difference between material peeled from the surface of samples treated with CaLoSiL® and that removed from the surface of artificially damaged samples (white dots). The evaluation considers the samples addressed to all the European exposure sites.

the surface cohesion characteristics of the specimens. Having been the Carrara marble samples treated on one surface by brush application of the consolidating agents, the STT results here presented are to be used for an evaluation of the surface consolidation and strengthening efficiency of the tested treatments.

3.4. Capillary water absorption

Capillarity water absorption test was performed on: i) sound and artificially damaged specimens before and after the exposure; ii) samples artificially damaged and treated with NANOMATCH1 and CaLoSiL® after the exposure. The amount of water (Qi) absorbed by specimens exposed in the sites of Florence, Cologne and Oviedo is reported in Fig. 11.

Comparing the test results, it is evident that sound specimens absorb less water before than after exposure. Results related to the specimens before exposure show that artificially damaged samples absorb ten times higher amount of water than the sound ones. It is well known that the higher quantity of water taken up is related to the higher open porosity: the additional porosity of damaged specimens disaggregated by thermal stress, as observed by OM and SEM, increases the capillary water absorption. Concerning the effect of consolidation of both tested products, results executed in laboratory as part of the EC

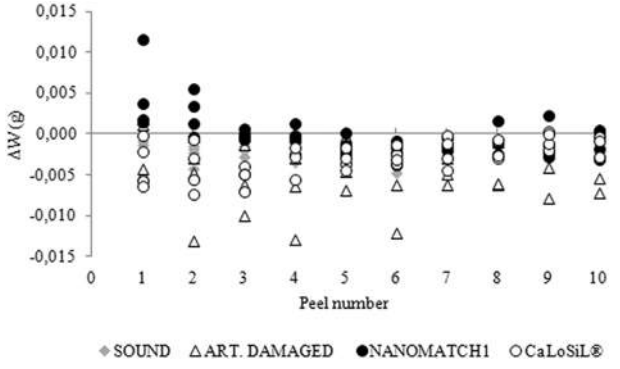

Fig. 10. Weight difference between material peeled from the surface of sound samples after exposure for eleven months in the four European sites and that removed from sound samples before exposure (grey rhombuses). Weight difference between material peeled from the surface of artificially damaged samples after exposure in the four European sites and that removed from artificially damaged samples before exposure (white triangles). Weight difference between material peeled from the surface of samples treated with NANOMATCH1 after exposure in the four European sites and that removed from the same samples before exposure (black dots). Weight difference between material peeled from the surface of samples treated with CaLoSiL® after exposure in the four European sites and that removed from the same samples before exposure (white dots).

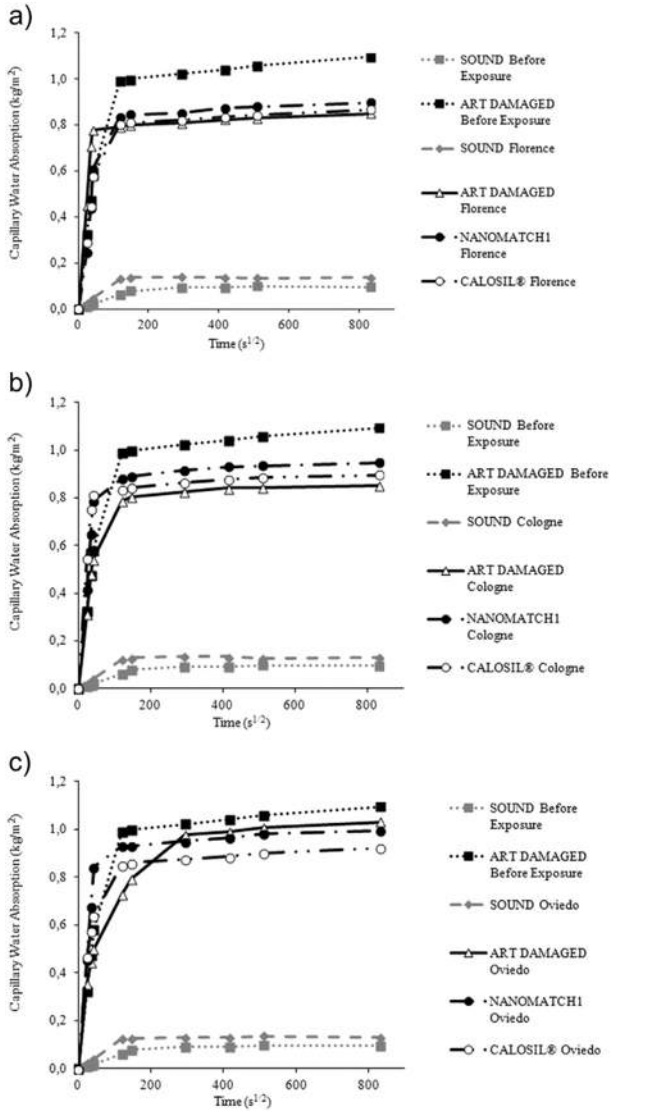

Fig. 11. Capillarity water absorption results referring to: sound and artificially damaged samples before exposure (grey and black squares respectively), sound (grey rhombuses), artificially damaged (white triangles), treated with NANOMATCH1 (black dots) and treated with CaLoSiL® (white dots) samples after exposure in Florence (a), Cologne (b) and Oviedo (c).

NANOMATCH Project demonstrated that the treated specimens presented absorption behaviour ($WAC_{Average} = 0.034$ kgm^{-2} s$^{-0.5}$ for NANOMATCH1 and $WAC_{Average} = 0.027$ kg m^{-2} s$^{-0.5}$ for CaLoSiL®) fairly similar to the artificially damaged samples ($WAC_{Average} = 0.029$ kg m^{-2} s$^{-0.5}$, Bourguignon et al., 2014). Comparing the water absorption capillarity of samples before and after exposure, artificially damaged specimens absorb in general less water after than before exposure, with a similar trend regardless the different site of exposure. This finding is congruent with the STT results obtained, for this class of samples, which highlighted an increase of surface cohesion. Moreover, the outcomes indicate that the different exposure site as well as the conservative products applied (both NANOMATCH1 and CaLoSiL®) do not significantly influence the capillary water absorption. Treated samples with both consolidants exposed in each site show a similar trend of water capillarity absorption.

3.5. Ultrasonic velocity

As for capillarity water absorption test, ultrasonic velocity was performed on: i) sound and artificially damaged specimens before and

after the exposure; ii) samples artificially damaged and treated with NANOMATCH1 and CaLoSiL® after the exposure in Florence, Cologne and Oviedo. The obtained results (Table 2) evidenced a decrease in ultrasonic velocity in the artificially damaged samples (V_{Avg} = 1433 m s^{-1}) with respect to the sound ones (V_{Avg} = 6130 m s^{-1}) before exposure. The measured values after thermal stress indicated that the samples underwent a total structural disintegration following the scale established by Köhler (1988). After the consolidating treatments, average ultrasonic velocity values equal to 1389 m s^{-1} for samples treated with NANOMATCH1 and 1308 m s^{-1} for those treated with CaLoSiL® were detected, slightly lower than those encountered for artificially damaged ones. The measurements for the freshly treated samples here reported were carried out as part of the tests conducted in laboratory within the framework of the EC Project NANOMATCH (Bourguignon et al., 2014). Following the execution of these analyses it has been evidenced higher velocity values near the treated surface with respect to the opposite untreated surface of the samples, which has been interpreted by the Bourguignon et al. (2014) at a first glance as caused by the different content of consolidant in the samples. Nevertheless, since this gradient was also found in artificially damaged samples, it cannot be linked exclusively to a different penetration of the consolidant, but textural inhomogeneity of the stone should also be considered as possible cause. Additionally, Bourguignon et al. (2014) pointed out that the difficulty in drawing sure interpretation concerning the penetration depth of consolidation treatments using ultrasonic velocity measurements is particularly exacerbated when dealing with very low porous lithotype as Carrara marble, even if damaged by thermal stress. After exposure sound samples present a slight decrease in ultrasonic velocity at all analysed sites (V_{Avg} = 5475 m s^{-1}), with values still characteristic of a quarry fresh marble following the scale established by Köhler (1988). This result is in accordance with the study done by Simon and Snethlage (1996)within the framework of the EUROCORE-EUROMARBLE exposure programme, who highlighted how the ultrasonic velocity of the bulk marble material may respond sensibly to the environmental impact in unsheltered conditions already after few months of exposure, even though surface morphological features and colour of stones are more rapidly influenced by environmental conditions being the ultrasonic velocity determined by the internal grain and pore structure. Additionally, they found that marbles with coarse-grained (e.g. Lass marble) presented almost no reduction in ultrasonic velocity because of the exposure, while slight decreases were detected for Carrara marble.

Concerning our results, a decrease was found for artificially damaged samples, particularly evident for those samples exposed in Oviedo, which present V_{Avg} = 584 m s^{-1}. Velocity decreases also for all samples treated with both consolidants exposed in Florence and Oviedo, while a slight increase is detected for specimens treated with NANOMATCH1 placed in Cologne. It should be pointed out that as a general rule, a scattering of at least 0.5 km s^{-1} should be admitted before changes of us-velocity can be ascribed to enhanced weathering (Sheremeti-Kabashi and Snethlage, 2000).

Table 2
Ultrasonic velocity measured in Carrara marble samples. V_1, V_2, V_3 (m s^{-1}) indicate three different measurements carried out on the same samples and their average value is expressed as V_{Avg} (m s^{-1}). Standard deviation (s.d.) is also reported.

SAMPLE	V_1 (m s^{-1})	V_2 (m s^{-1})	V_3 (m s^{-1})	V_{Avg} (m s^{-1})	s.d.
Sound_before exposure	6098	6410	5882	6130	265.4
Art. damaged_before exposure	1441	1453	1405	1433	24.9
Sound_Cologne	5484	5313	5313	5370	98.9
Sound_Florence	5426	5484	5484	5464	33.7
Sound_Oviedo	5568	5568	5632	5590	37.0
Art. damaged_Cologne	1302	1323	1295	1307	14.3
Art. damaged_Florence	1345	1273	1319	1312	36.1
Art. damaged_Oviedo	589	584	580	584	4.7
NANOMATCH1_Cologne	1443	1431	1435	1436	6.2
NANOMATCH1_Florence	1158	1216	1189	1188	28.8
NANOMATCH1_Oviedo	944	939	946	943	3.6
CaLoSiL®_Cologne	1416	1333	1302	1351	59.1
CaLoSiL®_Florence	1129	1116	1142	1129	12.7
CaLoSiL®_Oviedo	1126	1121	1111	1120	7.8

3.6. Significance of changes at the stone surface due to environmental impact

The analyses conducted under microscope pointed out that in spite of the granular disaggregation caused by thermal stress on Carrara marble samples, both consolidating products remained mainly at the surface of the samples creating an homogeneously distributed layer with higher thickness and compactness in the case of CaLoSiL®. This finding is consistent with the outcomes of the tests performed in laboratory within the framework of the EC project NANOMATCH for verifying the penetration depth of both consolidating agents on diverse lithotypes, including Carrara marble which was found to have a very low overall absorption even if decohesionated (Bourguignon et al., 2014).

The new surface layer formed after the application did not imply negative consequences on the colorimetric parameters with ΔE^* values not exceeding the threshold of acceptability. In spite of the negligible improvement of cohesion of the treated samples in their entirety, detected by ultrasonic velocity measurements, a surface consolidation was achieved as shown by the "peeling test".

The exposure in situ in unsheltered conditions to precipitation impact implied a weathering of all classes of exposed samples causing aesthetic changes generally below the threshold of acceptability, with the exception of the sample treated with NANOMATCH1 exposed in Bucharest, and a loss of the consolidating layers evident mainly in the specimens placed in Florence and Oviedo. Where still present they displayed under scanning electron microscope a clearly weathered morphology and rough and pitted surface. A direct relation between the increase of roughness and loss of material in carbonate stones, mainly low porous, with the rain impact have been evidenced by several authors (Viles, 1990; Simon and Snethlage, 1996; De, 2003; Sabbioni, 2003; Camuffo, 2013). Moreover, the surface recession caused by rain impact, including its clean and acid contribution, has been widely studied and several models and functions have been proposed for its quantification (Lipfert, 1989; Baedecker, 1990; Livingston, 1992; Webb et al., 1992; Tidblad et al., 2001; Kucera et al., 2007). In reviewing the existing functions, performed with the aim of their application for the production of scenarios of climate change impact on the surface recession of marble and limestone, Bonazza et al. (2009a) underlined the driving role of clean rain (the so-called karst effect) in determining the quantity of materials loss due to precipitation. This weathering phenomenon is naturally exacerbated in polluted areas because of an additional rain acidity due to the presence of sulfuric and nitric acid and of the dry deposition of gaseous pollutants (SO_2 and NO_X). In addition to the chemical dissolution process, the mechanical effect of rain needs also to be taken into consideration, which may significantly increase the surface recession especially in porous carbonate materials with high surface roughness during events of heavy precipitation (Camuffo, 2013). Simon and Snethlage (1996) during the EUROCORE-EUROMARBLE exposure programme found that the interaction between carbonate stones and incident rainfall produces clear morphological alterations even within a short term of exposure and higher rates of surface recession are found in sites affected by highest annual precipitation amount. Our results are in line with these outcomes having evidenced a major loss of consolidating agents in those sites characterised by the highest monthly rain amounts and frequency of heavy rain events (Florence and Oviedo). As both NANOMATCH1 and CALOSIL® are precursor of calcium carbonate, calcite and vaterite are the only two possible mineral phases expected to crystallize within stone porosity following their application, making them susceptible to chemical dissolution by rainfall. Besides the dissolution of the carbonate matrix, it is widely known

that as consequence of rainfall impact, precipitation of secondary calcite can occur as the water evaporates at the surface with formation of new low porous and hard calcareous crusts (calcrete) on carbonate stones (Dever et al., 1987; Cassar, 2002) Rainwater saturated with carbon dioxide acts in fact as an acid dissolving calcite and then redeposits it as a precipitate on the surfaces of the soil particles. The formation of a layer of secondary calcite observed by scanning electron microscope (Fig. 7) may be reasonably attributed to this phenomenon and constitutes a reliable explanation of the slight increase in the surface cohesive properties of the exposed samples, particularly artificially damaged ones detected by the "peeling test".

4. Conclusions

As consequence of the predicted increase over the 21st century of surface recession on carbonate materials, a deep understanding of the performance of conservative products in responding to environmental impact is essential for setting up suitable strategies of cultural heritage safeguard.

By performing filed exposure tests, the work presented allowed to investigate the effect of climate parameters, particularly rainfall, on Carrara marble in different state (quarry fresh, total structural disaggregated, treated with NANOMATCH1 and CaLoSiL®) exposed in four European sites with diverse environments. The conditions of exposure were set up and the analyses selected and conducted with the main purpose of exploring the surface changes occurring on Carrara marble samples i) after the application of the consolidating products and ii) before and after exposure. Moreover the innovative consolidating product synthetized in the framework of the EC Project NANOMATCH was tested in field.

Both conservative products were found to remain mainly on surface and did not penetrate deeply in the substrate. This implied only a surface cohesion of samples pointing out that the examined products behaved as protectives agents or surfaces of sacrifice rather than consolidants.

Following the exposure in situ a loss of the consolidating layers was found mainly for the samples exposed in the sites characterised by the highest monthly rain amounts and frequency of heavy rain events.

Further investigations are suggested in order to improve the penetration of the products taking into consideration the best environmental conditions and techniques of application, the proper materials to be treated and the most appropriate solvent. Following our results in fact it may be argued that marble substrates are not suitable materials to be treated with the tested consolidants, while porous limestones should be perhaps preferred. Additional studies should be also carried out in order to better characterise NANOMATCH1 product as well as to clarify which processes lead to the formation of the cracked layer observed on stone surface by SEM technique.

Acknowledgements

The NANOMATCH Project (Nano-systems for the conservation of immoveable and moveable polymaterial Cultural Heritage in a changing environment) has received funding from the European Union's Seventh Programme for research, technological development and demonstration under grant agreement No [283182]. Authors express their gratitude to the NANOMATCH consortium for the fruitful discussions and support during the duration of the Project. Authors are also grateful to Dr. Cristina Sabbioni for her contribution in the revision of the final stage of the manuscript.

References

Amoroso, G.G., 2002. Trattato di scienza della conservazione dei monumenti: etica della conservazione, degrado dei monumenti, interventi conservativi, consolidanti e protettivi. Florence, ALINEA Editrice.

Ashley-Smith, J., Burmester, A., Eibl, M. (Eds.), 2013. Climate for Collections: Standards and Uncertainties. Postprints of the Munich Climate Conference; 2012 Nov 7–9. Archetype Publications Ltd, London.

Baedecker, P.A., 1990. Dose–response functions for the chemical erosion of carbonate stone. Effects of acidic deposition on materials. NAPAP Report 19 on Acidic Deposition: State of Science and Technology. National Acidic Precipitation Assessment Program, Washington, D.C.

Bernardi, A., Favaro, M., Nijland, T., García, O., Detalle, V., Wittstadt, K., et al., 2012. NANOMATCH: a European project to develop consolidants through the synthesis of new inorganic nanomaterials for the conservation of built heritage. In: Ioannides, M., Frittsch, D., Leissner, J., David, R., Remondino, F., Caffo, R. (Eds.), International Journal of Heritage in the Digital Era 1(1): Proceedings of Euromed 2012 International Conference on Cultural Heritage; 2012 Oct 29 – Nov 3; Lemesos, Cyprus, pp. 307–312 http://dx.doi.org/10.1260/2047-4970.1.0.307.

Bonazza, A., Messina, P., Sabbioni, C., Grossi, C.M., Brimblecombe, P., 2009a. Mapping the impact of climate change on surface recession of carbonate buildings in Europe. Sci. Total Environ. 407 (6), 2039–2050. http://dx.doi.org/10.1016/j.scitotenv.2008.10.067.

Bonazza, A., Sabbioni, C., Messina, P., Guaraldi, C., De Nuntiis, P., 2009b. Climate change impact: mapping thermal stress on Carrara marble in Europe. Sci. Total Environ. 407 (15), 4506–4512. http://dx.doi.org/10.1016/j.scitotenv.2009.04.008.

Bourguignon, E., Lubelli, B., Bernardi, A., 2014. Evaluation of Compatibility, Performance and Durability of Nano-structured Materials on Stone. Nanomatch Project No [283182]. Deliverable 3.2. http://www.nanomatch-project.eu.

Bradley, R.S., Jones, P.D. (Eds.), 1995. Climate since AD 1500 (Revised Edition). Routledge, London.

Camaiti, M., 2000. Consolidamento e protezione dei materiali inorganici: considerazioni generali sui prodotti e sulle tecniche di applicazione. Proceedings of Consolidanti e protettivi in uso sui materiali inorganici porosi di interesse artistico ed archeologico; 1999 Feb 25–27; Trento, Italy. Provincia Autonoma di Trento. Servizio Beni Culturali, Trento, pp. 10–47.

Camuffo, D., 2013. Microclimate for Cultural Heritage: Conservation, Restoration, and Maintenance of Indoor and Outdoor Monuments. 2nd ed. E-book; Elsevier Science.

Cassar, J., 2002. Deterioration of Globigerina limestone of the Maltese Islands. In: Siegesmund, S., Weiss, T., Vollbrecht, A. (Eds.), Natural Stone, Weathering Phenomena, Conservation strategies and Case Studies 205. Geological Society, Special Publications, London, pp. 33–49.

Chelazzi, D., Poggi, G., Jaidar, Y., Toccafondi, N., Giorgi, R., Baglioni, P., 2013. Hydroxide nanoparticles for cultural heritage: consolidation and protection of wall paintings and carbonate materials. J. Colloid Interface Sci. 392 (1), 42–49. http://dx.doi.org/10.1016/j.jcis.2012.09.069.

De, A.K., 2003. Environmental Chemistry. 5th ed. New Age International (P.) Limited Publishers, New Delhi.

Dever, L., Fontes, J.C., Riché, G., 1987. Isotopic approach to calcite dissolution and precipitation in soils under semi-arid conditions. Chem. Geol. Isot. Geosci. 66 (3–4), 307–314. http://dx.doi.org/10.1016/0168-9622(87)90050-9.

Doehne, E., Price, C.A., 2010. Stone Conservation: An Overview of Current Research. 2nd ed. Los Angeles, Getty Conservation Institute.

Drdácký, M., Lesák, J., Rescic, S., Slížková, Z., Tiano, P., Valach, J., 2012. Standardization of peeling tests for assessing the cohesion and consolidation characteristics of historic stone surfaces. Mater. Struct. 45 (4), 505–520. http://dx.doi.org/10.1617/s11527-011-9778-x.

Duchêne, S., Detalle, V., Favaro, M., Ossola, F., Tomasin, P., De Zorzi, C., et al., 2012. Nanomaterials for consolidation of marble and wall paintings. Proceedings of the 12th International Congress on the Deterioration and Conservation of Stone; 2012 Oct 22-26. ICOM-CC, New York. New York.

EN 14579, 2004. Natural Stone Test Methods - Determination of Sound Speed Propagation.

Favaro, M., Simon, S., Menichelli, C., Fassina, V., Vigato, P.A., 2005. The four virtues of the Porta della Carta, Ducal Palace, Venice: assessment of the state of preservation and re-evaluation of the 1979 restoration. Stud. Conserv. 50 (2), 109–127.

Favaro, M., Mendichi, R., Ossola, F., Russo, U., Simon, S., Tomasin, P., et al., 2006. Evaluation of polymers for conservation treatments of outdoor exposed stone monuments. Part I: photo-oxidative weathering. Polym. Degrad. Stab. 91 (12), 3083–3096. http://dx.doi.org/10.1016/j.polymdegradstab.2006.08.012.

Favaro, M., Mendichi, R., Ossola, F., Simon, S., Tomasin, P., Vigato, P.A., 2007. Evaluation of polymers for conservation treatments of outdoor exposed stone monuments. Part II: photo-oxidative and salt-induced weathering of acrylic silicone mixtures. Polym. Degrad. Stab. 92 (3), 335–351. http://dx.doi.org/10.1016/j.polymdegradstab.2006.12.008.

Favaro, M., Tomasin, P., Ossola, F., Vigato, P.A., 2008. A novel approach to consolidation of historical limestone: the calcium alkoxides. Appl. Organomet. Chem. 22 (12), 698–704. http://dx.doi.org/10.1002/aoc.1462.

Favaro, M., Chiurato, M., Tomasin, P., Ossola, F., El Habra, N., Brianese, N., et al., 2014. Calcium and magnesium alkoxides for conservation treatment of stone and wood in built heritage. In: Toniolo, L., Boriani, M., Guidi, G. (Eds.), Built Heritage: Monitoring Conservation Management. Springer, New York, pp. 413–422 http://dx.doi.org/10.1007/978-3-319-08533-3.

Franzen, C., Baldracchi, P., Colla, C., Esposito, E., Gaigg, G., Pfluger, R., et al., 2011. Assessment of historic structures by IRT. Proceedings of European Workshop on Cultural Heritage Preservation EWCHP-2011; 2011 Sept 26–28. Fraunhofer IRB Verlag, Berlin. Stuttgart.

Giorgi, R., Dei, L., Baglioni, P., 2000. A new method for consolidating wall paintings based on dispersions of lime in alcohol. Stud. Conserv. 45 (3), 154–161. http://dx.doi.org/10.1179/sic.2000.45.3.154.

Grossi, C.M., Brimblecombe, P., Harris, I., 2007. Predicting long term freeze-thaw risks on Europe built heritage and archaeological sites in a changing climate. Sci. Total Environ. 377 (2–3), 273–281. http://dx.doi.org/10.1016/j.scitotenv.2007.02.014.

Grossi, C.M., Bonazza, A., Brinblecombe, P., Harris, I., Sabbioni, C., 2008. Predicting twenty-first century recession of architectural limestone in European cities. Environ. Geol. 56 (3), 455–461. http://dx.doi.org/10.1007/s00254-008-1442-6.

Grossi, C.M., Brimblecombe, P., Menéndez, B., Benavente, D., Harris, I., Déqué, M., 2011. Climatology of salt transitions and implications for stone weathering. Sci. Total Environ. 409 (13), 2577–2585. http://dx.doi.org/10.1016/j.scitotenv.2011.03.029.

Köhler, W., 1988. Preservation problems of Carrara-Marble Sculptures in Postdam-Sanssouci ("Radical Structural Destruction" of Carrara-Marble). In: Ciabach, J. (Ed.), Proceedings of the 6th International Congress on Deterioration and Conservation of Stone; 12–14 Sept 1988. Poland, Torùn, pp. 653–662.

Kottek, M., Grieser, J., Beck, C., Rudolf, B., Rubel, F., 2006. World map of the Köppen-Geiger climate classification updated. Meteorol. Z. 15 (3), 259–263. http://dx.doi.org/10.5194/hess-11-1633-2007.

Kucera, V., Tidblad, J., Samie, F., Schreiner, M., Melcher, M., Kreislova, K., et al., 2005. Publishable Final Report of the EU 5FP RTD Project: Model for Multi-Pollutant Impact and Assessment of Threshold Levels for Cultural Heritage (MULTI-ASSESS). http://www.corr-institute.se/MULTI-ASSESS/.

Kucera, V., Tiblad, J., Kreislova, K., Knotkova, D., Faller, M., Reiss, D., et al., 2007. UN/ECE ICP materials dose–response functions for the multi-pollutant situation. In: Brimblecombe, P., Hara, H., Houle, D., Novak, M. (Eds.), Acid Rain—Deposition to Recovery. Sprinter, pp. 249–258.

Lipfert, F.W., 1989. Atmospheric damage to calcareous stones: comparison and reconciliation of recent experimental findings. Atmos. Environ. 23, 415–429.

Livingston, R.A., 1992. Graphical methods for examining the effects of acid rain and sulfur dioxide on carbonate stones. In: Delgado Rodrigues, J., Henriques, F., Telmo Jeremias, F. (Eds.), Proceedings of the 7th International Congress on Deterioration and Conservation of Stone; 15–18 June 1992. Portugal, Lisbon, pp. 375–386.

Melo, M.J., Bracci, S., Camaiti, M., Chiantore, O., Piacenti, F., 1999. Photodegradation of acrylic resins used in the conservation of stone. Polym. Degrad. Stab. 66 (1), 23–30. http://dx.doi.org/10.1016/S0141-3910(99)00048-8.

Miliani, C., Velo-Simpson, M.L., Scherer, G.W., 2007. Particle-modified consolidants: a study on the effect of particles on sol-gel properties and consolidation effectiveness. J. Cult. Herit. 8 (1), 1–6. http://dx.doi.org/10.1016/j.culher.2006.10.002.

Mosquera, M.J., DM, d.l.S., Rivas, T., Sanmartin, P., Silva, B., 2009. New nanomaterials for protecting and consolidating stone. J. Nano Res. 8, 1–12. http://dx.doi.org/10.4028/www.scientific.net/JnanoR.8.1.

Natali, I., Saladino, M.L., Andriulo, F., Chillura Martino, D., Caponetti, E., Carretti, E., et al., 2014. Consolidation and protection by nanolime: recent advances for the conservation of the graffiti, Carceri dello Steri Palermo and of the 18th century lunettes, SS.Giuda e Simone Cloister, Corniola (Empoli). J. Cult. Herit. 15 (2), 151–158. http://dx.doi.org/10.1016/j.culher.2013.03.002.

Natali, I., Tomasin, P., Becherini, F., Bernardi, A., Ciantelli, C., Favaro, M., et al., 2015. Innovative consolidating products for stone materials: field exposure tests as a valid approach for assessing durability. Heritage Sci. 3 (6). http://dx.doi.org/10.1186/s40494-015-0036-3.

Ossola, F., Tomasin, P., De Zorzi, C., El Habra, N., Chiurato, M., Favaro, M., 2012. New calcium alkoxides for consolidation of carbonate rocks. Influence of precursors' characteristics on morphology, crystalline phase and consolidation effects. New J. Chem. 36, 2618–2624. http://dx.doi.org/10.1039/C2NJ40708F.

Ozga, I., Ghedini, N., Giosuè, C., Sabbioni, C., Tittarelli, F., Bonazza, A., 2014. Assessment of air pollutant sources in the deposit on monuments by multivariate analysis. Sci. Total Environ. 490, 776–784. http://dx.doi.org/10.1016/j.scitotenv.2014.05.084.

Peruzzo, V., Chiurato, M.A., Favaro, M., Tomasin, P., 2016. Mass Spectrometry in the Characterization of Reactive Metal Alkoxides. Mass spectrometry reviews Wiley http://dx.doi.org/10.1002/mas.21503.

Sabbioni, C., 2003. Mechanisms of air pollution damage to stone. In: Brimblecombe, P. (Ed.), The Effects of Air Pollution on the Built Environment. Imperial College Press, London, pp. 63–106.

Sabbioni, C., Brimblecombe, P., Bonazza, A., Grossi, C.M., Harris, I., Messina, P., 2007. Mapping climate change and cultural heritage. Proceedings of the 7th EC Prague Conference on Safeguarded Cultural Heritage - Understanding & Viability for the Enlarged Europe; 2006 May 31– Jun 3. ITAM, Prague. Prague.

Sabbioni, C., Brimblecombe, P., Cassar, M. (Eds.), 2012. The Atlas of Climate Change Impact on European Cultural Heritage. Scientific Analysis and Management Strategies. Anthem Press, London http://dx.doi.org/10.2777/11959.

Sheremeti-Kabashi, F., Snethlage, R., 2000. In: Fassina, V. (Ed.), Determination of structural anisotropy of Carrara marble with ultrasonic measurements. Proceedings of the 9th International Congress on Deterioration and Conservation of Stone vol 1.; 19–24 Jun 2000; Venice, Italy, pp. 247–253.

Simon, S., Snethlage, R., 1996. In: Riederer (Ed.), Marble weathering in Europe – results of the EUROCARE-EUROMARBLE exposure programme 1992–1994. Proceedings of the 8th International Congress on Deterioration and Conservation of Stone; 30 Sept – 4 Oct 1996; Berlin, Germany, pp. 159–166.

Tidblad, J., Kucera, V., Mikhailov, A.A., Henriksen, J., Kreislova, K., Yates, T., et al., 2001. UNECE ICP materials: dose–response functions on dry and wet acid deposition effects after 8 years of exposure. Water Air Soil Pollut. 130, 1457–1462. http://dx.doi.org/10.1023/A:1013965030909.

Turova, N.Y., Turevskaya, E.P., Kessler, V.G., Yanovskaya, M.I. (Eds.), 2002. The Chemistry of Metal Alkoxides. Springer.

UNI 8941:1987, 1987. Standard Colored surfaces. Milan, Italy.

UNI EN 15801:2010, 2010. Materiali lapidei naturali ed artificiali determinazione dell'assorbimento d'acqua per capillarità, Milan Italy.

Urosevic, M., Yebra-Rodríguez, A., Sebastián-Pardo, E., Cardell, C., 2012. Black soiling of an architectural limestone during two-year term exposure to urban air in the city of Granada (Spain). Sci. Total Environ. 414, 564–575. http://dx.doi.org/10.1016/j.scitotenv.2011.11.028.

Varas, M.J., Alvarez de Buergo, M., Fort, R., 2007. The influence of past protective treatments on the deterioration of historic stone façades: a case study. Stud. Conserv. 52, 110–124. http://dx.doi.org/10.2307/20619491.

Viles, H.A., 1990. The early stages of building stone decay in an urban environment. Atmos. Environ. 24, 229–232. http://dx.doi.org/10.1016/0960-1686(90)90459-Z.

Viles, H.A., Taylor, M.P., Yates, T.J.S., Massey, S.W., 2002. Soiling and decay of N.M.E.P. limestone tablets. Sci. Total Environ. 292 (3), 215–229. http://dx.doi.org/10.1016/S0048-9697(01)01124-X.

Watt, J., Tidblad, J., Kucera, V., Hamilton, R. (Eds.), 2009. The Effects of Air Pollution on Cultural Heritage. Springer, New York http://dx.doi.org/10.1007/978-0-387-84893-8.

WeatherOnline Ltd., d. Meteorological Services [last update: 24/11/2014]. Available from http://www.weatheronline.co.uk/.

WeatherSpark Beta, d. [last update: 31/03/2016]. Available from https://weatherspark.com.

Webb, A.H., Bawden, R.J., Busby, A.K., Hopkins, J.N., 1992. Studies on the effects of air pollution on limestone degradation in Great Britain. Atmos. Environ. 26B, 165–181. http://dx.doi.org/10.1016/0957-1272(92)90020-S.

World Climate & Temperature, d. [last update: 31/03/2016]. Available from http://www.climatemps.com.

World Meteorological Organization, d. World Weather Information Service - Official Forecasts [last update: 31/03/2016]. Available from http://worldweather.wmo.int.

Zappia, G., Sabbioni, C., Riontino, C., Gobbi, G., Favoni, O., 1998. Exposure tests of building materials in urban atmosphere. Sci. Total Environ. 224 (1–3), 235–244. http://dx.doi.org/10.1016/S0048-9697(98)00359-3.

Natali et al. Heritage Science (2015) 3:6
DOI 10.1186/s40494-015-0036-3

HERITAGE SCIENCE

RESEARCH ARTICLE Open Access

Innovative consolidating products for stone materials: field exposure tests as a valid approach for assessing durability

Irene Natali[1*], Patrizia Tomasin[3], Francesca Becherini[2], Adriana Bernardi[2], Chiara Ciantelli[1], Monica Favaro[3], Orlando Favoni[4], Vicente J Forrat Pérez[5], Iulian D Olteanu[6], Maria Dolores Romero Sanchez[5], Arianna Vivarelli[2] and Alessandra Bonazza[1]

Abstract

The impact of climate on cultural heritage surfaces leads to several damage processes and the protection and the preservation of works of art is a challenge for conservation scientists and restorers. Traditional and innovative products are used in consolidating treatments in order to reduce the effects of the interaction environment-materials. The EC NANOMATCH Project aims at the development of innovative consolidating agents for carbonate matrices, wood and glass whose features should result in high compatibility, efficiency and long-lasting effect. In this project, metal alkoxides, molecular precursors for the deposition of metal carbonate are synthesized, characterized, tested and proposed as an alternative to traditional consolidating agents as well as to calcium hydroxide nanoparticles. This paper gives an overall description of the methodological approach adopted for the in field evaluation of durability taking into account the environmental impact. Preliminary results of the analyses carried out on carbonate stones aimed at investigating the features of the consolidating treatment are here presented and discussed.

Keywords: Consolidating treatments, Metal alkoxides, Durability, Climate impact, Carbonate stones, Cultural heritage conservation

Introduction

Climate is predicted to change in the near and far future. The EC NOAH'S ARK Project [1-3] has contributed to the production of scenarios and maps representing the European situation concerning climatic events and related damage processes affecting outdoor built cultural heritage. The foreseen impact of climate change on carbonate stone, marble and limestone, for the 21st century indicates that they will undergo an increase of surface recession, resulting mainly from the yearly precipitation amount and the rise in carbon dioxide concentration; in addition, thermal stress will be experienced by marble, and increased salt crystallization by porous stone [4-7]. Although knowledge on deterioration processes of building materials have been greatly improved, no really effective solutions to preserve and protect these materials have been found yet.

Both organic and inorganic consolidating products have been traditionally used in order to recover the mechanical properties of damaged materials of built heritage. A wide range of synthetic polymers has been extensively used in stone conservation treatments, but their long lasting efficacy and performance in preventing further deterioration has been recently drastically reconsidered as they frequently undergo chemical modifications induced both by environmental conditions and irreversibility of the treatment [8-10]. Traditional inorganic treatments, though usually more compatible with the carbonate matrices, suffer from low solubility and therefore a resulting low amount of applied product as well as from a scarcely cohesive effect. Penetration depth, physico-chemical compatibility, stability, absence of by-products and partial filling of porosity are those characteristics to be evaluated in choosing the best consolidating material for a valid conservation treatment.

* Correspondence: i.natali@isac.cnr.it
[1]Istituto di Scienze dell'Atmosfera e del Clima, Consiglio Nazionale delle Ricerche (ISAC-CNR), Bologna, Italy
Full list of author information is available at the end of the article

In the last decade nanomaterials have been specifically developed for restoration procedures. In particular calcium, magnesium, barium hydroxide nanoparticles have been largely studied and their potentiality as surface consolidating agents has been demonstrated [11-13]. Although these innovative materials have been extensively characterized, little is known about their behaviour in outdoor environment and their durability.

The EC NANOMATCH Project is aimed at developing innovative consolidating products for carbonate matrices, wood and glass. In particular, metal alkoxides have been identified and then synthesized as molecular precursors for the deposition of metal carbonate as consolidating agent for carbonate stones, the same product as alkaline reservoir to prevent acidity of wooden materials and metal oxide as a glass consolidant. Alkaline earth and semimetal alkoxides are suitable molecular precursors because the corresponding solutions or nanoparticulate inorganic sols, upon evaporation of the solvent based carrier, undergo hydrolysis and condensation or carbonation inside the porous structure of the substrate. Particularly, calcium alkoxides, acting as precursors of corresponding carbonate [14,15], can be considered for stone strengthening as an indispensable and essential preliminary action for its conservation, as demonstrated within the bilateral Italian-French GALILEO Project [16]. The same material has been used for wood as these materials, besides strengthening effects, also ensure an alkaline supply to mitigate acidic deterioration processes of cellulose structures.

The expected features making them competitive respect to conventional conservation products are their (i) compatibility with the main materials used in built heritage like stone and wood -even painted- and glass, ensuring enhanced durability, re-treatability, sustainability and efficiency, (ii) easy and safe handling during applications, (iii) satisfactory selling prices.

In this paper we will briefly describe the methodological approach adopted for the evaluation in field of the performances of newly developed products compared to commercial ones applied on carbonate stones. Furthermore, the study here presented is part of the experimental work carried out within the project to achieve an exhaustive performance evaluation of the developed material by investigating its efficacy, compatibility and durability. As the latter aspect is intimately linked to climate impact, environmental parameters having a crucial role in damage processes have been prioritized for a correct evaluation of the durability of the NANOMATCH product during the test in field. Climate parameters have been considered more important than pollution parameters in addressing the objectives of the NANOMATCH project. The main parameters linked to climate change and trigging future damage on materials constituting immovable and movable heritage have been identified from the results of previous EU projects [17-21] and taken into account for the definition of methodologies to assess long-term behaviour of treatments. Rain, relative humidity, air temperature, wind, solar radiation contribute to trigger decohesion processes affecting carbonate stones and therefore believed to have priority for the evaluation of the compatibility, efficiency and performance of nano-structured materials in field. In addition, surface temperature has been also taken into account as an important parameter linked to the material constituent the work of art. The aim of this paper is to highlight how field exposure tests can constitute a valid tool to investigate compatibility and durability of innovative nanostructured consolidating agents, specifically developed to be applied on outdoor built heritage surfaces. The methodological approach adopted to achieve the project objectives is described and part of the results obtained by analysing samples before/after treatment and after exposure by means of different analytical techniques are presented and discussed.

Materials and methods

Synthesis of calcium alkoxides

Different synthetic routes have been tested and more than 20 different alkoxides have been obtained in order to identify the right products and the suitable methodology for its production at industrial scale. In first instance, calcium and magnesium alkoxides were believed adequate to be used in the field of conservation of cultural heritage.

Synthesis of calcium alkoxides, involving ammonia gas-assisted reactions with the corresponding alcohol, have been carried out in nitrogen-filled gloves-boxes with the exclusion of moisture and oxygen according to procedures already described in the literature [22]. The reaction mixture can arise as a white suspension or as a clear solution depending on the alkoxide: in the case of a white suspension, the white precipitate is recovered by centrifugation while in the case of a clear solution, the product is recovered by solvent evaporation.

Then, two alkoxides have been selected on the basis of their properties (solubility in common organic solvents, volatility of the corresponding alcohol, low toxicity): $Ca(OCH_2CH_3)_2$ (NANOMATCH2) and a $Ca(OTHF)_2$, where THF = tetrahydrofurfuryl moiety (NANOMATCH1). These have been up-scaled to produce about 3Kg of each compound.

Although several synthetic methodologies can be used [23] to synthesize magnesium alkoxides, preliminary carbonation tests performed with available commercial products demonstrated that they are unsuitable for conservation of built heritage [24,25].

Coatings investigation

Figure 1 show the possible pathways for the formation of calcium carbonate from calcium alkoxides. To assess the kinetic and the final products of the carbonation process, the calcium alkoxides produced by different synthetic pathways have been dissolved in alcohol and deposited on suitable substrates. The corresponding coatings have been analysed by different techniques (FT-IR, XRD; FEG ESEM) and details can be found in papers by Favaro et al. (2013) [24,25].

The effects of solvents and different relative humidity conditions (50 and 90%) on carbonation rate and phase formation as well as the effects of outdoor environment and liquid water have been investigated. The results evidenced the complexity of carbonation process, where the most kinetically favoured vaterite is always formed but it can evolve to the thermodynamically stable calcite by addition of water and with high relative humidity. The choice of the solvent is extremely important to control carbonation rate: higher vapour pressure (fast evaporation rate) leads to faster carbonation. Slow carbonation is also related to the formation of the thermodynamically favoured phase calcite.

Lithotypes selection and application trials

The selection of stones has been restricted to carbonate ones since the Ca-alkoxide products developed in the NANOMATCH project are mainly meant for the consolidation of calcite-based matrices by deposition of calcium carbonate. Stone materials have been selected on the basis of their Water Absorption Coefficient (WAC) and total porosity. In particular, lithotypes characterized by having very different values of these two properties have been chosen; then, the final choice took into account stones presenting extreme, completely different values of total porosity and WAC.

Therefore, Carrara marble, Savonnières limestone, Laspra dolostone and Albeşti limestone have been selected and used for testing in field (*vide infra*). Moreover, as the Ca-alkoxide products developed in the project aimed at treating substrates presenting granular disintegration (sugaring, powdering, sanding), it has been decided to carry out the tests on both sound stones and artificially deteriorated stones. Other lithotypes have been tested in laboratory as part of the experimental work planned within the project (Figure 2a), not presented in this paper.

Moreover, the Ca-alkoxide consolidants developed during the NANOMATCH project have been compared to a commercial consolidants currently on the market, CaLoSiL® manufactured by IBZ-Salzchemie (Freiberg, Germany).

A number of application trials (Figure 2b) have been carried out on all stones in order to optimize the application parameters of both compounds. The trials enabled to select the application solvent, the product concentration and the application conditions that gave the best results. Four different solvents (2 alcohols and 2 hydrocarbon based) or mixture of them at different concentration have been applied on the different lithotypes.

The best results have been obtained with solution of alkoxides with 20 g/L of Ca in ethanol:ligroin 1:1 applied by brush for two times (different application methods/condition gave worse results), on the basis of visual appearance, amount of consolidant introduced as well as scratch test.

Tests in field

Four European monuments have been selected as field exposure sites. For each of them one typical lithotype (Table 1) has been chosen to carry out the experimental work in order to assess the performance of the product when exposed to different natural conditions. In particular, Carrara marble, Savonnières limestone (oolitic limestone), Laspra dolostone and Albeşti limestone (nummulitic limestone) are lithotypes representative of Santa Croce Basilica in Florence, Cologne Cathedral, Oviedo Cathedral and Stavropoleos Monastery, respectively. Plaques with size of $10\times10\times5$ cm^3 for each lithotype has been prepared as model samples in order to test in field efficacy, compatibility towards stone and durability against climate impact of the alkaline earth metal alkoxides as consolidating agents. Although Carrara marble is typical of Florentine architecture, this lithotype has been exposed in all four sites together with one local lithotype, to evaluate the impact of climate on the same stone in different European geographical areas.

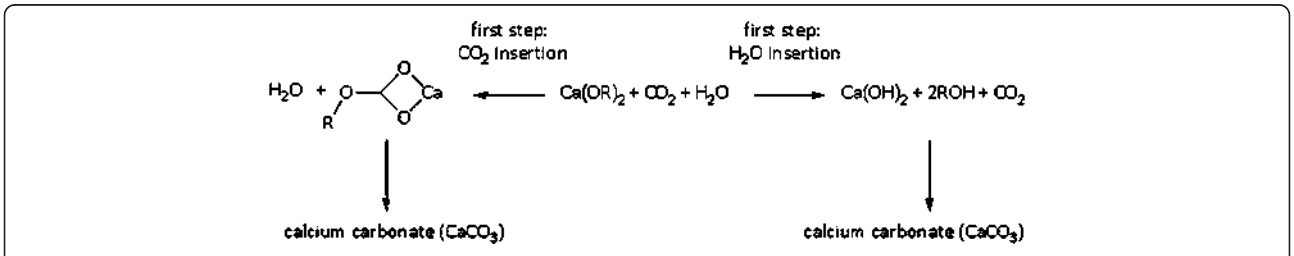

Figure 1 Possible pathways for the formation of $CaCO_3$ from $Ca(OR)_2$: insertion of CO_2 can either follow or precede the hydrolysis.

Figure 2 Samples of the stones selected for testing (left); application trials on different lithotypes (right).

For the exposure test, Carrara marble and Savonnières limestone have been previously artificially damaged respectively by thermal shock (heating treatment at 600°C for 1 h) and by contamination with sodium sulfate (5% w/w Na_2SO_4 solution). The thermal shock carried out on Carrara marble was aimed exclusively at obtaining samples characterized by a heavy intergranular decohesion (damage effect) without any purpose of simulating a realistic outdoor damage process. A set of samples of each of the two types of stone has been exposed undamaged, while four samples of each lithotype have been treated with the NANOMATCH1 product. Other identical sets have been treated with CaLoSiL® in order to make a comparison. Table 2 summarizes the artificial deterioration and the consolidating treatments carried out on the four lithotypes.

Model samples have been placed in galvanized rack (Figure 3) specifically built for field testing, located outdoor in an unsheltered area, exposed to environmental impact so that at each site of exposure specimens of the local lithotype are present and Carrara marble as well. Samples were exposed for 11 months in each site, from April/May 2013 to March/April 2014. In Florence the rack has been installed outside on the roof above the Pazzi's and Castellani's Chapels in the south-west side of Santa Croce Basilica. In Cologne the rack was installed at 20 m height on a small outside balcony at the south side of the Cathedral. Concerning Oviedo, samples have been placed in the "Patio de Carton", on the south side of the Cathedral, while in Bucharest in the southeast side of the courtyard of the Monastery. Climatic and microclimatic data (rain, wind, solar radiation, relative humidity, air and surface temperature) were continuously collected outdoors nearby the rack, close to the samples exposed, they were analysed, and their temporal evolution for the whole duration of the exposure was studied. During the monitoring campaign Florence and Oviedo were characterized by the highest cumulative amounts of rainfalls, both around 820 mm, followed by Cologne (460 mm) and Bucharest (275 mm). Florence and Oviedo were also characterized by the highest rain monthly amounts (respectively 144 mm in October in Florence and 152 in November in Oviedo). Average relative humidity was around 70-74% during the field exposure at all sites, with the highest values in Bucharest. The lowest air thermal value close to the stone samples was measured in Bucharest (−14°C in January), where it also snowed heavily at the beginning of February. Nevertheless, Bucharest was the site characterized by the lowest average values of thermo-hygrometric daily variations, respectively of 14°C for temperature and 55% for relative humidity. In the other sites, the average daily thermal variations were of 22-24°C, whilst the average daily hygrometric variations were between 60% (Cologne) and 75% (Florence). The risks for the most important physical damage processes for the material investigated (i.e. condensation, freeze-thaw cycles, salts crystallization etc.) were evaluated, as well as other potentially damage phenomena related to the climatic and microclimatic conditions (i.e. surface heating, thermo-hygrometric cycles, etc.). The results of the microclimatic monitoring are reported in details in [26].

It is well known that pollutants in synergy with environmental factors trigger many damage processes affecting surfaces. According to the methodological approach adopted in the NANOMATCH Project, samples have been placed outdoor, in an unsheltered area and so exposed to the rain-wash out. However, all samples were

Table 1 Lithotypes and sites of exposure selected for the field test within NANOMATCH Project

Lithotype	Site of exposure
Carrara Marble	Santa Croce Basilica Florence, Cologne Cathedral, Oviedo Cathedral, Stavropoleos Monastery Bucharest
Savonnières limestone	Cologne Cathedral
Laspra dolostone	Oviedo Cathedral
Albeşti limestone	Stavropoleos Monastery Bucharest

Table 2 Artificial deterioration and consolidating treatments carried out on the four lithotypes

Site	Model sample (10 × 10 × 5) cm^3	Artificial deterioration	Treatments
Florence	Carrara marble	Thermal shock	NANOMATCH1 solution in 1:1 ethanol:ligroin at 20 g/L of Ca
Cologne	Carrara marble	Thermal shock	
	Savonnières limestone	Contaminated with a 5% w/w Na_2SO_4 solution	
Oviedo	Carrara marble	Thermal shock	COMMERCIAL: CaLoSiL® – 20 g/L of Ca in ethanol
	Laspra dolostone	-	
Bucharest	Carrara marble	Thermal shock	
	Albesti limestone	-	

placed in urban environments therefore affected by problems related to the vehicular traffic, domestic heating and industry. Moreover, Cologne, Oviedo and Bucharest have also to face pollution caused by power plants (some of them also fuelled by coal) located within the cities or in their periphery. Oviedo is also placed in a coal mining area, implying a high concentration of SO_2, NO_X, CO_2 and traces of heavy metals in the atmosphere. However in Florence, Oviedo and Bucharest samples were exposed in pedestrian areas and therefore not directly exposed to vehicular traffic impact. On the contrary, Cologne cathedral is aside the railway station and in traffic congested area. The yearly reports about the air quality status for the year 2013 of the four cities confirm the main pollution problems are the still high concentration of nitrogen oxides and particulate matter, both connected with vehicular traffic emissions. Examining the yearly report about the air quality status of Tuscany for the year 2013 [27], some events of pollutants concentration exceeding suggested thresholds were observed in the congested monitoring station of Gramsci Avenue, located near Santa Croce Basilica. For example, the daily mean limit value of PM10 regulated by the European Directive 2008/50/EC and the Italian D.Lgs 155/2010 and D.Lgs 250/2012 was not respected as well as the concentration of ozone (O_3). Moreover, the concentration of NO_2 exceeded the annual limit value of 40 μgm^{-3}. During the 2013 there was also a reduction of the yearly mean concentration of carbon monoxide (CO) and sulfur dioxide (SO_2). Concerning Cologne, the annual report on air quality of the North Rhine-Westphalia relative to 2013 [28] highlighted that the amount of particulate matter slightly increased while the hourly limit value of nitrogen dioxide was respected in all the monitoring stations, although some excesses of the annual limit value occurred in congested areas such as the one located near the Cologne Cathedral. An improvement in the concentration of sulfur dioxide and ozone was observed, the latter facilitated by few long sunshine periods and by the decrease in emissions of precursors such as NO_X and volatile hydrocarbons. During the eleven months of stone samples exposition in Oviedo no excesses in sulfur dioxide concentration were recorded by the monitoring station nearest to the Cathedral, both of the hourly and the daily limits (respectively 350 μgm^{-3} and 125 μgm^{-3}) [29]. Moreover, there was an improvement in the emission of ozone in respect to the previous years while the concentration of nitrogen dioxide and particulate overtook the limits, remaining, however, below the number of possible excesses. The Rumanian annual report on air quality relative to 2013 [30] highlighted that the concentration of nitrogen oxides and of the particulate matter were still high in Bucharest while the sulfur dioxide emissions did not manifest any excess of the hourly and daily limit values.

Figure 3 Galvanized rack used for the field exposure test (Santa Croce Basilica, Florence).

Analytical techniques

Analyses on model samples have been performed before and after the consolidation treatments with both the NANOMATCH1 and commercial products. Then, samples have been exposed at the sites. Performance in terms of efficacy, compatibility and durability of the newly developed product have been evaluated by comparing results obtained before exposition, and after one

year of exposure of each treated/untreated stone by means of the following analyses:

- Optical Microscopy (OM) both in transmitted and reflected light on thin and polished cross sections of each lithotype using an Olympus BX51 microscope;
- Scanning Electron Microscopy - Energy Dispersive X-ray spectroscopy (SEM-EDX) using a ZEISS 1530 instrument, equipped with two different Secondary Electrons (SE) detectors, the InLens (IL) and the Everhart-Thornley detectors (ETD);
- Color measurements (spectrophotometry) carried out according to the CIE L*a*b* chromaticity diagram and to the UNI 8941 Standard Colored surfaces, using a KONICA MINOLTA CM700d Spectrophotometer, performing measurements with a spot size of 8 mm diameter in the 400–700 nm spectral range.
- Scotch Tape Test (STT)
- Capillarity water absorption test.

Objectives and analyses performed on the four lithotypes are summarized in Table 3.

Cohesion, surface properties, penetration depth, interactions with stone, porosity and water absorption have been therefore evaluated and compared.

Results and discussion

Analyses on collected samples have been carried out with the aim to verify the cohesive properties conferred to the surface by the treatments, the possible textural and structural modifications induced by the application of the nanomaterials to the stone surface, the penetration depth of the consolidating product, as well as possible interactions with the stone.

In this section the most important contributes obtained from each analytical technique, with exception of capillarity water absorption test, are shown in order to highlight the potentialities of the adopted methodological approach.

Intergranular decohesion induced by thermal shock is clearly visible in OM and SEM images of Carrara marble artificially damaged (Figure 4a and b, respectively). On all analysed samples, the treatment with NANOMATCH1 product has been identified as a surface homogeneous microcrystalline layer, whose thickness and penetration into the stone matrix depend on the lithotype's porosity and petrographic characteristics (Figure 5a, c, e). The treatment performed with CaLoSiL® (Figure 5b, d, f) also leads to a surface microcrystallization layer characterized by higher thickness values. In addition, the surface layers produced, although they are both constituted by calcium carbonate microcrystals, appear different in terms of compactness and distribution on samples' surfaces. The CaLoSiL® treatment induces the formation of a more compact layer adhering to the surface, while NANOMATCH1 treatment appears less compact, following the surface's shape of the stone, as highlighted by the red arrows in Figure 5.

Analyses performed after exposure have highlighted traces of NANOMATCH1 product within the stone matrix, filling intergranular spaces as calcium carbonate recrystallization (Figure 6a, b).

On the contrary, CaLoSiL® treatment is still clearly visible on Carrara Marble surface after exposure and it appears as a discontinuous brownish surface layer in plane polarized light, and as a bright greenish microcrystalline layer in cross polarized light (Figure 6c, d).

More information about the capability of the product to penetrate into fractures and cracks have been obtained by SEM investigation executed after the exposure. In particular, after 11 month of exposure in Florence and Cologne, morphological observations performed on cross sections of treated sample surfaces demonstrated different decay patterns according to the consolidating treatment (NANOMATCH1 or CaLoSiL®) and exposure. It can be pointed out that samples from Florence show

Table 3 Analyses performed on the four lithotypes samples and objectives

Objective	Analysis	When	Lithotype	Site
Colour change	colorimetry	Before/after treatment	all	all
		After exposure		
Cohesion, surface properties, penetration depth, interaction	SEM-EDX	Before/after treatment	Carrara marble, Savonniéres limestone	Florence, Cologne
		After exposure		
Cohesion, penetration depth, interaction	OM	Before/after treatment	Carrara marble, Savonniéres limestone	Florence, Cologne
		After exposure		
Cohesion	ScotchTapeTest	Before/after treatment	all	all
		After exposure		
Water absorption	capillarity water absorption	Before treatment/after exposure	Carrara marble, Savonniéres limestone (on selected samples purposely prepared)	Florence, Cologne

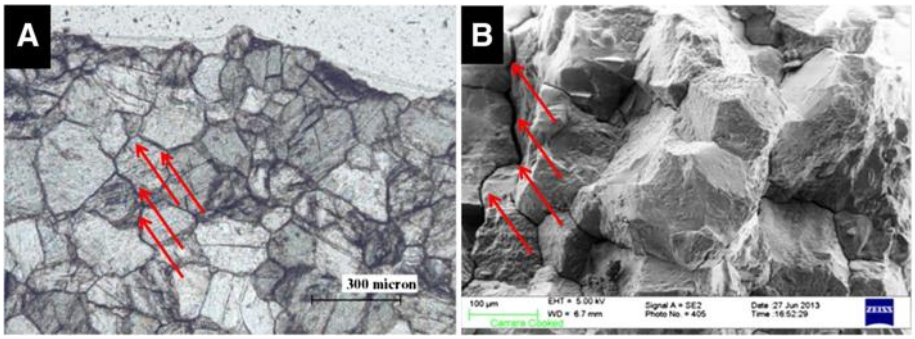

Figure 4 Optical micrograph (plane-polarized light) (a) and scanning electron micrograph (b) of Carrara Marble artificially damaged by thermal shock.

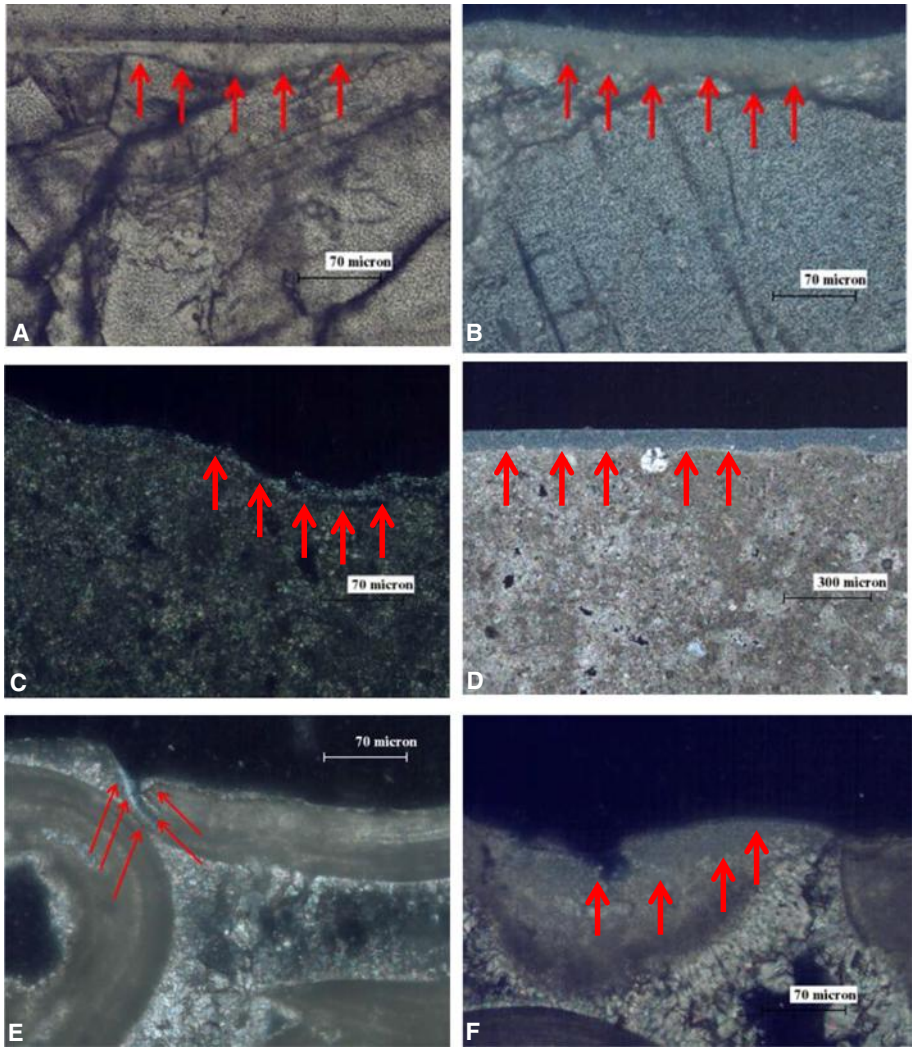

Figure 5 Optical micrographs of: Carrara Marble treated with NANOMATCH1 product (plane-polarized light) (a) and CaLoSiL® (crossed-polarized light) (b); Laspra dolostone treated with NANOMATCH1 product (crossed-polarized light) (c) and CaLoSiL® (crossed-polarized light) (d); Savonnières limestone treated with NANOMATCH1 product (crossed-polarized light) (e) and CaLoSiL® (crossed-polarized light) (f). Red arrows indicate the surface microcrystalline layer formed after the consolidating treatment executed with the two products.

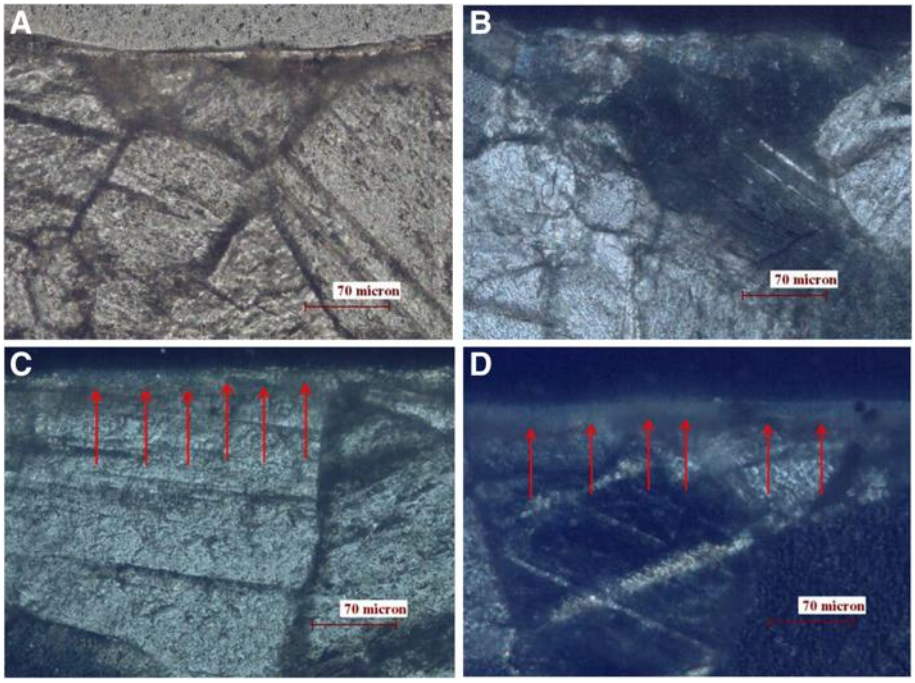

Figure 6 Optical micrographs of: Carrara Marble treated with NANOMATCH1 product after the exposure in plane-polarized light (a) and in crossed-polarized light (b); Carrara Marble treated with CaLoSiL® after the exposure in crossed-polarized light (c, d). Red arrows indicate the surface microcrystalline layer still present on the marble surface.

more severe effects of pitting on the surface, having the treatment layer been thinned and largely removed leaving uncovered and visible crystals of calcite (Figure 7a). This effect can be linked to the acid rain impact that partially dissolved the calcium carbonate formed by the treatment, being stone samples exposed outdoors in unsheltered positions. Taking into account the values of precipitation recorded during the exposure period it should be underlined that Florence, along with Oviedo, has been characterized by the highest cumulative amounts of rainfall during the monitoring campaigns (820 mm), followed by Cologne (460 mm). It is known that the main cause of rain acidification is essentially attributable to an increase of carbon dioxide concentration in the air and to other gaseous compounds such as NO_x and SO_2, whose concentration in urban environment is mostly linked to anthropogenic activity. Comparing acidifying agents concentrations registered by the local agencies from 22/07/2013 to 31/12/2013 it can be noticed that nitrogen oxides concentration registered close to Santa Croce Basilica [27] are higher than those recorded in Cologne [28] (Figure 8). Moreover, a similar distribution has been noticed observing samples treated with NANOMATCH1 product, independently from the site exposure. Indeed, the product is randomly distributed along the inner pores (Figure 7b) forming a superficial coating adhering to the calcite surface on wider pores (pore diameter > 20-30 um). Morphological observations performed on marble treated with CaLoSiL® and exposed in Florence and Cologne showed the uneven presence of the product mainly distributed along the surface (Figure 7d); the pitting effect has been also observed (Figure 7c).

In general, surface treatments adopted in conservation procedure should not strongly modify the aesthetic aspect of the work of art. Spectrophotometric measurements have been performed according to the CIE L*a*b* chromaticity diagram in order to verify if possible differences in colour of surfaces induced by NANOMATCH1 treatment would be noticed and if they might be considered negligible or not. Taking into account the indication given by García and Malaga [31] with regard to the threshold value of ΔE* accepted as reference in the evaluation of a conservation treatment, the ΔE* values, calculated using colour coordinates referred to the surface of the samples before and after treatment, cannot be seen by a human eye when they are < 5 units.

Each colour parameter has been acquired for each lithotype before and after the treatment and therefore the total colour difference has been calculated using the formula (1):

$$\Delta E^* = \sqrt{(L_2^*-L_1^*)^2 + (a_2^*-a_1^*)^2 + (b_2^*-b_1^*)^2} \quad (1)$$

As shown in Figure 9, the average values of the total colour differences calculated using colour parameters

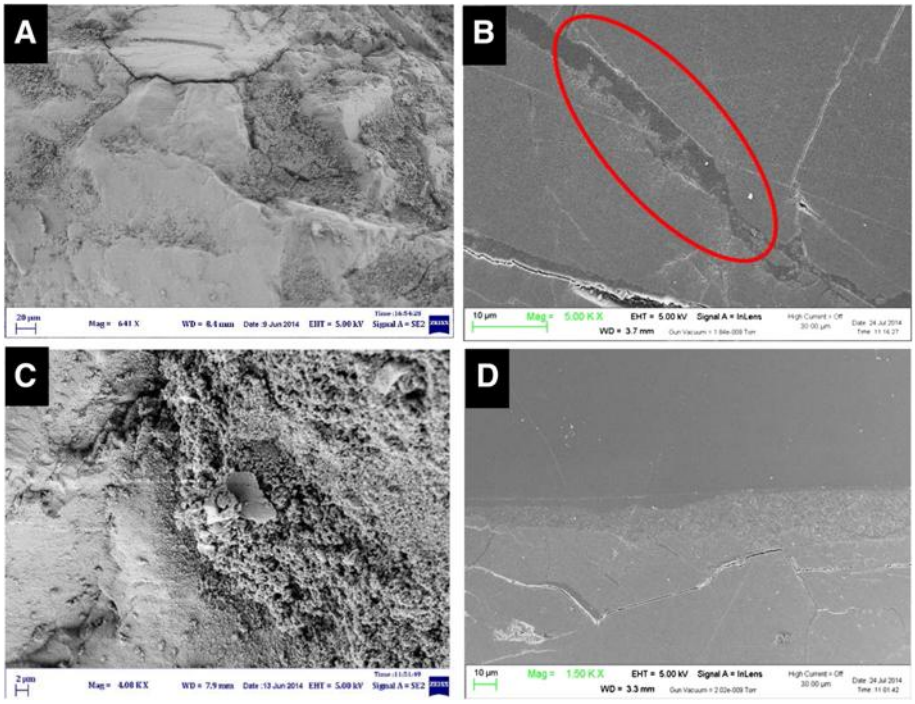

Figure 7 SEM micrographs of Carrara marble treated with: NANOMATCH1 product after exposure, bulk sample (a) and polished crossed section (b); CaLoSiL® product after exposure bulk sample (c) and polished crossed section (d). Red circle indicates the coating formed by the NANOMATCH1 treatment adhering to the calcite surface within pores.

acquired before and after NANOMATCH1 treatment lies under the threshold value ($\Delta E^* = 5$) for all lithotypes; on the contrary, CaLoSiL® treatment induces total colour differences higher respect to the threshold value, except for Carrara Marble samples. In addition, measurements highlighted that L* and b* are the colour parameters principally changing in consequence of the consolidating treatments, leading to a surface whitening and a yellowing effect respectively. It has been noticed that for a white coloured stone as Carrara Marble, the general increase in L* values is attributable in first instance to the heating treatment. The treatments do not contribute to further increase of this effect. A slight yellowing

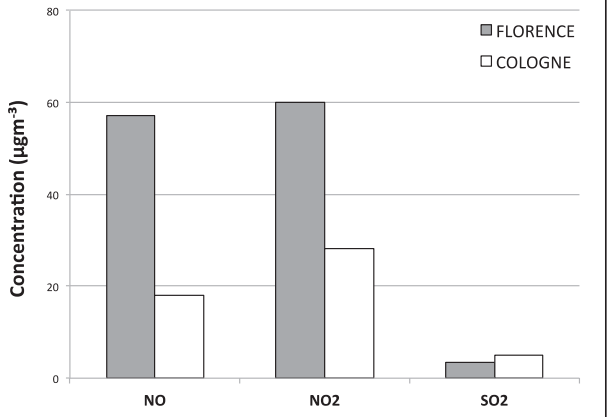

Figure 8 Hourly mean concentration of NO, NO_2 and SO_2 registered during the period 22/07/2013-31/12/2013 by the local agencies for the monitoring of the environment and air quality [27,28].

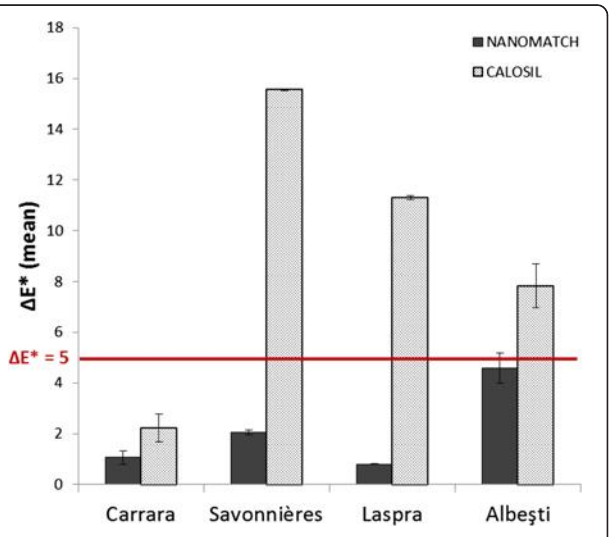

Figure 9 Total colour difference calculated using colour parameters acquired before and after treatment with NANOMATCH1 product and CaLoSiL®. The red line marks the threshold value indicated by García and Malaga [31].

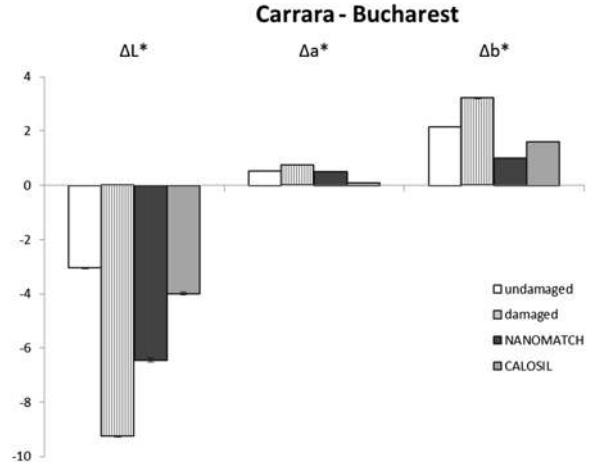

Figure 10 ΔL*, Δa*, Δb* referred to Carrara Marble exposed Bucharest calculated from data acquired before and after exposure.

effect has been observed in samples treated with NANOMATCH1 product.

Colour measurements carried out after the exposure have allowed to estimate the colour variation due to the outdoor exposure. Among obtained results, it was interesting to verify which set of samples had undergone major colour changes and, in particular, which colour parameters were mostly involved. In Figure 10 ΔL*, Δa*, Δb* values referred to Carrara Marble exposed in Bucharest, calculated from data acquired before and after exposure are presented. It can be pointed out that the highest variations for each colour parameter are referred to artificially damaged samples where the ΔL* reaches the highest negative value ($|\Delta L^*| = 9.25$), meaning a more pronounced darkening of the exposed surface with respect to undamaged and treated samples as well.

Surface cohesion characteristics of the stones before and after the consolidating treatment have been assessed by carrying out the peeling test recommended by many authors and standardized by Drdácký et al. [32]. It consists in applying and removing pressure sensitive tape over the surface of interest to evaluate the amount of incoherent material peeled from the surface by gravimetrical analysis (Figure 11). In Figure 12 results among those obtained by performing STT on Carrara marble and Albești limestone model samples are presented. In general, STT carried out on all stone samples show that the amount of material peeled from the surface after the NANOMATCH1 treatment is highly reduced as compared to the amount removed before the treatment; moreover, while the test performed on untreated samples highlights a reduction of the quantity of incoherent material removed from the surface in function of the number of peeling executed (the stone is much more detached and mechanically deteriorated on the surface respect to the inner part), samples treated with NANOMATCH1 product show that the amount of removed material is independent from the number of peeling carried out, suggesting a surface hardening effect. On the contrary, CaLoSiL® treatment seems to be ineffective in reducing the detachment of the surface, as the quantity of incoherent material removed before and after treatment are comparable.

Both untreated and treated samples after the exposure show a decrease of the material removed by the peeling action, probably due to the rain compacting action and to calcite dissolution and recrystallization phenomena. As an example, STT results referred to Carrara Marble exposed in Bucharest are reported in Figure 13. Concerning NANOMATCH1 treatment's behaviour, it could be noticed that a positive mild effect of exposure occurred, with general slight increase of cohesion in deeper layers. CaLoSiL® treatment demonstrate best results after exposure respect to before exposure, highlighting the slow kinetics of carbonation reaction being CaLoSiL® constituted by nanoparticles suspended in different alcohols and having sizes ranging between 50 and 150 nm depending on the production process.

Key outputs

In this paper the methodological approach adopted by field exposure tests in the EC NANOMATCH project

Figure 11 Scotch tape test on Carrara Marble samples.

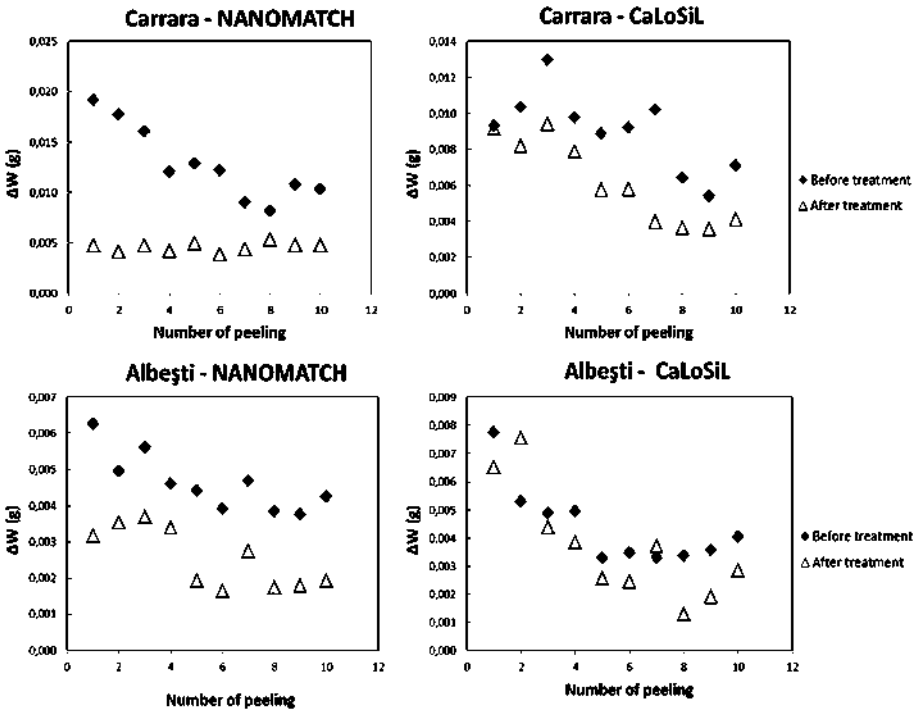

Figure 12 Scotch Tape Test data referred to samples of Carrara Marble (up) and to Albeşti limestone (bottom) treated with the two consolidating agents.

for the evaluation of climate impact on the performances of newly developed products was described. The presented data should be read as part of the preliminary results of the analyses carried out before and after the application of the product on stone samples.

In terms of aesthetic compatibility NANOMATCH1 product can be considered suitable to be used as consolidant for the selected lithotypes as it does not affect the appearance of the stone when appropriately applied. Results showed that it leads to the formation of microcrystalline aggregates on porous limestones' surfaces, somewhere penetrating the stone matrix; on stones characterized by low porosity or microporosity (as Carrara Marble) it forms a discontinuous microcrystalline surface layer. After exposure, morphological observations performed on stone surfaces and sections of samples treated with NANOMATCH1 and CaLoSiL® products, demonstrated that the calcium carbonate coating deriving NANOMATCH1 product is barely observable over the surface and is randomly distributed on wider pores and cracks below the stone surfaces, while the consolidant obtained from carbonation of CaLoSiL® is exclusively located on the outmost surface and it is affected by fissures as the substrate itself due to outdoor weathering.

A good surface cohesive effect is achievable in a short time after its application on stones, due to the fast reactions of alkoxides with atmospheric H_2O and CO_2. Moreover, greater cohesion of the surface has been detected

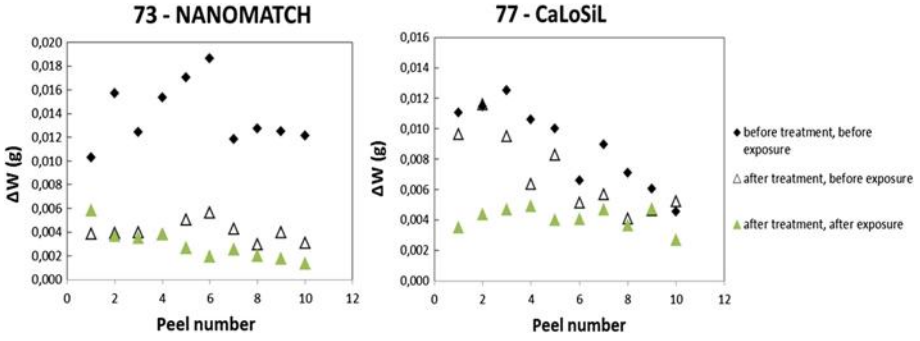

Figure 13 Scotch Tape Test data referred to samples of Carrara Marble treated with the two consolidating agents and exposed in Bucharest.

after the exposure period, even though the NANOMATCH product is almost absent on the stone surface, as confirmed by optical and electron scanning morphological observations. Comparing and combining OM and SEM results with those obtained by the peeling test (STT) it has been possible to argue for the calcium carbonate deriving from the calcium alkoxide a partial dissolution, penetration and recrystallization of the product within the porous matrix as a consequence of the exposure.

The comparison and the crosschecking of all the results obtained by the analyses of samples before/after treatment and after one year of exposure will allow to evaluate the durability of the nanostructured material developed within the NANOMATCH project and the climatic impact on the innovative treatment and the treated surfaces related to different geographical areas. The preliminary analyses carried out on Carrara Marble, the only lithotype exposed in all the sites, indicate that the differences in the environmental factors present at each site do not translate in significant differences between the marble samples exposed at the different sites.

Competing interests
The authors declare that they have no competing interests.

Authors' contributions
All the authors contributed in planning the research activities. IN and PT wrote the paper. AlB and FB critically reviewed the paper. MF and PT synthesized the metalalkoxides and carried out the coating investigation. IDO and PT carried out the application trials. IN and AlB set up the field exposure test. IN and CC performed the Optical Microscopy observation. IN and OF carried out the Scanning Electron Microscopy investigation. IN carried out color measurements and data elaboration. IN, VJFP, MDRS and IDO carried out the Scotch Tape Test and data elaboration. AV and FB performed the climate and microclimate monitoring as well as data processing. AlB coordinated the scientific analyses. AlB, AdB and MF conceived this study. AdB coordinated the project which has funded this research. All authors read and approved the final manuscript.

Acknowledgements
The NANOMATCH Project (Nano-systems for the conservation of immoveable and moveable polymaterial Cultural Heritage in a changing environment) has received funding from the European Union's Seventh Programme for research, technological development and demonstration under grant agreement No [283182]. Authors express their gratitude to Elsa Bourguignon and Vincent Detalle (CPP- LRMH, France), Barbara Lubelli and Rob Van Hees (TNO, Netherlands), Ulrike Brinkmann and Michael Hauck (Dombauverwaltung Köln, Germany), Martin Labouré (Eschlimann Atelier, France), Marco Pancani (Opera di Santa Croce, Firenze, Italy) and Luis Valdeón (Gea asesoría geológica, Spain) for the fruitful discussion and support during the experimental work.

Author details
[1]Istituto di Scienze dell'Atmosfera e del Clima, Consiglio Nazionale delle Ricerche (ISAC-CNR), Bologna, Italy. [2]Istituto di Scienze dell'Atmosfera e del Clima, Consiglio Nazionale delle Ricerche (ISAC-CNR), Padova, Italy. [3]Istituto per l'Energetica e le Interfasi, Consiglio Nazionale delle Ricerche (ISAC-IENI), Padova, Italy. [4]Dipartimento di Scienze e Ingegneria della Materia, dell'Ambiente ed Urbanistica - Università Politecnica delle Marche, Ancona, Italy. [5]Instituto Tecnológico de la Construcción (AIDICO), Novelda-Alicante, Spain. [6]DUCT SRL, Bucuresti, Romania.

Received: 30 September 2014 Accepted: 10 February 2015
Published online: 02 March 2015

References
1. Sabbioni C, Brimblecombe P, Bonazza A, Grossi CM, Harris I, Messina P. Mapping climate change and cultural heritage. In: Proceedings of 7th EC Prague Conference on Safeguarded Cultural Heritage - Understanding & Viability for the Enlarged Europe. Prague, Czech Republic: ITAM CAS; 2007.
2. Cassar M. Climate Change and the Historic Environment. London: Published by the Centre for Sustainable Heritage, University College London; 2005.
3. Sabbioni C, Brimblecombe P, Cassar M, editors. The Atlas of Climate Change Impact on European Cultural Heritage. Scientific Analysis and Management Strategies. London, UK: Anthem Press; 2012.
4. Grossi CM, Brimblecombe P, Menéndez B, Benavente D, Harris I, Dégué M. Climatology of salt transitions and implications for stone weathering. Sci Total Environ. 2011;409:2577–85.
5. Bonazza A, Messina P, Sabbioni C, Grossi CM, Brimblecombe P. Mapping the impact of climate change on surface recession of carbonate buildings in Europe. Sci Total Environ. 2009;407:2039–50.
6. Grossi CM, Brimblecombe P, Harris I. Predicting long term freeze–thaw risks on Europe built heritage and archaeological sites in a changing climate. Sci Total Environ. 2007;377:273–81.
7. Bonazza A, Sabbioni C, Messina P, Guaraldi C, De Nuntiis P. Climate change impact: mapping thermal stress on Carrara marble in Europe. Sci Total Environ. 2009;407:4506–12.
8. Melo MJ, Bracci S, Camaiti M, Chiantore O, Piacenti F. Photodegradation of acrylic resins used in the conservation of stone. Polym Degrad Stab. 1999;66:23–30.
9. Favaro M, Mendichi R, Ossola F, Russo U, Simon S, Tomasin P, et al. Evaluation of polymers for conservation treatments of outdoor exposed stone monuments. Part I: Photo-oxidative weathering. Polym Degrad Stab. 2006;91:3083–96.
10. Favaro M, Mendichi R, Ossola F, Simon S, Tomasin P, Vigato PA. Evaluation of polymers for conservation treatments of outdoor exposed stone monuments. Part II: photo-oxidative and salt-induced weathering of acrylic–silicone mixtures. Polym Degrad Stab. 2007;92:335–51.
11. Rodriguez-Navarro C, Ruiz-Agudo E, Ortega-Huertas M, Hansen E. Nanostructured and irreversible colloidal behavior of $Ca(OH)_2$: implications in cultural heritage conservation. Langmuir. 2005;21:10948–57.
12. Dei L, Salvadori B. Nanotechnology in cultural heritage conservation: nanometric slaked lime saves architectonic and artistic surfaces from decay. J Cult Herit. 2006;7:110–5.
13. Natali I, Saladino ML, Andriulo F, Chillura Martino D, Caponetti E, Carretti E, et al. Consolidation and protection by nanolime: Recent advances for the conservationof the graffiti, Carceri dello Steri Palermo and of the 18th century lunettes, SS.Giuda e Simone Cloister, Corniola (Empoli). J Cult Herit. 2014;15:151–8.
14. Ossola F, Tomasin P, De Zorzi C, El Habra N, Chiurato M, Favaro M. New calcium alkoxides for consolidation of carbonate rocks. Influence of precursors' characteristics on morphology, crystalline phase and consolidation effects. New J Chem. 2012;36:2618–24.
15. Favaro M, Tomasin P, Ossola F, Vigato PA. A novel approach to consolidation of historical limestone: the calcium alkoxides. App Organomet Chem. 2008;22:698–704.
16. Duchêne S, Detalle V, Favaro M, Ossola F, Tomasin P, De Zorzi C, et al. Nanomaterials for Consolidation of Marble and Wall Paintings. In: Proceedings of the 12th International Congress on the Deterioration and Conservation of Stone. New York, USA: Columbia University; 2012.
17. Bonazza A, Sabbioni C, Lopez-Aparicio S, Tittarelli F, Ozga I. Identification of pollutants and parameters affecting Cultural Heritage conservation and their change in the near and far future, TeACH project. Deliverable 2.1. www.isac.cnr.it/~microcl/staff/bernardi.php.
18. Bonazza A, Sabbioni C, Van Grieken R, Kontozova V, Krupinska B, Gatto Rotondo G. Prioritization of the most important pollutants and parameters for a preventive conservation of the immovable cultural heritage, TeACH project. Deliverable 2.2. www.isac.cnr.it/~microcl/staff/bernardi.php
19. Lopez-Aparicio S, Grøntoft T, Bonazza A. Prioritization of the most important pollutants and parameters for a preventive conservation of the movable cultural heritage, TeACH project. Deliverable 2.3. www.isac.cnr.it/~microcl/staff/bernardi.php
20. Sabbioni C, Bonazza A, Messina P. Global Climate Change and Archaeological Heritage: Prevision, Impact and Mapping. In: Nicolò M, Ingolf T, editors. ARCHAIA - Case studies on Research Planning,

Characterisation, Conservation and Management of Archaeologial Sites. Oxford, UK: Archaeopress; 2008.
21. Grøntoft T, Larssen S, Svenningsen G, Hamilton R, Ionescu A, Le Fèvre R, et al. Final assessment model for cultural heritage, CULT-STRAT Project. Deliverable 9. www.corr-institute.se
22. Drake SR, Otway DJ. The synthesis of metal organic compounds of calcium, strontium and barium by ammonia gas-saturated ethereal solvents. J Chem Soc Chem Commun. 1991;7:517–9.
23. Turova NY, Turevskaya EP, Kessler VG, Yanovskaya MI. The Chemistry of Metal Alkoxides. US: Springer; 2002.
24. Favaro M, Chiurato M, Tomasin P, Ossola F, El Habra N, Brianese N, Svensson I, Beckers E, Forrat Pérez V, Romero Sánchez M, Orial G, Bourguignon E, Bernardi A. Alkaline earth alkoxides for conservation treatment of stone and wood in built heritage. In Proceedings of 3rd European Workshop on Cultural Heritage Preservation (EWCHP) Bolzano, Italy. 2013.
25. Favaro M, Chiurato M, Tomasin P, Ossola F, El Habra N, Svensson I, Beckers E, Forrat Pérez V, Romero Sánchez M, Bernardi A. Calcium and magnesium alkoxides for conservation treatment of stone and wood in built heritage. In on-line Proceedings of Built Heritage Conference 2013 Monitoring Conservation Management. Milano, Italy. 2013.
26. Pockelé L, De Grandi S, Becherini F, Bernardi A, Vivarelli A. Assessment of the climatic measurement on sites, Nanomatch project. Deliverable 4.2 http://www.nanomatch-project.eu.
27. ARPAT, Agenzia Regionale per la Protezione Ambientale della Toscana www.arpat.toscana.it.
28. Landesamt für Natur, Umwelt und Verbraucherschutz NRW www.lanuv.nrw.de.
29. Oviedo.es Ayuntamiento www.oviedo.es.
30. Ministerul Mediului, Apelor și Pădurilor - Agenția Națională pentru Protecția Mediului www.anpm.ro
31. García O, Malaga K. Definition of the procedure to determine the suitability and durability of an anti-graffiti product for application on cultural heritage porous materials. J Cult Herit. 2012;13:77–82.
32. Drdácký M, Lesák J, Rescic S, Slížková Z, Tiano P, Valach J. Standardization of peeling tests for assessing the cohesion and consolidation characteristics of historic stone surfaces. Mater Struct. 2012;45:505–20.

Journal of Experimental and Integrative Medicine
www.jeim.org
DOI: 10.5455/jeim.160715.or.134

Original Article

Can an ozone system generator reduce indoor triggers in asthmatic patient?

Alessandro Zanasi[1], Paola De Nuntiis[2], Massimiliano Mazzolini[3], Chiara Ciantelli[2], Matteo Alemanni[4], Carla M.S. Ierna[3], Marianna Mastroroberto[5], Elena Nardi[5], Antonio M. Morselli Labate[5]

[1]Italian Association for Cough Study, Bologna, Italy.
[2]Institute of Atmospheric Sciences and Climate of the Italian National Research Council, Bologna, Italy.
[3]Department of Respiratory Medicine and Intensive Care Unit, Alma Mater Studiorum, University of Bologna, Sant'Orsola Malpighi Hospital, Bologna, Italy.
[4]Italian Society of Clinical Pharmacy, Cagliari, Italy.
[5]Department of Medical and Surgical Sciences, Alma Mater Studiorum, University of Bologna, Bologna, Italy

Address for correspondence:
Alessandro Zanasi,
Italian Association for Cough Study (AIST), Via Mazzini 12, 40138 Bologna, Italy.
alessandro.zanasi@aosp.bo.it

Received: June 29, 2015
Accepted: July 16, 2015
Published: December 30, 2015

ABSTRACT

Objective: During the last decades, an increase in the prevalence of asthma and other allergic diseases has been recorded, together with modifications in the living environment and consequent changes in the quality of indoor air. Indoor environment is favorable to the proliferation of allergens such as: house dust mites, fungal spores and cockroaches. The primary action to be undertaken for an effective eradication of infectious agents constitutes in modifying the house environmental conditions, which make it favorable to infestations. Ozone can play a sanitize role, but at the same time it can cause inflammation, especially in the lung. The aim of this study was to verify the role and safety of ozone in the sanitation of the bedroom of a subject suffering from asthma. **Methods:** A daily ozone treatment was carried during a 14-day time period in the bedroom of an asthmatic patient. Aerobiological sampling in indoor air, microbiological sampling and detection of ATP bioluminescence on the surface were performed before and after treatment at the first day, as well as after treatment at the 7th and 14th day of the study. An aerobiological measurement was also performed outdoor of the patient's bedroom only for the first day. **Results:** Our analysis confirms that low ozone levels induced a marked reduction of indoor air microbiological pollution without adverse effects on lung functionality of the asthmatic patient we considered. **Conclusion:** Our observations warrant further investigation on the role that ozone-based sterilization might have in controlling asthmatic symptoms.

KEY WORDS: Allergy, asthma, cough, environmental pollution, fungi, ozone

INTRODUCTION

Asthma is a common, chronic respiratory disease affecting 1-18% of the general population in different countries. Manifestations of this disease are heterogeneous with different symptoms including: wheeze, shortness of breath, chest tightness and/or cough, and variable expiratory airflow limitation. These symptoms are often triggered by different factors: exercise, exposure to allergens or irritant substances, weather changes or viral respiratory infections [1].

During last decades, an increase in the prevalence of asthma and other allergic diseases has been recorded, together with modifications of living environments and consequent changes in the quality of indoor air. As a matter of fact, an increase of time spent indoor may be associated with a higher risk of allergen exposure, resulting in the increase in sensitization and symptoms of asthma and allergy [2].

The indoor environment is favorable to proliferation of allergens such as house dust mites, fungal spores and cockroaches. Additionally, the number of household pets (mainly cats, dogs and rodents) has risen in the last decades [3-6]. The most common house dust mite species are *Dermatophagoides pteronyssinus* and *Dermatophagoides farinae*, with approximately 20% of the adult population in Europe being sensitized to *D.pteronyssinus*. Dust mite allergens are commonly found on dust collected from carpets, mattresses and other soft furnishings, whereas the primary site for cockroach allergen accumulation is the kitchen, but lower levels of allergen can be also found in bedding, on bedroom floor and in the dust coming from soft furnishings [3]. Indoor fungal contamination is affected by several environmental parameters, including moisture, temperature, ventilation and organic matter on building materials, as well as by outdoor fungal load [7, 8]. Fungal contamination can be a useful indicator of poor indoor air quality, with consequences for health and well-being [9].

The exposure to indoor allergens is thought to induce symptoms and exacerbations in sensitized individuals [10], as confirmed by Gent *et al* [11], who showed that asthma severity in children correlates to the level of exposure to common indoor allergens such as dust mites. However, conflicting evidence coming from several epidemiologic, experimental, and interventional studies still makes the relation between indoor allergens and asthma and allergy unclear [2].

According to the recent European Academy of Allergy and Clinical Immunology (EAACI) position paper [12], the effectiveness of interventions that reduce allergen exposure can be properly evaluated only when appropriate allergen measurements are performed, together with an accurate diagnosis of pathology and a comprehensive management of patients, in the context of routine surveillance of indoor environment (*e.g.*, work environment surveillance), interventional studies, or population-based studies assessing exposure-response relationships [12]. Nevertheless, exposure reduction or cessation are considered a key step in prevention and management of occupational asthma and allergy [13-15].

The use of bedding covers as the sole measure to prevent allergy-triggered attacks showed small or no benefit in improving quality of life and reduce symptoms of patients affected by asthma and rhinitis [16-18]. To minimize allergens exposure, it is important to reduce the presence of in site sources like carpets, upholstered furniture, as well as stuffed animals and to regularly vacuum-clean floors using devices with high-efficiency particular air filters [19]. Although the Environmental Protection Agency (EPA) recommends air filtration, a careful control of the sources of allergy-causing pollution and adequate indoor ventilation is considered to be more relevant. On the other hand, efforts should be made to eradicate house dust mites, fungi and bacteria infestations. The primary action for an effective eradication constitutes in modifying the house environment conditions that make it favorable to infestations. The use of modern dehumidifiers to maintain the relative humidity below 50% can reduce mite population and thus allergen exposure [20, 21]. In temperate climates, humidity regulation is an easy and effective measure, but in warm and humid regions, suitable humidity levels may be difficult to gain. Because of high temperature sensitivity of dust mites (> 50°C) [22], steam cleaning and hot air treatment (> 110°C) were reported as effective methods to kill them and to reduce environmental allergenic concentration [23, 24]. Unfortunately, these maneuvers have a limit: if temperature does not reach the target level, the steam could contribute itself to mite and mold proliferation. Several chemical agents have also been tested to control the levels of mite allergens, but evidences of their effectiveness in standard conditions are still scarce [25, 26].

Ozone is a trivalent oxygen molecule, and a gas present in nature. It was discovered in 1840 and is characterized by high instability and a peculiar chlorine smell. Ozone is commonly found in stratosphere and its concentration is maintained by the ozone-oxygen cycle. The ozone molecule is formed because of the action of short-wave ultraviolet radiations (mostly UVC) which split an oxygen (O_2) molecule in two oxygen (O) atoms. Atomic oxygen reacts with molecular oxygen to form an ozone (O_3) molecule, according to following reactions:

$$O_2 + UV \rightarrow 2O$$

$$O + O_2 \rightarrow O_3$$

UV rays with a wavelength between 240 and 310 nm are absorbed by ozone molecules, which are demolished to a molecule and an atom of oxygen:

$$O_3 + (240\ nm < UV < 310\ nm) \rightarrow O_2 + O$$

This mechanism is at the base of the so-called 'ozone shield', which, among the other effects, is essential in preventing oxidative damages of the DNA of living beings [27].

The ozone found at lower altitudes is formed instead through the interaction between sunlight and hydrocarbons or nitrogen oxides and it significantly contributes to air pollution [28]. In the ground atmosphere ozone is detectable at 0.02-0.04 ppm and even small concentrations of ozone can mask other smells, a characteristic that suggested its use as air purifier. Ozone usefulness for "air cleansing" was already a matter of debate in the early 20th century [29] and in recent times the disinfecting properties of ozone were better investigated. Ozone has to be produced immediately before its use because of its short half-life at atmospheric pressure. Most of the ozone generators use the corona discharge effect, which produces ozone plasma [30]. Ozone is already widely used for disinfection of wasted waters [31, 32] and it is approved by FDA for fruit cleaning. The microbicidal activity of ozone is influenced by several environmental factors such as relative humidity, temperature and pH. The gaseous ozone has been already tested on different bacterial strains [33]. Sharma and Hudson [34] demonstrated the *in vitro* efficacy of ozone generators in reducing Gram positive and Gram negative bacteria colonies; better results were observed with high levels of relative humidity (90%) and ozone concentrations of 25 ppm. In another study, higher concentrations (50-500 ppm) of ozone and hydrogen peroxide were tested in a large room (90 m^3) on healthcare-associated pathogens. After the gaseous ozone exposure, a significant reduction of the tested pathogens and spores were observed [35]. Ozone is also used in food industry in USA since 1997 (and earlier in Europe) with several applications [36] and research is still active. A recent study demonstrated its effectiveness to control mite infestations on smoked ham (speck): after 15 days (8 h/day) of treatment with ozone at the concentration of 0.4 ppm, a complete elimination of food mites was observed [37]. Others beneficial effects of ozone have been reported in the treatment of several conditions such as vertebral disc herniation [38-40], atherosclerosis [41] and ischemic insults [42, 43], mostly by means of infiltrations. The therapeutic action of ozone is thought to be mediated by an up-regulation of antioxidant activity following its administration [44, 45]. The most important precaution to ozone exposure, particularly in patients with asthma, is to avoid excessive concentrations. Indeed, prolonged exposure to high concentrations of ozone may result in a strong inflammatory response of the airways [46, 47], vagal stimulation, change in pulmonary function including bronchoconstriction [48], although studies on lower ozone concentrations (0.02 ppm) have shown controversial results [49, 50]. The recommended limit of exposure suggested by the World Health Organization (WHO) is 100 $\mu g/m^3$ (approx. equivalent to 50 ppb) for 8 h/day

(75 ppb for the United States Environmental Protection Agency) [51]. Because of the risk of dangerous effects of ozone on health, laboratory concentrations used to kill mites are not reachable in home settings. However, it has been demonstrated that subjects exposed to ozone under controlled conditions below 72 ppb had a non-statistically different change in lung function when compared to subjects exposed to filtered air. Moreover, when exposed to concentrations greater than 72 ppb, the subjects showed no adverse effect on lung functionality because observed effects were transient, reversible, low in severity and did not establish a progressive respiratory dysfunction [52].

Ozone can play a sanitizing role but, at the same time, it can cause inflammation, especially in the lung. The aim of this study was to verify the role and safety of ozone in the sanitation of the bedroom of a subject suffering from asthma.

MATERIALS AND METHODS

Patient characteristics

A 15-year-old male subject presented an intermittent, non-productive, hacking cough since infancy. His medical history was positive for atopy, and diagnosis of asthma was made in 2005. Postnasal drip syndrome, gastroesophageal reflux and postinfectious cough were excluded. Review of systems was unremarkable and the results of physical examination were normal. He had got no pets in his apartment. Spirometry revealed normal pulmonary function with reversibility after bronchodilator challenge with a β_2-agonist. Skin-prick test was positive for house dust mites. He used to record asthma symptoms by means of the Asthma Control Test (ACT) [53], and he had a good but not complete symptom control (ACT score equal to 23) during his therapy with inhaled corticosteroids, long acting β-adrenoreceptor agonist and antileukotriene drugs. Dextromethorphan was used as cough suppressant on demand.

In the last month he reported ACT score 23, because he had cough at night. Therefore, we decided to test the efficacy of bedroom conditioning with ozone prior to sleep by making environmental measurements in order to verify if a reduction of the microbial load both in the air and on surfaces was present during the test and to test if the patient had no change in his asthmatic status.

Protocol to detect sanitization effects of ozone treatment

The following procedure was developed for this study by the Institute of Atmospheric Sciences and Climate (ISAC) (National Research Council - Consiglio Nazionale delle Ricerche; CNR, Bologna, Italy). A daily ozone treatment was carried during a 14-day time period in the bedroom of the patient (12 m^2) using an ozone generator (ProWind MG100, MET Srl, San Lazzaro di Savena, Bologna, Italy) working for 60 min in order to keep air ozone at the fixed concentration of 0.06 ppm (60 ppb), followed by 120 min of post-exposure decanting process (depletion phase). The whole treatment was performed while maintaining door and windows closed and started at 7:00 pm. Only at the end of this 3 h period, the patient could sleep in the bedroom with door and windows closed. The ozone generator was located at 1.5 m above the ground. ProWind is a microprocessor-controlled device that gives the possibility of many treatment periods, on the basis of environmental contamination, without changing the levels of ozone concentration.

Experimental design

Sampling was performed weekly in the patient's bedroom during three different days (1st day, November 28th, 2013: twice, both pre- and post-ozone treatment; December 5th, 2013: after 7 days of ozone treatment; and December 12th, 2013: after 14 days of ozone treatment). Each sampling was carried-out collecting the following measures (Table 1):

Table 1. Sampling scheme of the protocol applied to detect sanitization effects of ozone treatment

Sampling time	Sample ID	Measures	Location and timing of sampling
	Ce	Airborne bioaerosol	Outside – air
	C1_0	Airborne bioaerosol	Inside, O_3 pre-treatment – air
	S1_0	Deposited bioaerosol	Inside, O_3 pre-treatment – surface
1st day	B1_0	ATP bioluminescence	Inside, O_3 pre-treatment – surface
	C1_3	Airborne bioaerosol	Inside, 3 h O_3 post-treatment (60') and depletion (120') – air
	S1_3	Deposited bioaerosol	Inside, 3 h O_3 post-treatment (60') and depletion (120') – surface
	B1_3	ATP bioluminescence	Inside, 3 h O_3 post-treatment (60') and depletion (120') - surface
	C7_3	Airborne bioaerosol	Inside, 3 h O_3 post-treatment (60') and depletion (120') – air
7th day	S7_3	Deposited bioaerosol	Inside, 3 h O_3 post-treatment (60') and depletion (120') – surface
	B7_3	ATP bioluminescence	Inside, 3 h O_3 post-treatment (60') and depletion (120') - surface
	C14_3	Airborne bioaerosol	Inside, 3 h O_3 post-treatment (60') and depletion (120') – air
14th day	S14_3	Deposited bioaerosol	Inside, 3 h O_3 post-treatment (60') and depletion (120') – surface
	B14_3	ATP bioluminescence	Inside, 3 h O_3 post-treatment (60') and depletion (120') - surface

Each sampling was coupled with temperature, humidity and ventilation measures

aerobiological sampling of airborne bioaerosol in indoor air, microbiological sampling (deposited bioaerosol) and detection of ATP bioluminescence on the surface; details of these measurements are given in the next sections. An aerobiological measurement was also performed outdoor of the patient's bedroom only for the first day. Temperature and relative humidity were measured during the whole course of the study (outside and inside before treatment at the 1st day as well as inside after the 3 h ozone treatment at the 1st, 7th, and 14th days) with a portable digital thermo-higrometer (Thermo-Higro, LPS Technologies, San Marcos, CA, USA). A portable hot-wire anemometer (TA 888, Dostmann Electronic GmbH, Wertheim, Germany) was used to measure indoor ventilation. The investigation of building structure (walls) of the bedroom was also performed in order to identify internal sources of biological contaminants (mold, fungi, *etc*). The study protocol was approved by the Italian Association for Cough Study institutional review board and conformed to the ethical guidelines of the Declaration of Helsinki. The study started after the informed consent was signed.

Aerobiological sampling

Active air sampling was performed by a portable surface air system (SAS super-100 sampler, PBI International, Milan, Italy) with a capacity of 100 l/min and a single-stage sampling head. Ninety millimeter Petri dishes, containing agar culture medium, were placed below the filter to trap viable particles. In detail, a plate count agar (PCA) (Oxoid Standard Plate Count Agar, Thermo Fisher Scientific Inc, Waltham, MA, USA) was used to grow viable bacteria, and a Sabouraud dextrose agar with chloramphenicol (SDA+CAF) (Oxoid Sabouraud Dextrose Agar, Thermo Fisher Scientific) was utilized for yeasts and molds. Before each sampling, the sampler was disinfected with denatured ethanol. Only for the first day, the aerobiological sampling was carried out in two different points: one at the center of the room for a volume of 100 liters of air (60 s of time), the other outside the room, for a volume of 33.3 l of air (20 s of time). In both cases, the sampler was placed at approximately 150 cm from the ground.

Subsequent aerobiological samplings were performed only inside the room, according to the scheme reported in Table 1. Collected Petri dishes, two for each culture medium, were stored at 25°C for 5-7 days (SDA+CAF) or at 22°C for 3 days (PCA). Following incubation, grown colonies were counted. Double-replicate plates were used. Positive-hole correction was applied to the raw value of colony forming units (CFU) as obtained from each plate, and then used along with sampling time and flow rate to calculate concentration, with the final value expressed as CFU per cubic meter of air (CFU/m^3). The results were expressed in total microbial load (TML), as well as in bacterial and fungal loads.

Surface sampling

Surface monitoring was performed on a stiff horizontal shelf, about 1 m above ground level, as reported in Table 1. The area investigated was continuous and without specific cleaning treatment. Sampling was carried out directly from the surface using a 55 mm contact plate with the same two culture media used for air sampling: PCA for viable bacteria, SDA+CAF for yeasts and moulds. All microbiological samplings were carried out twice on adjacent surfaces for each point and cultural medium type. A constant pressure of 500 g was applied on the plate for 10 s, as requested by ISO 18593 [54] procedure, to perform a standardized sampling. In order to evaluate microbial contamination, the number of colonies grown after incubation (with incubation conditions and counting procedure as detailed above for aerobiological sampling) was examined at the CNR-ISAC aerobiology laboratory. The results of surface monitoring were expressed as CFU/cm^2.

An assessment of biological contamination was also carried out directly on the bedroom surface through the detection of ATP bioluminescence (which is extensively used in the food industry as a tool for monitoring surface hygiene). We used a portable sampler (Hygenia System-Sure II Plus, RG Strumenti Srl, Parma, Italy) with disposable swabs provided with the necessary pre-dosed reagents. After sampling on horizontal surface squares of 10 x 10 cm, the swab was inserted into a reader and a quick numeric reading was produced within 15 s. The results were expressed as relative light units (RLU). We decided to perform such measurements in order to indirectly detect the presence of viable organisms on sampled surfaces, and in particular the amount of mites, since this assay has been already used as a suitable method able to detect mites viability by Ebina and Ohto in 2007 [55].

Asthma Control Test (ACT)

The ACT was firstly described by Nathan *et al* in 2004 [53]: it is a simple test for asthmatic people older than 12 years that analyzes the trend of the disease symptoms and the consequent effectiveness of therapy in the last four weeks. The test is composed by five questions that evaluate the following 5-point scales: limitation of activity, frequency of shortness of breath, night symptoms' severity (wheezing, coughing, shortness of breath, chest tightness or pain), necessity of rescue medication, and patient's point of view about his/her asthma control. Asthma control is achieved when the patient shows satisfaction about asthma in the last month, he/she does not declare coughing or wheezing, no night-time interruptions and no emergency visits to the doctor or hospital. The final score is a number between 5 and 25, with a total score of 19 or less meaning that the disease is not controlled, a score between 20 and 24 meaning that asthma is controlled, although not completely, and a score of 25 suggesting full disease control.

ACT was submitted to the patient the first day before the treatment start and one day after the last ozone treatment.

Data reporting

Data are reported as mean and standard deviation (SD) of the two replicates. No inferential statistics were applied because of the preliminary nature of the study that investigated a single case.

The analyzed room had a natural ventilation, domestic heating and no air-conditioning. Indoor wind speed was always less than 0.3 m/s. Air temperature was between 17-19°C indoor and 10-12°C outdoor. Indoor and outdoor relative humidity was 40-43% and 70%, respectively. The bedroom was free from damage by building moisture or visible molds.

RESULTS

Aerobiological result

Figure 1 shows the colonies grown on Petri dishes after the incubation period and before morphological analysis. The morphological evaluation of the total microbial load, as well as the bacterial and fungal loads, in air resulting from the aerobiological analysis (airborne bioaerosol) is reported in Figure 2. The outdoor value indicates a microbiological pollution lower than the internal one (Ce 185 CFU/m^3 *vs* C1_0 225 CFU/m^3; Figure 2a) which is characterized by a naturally high environmental variability. The concentration value after treatment (C1_3, C7_3 and C14_3) showed a conspicuous breakdown all over the time: there was an 84% reduction for the total microbial load by comparing pre- and post-treatment concentration of the first sampling day (C1_0 *vs* C1_3) and the TML remained low on subsequent sampling (C7_3, C14_3).

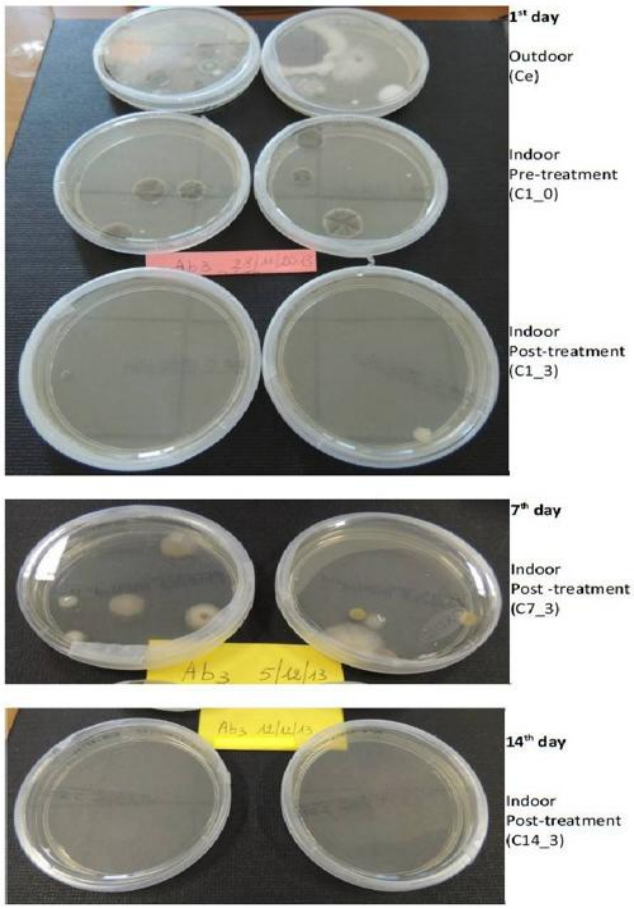

Figure 1. Aerobiological measurements: visible colonies in the used Petri dishes.

Figures 2bc shows the details of the different contribution of bacterial and fungal loads. The outdoor/indoor ratio (*i.e.*, Ce/C1_0) was in accordance to previous observations [34, 35] since the bacteria were abundant indoor (about four times more than outdoor) and rather constant between the indoor measurements, whereas fungal spore concentration was higher outdoor (about three times more than indoor) with conspicuous variation between outdoor measurements.

Consistently with what observed with the TML, in both cases both loads abruptly decreased after treatment in the first day of the study (C1_3 *vs* C1_0: 87% and 70% reduction for bacteria and fungi were observed, respectively) and stayed low in the following two weeks (C7_3 and C14_3). Notably, fungal load broke down completely at the end of the study period. The measurement variability before and after treatment showed a good stability of indoor environment.

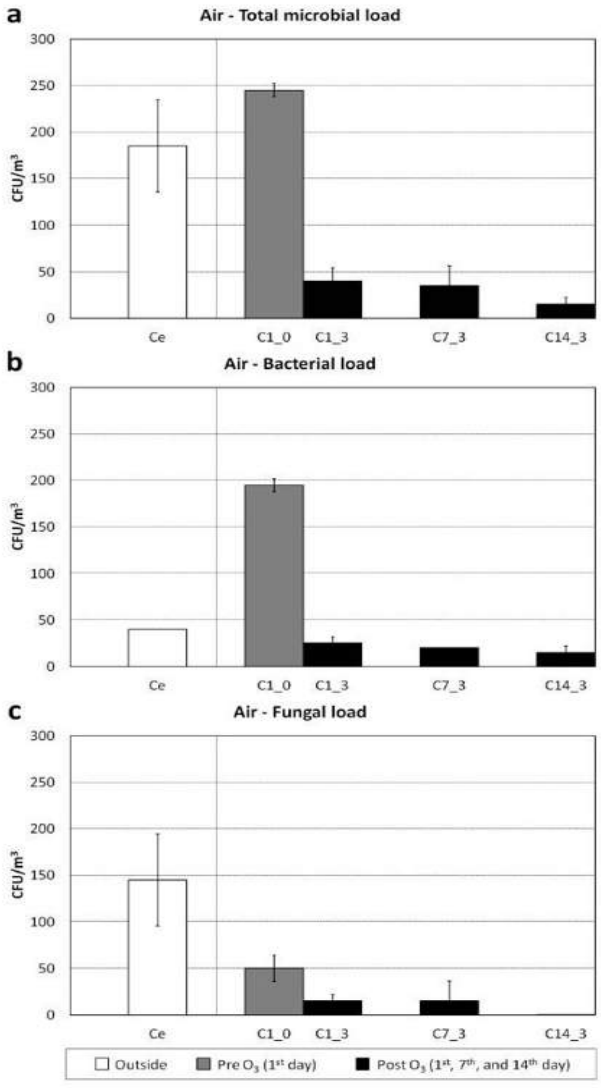

Figure 2. Total microbial **(a)**, bacterial **(b)**, and fungal loads **(c)**: aerobiological result during the two weeks of treatment (mean ± SD values of two replicates).

Surface result

The microbiological analysis of surfaces is shown in Figure 3. A rather low level of internal pollution was found even before treatment (the mean values of TML were always less than 100 CFU/cm^2). As far as the behavior of the two agents is concerned, the comparison between pre-and post-treatment values of bacterial load evaluated in the first day showed no evidence of sanitization, and afterwards the post-treatment bacterial load showed a decrease after two weeks only. On the other hand, the post-treatment fungal load showed a progressive increase during the two weeks of treatment, even if the values remained at a very low level.

Bioluminescence data showed a decrease with the treatment of the first day (B1_0: 126 RLU; B1_3: 44 RLU; before and after 3 ozone treatment, respectively) with an irregular behavior of the post-treatment values measured after 7 (B7_3: 179 RLU) and 14 (B14_3: 53 RLU) days. There was no apparent correlation between ATP bioluminescence and microbial loads, as shown in Figure 4.

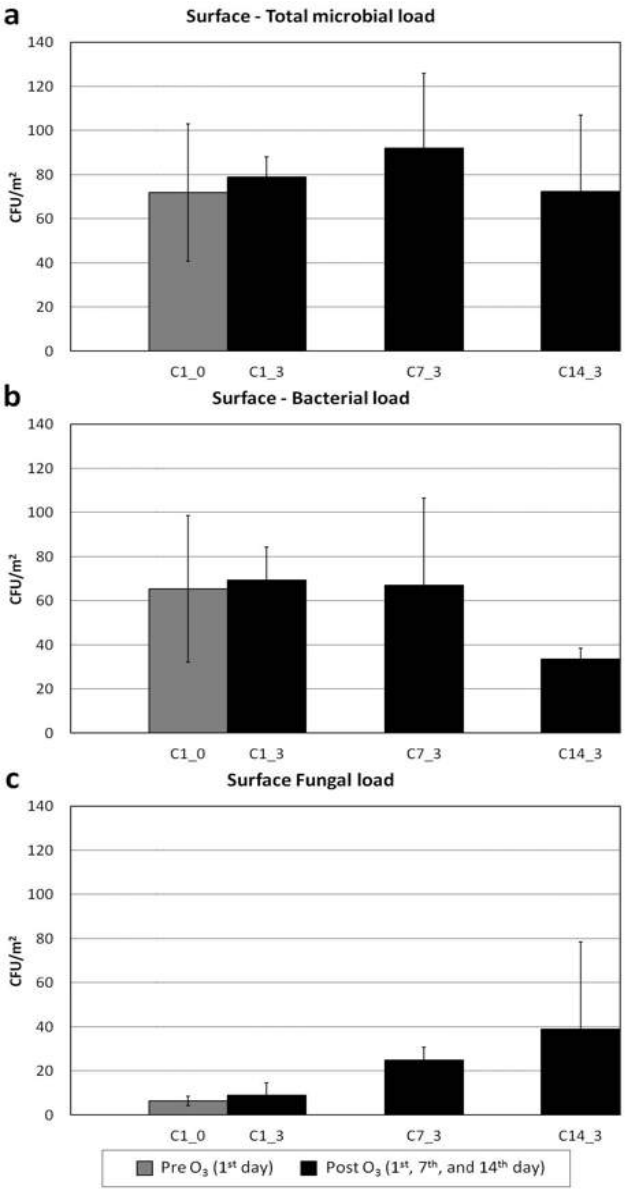

Figure 3. Total microbial **(a)**, bacterial **(b)**, and fungal loads **(c)**: surface contact measurements during the two weeks of treatment (mean ± SD values of two replicates).

Clinical result

Before ozone treatment the asthma was not completely controlled (ACT score 23) because the patient reported cough and the patient subjective evaluation of asthma was "well controlled" (both scored 4 in the questionnaire), while limitation of activity, frequency of shortness of breath, and necessity of rescue medication scored 5. At the end of the two-week time period of the study, although the patient reported a value of ACT score increased to 24 the asthma was still not completely controlled because, even if he reported not at all waking for coughing (score 5) during the 14-day chamber exposure study, he still defined his disease as "well controlled" (instead of "completely controlled").

DISCUSSION

In the present report, we assessed the effect of an ozone-based sterilizing technique on the indoor allergen load in the bedroom of an asthmatic patient. The first noteworthy observation we made was that indoor microbiological air pollution (assessed as TML) was higher than that observed outdoor. This confirms the effect of bioaerosol accumulation in absence of natural dispersion driven by wind, as well as, it suggests that lifestyles and sanitation strategies adopted by inhabitants may greatly affect indoor levels of allergens. As a consequence, indoor measurements seem to give more accurate indications on the exposure of people to pollutants, especially in industrial countries, where about 90% of the time is spent indoor.

Moreover, we evidenced that TML in air decreased after ozone treatment. This seems to confirm the efficacy of ozone in sanitizing indoor air, regardless of environmental re-contamination due to daily room opening. The same

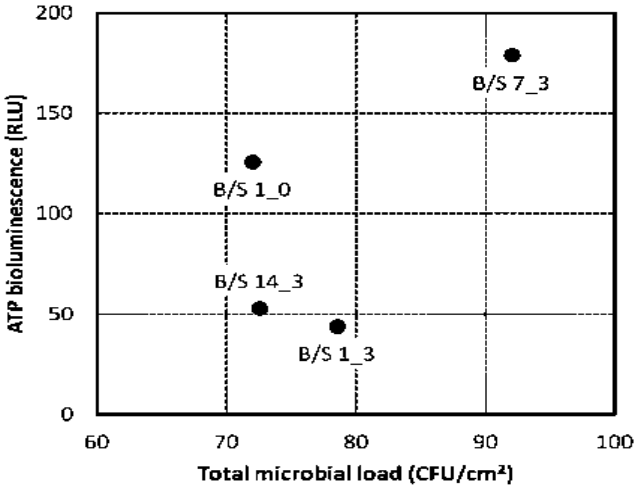

Figure 4. Direct comparison among ATP bioluminescence (relative light units, RLU) and total microbial load (TML, CFU/cm^2) in evaluating surface contact results.

applies to fungal and bacterial loads. The ozone sterilizing technique we employed was able to significantly reduce both bacterial and fungal indoor pollution since reference values of "very low" microbiological air pollution levels in domestic environments are less than 100 CFU/m^3 for bacterial load and less than 50 CFU/m^3 for fungal load [56]. Interestingly, while after 14 days of treatment bacterial load was clearly below the 100 CFU/m^3 threshold, fungal air pollution was completely abolished. On the contrary, no clear effect was observed for surface pollution. The preliminary nature of our observations makes risky to draw a general conclusion and our results should be confirmed by further analyses; however, many different explanations may account for the ambiguous effects observed for surface pollution. For instance, it is possible that the ozone surface treatment might require a longer period to be effective, or that longer exposures to ozone at each session are needed to achieve an effective surface sanitization. Additionally, considering the very low values initially observed, an ozone-related sanitization effect might have been hidden by background variability.

ATP bioluminescence data are in good agreement with sanitization. The relative light unit (RLU) decreased from 126 to 44 with the first treatment, and maintained a value of 53 after the last one, but surprisingly the intermediate treatment showed a value even higher than that detected with no treatment (179 RLU). It is hard to explain this result, but we have to mention that we could not control the cleaning activities of people living inside the apartment, although the inhabitants were properly trained in maintaining a constant and reproducible cleaning during the two-week time of this study.

The comparison between ATP bioluminescence and microbiological data showed no clear correlation. A larger sampling is indeed needed, but we may suggest that ATP bioluminescence might not be accurate enough as a measure of viable organisms: for example, fungal spores have a complex wall and, being resistant forms allowing fungi to survive under unfavorable conditions, they are not metabolically active. Our first intention was to use this method for indirectly detecting mite contamination since this measure has been applied to detect mite viability [55]. The results of this study do not support our hypothesis for the same above mentioned reasons and more analyses are needed in order to evaluate a possible role of ATP bioluminescence in detecting mite contamination.

Although, ozone seems to be useful in reducing indoor microbiological pollution, at least in the air, it should be kept in mind that some cautions are required when ozone is used. The most important one is to avoid excessive concentrations when ozone is used in sanitization for patients with asthma. Exposition to high concentrations of ozone may result in an increased inflammatory response of airways and in a reduction of pulmonary function [46, 47, 49, 50]. The used ozone concentrations were in line with the recommendations of the World Health Organization [51], and despite this 'limited exposure', an effective reduction of the total microbial load in the air was reached (Figure 2a), whereas this tendency was not confirmed by the analysis of surface pollution (Figure 3a). The killing effect of ozone on house microorganisms and dust mites is probably mediated by the production of oxidizing agents arising from the peroxidation of polyunsatured fatty acids and from oxidation of lipids and thiols, which could damage cell walls, membranes, cytoplasm components and DNA. Prolonged expositions to gaseous ozone could lead to a progressive damage of core constituent of microorganisms without significant adverse effects on patient's health [57], as well as the internal space was preserved since the surfaces were not physically damaged during the treatment with ozone.

It is difficult to anticipate whether the reduction of air TML we observed may have a clinical relevance in controlling asthma symptoms, since the patient we considered already had a good level of disease control, making hard the detecting of a further improvement in his symptomatology. Nevertheless, the moderate improvement of ACT score that was found at the end of the treatment period (due to the improvement of the night cough) confirms the safety of this maneuver, since an excessively high level of ozone would have likely led to symptoms deterioration and thus to ACT score reduction. Therefore, our observations on air TML, coupled with the absence of negative effects observed in the asthmatic patient, pose the basis for a further investigation on this technique involving a larger number of asthmatic patients, particularly by selecting those with a poorer control of symptoms.

Like the Roman God Janus, sterilization using ozone has two faces: it is effective in reducing the indoor microbial load but, if it is obtained through high ozone levels, it might pose a health risk, especially in asthmatic patients. Nevertheless, our analysis confirmed the effectiveness of low ozone levels to induce a marked reduction of air microbiological pollution, although the same effect was not apparent for surface pollution. At the same time, the low levels of ozone employed were safe for the asthmatic patient we considered, since we observed no deterioration in his symptomatology. Taken together, our observations warrant further investigation on the role ozone-based sterilization might have in controlling asthmatic symptoms.

ACKNOWLEDGEMENT

We thank to Dr. Elisabetta Maiolini for her support to environmental monitoring.

REFERENCES

1. Global Initiative for Asthma. Global Strategy for Asthma Management and Prevention, 2015.
2. Arshad SH. Does exposure to indoor allergens contribute to the development of asthma and allergy? Curr Allergy Asthma Rep 2010; 10:49-55.
3. Platts-Mills TA, Vervloet D, Thomas WR, Aalberse RC, Chapman MD. Indoor allergens and asthma: report of Third International Workshop. J Allergy Clin Immunol 1997; 100:S2-24.
4. Crameri R, Garbani. M, Rhyner C, Huitema C. Fungi: the neglected allergenic sources. Allergy 2014; 69:176-85.
5. Gent JF, Kezik JM, Hill ME, Tsai E, Li DW, Leaderer BP. Household mold and dust allergens: exposure, sensitization and childhood asthma morbidity. Environ Res 2012; 118:86-93.
6. Tischer CG, Hohmann C, Thiering E, Herbarth O, Müller A, Henderson J, Granell R, Fantini MP, Luciano L, Bergstrom A, Kull I, Link E, von Berg A, Kuehni CE, Strippoli MP, Gehring U, Wijga A, Eller E, Bindslev-Jensen C, Keil T, Heinrich J; ENRIECO consortium. Meta-analysis of mould and dampness exposure on asthma and allergy in eight European birth cohorts: an ENRIECO initiative. Allergy 2011; 66:1570-9.
7. Medrela-Kuder E. Seasonal variations in the occurrence of culturable airborne fungi in outdoor and indoor air in Cracow. Int Biodeterior Biodegrad 2003; 52:203-5.
8. Oliveira M, Ribeiro H, Abreu I. Annual variation of fungal spores in atmosphere of Porto. Ann Agric Environ Med 2003; 12:309-15.
9. World Health Organization. WHO Guidelines for Indoor Air Quality: Dampness and Mould. Copenhagen, 2009.
10. Salo PM, Arbes SJ Jr, Crockett PW, Thorne PS, Cohn RD, Zeldin DC. Exposure to multiple indoor allergens in US homes and relationship to asthma. J Allergy Clin Immunol 2008; 121:678-84.
11. Gent JF, Belanger K, Triche EW, Bracken MB, Beckett WS, Leaderer BP. Association of pediatric asthma severity with exposure to common household dust allergens. Environ Res 2009; 109:768-74.
12. Raulf M, Buters J, Chapman M, Cecchi L, de Blay F, Doekes G, Eduard W, Heederik D, Jeebhay MF, Kespohl S, Krop E, Moscato G, Pala G, Quirce S, Sander I, Schlunssen V, Sigsgaard T, Walusiak-Skorupa J, Wiszniewska M, Wouters IM, Annesi-Maesano I; European Academy of Allergy and Clinical Immunology. Monitoring of occupational and environmental aeroallergens- EAACI Position Paper. Concerted action of the EAACI IG Occupational Allergy and Aerobiology & Air Pollution. Allergy. 2014, 69:1280-99.
13. Tarlo SM, Balmes J, Balkisson R, Beach J, Beckett W, Bernstein D, Blanc PD, Brooks SM, Cowl CT, Daroowalla F, Harber P, Lemiere C, Liss GM, Pacheco KA, Redlich CA, Rowe B, Heitzer J. Diagnosis and management of work-related asthma: American College of Chest Physicians Consensus Statement. Chest 2008; 134:1-41S.
14. Nicholson PJ, Cullinan P, Taylor AJ, Burge PS, Boyle C. Evidence based guidelines for the prevention, identification, and management of occupational asthma. Occup Environ Med 2005; 62:290-9.
15. Vandenplas O. Asthma and rhinitis in the workplace. Current Allergy Asthma Rep 2010; 10:373-80.
16. Terreehorst I, Duivenvoorden HJ, Tempels-Pavlica Z, Oosting AJ, de Monchy JG, Bruijnzeel-Koomen CA, van Wijk RG. The effect of encasings on quality of life in adult house dust mite allergic patients with rhinitis, asthma and/or atopic dermatitis. Allergy 2005; 60:888-93.
17. de Vries MP, van den Bemt L, Aretz K, Thoonen BP, Muris JW, Kester AD, Cloosterman S, van Schayck CP. House dust mite allergen avoidance and self-management in allergic patients with asthma: randomised controlled trial. Br J Gen Pract 2007; 57:184-90.
18. Koopman LP, van Strien RT, Kerkhof M, Wijga A, Smit HA, de Jongste JC, Gerritsen J, Aalberse RC, Brunekreef B, Neijens HJ; Prevention and Incidence of Asthma and Mite Allergy (PIAMA) Study. Placebo-controlled trial of house dust mite- impermeable mattress covers: effect on symptoms in early childhood. Am J Respir Crit Care Med. 2002; 166:307-13.
19. United States Environmental Protection Agency. Air Quality Guide for Ozone - Protect Your Health. Available via http://nepis.epa.gov/Exe/ZyPDF.cgi/P1001FME.PDF?Dockey=P1001FME.PDF (Accessed 16 December 2015) March 2008.
20. Arlian LG, Neal JS, Morgan MS, Vyszenski-Moher DL, Rapp CM, Alexander AK. Reducing relative humidity is a practical way to control dust mites and their allergens in homes in temperate climates. J Allergy Clin Immunol 2001; 107:99-104.
21. Arlian LG, Neal JS, Vyszenski-Moher DL. Reducing relative humidity to control the house dust mite Dermatophagoides farinae. J Allergy Clin Immunol 1999; 104:852-6.
22. Chang JCS, Arlian LG, Dippoid JS, Rapp CM, Vyszenski-Moher DL. Survival of the house dust mite, Dermatophagoides farinae at high temperatures (40-80°C). Indoor Air 1998; 8:34-8.
23. Colloff MJ, Taylor C, Merrett TG. The use of domestic steam cleaning for the control of house dust mites. Clin Exp Allergy 1995; 25:1061-66.
24. Htut T, Higenbottam TW, Gill GW, Darwin R, Anderson PB, Syed N. Eradication of house dust mite from homes of atopic asthmatic subjects: a double blind trial. J Allergy Clin Immunol 2001; 107:55-60.
25. Hayden ML, Rose G, Diduch KB, Domson P, Chapman MD, Heymann PW, Platts-Mills TA. Benzyl benzoate moist powder: investigation of acaricidal (correction of acarical) activity in cultures and reduction of dust mite allergens in carpet. J Allergy Clin Immunol 1992; 89:536-45.
26. Woodfolk JA, Hayden ML, Miller JD, Rose G, Chapman MD, Platts-Mills TA. Chemical treatment of carpets to reduce allergen: a detailed study of the effects of tannic acid on indoor allergens. J Allergy Clin Immunol 1994; 94:19-26.
27. Kvam E, Tyrrell RM. Induction of oxidative DNA base damage in human skin cells by UV and near visible radiation. Carcinogenesis 1997; 18:2379-84.
28. Akimoto H. Global air quality and pollution. Science 2003; 302:1716-9.
29. Beckwith HL, Skolfield EM. The alleged purification of air by the ozone machine. JAMA. 1913; 61:1013-5.
30. Fraise AP, Maillard JY, Sattar S. Russell, Hugo & Ayliffe's: Principles and Practice of Disinfection, Preservation and Sterilization. Wiley-Blackwell, 5th edition, Hoboken, NJ, 2013.
31. Glaze WH. Drinking-water treatment with ozone. Environ Sci Technol 1987; 21:224-30.
32. Rice RG. Applications of ozone for industrial wastewater treatment - A review. Ozone Sci Engin 1996; 18:477-515.
33. Fontes B, Cattani Heimbecker AM, de Souza Brito G, Costa SF, van der Heijden IM, Levin AS, Rasslan S. Effect of low-dose gaseous ozone on pathogenic bacteria. BMC Infect Dis 2012; 12:358.
34. Sharma M, Hudson JB. Ozone gas is an effective and practical antibacterial agent. Am J Infect Control 2008; 36:559-63.
35. Zoutman D, Shannon M, Mandel A. Effectiveness of a novel ozone-based system for the rapid high-level disinfection of health care spaces and surfaces. Am J Infect Control 2011; 39:873-9.
36. Guzel-Seydim ZB, Greene AK, Seydim AC. Use of ozone in food industry. LWT Food Sci Technol 2004; 37:453-60.
37. Pirani S, Bersani C, Cantoni C. Ozone: alternative method for mite control on speck. Ital J Food Safety 2013; 6:83-4.
38. Andreula CF, Simonetti L, De Santis F, Agati R, Ricci R, Leonardi M. Minimally invasive oxygen-ozone theraphy for lumbar disk herniation. AJNR Am J Neuroradiol 2003; 24:996-1000.
39. Gallucci M, Limbucci N, Zugaro L, Barile A, Stavroulis E, Ricci A, Galzio R, Masciocchi C. Sciatica: treatment with intradiscal and intraforaminal injections of steroid and oxygen-ozone versus steroid only. Radiology. 2007; 242:907-13.
40. Bonetti M, Fontana A, Cotticelli B, Volta GD, Guindani M, Leonardi M. Intraforaminal O2-O3 versus periradicular steroidal infiltrations in lower back pain: randomized controlled study. AJNR Am J Neuroradiol 2005; 26:996-1000.
41. Delgado-Roche L, Martinez-Sanchez G, Re L. Ozone oxidative preconditioning prevents atherosclerosis development in New Zealand white rabbits. J Cardiovasc Pharmacol 2013; 61:160-5.
42. Ajamieh H, Merino N, Candelario-Jalil E, Menendez S, Martinez-Sanchez G, Re L, Giuliani A, Leon OS.. Similar protective effect of ischaemic and ozone oxidative preconditionings in liver ischaemia/reperfusion injury. Pharmacol Res 2002; 45:333-9.
43. Wainstein J, Feldbrin Z, Boaz M, Harman-Boehm I. Efficacy of ozone-oxygen therapy for the treatment of diabetic foot ulcers. Diabetes Technol Ther 2011; 13:1255-60.
44. Candelario-Jalil E, Mohammed-Al-Dalain S, Fernandez OS, Menendez S, Perez-Davison G, Merino N, Sam S, Ajamieh HH. Oxidative preconditioning affords protection against carbon tetrachloride-induced glycogen depletion and oxidative stress in rats. J Appl Toxicol 2001; 21:297-301.
45. Leon OS, Menendez S, Merino N, Castillo R, Sam S, Perez L, Cruz E, Bocci V. Ozone oxidative preconditioning: a protection against cellular damage by free radicals. Mediators Inflamm 1998; 7:289-4.

46. Graham D, Henderson F, House D. Neutrophil influx measured in nasal lavage of humans exposed to ozone. Arch Environ Health 1988; 43:228-33.
47. Kim CS, Alexis NE, Rappold AG, Kehrl H, Hazucha MJ, Lay JC, Schmitt MT, Case M, Devlin RB, Peden DB, Diaz-Sanchez D. Lung function and inflammatory responses in healthy young adults exposed to 0.06 ppm ozone for 6.6 hours. Am J Respir Crit Care Med 2011; 183:1215-21.
48. Schelegle ES, Carl ML, Coleridge HM, Coleridge JC, Green JF. Contribution of vagal afferents to respiratory reflexes evoked by acute inhalation of ozone in dogs. J Appl Physiol 1993; 74:2338-44.
49. McBride DE, Koenig JQ, Luchtel DL, Williams PV, Henderson WR Jr. Inflammatory effects of ozone in the upper airways of subjects with asthma. Am J Respir Crit Care Med 1994; 149:1192-7.
50. Scannel C, Chen L, Aris RM, Tager I, Christian D, Ferrando R, Welch B, Kelly T, Balmes JR. Greater ozone-induced inflammatory responses in subjects with asthma. Am J Respir Crit Care Med 1996; 154:24-9.
51. WHO Air quality guidelines for particulate matter, ozone, nitrogen dioxide and sulfur dioxide. Global update 2005; summary of risk assessment. WHO Press, Geneva, 2006.
52. Goodman JE, Prueitt RL, Chandalia J, Sax SN. Evaluation of adverse human lung function effects in controlled ozone exposure studies. J Appl Toxicol 2014; 34:516-24.
53. Nathan RA, Sorkness CA, Kosinski M, Schatz M, Li JT, Marcus P, Murray JJ, Pendergraft TB. Development of the asthma control test: a survey for assessing asthma control. J Allergy Clin Immunol. 2004; 113:59-65.
54. ISO 18593:2004 - Microbiology of food and animal feeding stuffs - Horizontal methods for sampling techniques from surfaces using contact plates and swabs. Available via http://www.iso.org/iso/catalogue_detail.htm?csnumber=39849 (Accessed 18 December 2015).
55. Ebina T, Ohto K. ATP assay for determining the viability of the two-spotted spider mite (Tetranychus urticae Koch) and the European red mite (Panonychus ulmi (Koch) (Acari: Tetranychidae) during diapauses. Appl. Entomol. Zool 2007; 42:291-6.
56. European Collaborative Action, Indoor Air Quality & Its Impact on Man, Report No.12, Biological Particles in Indoor Environments, Commission of the European Communities EUR 14988 EN 1993.
57. Pryor W. Free Radicals in Biology. Volume 1, Chapter 4, Academic Press, New York, NY, pp 189-198, 1976.

Conflict of Interest None declared

Defensive Architecture of the Mediterranean. XV to XVIII centuries / Vol II / Rodríguez-Navarro (Ed.)

DOI: http://dx.doi.org/10.4995/FORTMED2015.2015.1754

San Fernando Batteries in Portobelo - Panama: building materials characterization and the environmental impact evaluation

Chiara Ciantelli[a,c], Alessandra Bonazza[a], Cristina Sabbioni[a], Rodolfo A. Suñé Martínez[b], Carmela Vaccaro[c]

[a] Institute of Atmospheric Sciences and Climate, ISAC-CNR, Bologna, Italy, c.ciantelli@isac.cnr.it, a.bonazza@isac.cnr.it, [b] Patronato de Portobelo y San Lorenzo, República de Panamá, rsuneppsl@gmail.com, [c] Dipartimento di Fisica e Scienze della Terra, Università degli studi di Ferrara, Ferrara, Italy, vcr@unife.it

Abstract

The UNESCO site of San Fernando arises in the northern part of the Bay of Portobelo, on the Panamanian Caribbean coast, and belongs to a group of military fortifications erected during the XVII-XVIII centuries by the Spanish Empire. These defence structures were aimed at protecting the strategic outpost for the transoceanic trade, between the "New" and the "Old World", from the pirate attacks.

In order to safeguard this impressive site, the Institute of Atmospheric Sciences and Climate, ISAC-CNR (Bologna), the "Patronato de Portobelo y San Lorenzo" and the Department of Physics and Earth Sciences of the University of Ferrara have started a collaboration for characterizing and evaluating the state of conservation of the construction materials, considering the environmental impact on them.

Specifically this paper shows preliminary results obtained by mineralogical and petrographic characterization carried out by Polarized Light Microscopy (PLM), Environmental Scanning Electron Microscopy (ESEM-EDX) and X-Ray Diffraction (XRD) investigations.

Keywords: construction materials, environmental impact, Panamanian fortifications.

1. Historical background

1.1. San Fernando construction

Designed by the military engineer Ignacio Sala in 1753 and erected by Manuel Hernández in the period from 1753 to 1760, the current San Fernando batteries are part of the third stage of Portobelo's Military Architecture, named after King Ferdinand VI of Spain.

The constructions arise on the northern side of the bay of Portobelo and they are formed by a Fort and a Hilltop Stronghold. Specifically, the first one is made up of a Lower and an Upper Battery, connected by a covered way, which nowadays is shown by its remains; while the second one is located above the Upper Battery, about 100 meters height above sea level. Together with the Santiago de la Gloria and San Jerónimo ramparts, placed on the opposite coast, they represent the most strategic defence structures of the cove, allowing an attack from two frontlines of the enemy vessels which tried to penetrate the bay (World Monuments Fund, 2003; Tejera Davis, 2007; Gobierno Nacional República de Panamá et al., 2014).

1.2. 20th century and current situation

From the beginning of the XX century until the 70's the San Fernando Fortifications were described, by historical evidences, as mainly covered by vegetation, in particular the Lower Battery and the Stronghold, which were hidden by the forest. During 1970-71 the Instituto Panameño De Turismo (IPAT) performed the

"Portobelo Pilot Plan" in order to develop a documentation and a conservation campaign, carrying out deforestation and consolidation works at the site (World Monuments Fund, 2003).

In 1980 all the Caribbean Fortifications of Panama were included in the World Heritage List of UNESCO (http://whc.unesco.org/en/list/135); evertheless, in 2002, an inspection of the World Monuments Fund described the Fort of San Fernando in a poor state of conservation (World Monuments Fund, 2003). Later, they have belonged to the List of World Heritage in Danger since 2012. One year later the Instituto Nacional de Cultura of the Panamanian Government developed a Risk Assessment Study and published an Emergency Plan in order to safeguard the sites. Unfortunately this plan has not been executed yet, but thanks to the Patronato of Portobelo and San Lorenzo on site staff, cleaning, maintenance and some consolidation works have been performed (Osorio Ugarte, 2015).

With the aim of enhancing the knowledge of these structures and allowing a better preservation of the site, the following preliminary analysis define a characterization of the raw materials utilized and an investigation of the environmental impact on the buildings.

2. Environmental context

Situated on the Atlantic side of the isthmus, the Portobelo defence complex arises in a inlet of the Caribbean Sea.

According to the Panamanian geographer and historian, Dr. Alberto McKay, Portobelo climate is classified as "Tropical Oceanic Climate with short dry season", characterized by temperature mean values around 25.5°C on the coastal area and 26.5°C in the continental part. Abundant precipitations may reach annual amounts of 4760 mm, indeed the dry season has a brief duration of 4-10 weeks, with 40-90 mm of rain between February and March (Gobierno Nacional República de Panamá and Autoridad Nacional del Ambiente, 2010). These conditions allow high growth of vegetation, with high forest coverage, as aforementioned, also supported by the low urbanization of the bay, which can be considered a rural area especially on the side of San Fernando.

It has to be taken into account also the tidal variations, which affect the Lower Battery, being in proximity of the sea (Fig.1); indeed, even the inner part of the Fort is subjected to the water permeation.

Fig. 1- Overview of the Lower Battery. The proximity of the sea is clearly visible.

3. Materials and Methods

Sampling was performed in each of the three components of the defence group, specifically collecting 11 samples of construction materials (stone, mortar and plaster); in addition salt efflorescences were sampled from the inner part of the moat.

In this paper, they will be shown only the results related to the stone materials, collected from the two Batteries (Table 1).

In order to carry out mineralogical petrographic characterization, polarized light microscopy (PLM) observations were performed on thin sections using an Olympus BX 51 microscope, equipped with scanner and the MICROMAX software “Primoplus_32” vers. 8.11.02.. In conjunction, both on thin sections and on bulk samples, Environmental Scanning Electron Microscopy and microchemical investigations (ESEM-EDX) were carried out, utilizing a ZEISS EVO LS 10 with LaB6 source. Additionally, X-Ray Diffraction analyses (XRD) were performed for acquiring qualitative and semi-quantitative data on the crystalline phases

present in a concentration of at least 3-4%. This determination was obtained through a Philips PW 1730 diffractometer equipped with a copper anticathode and a nickel filter. The measurement conditions have a diffraction interval of 2θ, between 5° and 50°, and a 2°/minute step at 40kV voltage and 30 mA current intensity.

Site	*Sample*	*Location of sampling*
Lower Battery	PB SF 1	W-N wall, 2° embrasure (counted from the N side). h 125 cm (from the sole) - 60 cm from the external right corner of the mouth.
	PB SF 2	W-N wall, 2° embrasure (counted from the N side). S cheek, h 130 cm (from the sole) - 230 cm from the external left corner of the mouth.
	PB SF 5 (salts effloresc.)	Moat, west wall, between 6°-7° embrasure (counted from the N side). N cheek, h 125 cm - 130 cm from the 6°embrasure.
	PB SF 6	External part of the Fort, at the entrance by the sea.
	PB SF ramp	Belonging to the upper part of the ramp
Upper Battery	PB SF 7	Both from the masonry in the area called "Nave para artilleria y para la guardia". h 120 cm - 270 cm from the N wall.
	PB SF 8	
Outcrop	PB SF 11	Eastern outer part of the Lower Battery.

Table 1- Samples, sites and locations of sampling (for the description of the Fort elements ref. Spiteri, 1994)

4. Results and Discussion

Preliminary observations allowed us to identify the utilization of different materials, depending on the position and the function.

Coral limestones were identified in both the Batteries, by PLM observations (samples PB SF 2 and PB SF 8). The two samples of Scleractinian Reef Corals, probably ascribable to the family of Faviidae (Budd A. F. and Stolarski, 2011), have different wall structures, but showing the same primary intragranular porosity, where rare micritic calcite cement is present. In particular, the corallite having the structure observed in sample PB SF 2 is the mainly utilized and it was largely noticed in the: embrasures, banquettes, pavements and in the rests of the covered way. Considering the banquettes of the Lower Battery, the coral limestone was observed in specific zones like corners and embrasure entrance sills, thus parts which need strong materials. Indeed this rock shown high strength during the sampling. Nevertheless, both samples have an incomplete transformation of aragonite in calcite, since XRD results underline aragonite as dominant mineral, while calcite is only present or even in traces (Table 2).

Another sedimentary stone, a biogenic limestone (sample PB SF 1), was detected, through Optical Microscopy. It is characterized by macrofossils, as: lamellibranchia, foraminifera and bryozoa, set by scarce muddy cement, showing both a primary intragranular porosity and a secondary porosity mainly due to dissolution. In this case, diffraction analyses revealed calcite as dominant mineral, while quartz traces have been detected (Table 2). This kind of limestone was less utilized in comparison with the previous one.

Orogenic igneous rocks were identified, as basalt andesite of calcalkaline series in the masonry (samples PB SF 6 and PB SF 7), while basalt andesite of high-K calcalkaline series was collected from an outcrop present next to the entrance of the Lower Battery (sample PB SF 11). Notably, PLM observations revealed a porphyrytic - glomeroporphyrytic structure, mainly characterized by plagioclases and clinopyroxenes; in addition magnetite was also present. This is confirmed also by XRD analysis which shown albite and oligoclase as main crystal phases, followed by traces of augite and magnetite (Table 2). By Optical Microscopy study they were also noticeable zoned plagioclases with sericitized parts and devitrified zones in the vitric groundmass. Furthermore amygdales filled by zeolites were recognized and confirmed by ESEM-EDX analyses, detecting Si, O, Al, Ca, K, Na and Mg in ascending order of abundance.

Finally, sub-aphyric andesite was identified by PLM analysis, in the upper part of the ramp of Lower Battery (sample PB SF ramp). The reddish hue shown by the stone is due to the presence of iron oxides.

All these volcanic rocks were largely observed in the masonry, especially in the Upper Battery,

where they were utilized in the sole of the embrasures, where cannons were leant on. Additionally, the cobblestones present at the entrance of the Fort are possibly made by the same igneous rocks, as well as the base of the Lower Battery entrance.

Considering the environmental impact on the masonries, the mainly factor of surface deterioration can be attributed to biological colonization, in terms of moss and algae. In addition, salt efflorescences sampled from the moat (sample PB SF 5) revealed calcite as main crystalline phase recognized by XRD analysis (Table 2) and confirmed by ESEM-EDX investigations.

SAMPLE	ARAGONITE	CALCITE	MAGNETITE	PLAGIOCLASE	PYROXENE	QUARTZ
PB SF 1	-	+++	-	-	-	traces
PB SF 2	+++	+	-	-	-	-
PB SF 5	-	+++	-	-	-	-
PB SF 6	-	-	?	+++	traces	-
PB SF 7	-	-	traces	+++	traces/+	-
PB SF 8	+++	traces	-	-	-	-
PB SF 11	-	-	-	+++	+	+

Table 2 - X-Ray Powder Diffraction data of PB SF samples. Legend : +++ =dominant; ++ = abundant; + =present; traces; - =absent

5. Conclusions

The materials characterization highlighted four kind of stones in the masonries: corallite, biogenic limestone, basalt andesite and andesite. It has been observed that their use depends on the function, thus according to the strength of the stones, they have been utilized in different parts.

Environmental impact is mainly due to natural and climate factors, as biodeterioration and salt efflorescences. These latter ones are mainly composed by calcite, highlighting the aggressive effects of high percentage of relative humidity and water permeation phenomena which can dissolve calcium carbonate.

Therefore further analysis are ongoing to complete these preliminary investigations, in order to produce guidelines for current and future conservation works.

Acknowledgments

The authors want to thank the staff of Patronato de Portobelo y San Lorenzo for the availability and collaboration. A special acknowledgment to Franco Corticelli for ESEM-EDX analysis support.

References

Budd A. F. and Stolarski J. (2011), *Corallite Wall and Septal Microstructure in Scleractinian Reef Corals: Comparison of Molecular Clades Within the Family Faviidae*. Journal of Morphology 272. pp. 66–88.

Gobierno Nacional República de Panamá, Autoridad Nacional del Ambiente, *Atlas Ambiental*, (2010) pp. 26-31.

Gobierno Nacional República de Panamá, Instituto Nacional De Cultura Dirección Nacional Del Patrimonio Histórico, Oficina Del Casco Antiguo, Ciudad De Panamá (OCA) (2014), *Plan de emergencia de la propiedad C135, Fortificaciones de la Costa Caribeña de Panamá: Portobelo - San Lorenzo*. pp. 13-36.

http://whc.unesco.org/en/list/135

Osorio Ugarte K. (2015), *Report for the UNESCO World Heritage centre about the state of conservation. Fortifications On The Caribbean Side Of Panama: Portobelo - San Lorenzo*. pp. 10.

Spiteri, S.C. (1994). *Illustrated Glossary of Terms used in Military Architecture.*

Tejera Davis, E., (2007), Panamá: *Guía de Arquitectura y Paisaje - An Architectural and Landscape Guide*, Ed. bilingüe [1ª ed.], Junta de Andalucia, Instituto Panameño de Turismo, Gobierno de España.

World Monuments Fund (2003), *Portobelo - San Lorenzo: An approach to integrated conservation for sites containing endangered cultural and natural resources*. pp. 8-71.

TECHNART 2017, Non-destructive and microanalytical techniques in art and cultural heritage,
Bilbao, May 2 - 6, 2017 - ACCEPTED

Investigation on construction materials and their environmental interaction at the Panamanian UNESCO sites

Chiara Ciantelli[1,2*], Alessandro Sardella[1], Carmela Vaccaro[2] and Alessandra Bonazza[1]

(1) Institute of Atmospheric Sciences and Climate of the National Research Council of Italy, ISAC-CNR, Via Gobetti 101, 40129, Bologna, Italy
**email: C.Ciantelli@isac.cnr.it*

(2) Department of Physics and Earth Sciences - University of Ferrara, Via Saragat 1, 44100 - Ferrara, Italy

Two UNESCO sites belong to the Panamanian isthmus. Specifically, on the North coast, examples of military fortifications face the Caribbean Sea: the Fortresses of Portobelo Bay and Fort San Lorenzo (XVII-XVIII cent.); while, on the opposite shore, the first Spanish settlement arises on the Pacific Ocean: the nowadays called Monumental site of Panamá Viejo (XVI cent.) [1,2].

In order to improve the knowledge on the materials characterisation [3,4] and to evaluate the state of conservation related to the environmental impact, specimens sampled at the sites underwent mineralogical-petrographic, physical and chemical analyses (Stereomicroscope, PLM, XRPD, SEM-EDX, XRF, MIP and IC), highlighting at Panamá Viejo, masonries mainly composed of polygenic breccias, tuffites, basaltic andesites, rhyolites and sporadic rhyodacites. Considering Portobelo fortifications, coral limestones and sandstones have been identified as principal building materials, while basaltic andesite has been observed only at Fuerte de San Fernando. Finally, at Fuerte de San Lorenzo, tuffites and grainstones have been detected in the masonries; these latter ones were mainly utilized for realizing corners (as ornamental parts of the portals and the base blocks). Furthermore, potential quarries of raw materials have been identified and sampled, in order to define the provenance of the stones employed in the fabrication of buildings, and to compare the differences between the preservation of the rocks utilized in the masonries with the outcropping ones.

Lastly, this study allowed us to investigate the past, present and future interaction between these materials and the environment, utilizing dose-response functions for evaluating the damages due to the surface recession, salts cycles and biomass growth [5-7].

[1] Patronato de Panamá Viejo y Embajada de España en Panama. Panamá Viejo, de la aldea a la urbe, from village to city, 2006.
[2] World Monuments Fund, Instituto Nacional de Cultura (Panama), American Express Company, World Monuments Watch. Portobelo - San Lorenzo: An approach to integrated conservation for sites containing endangered cultural and natural resources, 2003, pp.8-71.
[3] Torres Montes L. Informe preliminar del examen mesoscópico de las ruinas de Panamá Viejo, 1996.
[4] Sanchez Nava M., Diagnostico del Deterioro de los Materiales Petreos de Construccion de la Ciudad de Panama Viejo, midiante su caracterizacion fisicoquimica. Thesis in quimica pharmaceutica biologa, Facultad de Quimica, Universidad Nacional Autonoma de Mexico, 2000.
[5] Bonazza A., Messina P., Sabbioni C., Grossi C. M., Brimblecombe P. Mapping the impact of climate change on surface recession of carbonate buildings in Europe. Science of the Total Environment (407), 2009, pp.2039-2050.
[6] Grossi C.M., Brimblecombe P., Menéndez B., Benavente D., Harris I., Déqué M. Climatology of salt transitions and implications for stone weathering. Science of the Total Environment (409), 2011, pp. 2577–2585.
[7] Gómez-Bolea A., Llop E., Ariño X., Saiz-Jimenez C., Bonazza A., Messina P., Sabbioni C. Mapping the impact of climate change on biomass accumulation on stone. Journal of Cultural Heritage (13), 2012, pp. 254–258.

The Panamanian UNESCO sites: construction materials and environmental decay

Chiara Ciantelli ([a,c*]), Alessandra Bonazza ([a]), Orlando Favoni ([b]), Renzo Tassinari ([c]) & Carmela Vaccaro ([c])

([a]) Institute of Atmospheric Sciences and Climate, ISAC-CNR, Via Gobetti 101, 40129 –Bologna, Italy *email: c.ciantelli@isac.cnr.it /cntchr@unife.it

([b]) Department of Materials, Environmental Sciences and Urban Planning - Università Politecnica delle Marche, Via Brecce Bianche 12, 60131 Ancona, Italy

([c]) Department of Physics and Earth Sciences - University of Ferrara, Via Saragat 1, 44122 –Italy

The preliminary results of the environmental impact on the UNESCO sites located in Panama here are presented.
This research project was born within a collaboration among the Italian National Research Council, Institute of Atmospheric Sciences and Climate, the University of Ferrara, Department of Earth Sciences, and the Patronages of Panama Viejo and Portobelo-San Lorenzo.
A first census of the rocks typologies utilized in the masonries of the monumental site of Panama Viejo and of the fortresses situated in Portobelo and San Lorenzo was performed, in order to understand which are the possible future damages processes, to whom the construction materials of these sites can undergo. In conjunction to this characterization, the evaluation of the current state of conservation was investigated, being a fundamental step for having a clearer hypothesis of the future situations.
According to the aforementioned purposes, several samples of natural stone have been collected and analysed from different buildings belonging to the archaeological site and to the fortifications. Specifically, observations of thin sections by Polarized Light Microscopy (PLM), followed by X-Ray Powder Diffraction (XRPD) were carried out for a mineralogical and petrographic characterization and for a primary evaluation of the state of conservation. Moreover, the Environmental Scanning Electron Microscopy (ESEM-EDX) was performed, on both thin sections and bulk samples, to investigate more in detail specific points previously selected by PLM. Furthermore, with the aim to classify the volcanic rocks, the X-Ray Fluorescence (XRF) technique was utilized to obtain the TAS (*Total Alkali* versus *Silica*) classification (Le Bas et al, 1986; Le Maitre 1989).
Finally, in order to study the physical features, as density and porosity, of the materials, Mercury Intrusion Porosimetry analysis (MIP) was realized.
Together with the materials study, for evaluating the potential risks, which can occur to these monuments, related to the tropical climate (Gobierno Nacional-República de Panamá, 2010) the environmental context was investigated, considering several climatic factors and parameters. For this reason, monitoring stations have been selected in proximity of the two areas under study, obtaining 30 years (1975-2005) of data concerning rainfall, temperature and relative humidity (http://biogeodb.stri.si.edu/physical_monitoring/research/panamacanalauthority).
Concluding, for the first time the construction materials belonging to the Panamanian cultural heritage, inscribed on the World Heritage List, have been characterized contextually to surrounding environment, basic element for future protection of such important heritage.

References

Gobierno Nacional -República de Panamá, Autoridad Nacional del Ambiente, Atlas Ambiental, (2010) 26-31
http://biogeodb.stri.si.edu/physical_monitoring/research/panamacanalauthority
Le Bas, M.J., Le Maitre , R.W.; Streckeisen, A., Zanettin, B.; A Chemical Classification of Volcanic Rocks based on the Total-Alkali-Silica Diagram; Journ. of Petrol., Vol.: 27, (1986) 745-750
Le Maitre, R.W., A Classification of Igneous Rocks and Glossary of Terms; Recommendations of the IUGS, Subcommission on the Systematics of Igneous Rocks, (1989) 33-38

Rend. Online Soc. Geol. It., Suppl. n. 1 al Vol. 40 (2016) 88° Congresso SGI, Napoli 2016

Impact of a Changing Environment on Panamanian UNESCO sites for a Sustainable Culture

Ciantelli C.[1-4], Déqué M.[2], Palazzi E.[3], Vaccaro C.[4], von Hardenberg J.[3] & Bonazza A.[1]

1. Institute of Atmospheric Sciences and Climate, ISAC-CNR, Bologna, Italy. 2. Météo-France/CNRM, CNRS, 42 Avenue Coriolis, F-31057 Toulouse, Cedex 01, France. 3. Institute of Atmospheric Sciences and Climate, ISAC-CNR, Torino, Italy. 4. Department of Physics and Earth Sciences - University of Ferrara, Italy.

Corresponding email: c.ciantelli@isac.cnr.it

Keywords: material characterization, cultural heritage, climate change, damage functions.

Panama, the narrowest strip of land of Central America, hosts two sites inscribed on the World Heritage List: the Archaeological site of Panama Viejo (XVI cent.) and the Fortresses of Portobelo and San Lorenzo (XVII-XVIII cent.).

In order to support the conservation and valorisation of these places, in 2014 a collaboration work was started between the Patronage of Panama Viejo, the Patronage of Portobelo and San Lorenzo, the Institute of Atmospheric Sciences and Climate of the Italian National Research Council (ISAC-CNR) and the Department of Earth Sciences of the University of Ferrara.

As a first step, the study was devoted to the characterization and the evaluation of the state of conservation of the building materials, obtained by mineralogical-petrographic, physical and chemical analyses (PLM, XRD, SEM-EDX, XRF, MIP and IC). Successively, in order to determine the environmental context, a selection of monitoring stations, near the sites of interest, recording climate parameters (near-surface air temperature, relative humidity and rainfall amount), have been selected among the network of the Authority Panama Canal. Moreover, the same parameters were collected from ARPEGE climate models (Déqué, 2010), both historical and scenario simulations, in order to utilize them for future damage predictions. Indeed, utilizing environmental data and applying specific damage functions it is possible to assess the deterioration phenomena occurring on heritage materials, for instance surface recession, biomass accumulation and transition of salts (respectively Bonazza et al., 2009; Gómez-Bolea et al., 2012; Grossi et al., 2011), as demonstrated within the 6 FP EC Noah's Ark Project (Sabbioni et al., 2012).

Therefore, this research work has allowed us to produce projections of possible climate change impacts on the Panamanian heritage, for the near to the far future (2011-2100), compared to the recent past (1985-2010).

Bonazza A., Messina P., Sabbioni C., Grossi C.M. & Brimblecombe P. 2009. Mapping the impact of climate change on surface recession of carbonate buildings in Europe. Science of the Total Environment, 407, 2039-2050.

Déqué M. 2010. Regional climate simulation with a mosaic of RCMs. Meteorologische Zeitschrift, 19, 3, Special Issue : Part 1 Sp. Iss. SI, 259-266, Doi: 10.1127/0941-2948/2010/0455.

Gómez-Bolea A., Llop E., Ariño X., Saiz-Jimenez C., Bonazza A., Messina P. & Sabbioni C. 2012. Mapping the impact of climate change on biomass accumulation on stone. Journal of Cultural Heritage 13, 254–258.

Grossi C.M., Brimblecombe P., Menéndez B., Benavente D., Harris I. & Déqué M. 2011. Climatology of salt transitions and implications for stone weathering. Science of the Total Environment 409, 2577–2585.

Noah's Ark Project, (2004-2007), http://noahsark.isac.cnr.it/

Sabbioni C., Brimblecombe P. & Cassar M. 2012. The Atlas of Climate Change Impact on European Cultural Heritage Scientific Analysis and Management Strategies, Anthem Press.

CONGRESO DE ANTROPOLOGÍA E HISTORIA DE PANAMÁ 2016

7, 8 y 9 de Septiembre de 2016

Título de póster: El conjunto monumental de Panamá Viejo: impacto del medio ambiente sobre los monumentos

Palabras clave: Panamá Viejo, Patrimonio Cultural, Conservación, Caracterización de materiales, Impacto del medio ambiente

Autores: Chiara Ciantelli [a,c], Silvia I. Arroyo [b], Carmela Vaccaro [c], Alessandra Bonazza [a]

[a] Instituto de Ciencias Atmosféricas y el Clima del Consejo Nacional de la Investigación de Italia (ISAC-CNR), via Gobetti 101, 40129, Bologna – Italia

[b] Patronato Panamá Viejo, Vía Cincuentenario, Panamá

[c] Departamento de Física y Ciencias de la Tierra, Universidad de Ferrara, via Saragat 1, 44122, Ferrara - Italia

Resumen

Panamá Viejo fue la primera ciudad fundada en el Pacífico Americano por los españoles, sobre una aldea de pescadores, en 1519. Fue inscrito en la lista de Patrimonio Mundial de la UNESCO como una extensión del distrito histórico de Panamá en el 2003, con una superficie aproximada de 28 hectáreas. Actualmente, se ha convertido en un sitio arqueológico en medio de una ciudad en crecimiento.

Dada su importancia local y global , es fundamental preservarla eficientemente. Por esta razón se realizó una investigación para evaluar los efectos de la contaminación y el cambio climático en el deterioro del sitio arquitectónico de Panamá Viejo. Este trabajo es el resultado de una colaboración entre el Patronato Panamá Viejo, Instituto de Ciencias Atmosféricas y el Clima del Consejo Nacional de la Investigación de Italia (ISAC-CNR) y el Departamento de Física y Ciencias de la Tierra de la Universidad de Ferrara.

Por lo tanto, se procedió a la caracterización de los materiales de un grupo de monumentos dentro del conjunto que se encuentre más afectado por el cambios climáticos y la polución, ya sea por su proximidad a carreteras o al mar. Estos son los conventos de la Merced, San Francisco, Compañía de Jesús y la Concepción, la torre de la Catedral, la casa Terrín, el fortín de la Natividad y las Casas Reales. También, el estudio evaluó el estado actual de conservación, es decir, el deterioro de los materiales de construcción en climas de estas latitudes.

Por último, a través de la utilización de modelos de diferentes escenarios ambientales y funciones de daño, será posible la identificación de riesgos y efectos a futuro en estos materiales para elaborar estrategias sostenibles para la conservación de la zona arqueológica.

Environmental effects on monuments exposed in the Panamanian Climate: the Archaeological Site of Panamá Viejo

Chiara Ciantelli[(1)*], Alessandra Bonazza[(1)], Yumo Ma[(1)], Paola De Nuntiis[(1)], Carmela Vaccaro[(2)], and Cristina Sabbioni[(1)]

(1) Institute of Atmospheric Sciences and Climate, ISAC-CNR, Via Gobetti 101, 40129, Bologna, Italy,
[*]email: C.Ciantelli@isac.cnr.it
(2) Dipartimento di Fisica e Scienze della Terra, Università degli studi di Ferrara, Via Saragat 1, 44100 - Ferrara, Italy

In the Isthmus of Panama several natural and cultural UNESCO sites are present [1], which unfortunately are at risk for the increase of human pressure and climate impact.
Specifically, this region has been classified as an equatorial zone [2], therefore it implies no significant variations of temperature during the whole year, which shows 27°C as annual mean value, in both the dry and rainy season, and yearly precipitation amounts of 3500 mm, on the Caribbean coast, and 2300 mm on the Pacific littoral [3].
Aim of this work is to analyze problems related to the preservation of the UNESCO archaeological site of Panamá Viejo, the first Spaniard settlement on the Pacific coast (XVI cent.), now located in the downtown of Panama City [4] .
Petrographic approach, carried out through observations in Optical Microscopy (OM) and Scanning Electron Microscopy (SEM-EDX), and non invasive X-Ray Fluorescence microanalysis (XRF), was used for the characterization of the materials, identifying principally silicate and carbonate rocks at the site. In addition, these chemical and mineralogical analyses were used to evaluate the state of conservation of materials, to identify the responsible agents of their deterioration and to highlight which are the effects and the degradation processes developed in these environmental conditions. The main decay causes observed are due to biodeterioration and chemical-physical decay, connected with the presence of high humidity, which can lead to cracks and detachments. Furthermore, the investigations allowed us to recognize quarries of raw materials supply, fundamental for future compatible restoration works.
Finally, monitoring stations of climate parameters were selected in the area under study, with the purpose of collecting data suitable for the application of damage functions with the aim of achieving a quantitative evaluation of the identified deterioration processes, such as biomass accumulation on stones [5] and surface recession [6].

[1] http://whc.unesco.org/en/list/
[2] Kottek, M., J. Grieser, C. Beck, B. Rudolf, And F. Rubel, World Map Of Köppen-Geiger Climate Classification Updated. Meteorol. Z. (15), (2006), 259-263.
[3] Gobierno Nacional - República de Panamá, Autoridad Nacional del Ambiente, Atlas Ambiental, (2010) 26-31
[4] Patronato de Panama Viejo e Emajada de Espana en Panama, (2006). Panama Viejo, de la aldea a la urbe, from village to city.
[5] Gómez-Bolea A., Llop E. , Ariño X., Saiz-Jimenez C., Bonazza A., Messina P., Sabbioni C., Mapping the impact of climate change on biomass accumulation on stone, Journal of Cultural Heritage 13 (2012) 254–258
[6] Bonazza A., Messina P., Sabbioni C., Grossi C. M., Brimblecombe P. Mapping the impact of climate change on surface recession of carbonate buildings in Europe. Science of the Total Environment 407, (2009) 2039-2050